METHODS FOR IMPROVING CRANE PERFORMANCE AND EASE OF USE

A Dissertation
Presented to
The Academic Faculty

by

Kelvin Chen-Chih Peng

In Partial Fulfillment
of the Requirements for the Degree
Doctor of Philosophy in the
The Woodruff School of Mechanical Engineering

Georgia Institute of Technology
December 2013

METHODS FOR IMPROVING CRANE PERFORMANCE AND EASE OF USE

Approved by:

William Singhose, Advisor
School of Mechanical Engineering
Georgia Institute of Technology

Aldo Ferri
School of Mechanical Engineering
Georgia Institute of Technology

Mark Costello
School of Aerospace Engineering, School of Mechanical Engineering
Georgia Institute of Technology

Wayne Li
School of Industrial Design
Georgia Institute of Technology

David Frakes
School of Biological and Health Systems Engineering, School of Electrical, Computer, and Energy Engineering
Arizona State University

Date Approved: November 1, 2013

Thou shalt not waste paper and pages
with double-spacing and
single-sided printing;
Nor on vain, grandiose quotations,
which, despite its brevity,
typically occupies an entire page such as this one;
Its notion of self-glorification accentuated
by the vast unused white space that surrounds it.

- God of saving the rain forests[1]

[1]You should be reading this on a screen, rather than wastefully printing this out on paper anyway. Besides, who really reads these dedications, let alone other people's dissertations anyway?

ACKNOWLEDGEMENTS

I would like to thank and acknowledge the following:

- My family, for their loving support.
- My advisor, Dr. Bill Singhose, for tolerating me for so many years and giving me good suggestions and feedback on my research. Also, for giving me ample freedom to do my own things, A.K.A. procrastination, and for providing me the sustenance I needed in order to survive, A.K.A. salary.
- My committee members, for listening to me rant for a few hours and "perusing" my long and protracted dissertation. But most of all, I want to acknowledge my committee for graciously signing a piece of paper. Even though it is just a piece of paper, its significance is great, for it is essentially my release document from many years of voluntary self-imprisonment that is graduate school.
- Group members that came before me: Dr. Joshua Vaughan, Dr. Khalid Sorensen, and by extension, Dr. John Huey and Dr. Jason Lawrence. Many parts of this dissertation were built upon the foundations of their work, i.e. to ctrl-c and ctrl-v from.
- My labmates, for their companionship. Also, for the free food. Never forget the food. Furthermore, there is an unspoken rule that the food one brings to group meetings permanently becomes the group's food, by default. Do not take home yummy food that is sure to be popular with the group and thus would be consumed after the meeting. If the food one brings is yucky, feel free to take that home: a) one should have never brought yucky food in the first place, and b) one shall never leave yucky food to rot in the fridge. May the Singhose group member reading this sentence right now remember to never violate these rules.
- All the friends I have made during my time in Atlanta.
- My collaborators: Joe Bhaumik, Lee Stokes, Nathan Knight, Dr. Sirri Sunay Gurleyuk, Ranj Saeed, John Danielson from the Boeing Company, and Dr. Mikko Heikkila and Kari Wallgren from Konecranes.
- My sponsors: Siemens Energy and Automation and Boeing Research and Technology for their support of this work.

TABLE OF CONTENTS

LIST OF TABLES

LIST OF FIGURES

SUMMARY

Cranes are widely used in material-handling and transportation applications, e.g. in shipyards, construction sites, and warehouses. As they are critical to the economic vitality of modern-day industries, improving crane performance and ease of use are important contributors to industrial productivity, low production costs, and workplace safety.

In a typical crane operation, a payload is lifted, moved to its destination, and then lowered into place. This dissertation aims to improve crane performance and reduce task difficulty for the human operator in the movements mentioned above, namely: 1) Moving payloads laterally in the horizontal plane, 2) Lifting payloads off the ground, and 3) Lowering or laying down payloads on the ground.

The design of a novel and intuitive human-machine control interface is the focus for improving operations that involve moving payloads laterally. The interface allows operators to drive a crane by simply moving a hand-held device through the desired path. The position of the device, which is tracked by sensors, is used to generate command signals to drive the crane. This command is then input-shaped such that payload oscillations are greatly reduced, making it much easier for the operator to drive the crane. Several facets of this crane control method are examined, such as control structure and stability, usability contexts, modes of operation, and quantitative measures (by means of human operator studies) of performance improvements over standard crane control interfaces.

Lifting up a payload can be difficult for the operator, if the hoist is not properly centered above the payload. In these potentially dangerous and costly "off-centered" lifts, the payload may slide on the ground and/or oscillate in the air after it is hoisted. Newtonian and Coulomb friction models that focus on the stiction-sliding-separation contact dynamics are derived and experimentally verified to study off-centered lifts. Then, with the goal of aiding operators during lift operations, simple but practical, self-centering solutions are proposed and implemented.

Laying down or lowering a payload to the ground can also be challenging for operators in certain situations. For example, laying down a long, slender payload from a vertical orientation in the air, to a horizontal position on a flat surface. If the operator does not properly coordinate the motions of the crane in the vertical and horizontal directions simultaneously, then the potential hazards that may occur during these operations include: 1) slipping of the pivot about which the payload rotates, leading to sudden and dangerous payload movements; and 2) excessive hoist cable angles that lead to "side-pull" problems. Newtonian and Coulomb friction models are derived to describe this lay-down scenario. The forces and motions experienced by the payload are then used to determine the motion trajectories that the crane and payload should follow to execute a successful lay-down maneuver.

Finally, a special chapter is included to address the oscillation control of systems that have on-off nonlinear actuators, such as cranes powered by relay-controlled circuits. Due to their simplicity, ruggedness, and long service life, this type of crane can be commonly found in older factories or in applications where precise motion control is not a strict requirement. However, controlling payload oscillations on this type of crane is challenging for two reasons: 1) Relays that can only be turned on or off allow for only limited control over the crane velocity; and 2) These cranes typically have nonlinear asymmetrical acceleration and deceleration properties. Methods are derived for determining the relay switch-times that move single-pendulum and double-pendulum payloads with low residual oscillations.

CHAPTER I

INTRODUCTION

Cranes are used to transport heavy loads at construction sites, shipyards, factories, and warehouses throughout the world. They are critical to the economic vitality of modern-day industries. Therefore, improving crane performance and ease of use are important contributors to industrial productivity, low production costs, and workplace safety. Figure 1.1(a) is a picture of a bridge crane, a type of crane that is the focus of this dissertation. Specifically, it is the 10-Ton industrial bridge crane in the HiBay of the MaRC building at Georgia Tech. This particular crane was used in many experiments in this dissertation.

Figure 1.1(b) shows a schematic of a typical bridge crane. A bridge crane consists of a fixed overhead runway, a bridge that travels along the runway, and a trolley that travels along the bridge. The hook is suspended from the trolley by hoist cable(s). Depending on the configuration, the payload and hook may be considered to be the same body (or point mass), as in Figure 1.1(a), or the payload and hook may be multiple, separate bodies, as in Figure 1.1(b).

All cranes use vertical suspension cables to lift payloads, thereby creating the possibility of pendulum-like payload oscillation. Depending on payload configurations, more complicated oscillation dynamics may become significant, such as double-pendulum [118, 45, 2], or hoist-related oscillatory dynamics [122]. Cranes that contain rotational joints are more difficult to control because their nonlinear dynamics create additional complexities [68, 47, 81, 64]. A primary method utilized by the industry to limit this motion-induced oscillation has been to train a skilled operator and to move slowly. Another method is to employ additional people physically manipulating the payload using ropes, or by directly pushing and pulling on it. While this does serve to reduce payload oscillation and, thereby, increase safety, it does not provide efficient operating conditions.

Significant efforts have been made by researchers to develop crane controllers that reduce the oscillatory response from issued commands and/or external disturbances. An overview of these efforts in crane control, as well as dynamic crane models, is provided in [1]. Crane control methods can be divided into open and closed-loop methods. For crane control, the open-loop methods can be further divided into optimal trajectory planning and input shaping.

Closed-loop crane controllers use information about the current state of the system (e.g. payload swing angle, trolley position, etc.) to generate commands that drive the system toward the desired state. Many researchers have advocated a wide variety of feedback methods for crane control. Examples include: state feedback [80, 3], wave-based [67], sliding-mode [65], neural networks [62], and H_∞ [40]. One primary disadvantage of these methods is that the current state of the system must be well known. In practice, this is often difficult to achieve. Of particular difficulty is sensing the hook and payload positions.

Optimal trajectory planning methods seek to eliminate vibration, while avoiding the sensing problems of closed-loop methods, by using pre-planned trajectories to move the crane through the workspace. The problem is typically formulated as a minimum time optimization problem, subject to vibration constraints [24, 35]. The primary restriction of this method is that the desired motion of the crane must be known in advance, in addition to the initial conditions of the maneuver. Another major drawback is that generating the optimal profiles can be computationally expensive.

In this dissertation, input shaping is used extensively to remove complex oscillatory dynamics, which allows operators to contend with much simpler rigid-body dynamics. This significantly reduces the complexity of the operator's task, freeing the operator to focus on higher-level tasks, such as path planning and paying greater attention to surroundings.

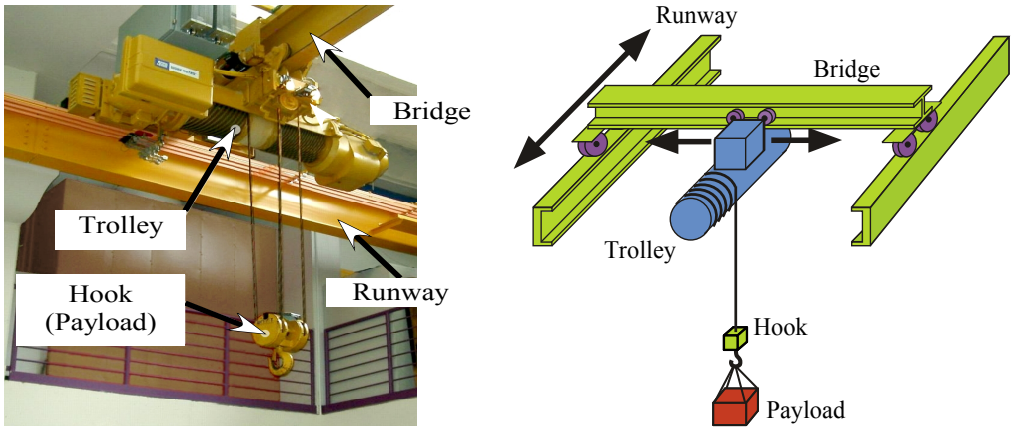

(a) HiBay Crane (b) Schematic

Figure 1.1: Bridge Crane

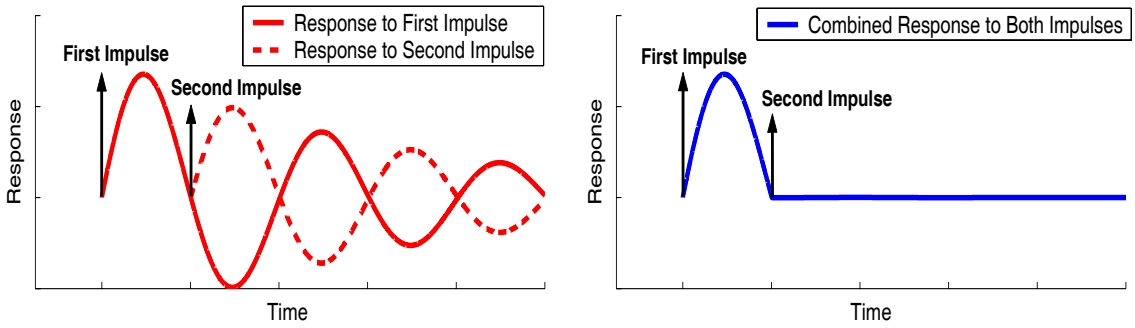

(a) System Response to Each Impulse (b) System Response to Both Impulses

Figure 1.2: Destructive Interference Caused by a Sequence of Impulses

1.1 Input Shaping

Input shaping is a command filtering technique that was designed for the purpose of reducing motion-induced oscillation in flexible systems [98, 85]. Reference commands modified by an input-shaping filter are issued to a system instead of unfiltered commands. The modified commands cause the system to cancel out its own motion-induced oscillation.

To demonstrate this fundamental interference principle, consider the response of a lightly damped second-order system to a series of two impulses, as shown in Figure 1.2(a). Figure 1.2(b) shows the combined system response resulting from superposition. These figures demonstrate that impulses of appropriate amplitudes and times can be applied to a system in such a way that the resonant modes of the system combine destructively, resulting in zero residual oscillation.

The input-shaping process is an extension of the concept illustrated in Figure 1.2(b) that allows arbitrary reference commands, rather than just sequences of impulses, to produce low residual oscillation. This process, shown in Figure 1.3, convolves an appropriate impulse sequence, known as an input shaper, with a reference command to produce a shaped command. The shaped command has the same oscillation-reducing properties as the original set of impulses.

It has been shown that operators who drive a crane assisted by input shapers generate safer and more efficient crane motions than operators without such assistance [68, 44, 45, 118]. Furthermore, input shaping has been successfully implemented on many systems where vibration is problematic, such as bridge cranes [92, 103], tower cranes [10, 51, 118], coordinate measurement machines [82, 90],

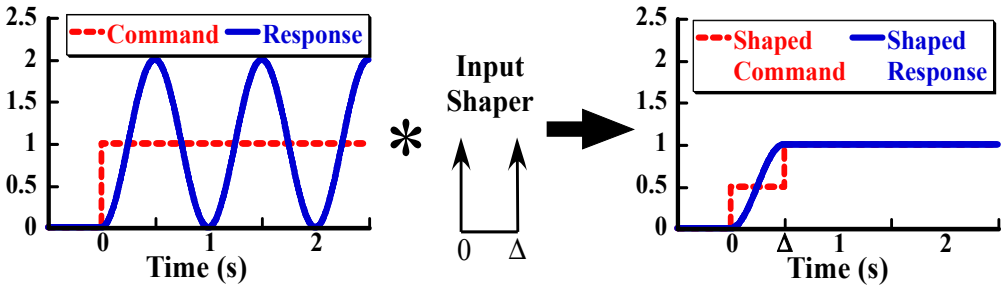

Figure 1.3: The Input-Shaping Process

robotic arms [50, 57], micro-milling machines [18], and spacecrafts [93, 112].

1.1.1 Input Shaper Constraint Equations

In order to determine the impulse amplitudes and time locations of an input shaper, certain design constraints must be satisfied. The primary design constraint is a limit on the amplitude of vibration caused by the shaper. The normalized, percentage residual vibration (PRV) amplitude of an under-damped, second-order system from a sequence of n-impulses is given by [85]:

$$PRV = V(\omega,\zeta) = e^{-\zeta\omega t_n}\sqrt{[C(\omega,\zeta)]^2 + [S(\omega,\zeta)]^2} \tag{1.1}$$

where,

$$C(\omega,\zeta) = \sum_{i=1}^{n} A_i e^{\zeta\omega t_i}\cos(\omega t_i\sqrt{1-\zeta^2}) \tag{1.2}$$

$$S(\omega,\zeta) = \sum_{i=1}^{n} A_i e^{\zeta\omega t_i}\sin(\omega t_i\sqrt{1-\zeta^2}) \tag{1.3}$$

and ω is the natural frequency of the system, ζ is the damping ratio, and A_i and t_i are the i^{th}-impulse amplitude and time, respectively.

Equation (1.1) gives the ratio of vibration with input shaping to that without input shaping. A constraint on residual vibration amplitude can be formed by setting (1.1) less than or equal to a tolerable level of residual vibration, V_{tol}, at the modeled natural frequency and damping ratio. This can be expressed as:

$$V(\omega,\zeta) \leq V_{tol} \tag{1.4}$$

Given the transcendental nature of (1.4) there are an infinite number of solutions. Therefore, additional constraints must be imposed to reach a solution. To ensure the fastest solution possible, the time of the last impulse is typically minimized:

$$\min(t_n) \tag{1.5}$$

Impulses amplitudes should also sum to one, which ensures the shaped command reaches the same set-point as the unshaped command. This constraint is expressed as:

$$\sum_{i=1}^{n} A_i = 1 \tag{1.6}$$

Additional constraints on impulse amplitude are still required, as those listed thus far will drive impulse amplitudes toward positive and negative infinity. One such constraint requires that the input shaper be comprised only of positive impulses. Accordingly, this class of filters is called positive input shapers. An alternative constraint permits the impulses to assume negative, but finite, values. Therefore, this class of filters is called negative input shapers.

1.1.2 ZV Shaper

The most basic shaper can be obtained by solving (1.1) when V is set equal to zero. Accordingly, this filter is aptly named the zero-vibration (ZV) input shaper [98, 85]. The impulse amplitudes and times are:

$$\begin{bmatrix} A_i \\ t_i \end{bmatrix} = \begin{bmatrix} \frac{1}{1+K} & \frac{K}{1+K} \\ 0 & \pi/\omega_d \end{bmatrix} \tag{1.7}$$

where,

$$K = exp\left(\frac{-\zeta\pi}{\sqrt{1-\zeta^2}}\right)$$

and,

$$\omega_d = \omega_n\sqrt{1-\zeta^2}$$

1.1.3 ZVD Shaper

While the ZV shaper performs well when the modeled frequency is at or very near the actual system frequency, large modeling errors can result in unacceptably high oscillation. An input shaper that is more robust to frequency uncertainty can be obtained by setting to zero the derivative of (1.1) with respect to frequency. Accordingly, this filter is named the zero-vibration and derivative (ZVD) shaper [85]. The impulse amplitudes and times are:

$$\begin{bmatrix} A_i \\ t_i \end{bmatrix} = \begin{bmatrix} \frac{1}{(1+K)^2} & \frac{2K}{(1+K)^2} & \frac{K^2}{(1+K)^2} \\ 0 & \pi/\omega_d & 2\pi/\omega_d \end{bmatrix} \tag{1.8}$$

Furthermore, additional robustness to frequency modeling errors may be obtained by setting the second, and third derivatives of (1.1) to zero, to obtain ZVDD and ZVDDD shapers, respectively [85].

1.1.4 EI Shaper

To this point, the shapers discussed have been formed using a constraint that there be zero residual vibration at the modeled frequency. However, even in real world systems for which a good model exists, there will be some modeling error and vibration will occur at the design frequency. Realizing this, the designer should relax this constraint to one in which residual vibration remains below some tolerable level, V_{tol}, at the modeled frequency [94].

The first shaper utilizing this idea was called the Extra Insensitive (EI) shaper [94]. The EI shaper has the same impulse times as the ZVD shaper, but has different amplitude values that lead to greater robustness. For undamped systems, it has the form:

$$EI = \begin{bmatrix} A_i \\ t_i \end{bmatrix} = \begin{bmatrix} \frac{1+V_{tol}}{4} & \frac{1-V_{tol}}{2} & \frac{1+V_{tol}}{4} \\ 0 & \frac{\tau}{2} & \tau \end{bmatrix} \tag{1.9}$$

where V_{tol} is the tolerable level of vibration (*e.g.* $0.05 = 5\%$) and τ is the undamped vibration period of the system.

1.1.5 Sensitivity Curves and Insensitivity

Most measures of input-shaping robustness focus on the sensitivity curve of the input shaper. The natural frequency sensitivity curve for a ZV shaper is shown by the solid line in Figure 1.4. The vertical axis is the Percent Residual Vibration (PRV) and the horizontal axis is the actual natural frequency, ω, normalized by the modeled frequency, ω_m. The curve indicates the amplitude of

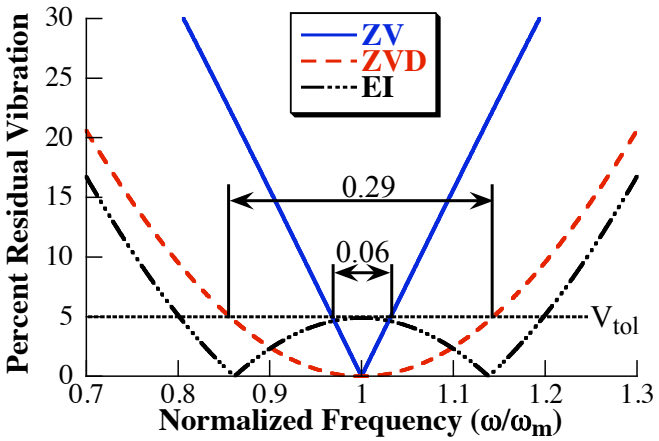

Figure 1.4: Sensitivity Curves for ZV, ZVD, and EI Shapers

residual vibration as a function of modeling errors in frequency. While a sensitivity curve itself is not a measure of robustness, a qualitative picture of the robustness of a command can be obtained from it and quantitative measures can be extracted from it.

One key quantitative measure of robustness derived from the sensitivity curve is *Insensitvity* [94]. Insensitivity is the width of the sensitivity curve at a tolerable vibration level, V_{tol}, with respect to the parameter of interest. For example, Figure 1.4 shows the ZV shaper has an Insensitivity at $V_{tol} = 5\%$, $I(5\%)$, of 0.06. The ZVD shaper has an Insensitivity at the same level of 0.29.

The sensitivity curve of the EI shaper is also shown in Figure 1.4. Note that the EI is the same duration as the ZVD shaper, but has much more Insensitivity, as the figure clearly shows. Also, note the characteristic hump of the EI shaper's sensitivity curve. Its PRV is equal to V_{tol} at the modeled frequency, and zero at two points on either side of the normalized frequency. Shapers that extend on the concept of EI have progressively larger number of humps and are called Multi-Hump EI Shapers [93].

The large robustness (width of frequency suppression range) provided by both the ZVD and EI shapers shown in Figure 1.4 does not come without cost. Each of these robust shapers is longer than the relatively non-robust ZV shaper. This trend continues across all robust shaping methods [121].

1.1.6 UMZV Shaper

The input shapers discussed so far consist of only positive impulses. Shorter duration input shapers may be obtained if the impulse amplitudes are permitted to assume negative values [96]. If the impulse amplitudes are constrained to equal 1 or -1, then the shaper can be used to produce time-optimal or fuel-optimal commands [53, 88]. A frequently encountered negative input shaper is obtained by enforcing the unity-magnitude constraint, and solving (1.1) when V is set equal to zero. These unity-magnitude (UM) shapers also have the property that when convolved with an appropriate baseline command (e.g. a step), they produce a shaped command that is suitable for on-off (e.g. relays) actuators. The UM zero-vibration, or UMZV, shaper may be expressed as [96]:

$$\begin{bmatrix} A_i \\ t_i \end{bmatrix} = \begin{bmatrix} 1 & -1 & 1 \\ 0 & t_2 & t_3 \end{bmatrix} \tag{1.10}$$

where,

$$\begin{bmatrix} t_2 \\ t_3 \end{bmatrix} \cong \begin{bmatrix} (2\pi/\omega_d)(1/6 + 0.272\zeta + 0.203\zeta^2) \\ (2\pi/\omega_d)(1/3 + 0.005\zeta + 0.179\zeta^2) \end{bmatrix}$$

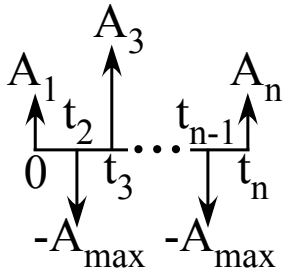

Figure 1.5: Specified Negative Amplitude Input Shaper

The expression in (1.10) is the product of curve fitting numerical solutions for the impulse times. It provides the exact solutions for t_2 and t_3 when $\zeta = 0$. Furthermore, the resulting impulse times for lightly damped systems are within 0.5% of their actual values over the range of $0 < \zeta \leq 0.3$.

1.1.7 Specified Negative Amplitude Shaper

Another method to remove the positive amplitude constraint is to specify the maximum negative impulse amplitude the input shaper may contain. This constraint can be stated as:

$$0 < A_i \leq 1 \qquad \text{when } i \text{ is odd} \tag{1.11}$$

$$A_i = -A_{max} \qquad \text{when } i \text{ is even} \tag{1.12}$$

where A_{max} is the maximum negative amplitude allowed. Shapers formed using this amplitude constraint are called Specified Negative Amplitude (SNA) shapers [87] and follow a form similar to that shown in Figure 1.5.

SNA shapers are also named according to the additional constraints used to form them. The SNA-ZV shaper is formed using the zero vibration constraint, analogous to the ZV shaper. For undamped systems, its form is given by:

$$\begin{bmatrix} A_i \\ t_i \end{bmatrix} = \begin{bmatrix} A_1 & -A_{max} & A_3 \\ 0 & \frac{1}{\omega}\cos^{-1}\left(\frac{A_{max}}{2A_1}\right) & \frac{1}{\omega}\cos^{-1}\left(\frac{A_{max}^2}{2A_1^2} - 1\right) \end{bmatrix} \tag{1.13}$$

where

$$A_1 = A_3 = \frac{1 + A_{max}}{2}$$

1.1.8 Multi-Mode Shaper

There are two primary methods for designing shapers for systems where multiple modes of vibration need to be reduced [34, 89]. The first is the convolution method, where an input shaper is designed independently for each mode of vibration. Then, the individual shapers are convolved together to produce a multi-mode shaper. This process is demonstrated in Figure 1.6. The duration of the multi-mode shaper is equal to the sum of the durations of the individual shapers. Incidentally, the ZVD shaper discussed previously is simply two identical ZV shapers convolved together.

An alternative method is one that generates 'simultaneous' shapers. Unlike the convolution method, where vibration constraints on each mode are satisfied separately, a direct solution can be obtained by simultaneously satisfying the constraint equations for each mode. For example, the zero-vibration equations for two distinct frequencies, ω_1 and ω_2, that have associated damping

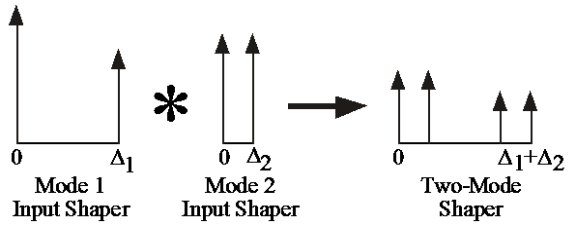

Figure 1.6: Generating a Multi-Mode Input Shaper by Convolution

ratios of ζ_1 and ζ_2 are:

$$\begin{aligned}
0 &= \sum_{i=1}^{n} A_i e^{\zeta_1 \omega_1 t_i} \cos(\omega_1 t_i \sqrt{1-\zeta_1^2}) \\
0 &= \sum_{i=1}^{n} A_i e^{\zeta_1 \omega_1 t_i} \sin(\omega_1 t_i \sqrt{1-\zeta_1^2}) \\
0 &= \sum_{i=1}^{n} A_i e^{\zeta_2 \omega_2 t_i} \cos(\omega_2 t_i \sqrt{1-\zeta_2^2}) \\
0 &= \sum_{i=1}^{n} A_i e^{\zeta_2 \omega_2 t_i} \sin(\omega_2 t_i \sqrt{1-\zeta_2^2})
\end{aligned}$$

These equations can be solved simultaneously to determine the impulse amplitudes and time locations of the shortest duration two-mode ZV shaper. Simultaneous shapers are more difficult to generate than convolving two single-mode shapers obtained from closed-form equations. However, simultaneous shapers always have shorter durations than a convolved shaper.

1.1.9 SI Shaper

It is desirable to tailor the robustness of a shaper to the specific system for which it is being designed. The Specified Insensitivity (SI) Shaper does this by generating constraint equations to match the desired level of robustness [90]. An SI shaper can be generated for any desired level of Insensitivity using the frequency-sampling method. This is an approximation method in which the vibration is limited to below some tolerable level at M points within the desired range of frequency suppression.

This frequency-sampling process is shown graphically in Figure 1.7. Shaper impulse amplitudes and times are then generated using optimization routines. In theory, an infinite number of points is needed to assure that the vibration remains below the tolerable level. However, in practice, because sensitivity curves cannot rapidly change their slope, a small number of points (therefore less computationally expensive) can be used to effectively suppress vibration over a wide range of parameters.

Specified Insensitivity shapers provide the greatest level of robustness for any given shaper duration [90]. Another advantage of SI shapers is that they can be designed to have non-symmetric sensitivity curves, such that the shaper is more robust to increases in frequency than decreases, or vice versa. SI shapers can also be designed for any level of tolerable vibration, and for systems with multiple modes of vibration. One disadvantage of the SI shaper is that an optimization is required to solve for the impulse amplitudes and time locations.

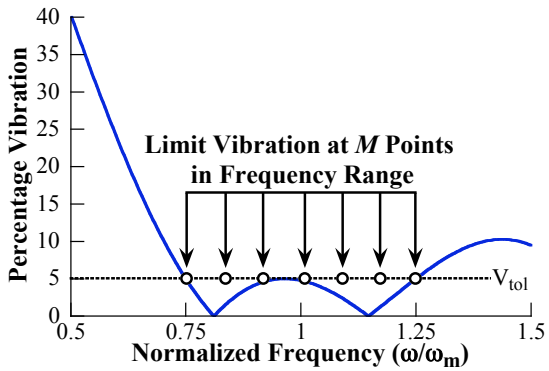

Figure 1.7: SI Shaper Frequency Sampling Solution Method

1.2 Dissertation Contributions and Organization

As stated before, in this dissertation, input shaping is the primary way of controlling payload oscillations. Solving the oscillation problem allows researchers to explore other aspects of improving crane operation. These aspects are introduced below, and further background information is provided in the corresponding chapters of this dissertation.

In a typical crane operation, a payload is lifted, moved to its destination, and then lowered into place. This dissertation aims to improve crane performance and reduce task difficulty for the human operator in the movements mentioned above, namely: 1) Moving payloads laterally in the horizontal plane, 2) Lifting payloads off the ground, and 3) Lowering or laying down payloads on the ground.

The design of a novel and intuitive human-machine control interface is the focus for improving operations that involve moving payloads laterally. The interface allows operators to drive a crane by simply moving a hand-held device through the desired path. The position of the device, which is tracked by sensors, is used to generate command signals to drive the crane. This command is then input-shaped such that payload oscillations are greatly reduced, making it much easier for the operator to drive the crane. Several facets of this crane control method are examined, such as control structure and stability, usability contexts, modes of operation, and quantitative measures (by means of human operator studies) of performance improvements over standard crane control interfaces.

Lifting up a payload can be difficult for the operator, if the hoist is not properly centered above the payload. In these potentially dangerous and costly "off-centered" lifts, the payload may slide on the ground and/or oscillate in the air after it is hoisted. Newtonian and Coulomb friction models that focus on the stiction-sliding-separation contact dynamics are derived and experimentally verified to study off-centered lifts. Then, with the goal of aiding operators during lift operations, simple but practical, self-centering solutions are proposed and implemented.

Laying down or lowering a payload to the ground can also be challenging for operators in certain situations. For example, laying down a long, slender payload from a vertical orientation in the air, to a horizontal position on a flat surface. If the operator does not properly coordinate the motions of the crane in the vertical and horizontal directions simultaneously, then the potential hazards that may occur during these operations include: 1) slipping of the pivot about which the payload rotates, leading to sudden and dangerous payload movements; and 2) excessive hoist cable angles that lead to "side-pull" problems. Newtonian and Coulomb friction models are derived to describe this lay-down scenario. The forces and motions experienced by the payload are then used to determine the motion trajectories that the crane and payload should follow to execute a successful lay-down maneuver.

Finally, a special chapter is included to address the oscillation control of systems that have on-off nonlinear actuators, such as cranes powered by relay-controlled circuits. Due to their simplicity, ruggedness, and long service life, this type of crane can be commonly found in older factories or in applications where precise motion control is not a strict requirement. However, controlling payload oscillations on this type of crane is challenging for two reasons: 1) Relays that can only be turned on or off allow for only limited control over the crane velocity; and 2) These cranes typically have nonlinear asymmetrical acceleration and deceleration properties. Methods are derived for determining the relay switch-times that move single-pendulum and double-pendulum payloads with low residual oscillations.

This dissertation is organized as follows: In Chapter 2, the hand-motion crane control interface is introduced and described. Its control architecture and stability are analyzed. Formed from this work is the shaper and integrator in the loop of a feedback controller that moves systems in minimal time without overshoot or residual oscillations. In Chapter 4, various modes of operation using hand-motion control are explored. Results from operator studies are summarized to quantify the improvement of hand-motion over traditional interfaces. Chapter 5 focuses on lifting payloads off the ground. The problems associated with off-centered lifts and auto-centering techniques are discussed. The topic of Chapter 6 is laying down long slender payloads. Chapter 7 examines controlling oscillations on relay controlled cranes with nonlinear actuators. Finally, the dissertation concludes in Chapter 8, where future work is also discussed.

CHAPTER II

HAND-MOTION CRANE CONTROL

Traditional crane control interfaces (e.g. push-button pendents, joysticks, and directional levers) require operators to be skilled in the cognitive process of transferring the desired manipulation path into a sequence of precisely interface actions. Additionally, operators can only directly drive the overhead trolley, not the payload. Therefore, the operators must account for the large offset in the vertical direction and the time lag between their commands, and the delayed oscillatory response of the payload.

For example, Figure 2.1 illustrates pendent control of a typical overhead crane. If the operator wants to drive the crane through a cluttered workspace, then the desired path must be mapped into a sequence of events where the "Forward (F)", "Backward (B)", "Left (L)", and "Right (R)" buttons are pushed at the correct times and in the correct sequence. Furthermore, as operators move through the workspace, they may rotate their bodies and change the direction they are facing. In such cases, operators must account for their body orientation relative to the crane, because the Forward button might not coincide with the "forward" direction of the operator (i.e. the direction that they are facing). Instead, the button might cause motions to the left, right, backward, or in any direction 360° relative to the operator.

Figure 2.2(a) shows an example move through a cluttered workspace. The solid line represents a typical trolley path that the operator would have in his/her mind for navigating around some obstacles. Ideally, the payload should also follow this path. Figure 2.2(b) shows the sequence of pushes on a 4-button pendent that would move the trolley along that path. The operator would need to execute this sequence by pressing each button at specific times and for specific durations. Furthermore, as the operator moves through the workspace, he/she would need to be mindful of the direction of motion (relative to their body) that each button induces. Figure 2.2(c) emphasizes the point that even if the trolley was moved along the path, the operator still needs to account for the payload oscillations induced by the trolley motion. Such payload oscillations are dangerous, time-consuming, and can cause costly accidents.

In short, standard crane control interfaces have much room for improvement. A higher performing interface can increase the efficiency of cranes, reduce costs, and improve safety. Such an interface would need to simultaneously address two issues:

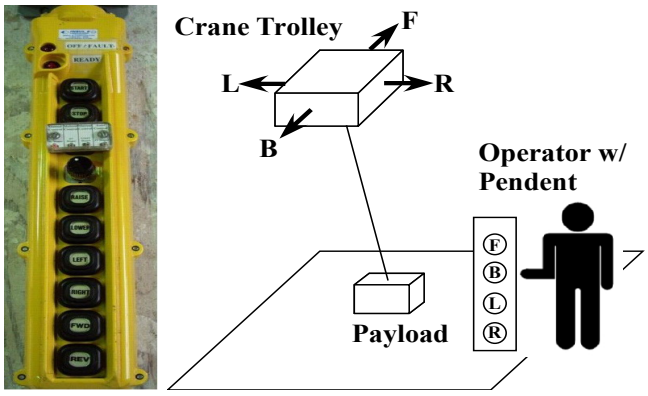

(a) Pendent (b) Schematic

Figure 2.1: Push-Button Pendent Crane Control

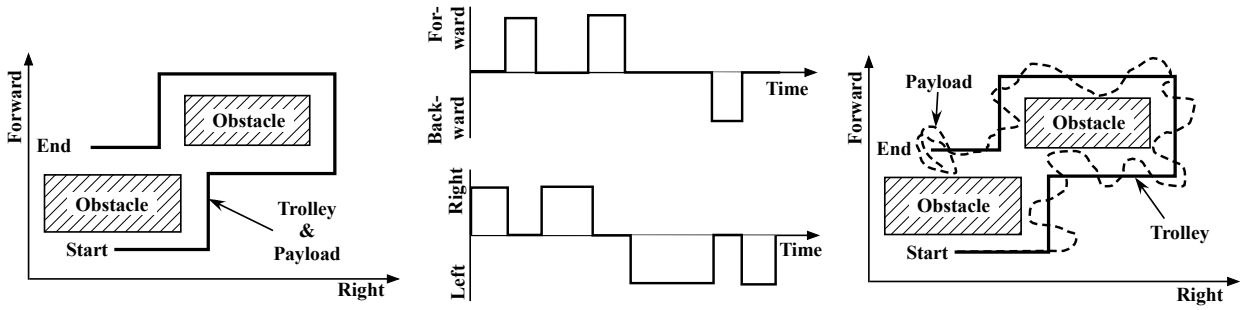

(a) Ideal Trolley & Payload Paths (b) Button-Pushing Sequence (c) Actual Payload Response

Figure 2.2: Push-Button Crane-Driving Example

- Easing the cognitive process of transferring the desired path into interface actions.
- Reducing problematic payload oscillations induced by trolley motion.

This dissertation presents a novel and intuitive control interface that allows an operator to drive a crane by simply moving a hand-held device. Various sensors track the position of the hand-held device, which is used to generate command signals to drive the crane. These command signals are then input shaped to eliminate payload oscillations.

2.1 Background

While significant efforts have been made to improve crane operation by controlling the dynamic response (i.e. problematic payload oscillations) to issued commands, relatively little consideration has been given to the way (or interface) in which the operator issues those commands [104]. In Section 2.1.1, past work on crane-related interface design is reviewed. Section 2.1.2 takes a closer examination of efforts to improve interfaces in industrial settings.

2.1.1 Design of Interfaces

Historically, interface design has been the collaborative work between many different fields: psychology, human computer interaction (HCI), and industrial design, to name a few. Presented here are some significant findings in this field that pertain, or may be readily applied to, crane control.

Sheridan developed a supervisory control model for automation systems that describes the modes of interaction between a human operator and the controlled system [83]. A complementary interaction model was developed by Stahre [105] that divided the process control system into two interconnected processes. When applied to cranes, these are the human interface and the crane instruction processes. Rasmussen associated operator tasks with operator cognitive behavior [77]. An informative and descriptive framework for evaluating operator tasks and associated cognitive behaviors is the cognitive activity demand matrix, developed by Hollnagel [30]. Amat [4], and Frigola [19], emphasized the importance of gesture-based control because of its low-effort intuition-based cognitive demand. Finally, Fujita distinguished between skilled and unskilled human operators based upon in-the-loop operational ability [20].

It has been proven that interfaces that are tailored to the cognitive processes associated with specific control systems have beneficial effects [26, 37, 116]. For example, in the field of laparoscopic surgery, medical robots such as the da Vinci improve on the traditional procedure by allowing surgeons to operate in a more ergonomic manner and with less cognitive load [110, 6]. The controls move in the same direction as the the end effectors for da Vinci, unlike traditional laparoscopic procedures where surgeons have to reverse map the controls due to the instruments' pivot point at the point of insertion.

Another way to improve interfaces is to capitalize on familiar concepts. The goal of skeuomorphism is to deliberately make the new look comfortably old and familiar. It has been the 'soul' of the design philosophy behind many Apple products [36, 111, 61]. The range of physical metaphors and physical gestures that users employed to control the Macintosh, iPhone, and iPad map directly with what people already do in the real world. For example, click, drag, and drop with the mouse to emulate physically picking up, moving, and releasing objects; swiping across the touchscreen to simulate page turning; and scrolling that mimics the physics of turning a wheel.

2.1.2 Innovative Interfaces in Industrial Applications

While there has been much work on user interfaces for consumer products, relatively less has focussed on industrial, crane-like applications. For industrial interfaces, the goal is usually to a) determine operator intent, and b) communicate the operator's intent to controllers and actuators, which in turn provide the operator with assistive forces and/or motions.

Kazerooni et al. [41, 43] championed the "Extender", which was a wearable robotic power suit that amplified the amount of force exerted by the wearer. The system works much like power steering that amplifies the steering effort exerted by a driver. A prototype of an arm-based extender was built for the application of material handling. The "Magic Glove" [42], used pressure sensors to measure the amount of force users applied to a payload, which is directly manipulated by a material-handling robot. The amount of force that the user applies is used to generate a proportionate amount of motion assistance in the robot.

The Laboratory for Intelligent Mechanical Systems (LIMS) at Northwestern University invented Intelligent Assist Devices (IAD's) and Collaborative Robots, or Cobots [13, 55, 76]. IAD's are similar to Extenders in that they sense human-intent and provide assistive forces to help operators manipulate payloads. Similarly, Cobots were designed as material-handling robots that also had the ability to constrain movement along virtual walls. This ability can help users move payloads along a precise trajectory. Cobots were implemented for a car-assembly application where the front dashboard and center console must be orientated and moved through a complex trajectory to the front of the car interior.

Several commercial companies focus on ergonomic and intuitive material handling solutions. Cobotics Inc. (acquired by Stanley Assembly Technologies in 2002), was a start up company that specialized in IAD's. Figure 2.3(a) shows the rigid-arm variant in the iTrolley series. The operator intent is sensed by a pressure-sensitive grip, and the operator pushes or pulls the arm to move payloads. The wire-rope variant, shown in Figure 2.3(b), uses cable angle sensors to detect when the operator is pushing on a suspended payload. The trolley carrying the suspended payload then moves accordingly.

Figure 2.3(c) shows an air-balancer from Gorbel's "Intelligent Lifting Devices" product line. Air-balancers are similar to cranes, except they are only motorized in the vertical direction. Payloads too heavy for the operator to lift manually are 'balanced in the air', as the hoist motors automatically sense the weight of the payload and provide the correct amount of assistive lifting force. The trolley is free to move on the overhead tracks, so lateral movement is provided by operators directly pushing or pulling on the suspended payload. However, this type of system is typically designed to carry small payloads (on the order of a few hundred kilograms).

Traditional interfaces such as push-button pendents, levers, and joysticks, have long been held as the de-facto industry standard. Sorensen et al. were one of the first to thoroughly explore the effects of controlling cranes using alternative interfaces. In [108], a touch screen tablet computer was used to drive a crane. It was also used as a flexible platform to provide feedback information, an easily configurable GUI, and for simple touch-based interface actions.

Another interface by Sorensen utilized an overhead view representation of the workspace that is displayed on a computer screen [99]. The user simply clicks on a point inside this view to

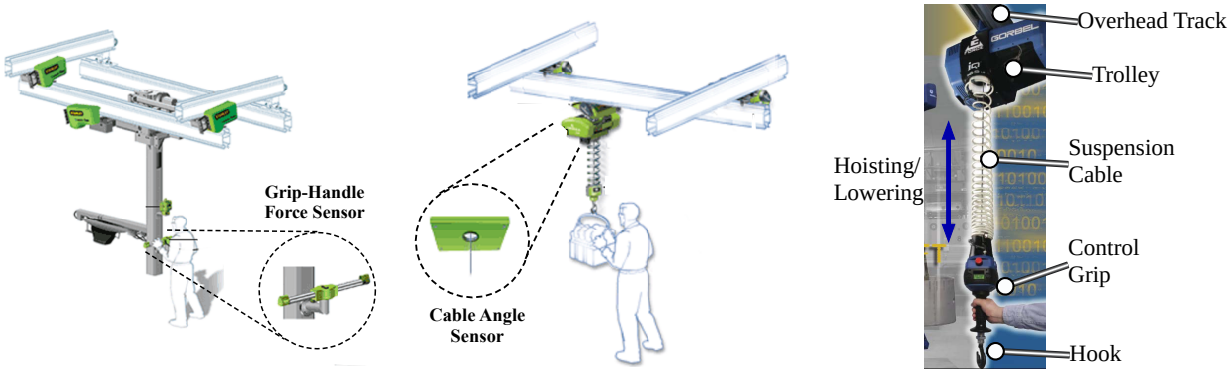

(a) iTrolley, Rigid-Arm (Courtesy of Stanley Assembly Technologies) (b) iTrolley, Wire-Rope (Courtesy of Stanley Assembly Technologies) (c) Gorbel Intelligent Lifting Device (Courtesy of Gorbel)

Figure 2.3: Examples of Industrial Products with Non-Traditional Interfaces

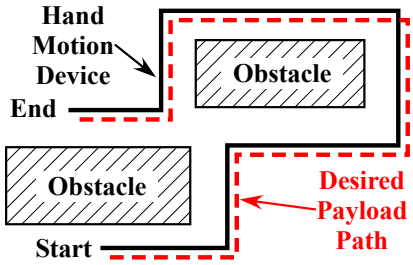

Figure 2.4: Specifying the Desired Payload Path with Hand-Motion Control

command the crane to move to the corresponding point in the workspace. This idea was extended to incorporate an overhead camera that provided live video overlooking the workspace [104, 101].

2.2 Hand-Motion Crane Control

Hand-motion is a novel and intuitive control interface that allows an operator to drive a crane by simply moving a hand-held device. Sensors track the position of the hand-held device, which is used to generate command signals. These command signals are then input shaped in order to eliminate payload oscillations, and the shaped command is used to drive the crane. In its simplest form, hand-motion control moves the trolley such that the payload follows the hand-held device without oscillation.

Hand-motion control is well tailored to the task of driving a crane because it reduces the cognitive load that is necessary with traditional interfaces. Fundamentally, the operator uses the hand-motion device to communicate the desired payload location and/or path to the crane. This is inherently more intuitive than traditional interfaces, because the operator moves the hand-motion device in *the same* physical space as the desired payload path. This is illustrated in Figure 2.4, where hand-motion control is used to drive around the same obstacles as in Figure 2.2. Note the path of the hand-motion device mirrors the desired payload path.

It is this *direct* connection between interface action and desired payload motion that simplifies and reduces operator cognitive load. The direction of crane motion is irrelevant, so operators no longer need to account for the direction in which they are facing. Because hand-motion allows the operator to specify the desired payload path directly, there is no cognitive disconnect between only being able to directly drive the trolley and the actual delayed response of the payload. Additionally,

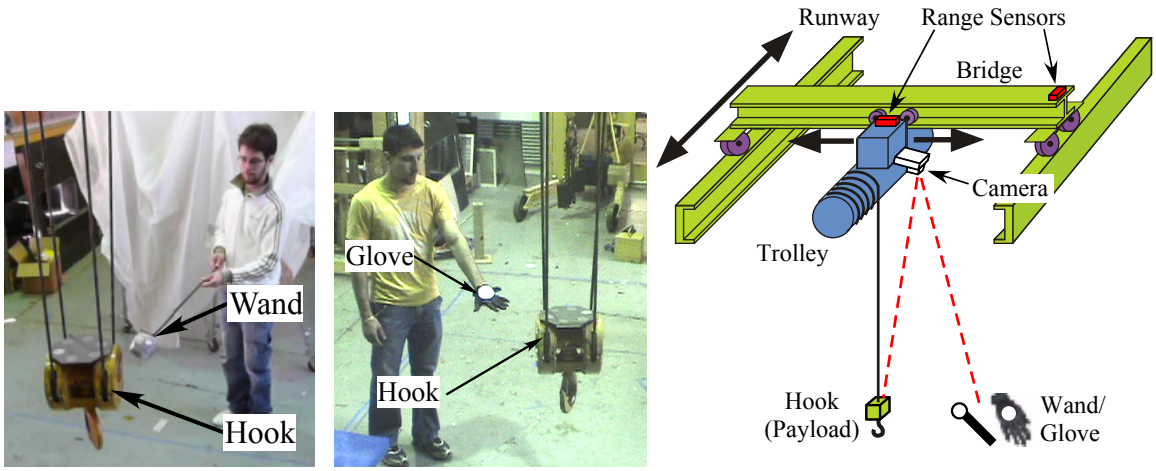

(a) Wand (b) Glove (c) Schematic

Figure 2.5: Vision-Based Hand-Motion Control

because less buttons/interface actuators are required, the manual dexterity required for safe and efficient operation is reduced. Finally, the burden of manually reducing payload oscillation is removed by the input shaper. This allows the operator to concentrate on higher level tasks, such as path planning, final positioning of the payload, and avoiding obstacles in a dynamic factory/warehouse environment.

Two major hand-motion control interface variants are presented. The first is vision-based, which relies on a crane-mounted camera. The second uses a radio-frequency (RF) real-time location system (RTLS). The MaRC HiBay crane, which was shown in Figure 1.1(a), was used as the platform for demonstrating the hand-motion interface and for conducting experiments.

2.2.1 Vision-Based

There are two hand-held devices for vision-based hand-motion crane control [74]: the wand, shown in Figure 2.5(a), is a reflective ball mounted to the end of a hand-held pole; and the glove, shown in Figure 2.5(b), has a circular reflector attached to the backside.

Figure 2.5(c) is a schematic diagram of a bridge crane equipped for vision-based hand-motion control. Laser range sensors measure the trolley position along bridge, and the bridge position along the runway. For this research, the hook is used to represent a single-pendulum, point-mass payload. A Siemens programmable logic controller (PLC) is used to control the motor drives and acts as the central control unit. A downward-pointing Siemens Simatic VS723-2 smart camera is mounted on the trolley. The camera tracks the positions of the hook and wand/glove, simultaneously [73]. Reflectors are also present on the topside of the hook to aid vision-detection algorithms [28].

Because all reflectors appear as bright blobs in the camera image, a K-means clustering algorithm is used to distinguish the wand/glove reflectors from the hook reflectors [54, 71]. The camera refresh rate is approximately 140 ms.

Note that from the perspective of discussing control architectures (this is the topic of Chapter 3), the wand and the glove are identical. Both devices are used to communicate the operator-desired position to the controller. For this reason, there is no distinction between the wand and glove in the presented simulation and experimental results. However, in terms of ergonomics during operation, the wand has a greater reach and can drive the crane towards tight spaces, such as corners. On the other hand, the glove sacrifices range of reach for ease of use.

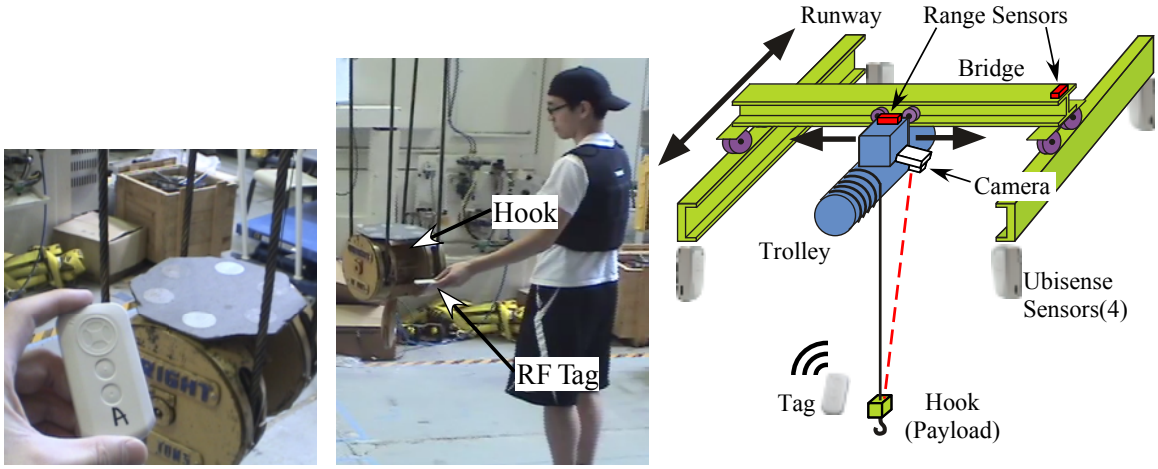

(a) RF-Tag (b) Operator Driving with Tag (c) Schematic

Figure 2.6: RF-Based Hand-Motion Control

2.2.2 RF-Based

Figure 2.6(a) shows the RF tag, and Figure 2.6(b) shows an operator using the tag for hand motion crane control. The tag is small enough to easily fit in the operator's hand. The operator presses a button on the tag to signal the hand-motion controller to activate.

Figure 2.6(c) is a schematic of the RF-based real-time location system (RTLS) and hand-motion control. A number of sensors are positioned around the workspace, typically on the upper corners and edges of an imaginary rectangular workspace. These sensors receive RF signals emitted from the RF-tag, and calculate the tag's 3-D position. Like an indoor GPS, the 3-D location of the tag is calculated from the RF signals' time difference of arrival and angle of arrival at the sensors. For this research, the hook is used to represent a single-pendulum, point-mass payload. The crane mounted camera is used in this case to track the position of the hook. However, the hook can also be tracked using the RF-RTLS by mounting a tag to it.

The RF-based system has several advantages over the vision-based system. First, the camera has a limited field of view. Therefore, the wand/glove can only be operated within a certain area beneath the trolley-mounted camera. The field of view can be increased with multiple cameras, such as a Vicon system, however the monetary and computation costs can quickly escalate. Cameras are inevitably still subjected to common machine vision problems, such as occlusions (e.g. from the suspension cables or when the operator inadvertently blocks the device from the view of the camera), non-uniform lighting, and environmental clutter (e.g. other bright objects that could be mistaken for the reflective marker).

Furthermore, when the camera is mounted on a moving object like the crane trolley, its point of reference may not be fixed, and is therefore unreliable. For example, depending on the trolley's position, the bridge of the HiBay crane can twist, because the trolley mass is not symmetrically distributed on both sides of the bridge. Also, the trolley can rotate about a vertical axis, due to the asymmetrical arrangement of the driven wheel (i.e. only one wheel is driven). These phenomenons can change the direction that the camera is facing (only a small rotational motion is enough to make a large difference. The problem worsens for higher cranes), which leads to erroneous position measurements of the reflectors. This problem is exacerbated by the fact that the trolley also rocks about the bridge when the bridge is moving.

Many of the problems with machine vision are eliminated with the RF-RTLS:

- The size of the sensor range is greatly enhanced, and can be increased indefinitely by adding

more sensors. Increasing the number of sensors over a fixed space also improves measurement robustness.

- Occlusion is less of a problem because location measurements using RF signals do not have strict requirements for line of sight. This is because 1) RF signals are capable of penetrating some materials, and 2) location is still possible (although with degraded quality) using signals that are reflected off obstacles. Additionally, encoded signals between the tag and sensors ensure that each tag is uniquely identified.

- The 3-D location of the tag is easily attainable with RF-RTLS. Even with multiple cameras, robust 3-D location would be difficult and costly to obtain in a cluttered workspace.

- Two-way communication with the tag allows a richer interface with the operator, e.g. buttons on the tag can be used to change the operational mode.

- RF-tag location systems are common in many industrial/warehouse/factory crane environments. In fact, the system used in this dissertation was originally designed to track inventory and stock in indoor spaces.

The downside of using the RF-RTLS is that it has a greater upfront cost than the single, trolley-mounted camera of the vision-based system. It also requires a larger number of supporting networking and computer equipment.

2.2.3 Auxiliary Interface Devices

To facilitate richer interactions between the operator and hand-motion crane control, the RF-tag was supplemented with a wireless button transmitter (similar to a garage opener), as shown in Figure 2.7(a). In this combination, the RF-tag provided the location of the operator's hand, while the button transmitter reliably communicated the control mode, e.g. activating and deactivating hand-motion control.

The button transmitter can be replaced with a touchscreen mobile device (e.g. an iOS device such as an iPod or iPhone), shown in Figure 2.7(b). While it lacks the tactile feedback of physical buttons, the touchscreen device is capable of providing even richer interactions with the operator:

- The touchscreen provides visual and aural feedback to the operator, e.g. playing a sound when a button is pressed, and give information on the state of the crane, such as displaying warnings in the event of communication problems.

- The vibrational functions of certain devices can provide tactile feedback.

- The touchscreen enables flexible graphical user interface (GUI) designs. Buttons, sliders, or gesture controls such as finger swiping can be easily implemented.

- Some touchscreen devices contain additional sensors such as GPS, compass, accelerometer, and gyroscope. These sensors can be exploited and/or combined with hand-motion control to create more crane-control features.

2.3 Accuracy of RF-RTLS Tag Location Measurements[1]

The particular RF-RTLS system used in this dissertation is a commercial product from Ubisense. Ubisense's proprietary technology utilizes ultra wide band (UWB) RF signals, which has the advantage that spurious signals resulting from reflections off surfaces can be easily distinguished from

[1] ***This work was performed with the assistance of Lee Stokes***

(a) Wireless Button Transmitter (b) Touchscreen Device

Figure 2.7: RF-Tag (White Square, Top) with Auxiliary Interface Devices

direct, straight-path signals. This allows the system to achieve a nominal accuracy of around 0.15 m over a large three-dimensional volume. Increasing the number of sensors also increases the robustness and reliability of the measurement. Additionally, the system is designed to track multiple tags simultaneously.

The tracking accuracy of the Ubisense RF-RTLS is crucial to the performance of hand-motion control. However, Ubisense does not have publicly available sensor accuracy studies. Furthermore, hand-motion control uses the RF-RTLS system in a way that differs from original intended purpose. Therefore, studies were conducted to quantify the tag location measurement accuracy under a variety of conditions.

2.3.1 Accuracy Over the Nominal Crane Workspace

To measure tracking accuracy, 104 markers were laid out on the floor in 0.5 m increments over the nominal crane workspace to create a 2-D grid in the X and Y directions of known positions. Then, using a tripod, the tag was positioned at each point on the grid at heights of Z=0, 0.63, 1, and 1.5m. Then, tag location measurements were recorded at each point. Measurement errors were calculated from the absolute 3-D Euclidean distance between the measured tag coordinates and the true tag coordinates.

Figure 2.8(a) shows a top-down view of the measurement error distribution when the tag height was Z=0m. The crosses represent the X, Y coordinates of five stationary sensors. Note these sensors are located high above the floor at heights ranging from 3.3 to 4.3m. The color of the surface represents the tag location measurement error. These are interpolated from the 104 data points. Note that the rectangular colored area represents the nominal crane workspace (where the crane can physically operate in). The sensors are located outside this space and enclose a larger area. Also note the lack of data in the bottom left corner of the workspace. This was an area where the sensors were unable to obtain an accurate reading, most likely due to the tag being out of the sensor range and/or in a sensor blind spot.

The other plots in Figure 2.8 shows similar data for tag heights of Z=0.63, 1, and 1.5m. Two things are noteworthy: 1) Measurement errors are high near the floor, but decrease as the height increases; and 2) noticeable increase in measurement error at the corners of the workspace (top right and bottom left), which is most likely due to the tag being in sensor blind spots (the sensors are directional - they receive RF signals coming from the direction that they are facing in).

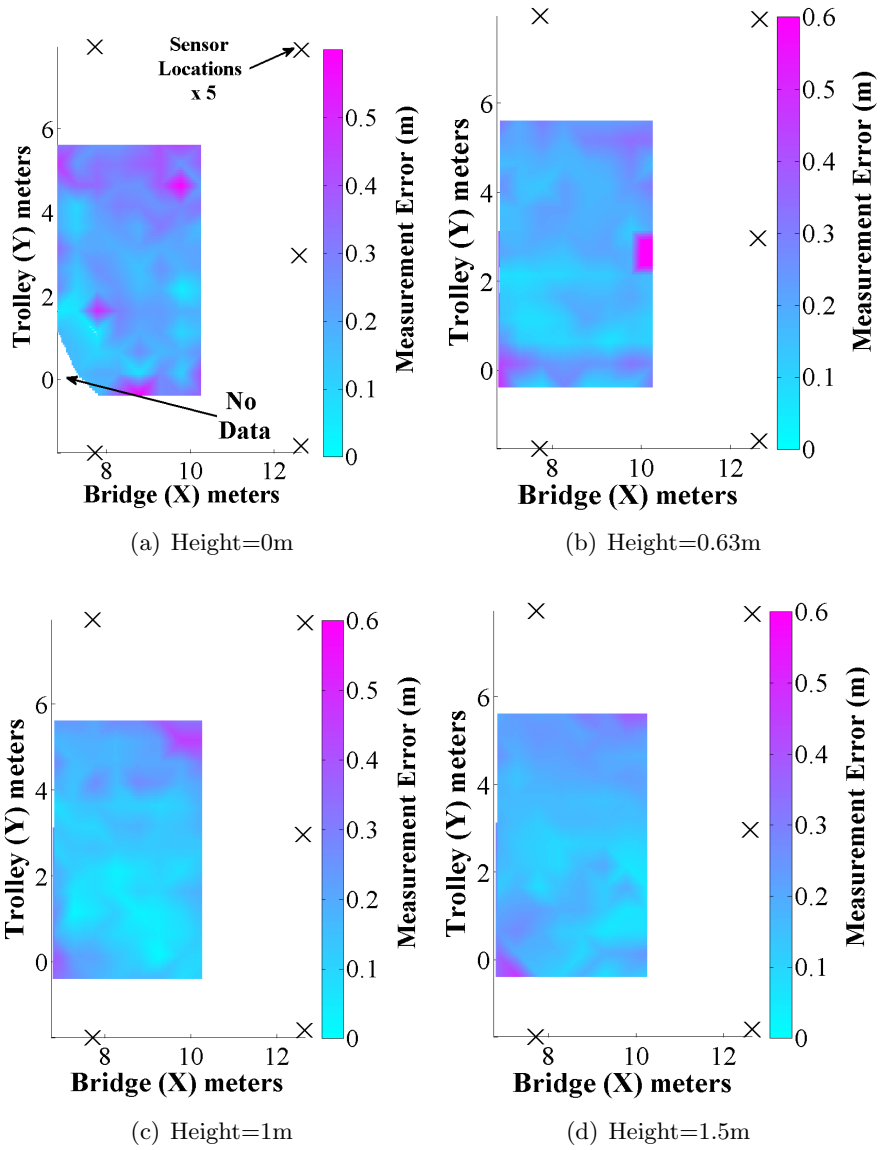

(a) Height=0m

(b) Height=0.63m

(c) Height=1m

(d) Height=1.5m

Figure 2.8: RF-Tag Location Measurement Errors Over the Nominal Crane Workspace

Table 2.1 summarizes the measurement errors over the nominal crane workspace. Measurement errors are greater when the tag is on the floor, evident by the higher mean error of 0.24m. One explanation for this phenomenon is that when the tag is closer to the floor, location accuracy is degraded by more RF waves reflecting off the floor. However, measurement error quickly decreases to the nominal level (less than 0.20m) when the tag height is increased.

Table 2.1: RF-RTLS Measurement Errors Over the Nominal Crane Workspace

Tag height (m)	Max. Error (m)	Min. Error (m)	Mean Error (m)
0	0.61	0.04	0.24
0.63	0.52	0.06	0.19
1.0	0.45	0.01	0.16
1.5	0.47	0.05	0.18

Figure 2.9: Measuring the Location Accuracy Around a Scissors Lift

2.3.2 Accuracy Around a Large Object

Because cranes are often in cluttered workspaces, it is important to understand how large objects (e.g. heavy machinery) affect the accuracy of tag location measurements. The obstacle used in the experiments is a mobile scissors lift, shown in Figure 2.9. The scissors lift can be considered as a rectangular metallic object approximately 1.5m high. Also visible in the picture is the grid of floor markers and the tripod for placing the tag at various heights.

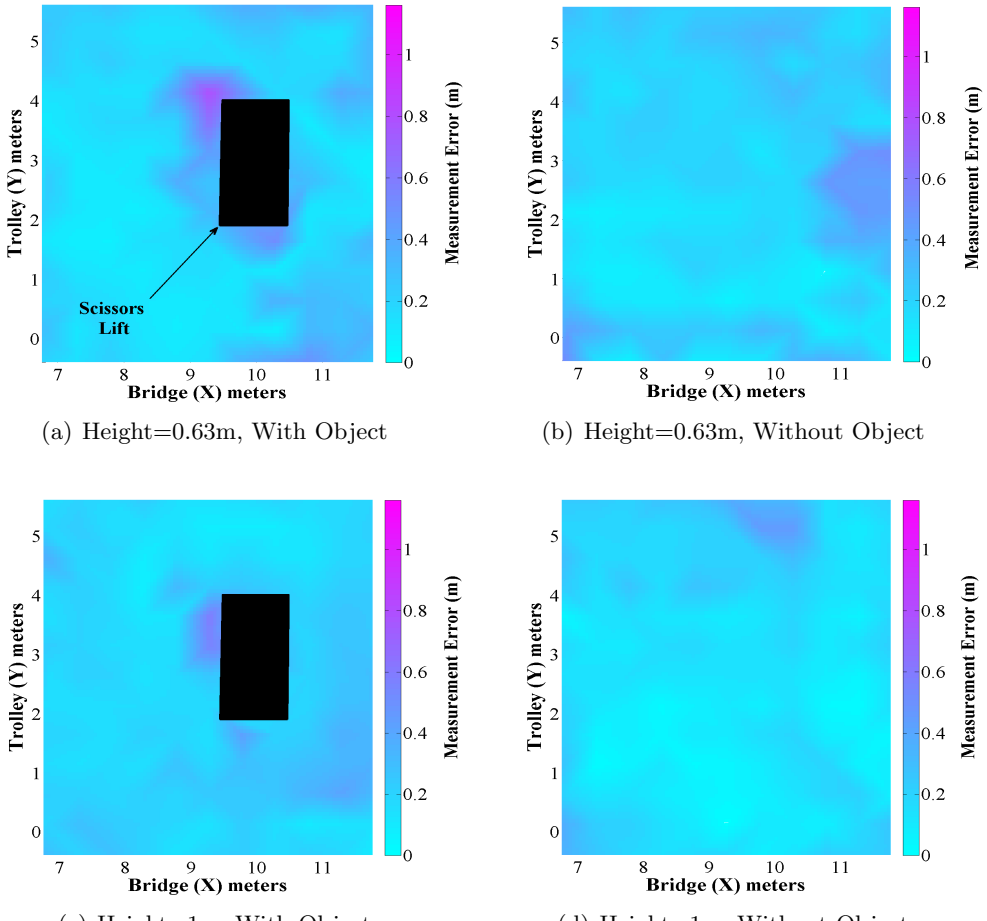

(a) Height=0.63m, With Object

(b) Height=0.63m, Without Object

(c) Height=1m, With Object

(d) Height=1m, Without Object

Figure 2.10: Large Metallic Object and RF-Tag Location Measurement Errors

Figures 2.10(a) and 2.10(b) show the error distribution of tag location measurements for tag

height of 0.63m, with and without the object, respectively. The black box represents the area occupied by the object. Clearly, measurement errors are greater in the area to the top left of the object, when it is present. In this region, it is estimated that the object increased the measurement error by 0.4 to 0.7m. A similar phenomenon occurs around the bottom edge of the object, but to a lesser extent. These observations can be explained by the fact that when the tag is at this height, its line of sight to some sensors are completely obstructed by the object.

Figures 2.10(c) and 2.10(d) show similar data for tag height of 1m. There is some increase in measurement error relative to the obstacle-free case, but to a lesser extent than when the tag was at 0.63m. In the region near the upper left of the obstacle, the measurement error increased by around 0.5m. At higher tag heights, the object has less obstruction to the line of sight between the tag and sensors, and thus less degradation to the measurement accuracy.

From these experiments, it can be concluded that measurement accuracy are affected around large objects, especially when the tag line of sight to sensors is obstructed. In some cases, the measurement error may be increased by 0.5m or more.

2.4 Pulling (Come-Here) and Pushing Modes

In its most basic form, Hand-Motion (HM) control moves the trolley such that the payload (without oscillating) follows the hand-held device. In collaboration with Konecranes (one of the largest crane manufacturers in the world), various hand-motion control operating modes were developed and tested.

The first step in the development process was to explore ways in which the concept of hand-motion control can be exploited to improve crane operating performance. To reiterate, the strength of hand-motion control is that it allows the operator to directly communicate the desired payload location/path to the crane. This is done by moving the hand-motion device (the RF-tag is used in most examples from this point on) in the *same* physical space as the payload.

The most basic form of operation is the "Pull", or "Come-Here" mode. The operator presses a button on the hand-motion device (tag) to activate the mode. While the button is held-down, the payload moves in a straight line directly towards the operator, as shown in Figure 2.11(a). The payload stops when it is close to the tag. Conversely, during the "Push" mode, the payload moves in a straight line away from the tag.

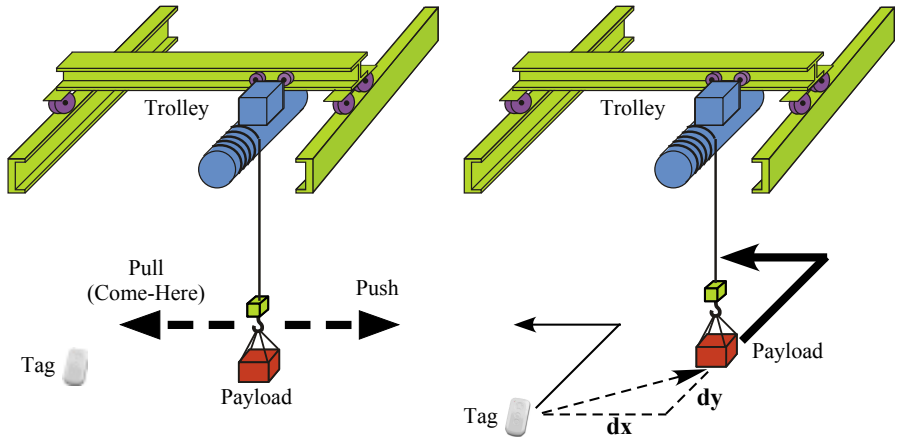

(a) Pulling (Come-Here) and Pushing Modes (b) Fixed Relative Positioning (FRP) Mode

Figure 2.11: Hand-Motion Control Modes

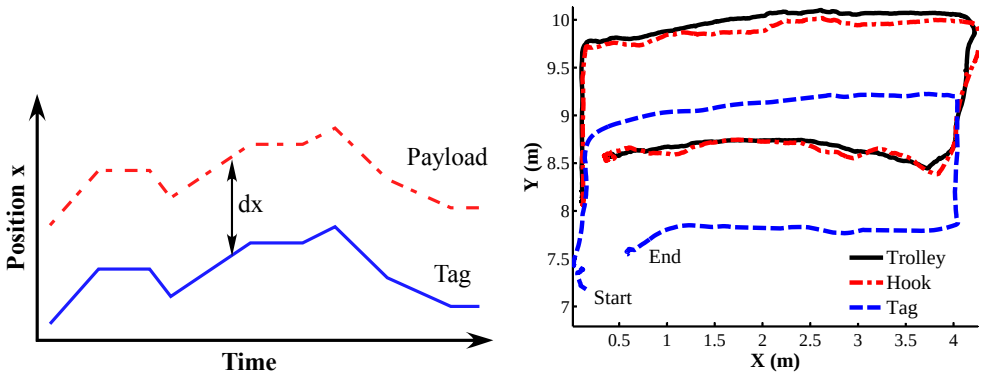

(a) Theoretical Ideal (b) Experimental

Figure 2.12: Good FRP Responses

2.5 Fixed Relative Positioning Mode

The fixed relative positioning (FRP) mode is illustrated in Figure 2.11(b). When this mode is activated, the crane moves the payload such that its position relative to the tag is fixed. For example, as Figure 2.11(b) shows, the relative position of the payload to the tag is dx and dy in the trolley and bridge directions, respectively. When FRP is activated and the tag is moved, the crane moves the payload so that dx and dy remain fixed.

The FRP mode was inspired by the fact that operators often move a payload while walking by the side it. This is safer than the Come-Here mode because the operator is not required to stand in front of and in the path of the traveling payload. Because the payload moves in whichever direction needed to maintain the same relative position, the FRP mode encapsulates aspects of both the pulling and pushing modes.

2.5.1 Ideal FRP Behavior

At this juncture it should be noted that the FRP mode has different priorities than the Come-Here mode. For the Come-Here mode, the priority is speed. The crane should move the payload to the Hand-Motion (HM) device as quickly as possible. With FRP, speed is also important, but greater priority is placed on the accurate positioning of the trolley and payload. This is so that the initial relative position between tag and payload remains fixed.

Figure 2.12(a) shows an example of the ideal FRP response in one dimension, x. The positions of the payload and tag are plotted over time. Ideally, the payload should be moved such that the relative position between the payload and tag, dx, is fixed for all time. This, however, is unrealistic, because it assumes the crane has infinite acceleration (and possibly velocity) to overcome the large inertia of the trolley and payload.

More realistically, one can expect the FRP mode to move the crane such that dx is maintained within a reasonable proximity to the desired value, and that this is accomplished within a reasonable time frame (and as quickly as possible). An experimental example of this type of realistic movement is shown in Figure 2.12(b). The positions of the trolley, hook (used to represent a payload in this case), and tag are plotted over X and Y in an overhead view. The tag was moved from start to end, tracing out a rectangular shape. The FRP mode moved the trolley and hook in a way that replicates the shape of the rectangle to a high level of fidelity. Note that in order to achieve this level of fidelity, the tag was moved at a speed slower than or equal to, the crane's maximum speed, which makes it feasible for the crane to maintain the desired dx and dy.

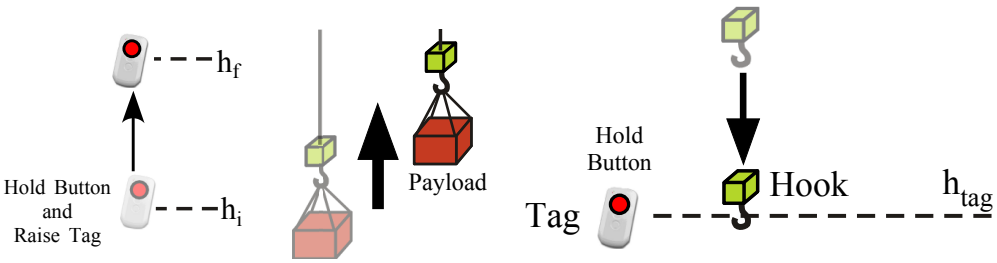

(a) Gesture-Hoisting Mode (b) Go-To-Height

Figure 2.13: Hand-Motion Hoisting/Lowering Modes

2.5.2 Prototype Usage Tests

A three-person test was conducted to gauge the usability of the FRP mode. Test subjects were asked to maneuver a payload in the horizontal plane around the workspace using 1) the standard push-button pendent, 2) Come-Here mode, and 3) FRP mode. The feedback from the tests were generally positive. Users reported FRP was "much better" than using the pendent and Come-Here mode.

However, some subjects reported controller unresponsiveness while using FRP. This is an undesirable trait where the HM device was moved small distances, yet the crane did not respond. This is a problem with the underlying controller architecture, which contains a deadzone around the location where FRP is activated, and the selection of controller parameters. Chapter 3, and specifically Section 3.4.2 discusses these controller issues in more detail.

2.6 Hoisting (Vertical Movement) Modes

Two variants were developed to hoist and lower the payload/hook. Figure 2.13(a) illustrates the Gesture-Hoisting mode. The operator presses and holds a button while the tag is at initial height h_i to activate the mode. Then, the operator raises the tag to height h_f. If $h_f > h_i + h_d$, where h_d is the size of vertical deadzone around the initial height, then the crane raises the hook and payload. Vice versa for lowering the hook/payload. The magnitude of h_d is determined by the sensor accuracy in the vertical direction and the vertical range of motion of a typical operator's hands.

Figure 2.13(b) illustrates the Go-To-Height mode. When this mode is activated by holding a button, the hook will be raised or lowered to the same height as the tag, h_{tag}.

2.6.1 Combined Gesture-Hoist and Go-To-Height Mode

Figure 2.14 illustrates the combined gesture and go-to-height mode. The mode is still activated by pressing and holding the button. However, depending on the tag height, different behaviors will result. If the mode is activated while the tag is in zone 1, the hook will go to the same height as the tag. Zone 1 is an approximate vertical region from the waist to shoulder heights. If the tag is in zone 2 (above shoulders), then the hook will be hoisted up until the button is released. If the tag is in zone 3 (below waist), then the hook will be lowered until the button is released.

2.6.2 Prototype Usage Tests

A three-person test was conducted to gauge the usability of the hoisting modes. The test subjects were tasked with picking up and lowering a payload using 1) a touchscreen[2] with "Up/Down"

[2]See Section 2.2.3

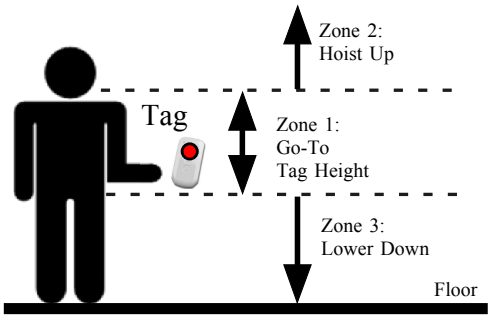

Figure 2.14: Combined Gesture-Hoist and Go-To-Height Mode

buttons that hoists/lowers the crane hook, 2) the Gesture-Hoist, and 3) Go-To-Height hoisting modes. The user feedback from the tests include:

- Both hoisting modes only send 100% speed commands to the hoist motor. Test subjects felt this full speed motion can be imprecise, and suggested the option to hoist at slower speeds, or even an inching/stepping modes for hoisting.
- One person preferred the immediacy of pressing buttons to hoist, rather than the extra effort and time required to moves his arms with the hand-motion hoist modes.
- The Go-To-Height mode is useful in situations where the hook is required to be at around the operator's height. However, due to the a person's limited vertical range of motion, this mode should always be accompanied by a gesture-based hoist mode. This was the motivation in the creation of the combined mode illustrated in Figure 2.14.

From the tests and personal experiences of the researchers and designers, it quickly became obvious that the hand-motion control concept is *not* suitable for commanding vertical motions. The reasonings are as follows:

- The relatively large sensor inaccuracy of the RF RTLS reduces the already-limited range of human vertical motions. The sensor accuracy study of the RF RTLS in Section 2.3 showed that the nominal accuracy of the RF RTLS is around 0.20m, but is actually less accurate in the vertical direction. Therefore, for hand-motion hoisting to work reliably, the tag must move vertically by *more* than 0.20m.

  To put that into perspective, the height difference between the shoulders and hand (arms dropped by side of body) of a 6 foot tall person is only about 0.70m [16]. The RF RTLS sensor accuracy occupies a large proportion (29%) of this vertical range of motion.
- The location accuracy of the RF RTLS degrades when the tag is close to the floor (See Section 2.3. This further reduces the range of reliable vertical motions available to the operator.
- Even if the RF RTLS was replaced with significantly more accurate vision-based system (such as Vicon), operators still have limited vertical range of motions. In contrast, the horizontal range of motion is practically limitless because operators are free to move anywhere (ignoring obstacles) in the horizontal plane.
- Test subjects felt it was tiring to hold their arms at un-ergonomic positions (such as above the shoulders or stooping to reach below the knees) for long durations to hoist/lower the hook.

For the reasons above, hoisting/lowering while using hand-motion control is still best implemented with traditional, already-proven interfaces, such as pushing buttons.

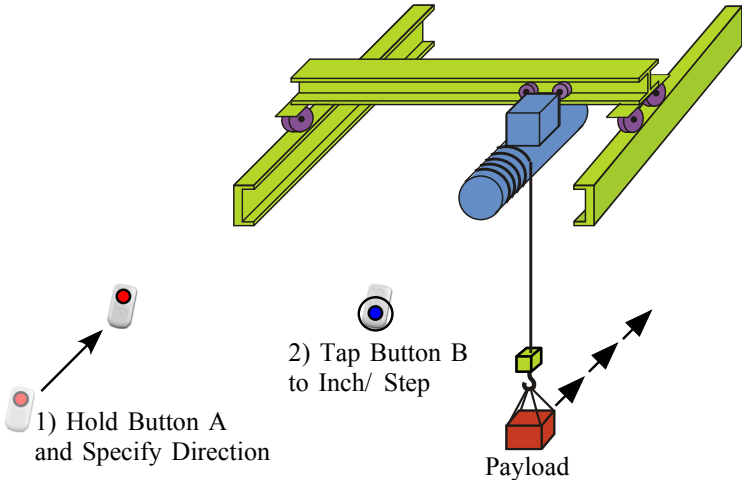

Figure 2.15: Inching/Stepping Mode

2.7 Inching/Stepping Mode

The inching/stepping mode is a feature that can be found on many cranes. Its purpose is to allow the operator to make fine adjustments by moving the crane only a small distance[3] with each interface action. In a typical example of inching mode, the operator flips a switch to activate the mode. Then, the operator presses a directional button (forward, reverse, left, right) to move the crane one step. The crane makes the same number of steps as the number of times the button is pressed. A similar feature that can be found on many cranes is the slow/snail mode. In this mode, the crane is restricted to move at a fraction of its nominal velocity.

Figure 2.15 illustrates the hand-motion implementation of the inching mode. In step 1, the operator holds button A and moves the tag in the desired stepping direction, which is then stored in memory. Button A is then released. The range of the desired direction is 360 degrees in the horizontal plane. Therefore, the operator is not limited to inch in only the four cardinal directions, as with traditional interfaces. In step 2, the operator taps button B to step the crane in the desired direction.

2.7.1 Prototype Usage Tests

A three-person test was conducted to gauge the usability of the inching/stepping mode. The test subjects were tasked with using the inching mode to move a payload precisely into a small area. The user feedback from the test include:

- Users noted that setting the direction in step 1 was occasionally imprecise. This was caused by a) sensor inaccuracy; and b) there was no feedback to the user on the actual direction that was set; users had to effectively set the direction by dead reckoning.
- Test subjects reported difficulty in remembering the two-step (1. set direction with button A, 2. tap button B to inch/step) procedure.

From conducting these tests and from the experiences of the researchers, it became clear that the hand-motion concept, when implemented in this manner, is not capable of offering improvements over traditional interfaces in the inching/stepping mode. Namely, the method of setting the direction (i.e. step 1 in Figure 2.15) was not an effective use of the hand-motion concept. Furthermore, the somewhat complex two-step process shifts *away* from the goal of hand-motion control, which is to improve ease of use by simplifying interfaces.

[3]On some cranes, this distance is adjustable by the operator

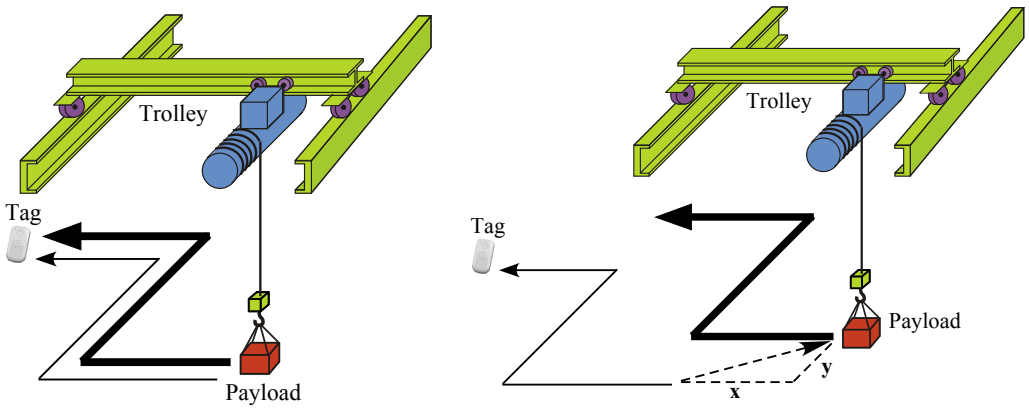

(a) Nominal Path Following (b) FRP Path Following

Figure 2.16: Path Following Modes

The outcome of these studies was that the inching mode is better implemented using traditional interfaces, for now. However, one idea that originated from these results was that the inching mode may be better implemented by combining with a basic mode, such as Come-Here. The operator would press button A for the nominal Come-Here mode, but tap button B for to inch/step (or move at snail speed) towards the operator. The same can be implemented for the push mode. This mode was not investigated in this research and is suggested for future work in Section 8.1.

2.8 Path Following Modes

Come-Here, Push, and FRP modes use the current tag location, and neglect all past movements of the tag. One of the inconveniences when operating in those modes is that the operator needs to wait at certain key locations (such as at a sharp turn) for the payload to catch up before proceeding in the desired path. Otherwise, the payload will cut the corner.

A path following mode was developed where the crane follows the "recorded" path traveled by the tag. In this mode, time plays a significant role. Essentially, the hand-motion controller records a time series of past tag movements, and then follows the time series. This concept is illustrated in Figure 2.16(a), where the payload follows the path that was traveled by the tag beforehand. The operator may choose to have the crane immediately follow the path as soon as the tag is moved, or to have the crane start moving only after the operator has finished tracing out the desired path (by pressing a secondary button). Furthermore, the path following mode can be combined with FRP, as illustrated in Figure 2.16(b), so that the payload path follows the tag path at a fixed offset. This allows operators to use the path following mode while walking alongside the payload, rather than in front of it.

Path following is implemented using a waypoint system. Figure 2.17(a) shows path following using manually-set waypoints. The operator sequentially moves the tag to critical locations on the desired path, such as sharp turns, and presses a button to set waypoints at those locations. The crane moves through the series of waypoints using a simple, acceptable-distance algorithm:

1. Move towards the i^{th} waypoint.

2. If the trolley or payload is within the acceptable distance to the i^{th} waypoint, move towards the $(i+1)^{th}$ waypoint.

Alternatively, waypoints can be set automatically while the operator moves the tag through the desired path. Figure 2.17(b) illustrates waypoints that are automatically set at preset distance intervals. Automatic waypoints can also be set at preset time intervals. Figure 2.18(a) shows

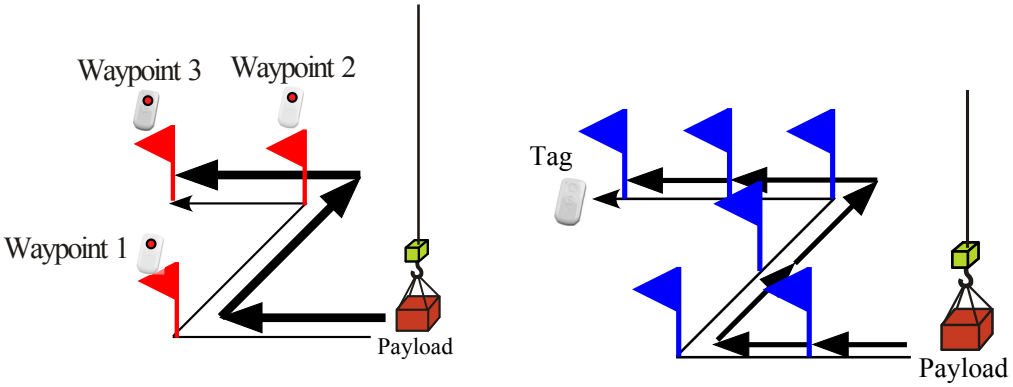

(a) Manual Waypoints (b) Automatic Waypoints

Figure 2.17: Setting Waypoints in the Path Following Mode

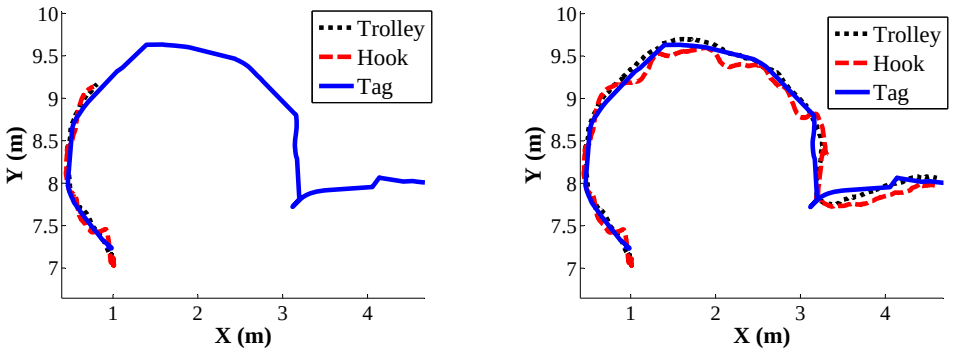

(a) Traveled Paths When The Tag Has Finished (b) Traveled Paths When The Trolley Has Finished

Figure 2.18: Path Following Using Automatic Waypoints, Overhead Views

an overhead view of path following using automatic waypoints, implemented on the HiBay crane. Plotted are the X, Y positions of the trolley, hook, and tag. At the instant shown in Figure 2.18(a), the operator has just finished moving the tag through the desired path, which resembles a sideways "?" question mark. Because the crane is slower than the operator, it has only partially traveled the desired path. Figure 2.18(b) illustrates the instant when the crane has also completed traveling through the desired path. The path traveled by the trolley and hook closely followed that of the tag.

One issue with the acceptable-distance algorithm is that the crane decelerates as it approaches each waypoint. This algorithm is sufficient for manual waypoint path following, assuming the operator intelligently sets waypoints at critical locations, such as at sharp turns. The crane will approach each turn slowly before proceeding. However, with automatic waypoints, it is possible for a series of waypoints to be set along a straight line. In this case, it is inefficient and slow for the crane to slow-down at each waypoint. Fortunately, this is a well-studied problem, and many path-following algorithms can be used to travel past waypoints along straight lines (or curves) without slowing down excessively. One such algorithm is the path-following steering algorithm, originally designed for video game characters [78]. This algorithm "steers" (i.e. send corrective directional velocity commands) the crane towards the desired path, if it determines the predicted future position of the crane will veer too far from the path.

The path following modes were implemented and used as a proof of concept to demonstrate its feasibility. However, this concept was not pursued further, due to the results from a comprehensive

operator study, which will be presented in Section 4.4. The study results indicate that by incorporating additional features, such as path following, hand-motion control actually increases the mental burden on the operator. Using a path following example, the operator needs to memorize the shape of the path that he/she has traveled, while simultaneously moving forward along the desired path. This is contrary to the original goal of hand-motion control, which is to simplify and make interfaces easier to use. Nevertheless, path following is suggested in Section 8.1 as a candidate for future improvements.

CHAPTER III

HAND-MOTION CRANE CONTROLLER DESIGN

Hand-motion crane control can be largely separated into two major components. The first component is the "interface", which was covered in Chapter 2. The interface can be thought of as the "frontend" of hand-motion control. It encompasses aspects such as 1) the location sensors (vision or RF), 2) the hand-motion device, 3) the interfaces and GUI's that operators interact with, and 4) hand-motion operating modes. The second major component, which is the subject of this chapter, is the "backend" design of the control laws and algorithms. This component is responsible for generating the command signals necessary for efficient hand-motion control, as well as ensuring controller stability.

3.1 Background

Hand-motion control inherently requires a feedback loop. Combined with the fact that input shaping is the primary way of controlling oscillations in this dissertation, hand-motion control is an example of a Closed-Loop Signal Shaping (CLSS) system. Section 3.1.1 discusses past work in CLSS. Hard nonlinear elements are present in one version of the hand-motion controller. They are also present in many real-world cranes. Section 3.1.2 introduces the reader to describing functions (DF), which are used to analyze the stability of the nonlinear hand-motion feedback loop.

3.1.1 Closed-Loop Signal Shaping

Input shaping is most often used in an open loop manner, as shown in the block diagram of Figure 3.1(a). The input shaper modifies the original command and the shaped command goes to the plant, which could contain feedback loops. Input shapers may also be placed inside the feedback loop of a control system, as shown in Figure 3.1(b). This is known as Closed-Loop Signal Shaping (CLSS) [33, 31]. Note that the control signals are input shaped before they reach the plant.

Several researchers investigated various aspects of CLSS systems. Kapila et. al and Tzes considered the robustness of CLSS controllers to modeling errors [39, 113]. In [15, 123], comparisons are made between the performance of CLSS controllers, proportional-integral-derivative (PID) controllers, and standard open-loop input-shaping controllers. Sorensen implemented a CLSS system with two PD feedback loops: one for precise position control of a crane trolley and the other for the rejection of disturbances to the payload [103]. Some hard nonlinearities in the motor drives were also considered.

Because input shaping inside a feedback control loop causes a partial time delay, stability of the CLSS design is a primary concern. This issue has been previously addressed [57, 39, 123, 109]. Perhaps the most comprehensive work on CLSS was conducted by Huey [33, 31, 32]. However,

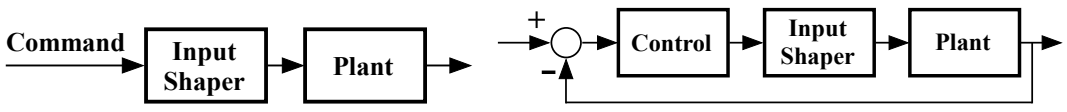

(a) Open-Loop Shaping (b) Closed-Loop Signal Shaping

Figure 3.1: Input Shaping Block Diagrams

extensive linearity assumptions were made because the stability analysis was based on root loci and Bode plots.

3.1.2 Describing Functions

All real-world systems contain some form of nonlinearity. Examples of hard nonlinearities that may be found in cranes include: relays (some older cranes rely on mechanical relays to turn on the motors); deadzone and backlash (worn actuators); saturation and rate-limiting (common safety and self-preservation features in variable frequency electric motor drives). One way to assess the stability of a closed-loop crane control system containing such nonlinearities is to use the describing function method.

The describing function (DF) method is an approximate procedure based on quasi-linearization and frequency response. It predicts limit cycles in feedback systems with hard nonlinearities. Figure 3.2(a) shows a classical nonlinear system used to demonstrate the DF method. The closed loop consists of a describing function (an approximation of an actual nonlinear element), $N(A,\omega)$, and a linear element, $G(j\omega)$. The input signal into the describing function is $x(t)$, and its output is $y(t)$. The output of the linear element is $z(t)$. The input into the feedback loop is zero, because a self-sustaining limit cycle is assumed.

Signals that propagate through the closed loop in a limit-cycling system can usually be approximated as a sinusoid. Using this observation, the main assumption in the DF method is that if the input to the nonlinearity is a sinusoid, (i.e. $x(t) = A\sin(\omega t)$ with amplitude A and frequency ω), then only the fundamental component of the output needs to be considered. Higher-frequency harmonics in the output are neglected. For this to be valid, the linear component needs to contain sufficient low-pass properties [97, 22]. When all assumptions are satisfied, the describing function, $N(A,\omega)$, is a function of the input amplitude, A, and frequency, ω. It is a quasi-linear approximation of the nonlinearity, defined as the complex ratio of the output fundamental component to the input sinusoid [97, 25]:

$$N(A,\omega) = \frac{1}{A}\left(b_1 + ja_1\right), \tag{3.1}$$

where a_1 and b_1 are the first coefficients in the Fourier series approximation of the output, $y(t)$. They are given by:

$$a_1 = \frac{1}{\pi}\int_{-\pi}^{\pi} r(t)\cos(\omega t)d(\omega t) \tag{3.2}$$

$$b_1 = \frac{1}{\pi}\int_{-\pi}^{\pi} r(t)\sin(\omega t)d(\omega t) \tag{3.3}$$

If a self-sustaining oscillation of amplitude A and frequency ω exists in the system of Figure 3.2(a), then the variables in the loop must satisfy the following relations:

$$\begin{aligned} x &= -z \\ y &= N(A,\omega)x \\ z &\approx G(j\omega)y \end{aligned}$$

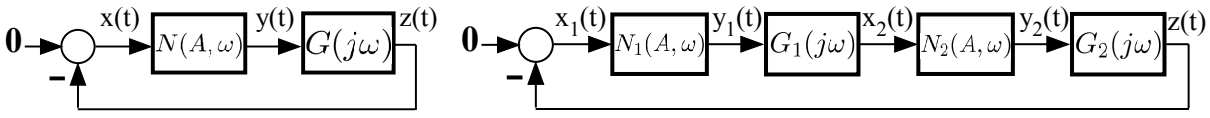

(a) Single Nonlinearity (b) Multiple Nonlinearities

Figure 3.2: Describing Function Analysis of Nonlinear Systems

Therefore, $z = G(j\omega)N(A,\omega)(-z)$. Because $z \neq 0$, this implies [97]:[1]

$$N(A,\omega)G(j\omega) = -1 + 0j \tag{3.4}$$

which can also be written as

$$G(j\omega) = \frac{-1}{N(A,\omega)} \tag{3.5}$$

To predict the existence of limit cycles, one must solve for A and ω such that (3.4) or (3.5) are satisfied. If the equations have no solutions, then the nonlinear system has no limit cycles.

As (3.4) and (3.5) are generally difficult to solve using analytical methods, especially for high-order systems, graphical techniques are usually employed. One technique plots $N(A,\omega)G(j\omega)$ in the real and imaginary plane, for various A's and ω's. The points at which the plots intersect $-1+0j$ indicate the existence of limit cycles. Alternatively, if the describing function is independent of frequency, then one can plot $-1/N(A)$ and $G(j\omega)$. The intersection of those two plots indicates the existence of limit cycles [97].

The DF method may also be extended to systems with multiple nonlinearities, such as the one shown in Figure 3.2(b). The input sinusoids into N_1 and N_2 are $x_1(t) = A_1\sin(\omega t)$ and $x_2(t) = A_2\sin(\omega t)$, respectively. The characteristic equation is solved in the same manner as the single nonlinearity case, that is:

$$N_1(A,\omega)G_1(j\omega)N_2(A,\omega)G_2(j\omega) = -1 + 0j \tag{3.6}$$

Note that only one frequency, ω, propagates through the system. Also, A_1 and A_2 are related by [22]:

$$A_2 = A_1|N_1(A,\omega)||G_1(\omega)| \tag{3.7}$$

Therefore, solving (3.6) requires solving for ω, and either A_1 or A_2. This is essentially the same technique as solving for the single nonlinearity case. This method is valid so long as the linear elements (G_1 and G_2) between each nonlinearity have sufficient low-pass properties [22, 14].

3.2 Hand-Motion Control Architectures

From the aspect of controller design, the interfaces presented in Chapter 2 (vision-based and RF-based) are all identical. The various interfaces all serve the same purpose: to provide the hand-motion controller with the location of the operator's hand and the desired path of the crane/payload. The term "hand-motion (HM) device" will be used as a blanket term to refer to the vision-based wand/glove, and the RF-based tag with and without the auxiliary interfaces (wireless button transmitter and touchscreen).

The first design question that must be answered is the form of the control architecture. A block diagram for hand-motion crane control must contain the following elements:

- The hand-motion device. The operator controls the crane by controlling its location.
- The crane trolley. Or, more specifically, the location of the trolley, which can be decomposed into the trolley position along the bridge, and the bridge position along the runway. However, without loss of generality, and for the purpose of discussing controller design, only movements in one direction need to be considered.
- The payload, suspended from the trolley by hoist cables.
- An input shaper to reduce unwanted payload oscillations.
- A hand-motion control law that converts the hand-motion device location into command signals to drive the crane. This controller must be inside a feedback loop because the location of the device can be continuously moved by the operator.

[1] (3.4) is equivalent to the Nyquist criterion and the characteristic equation of closed-loop systems.

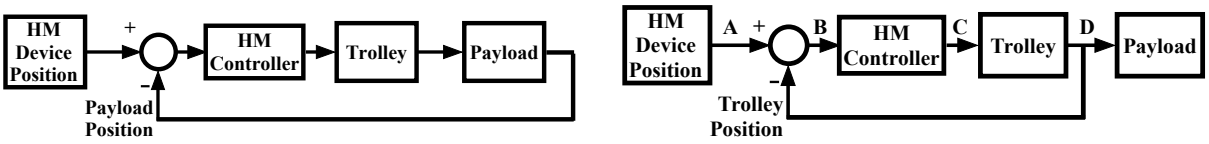

(a) Payload Feedback

(b) Trolley Feedback

Figure 3.3: Choice of Feedback Signals

3.2.1 Choice of Feedback Signals

Given the required elements, the next goal is to select the signal for the feedback loop. There are two possibilities: 1) payload position, 2) trolley position. Figures 3.3(a) and 3.3(b) depict exemplary hand-motion control block diagrams (without the input shaper) for payload and trolley position feedbacks, respectively. Note that "HM" denote "Hand-Motion".

At this juncture it is necessary to consider the practical aspects of implementing both forms of feedback. Measuring the position of the payload is a challenging task. Sensors that have been used in the past include cameras [28], accelerometers and gyroscopes (used in conjunction with some integral component) [46], and EMF-field hoist cable angle sensors [13]. Generally, these sensors are difficult to implement reliably. For example, occlusion of the payload (often from the hoist cables) and spurious observations are common problems for machine vision. Accelerometers and gyroscopes suffer from sensor drift over time, and cable angle sensors typically require modifications to the hoist mechanisms, which can be extensive. Furthermore, these sensors usually track the hook, which is always part of the crane, rather than tracking the payload directly. As the payload complexity increases, as in the case of double-pendulum or multi-mode oscillatory payloads, so does the difficulty of measuring all payload states.

On the other hand, the position of the trolley is typically measured by encoders or laser distance sensors. These are commonly used sensors that have proven to be accurate, robust, and reliable. Furthermore, suspended payloads are inherently stable. The payload will always come to rest directly beneath a stationary crane. Therefore, if the trolley is correctly positioned over the desired position, then the payload is also ensured to be positioned over the desired position (in steady state, neglecting transient oscillations). For the reasons stated above, hand-motion control uses the trolley, rather than the payload, as the feedback signal.

3.2.2 Placement of the Input Shaper

Having justified the choice for feedback signal, the next step is to choose the placement of the input shaper. Recall from Section 1.1, the primary role of the input shaper is to reduce unwanted payload oscillations, i.e. the input shaper is designed specifically for natural frequencies and damping ratios inside the "payload" block. With reference to the trolley feedback block diagram in Figure 3.3(b), there are four possible choices to place the input shaper, A, B, C, and D. The main consideration for input shaper placement is whether the oscillation-reduction properties of the shaped signal are able to reach the payload block uncorrupted. The following considers the candidates for the placement of the input shaper:

- Location A is after the hand-motion device and before the feedback loop comparison. Because the input shaper is outside of the feedback loop, this is architecture is known as Outside-the-Loop Input Shaping (OLIS) [33].

  Placing the input shaper here requires that the shaped signal properties are preserved when the shaped signal passes through the entire feedback loop. This requires not only a carefully designed hand-motion controller, but also an extensive analysis of the behavior of the shaped signal after the trolley position is subtracted from it at the comparison block.

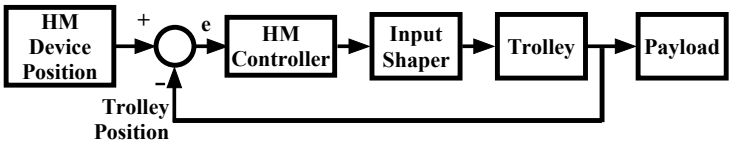

Figure 3.4: Hand-Motion Control Block Diagram

One caveat of subtracting (or adding) quantities directly from a shaped signal is the risk of potentially corruptive saturation. For example, if the shaped signal commands the motors to move at -100%, then subtracting from this will over-saturate the motors, thereby corrupting the vibration-reducing properties of the shaped signal.

- Location B is between the feedback loop comparison and the hand-motion controller. Placing the input shaper here is a simpler task than location A. However, the hand-motion controller still needs to be carefully designed, because the shaped signal needs to pass through both the HM controller and trolley blocks to reach the payload.

- Location C is between the hand-motion controller and the trolley. This location is ideal because it is the closest location to the payload that is also physically realizable. In most applications, the input shaper is placed as close as possible to the source of problematic oscillations, so that the shaped signal reaches the source with minimal corruption.

  By placing the input shaper at location C, the shaped signal is sent directly to the trolley. As the trolley block is usually linear (in some cases there are nonlinearities that may or may not be corruptive), the oscillation-reduction properties of the shaped signal are preserved when it arrives at the payload. This location also allows more freedom in the design of the HM Controller block.

- Location D, between the trolley and payload, is not physically realizable because there are no actuators that physically move the hoist cables tangentially relative to the trolley.

In conclusion, the simplest and most suitable location to place the input shaper is at location C. Figure 3.4 is a block diagram that shows the selected hand-motion control architecture. The "e" denotes the error signal, which is generated from the different between hand-motion device and trolley positions. The error signal goes to the hand-motion controller and is used to command the crane.

The generation of the error signal is shown schematically in Figure 3.5(a) for vision-based, and in Figure 3.5(b) for RF-based hand-motion control. The position of the hand-motion device (wand, glove, or RF tag) relative to the crane trolley (ignoring the difference in vertical height) is used to generate the error signal.

Figure 3.6 is the augmented hand-motion control block diagram, which shows more details than Figure 3.4. Every element inside the dashed box on the left represent actions that can be performed by the operator. In the leftmost element, the operator decides on a path for the HM device based on the manipulation goal. The operator is also influenced by observing (e.g. by sight) the behavior of the trolley and payload (represented by dashed feedback lines). The switch on the right edge of the dashed box represents the operator's choice to activate or deactivate hand-motion control. When activated (e.g. by pressing a button on the RF tag or auxiliary devices, or by showing the wand/glove to the camera), the HM device position is compared to the position of the overhead trolley (neglecting the vertical height difference) to generate the error signal, e. When deactivated, e is set to 0, which effectively stops the crane.

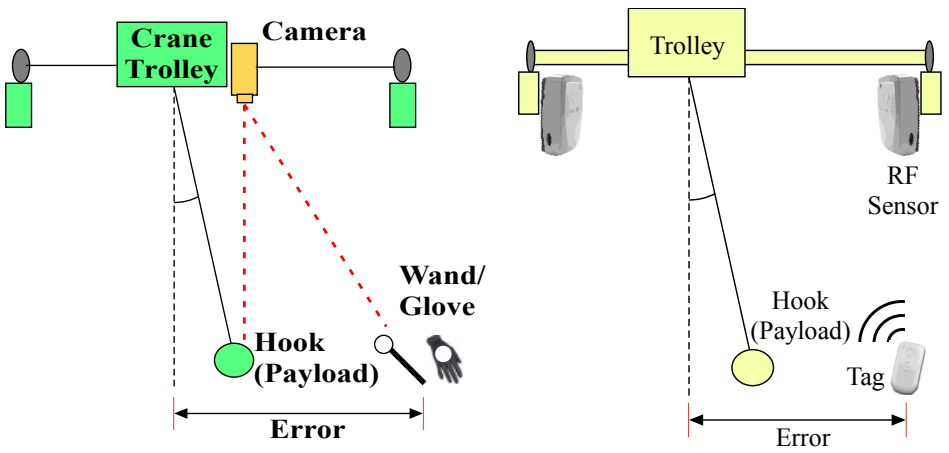

(a) Vision-Based (b) RF-Based

Figure 3.5: Generating the Error Signal

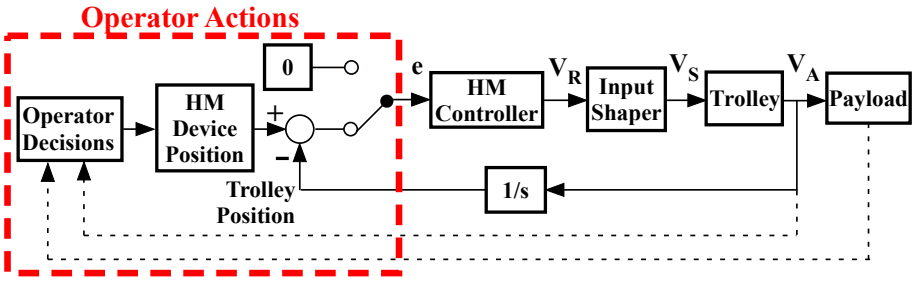

Figure 3.6: Augmented Hand-Motion Control Block Diagram

The HM controller then converts e, a distance measure, into a reference velocity command, V_R.[2] This signal is then modified by an input shaper so that movements of the trolley will not induce payload swing. The output of the input shaper is a shaped command, V_S, that is sent to the motor drives. The actual velocity of the trolley is V_A. The payload is then moved by the trolley. Note the $1/S$ element in the feedback loop that is required to form the trolley position from the integration of V_A.

Having now determined the general control architecture of hand-motion control, the next step is to design the the hand-motion control law, i.e. the "HM Controller" block in Figure 3.6.

3.3 Proportional-Derivative Controller

A basic version of the hand-motion controller can use the proportional-derivative (PD) CLSS system that was used for precise trolley positioning in [103]. In essence, the hand-motion controller is identical to the trolley positioning controller, because it has the same goal of placing the trolley over a desired location (the HM device). However, minor changes are needed for hand-motion. Figure 3.7 is a block diagram that shows the internal components of the PD hand-motion controller. First, e is converted into a properly scaled velocity command, $V_{\%}$. This then goes to the PD element, with proportional gain, K_p, and derivative gain, K_d. The PD output is saturated between -100% and 100% so that the reference velocity command, V_R, does not exceed motor limits.

[2]Variable Frequency Drive (VFD) motor drives typically receive velocity commands

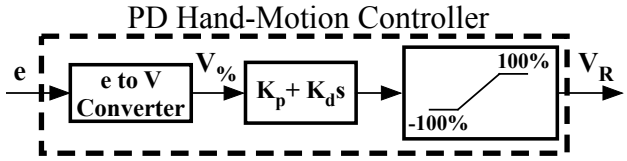

Figure 3.7: PD Hand-Motion Controller

The conversion from e to $V_{\%}$ is:

$$V_{\%} = \begin{cases} 0\% & : |e| \leq e_0 \\ 100\% \times \frac{|e|-e_0}{e_{100}-e_0}\mathsf{sign}(e) & : e_0 < |e| < e_{100} \\ 100\% \times \mathsf{sign}(e) & : |e| \geq e_{100} \end{cases} \tag{3.8}$$

Where e_0 and e_{100} are positive constants (in meters) that scale e into velocity commands between 0% and 100%. For instance, let $e_0 = 0.5m$ and $e_{100} = 2m$. If $e \leq 0.5m$, then $V_{\%} = 0$. If $e \geq 2m$, then $V_{\%} = 100$. If e is between e_0 and e_{100}, then $V_{\%}$ is proportionally scaled between 0% and 100%.

Note that e_0 is effectively a deadzone. Physically, it is a distance (between the HM device and the trolley) below which zero velocity command is generated. Deadzones are necessary because of the inherent noise from the HM device location sensors. If there is no deadzone, i.e. $e_0 = 0m$, then the sensor noise can create chatter in the system. Furthermore, without a deadzone, sensor noise continuously generates velocity commands, which can cause incessant drifting, and the crane never fully stops. This not only wastes energy but can also cause the operator to lose confidence in their control over the crane. In practice, e_0 is set to a distance slightly larger than the sensor location accuracy (around 0.3m for the RF sensors).

Similarly, e_{100} represents a physical distance (between the HM device and trolley) above which maximum velocity command is desired. This parameter is necessary because the operator should only need to walk a finite distance away from the trolley in order to send maximum velocity commands. The constant e_{100} gives the designer a parameter to specify what this distance should be. In practice, it is set a few meters, such that the operator needs to only walk a few steps to send maximum velocity commands.

Note that there are effectively two saturators in the PD controller of Figure 3.7. The first saturation is in the scaling of 0 to 100% velocity in the conversion of e to $V_{\%}$. The second is after the PD element. Both are necessary 1) for the designer to properly scale 0 and the maximum commanded velocities, and 2) to prevent the PD element from sending commands that exceed motor limits.

3.3.1 Selection of PD Gains

If e_0 and e_{100} have been selected, and the input shaper has been designed to reduce payload oscillations, then the next step is to select the proportional and derivative gains, K_p and K_d. The range of stable gains can be determined by root loci (or Bode plots), using the methods described in [33, 31, 32]. However, this method assumes the system is linear. Therefore it is restricted to systems that either a) stay within the linear range of nonlinearities, or b) where the effects of nonlinearities are minimal. Note that although the operator can always choose to deactivate hand-motion control (i.e. the switch in Figure 3.6 that makes $e = 0$) to stop the crane in cases of controller instability or emergencies. However, it is still important for the designer to pick controller parameters that do not lead to unstable behaviors.

The selection of gains for hand-motion control is discussed in detail in [71]. The first obstacle in plotting the root loci of CLSS systems is that the shaper contains time delays, i.e. $e^{-\tau s}$. However, this can be solved using a simple pivoting algorithm by Nishioka [66]. In essence, the open-loop

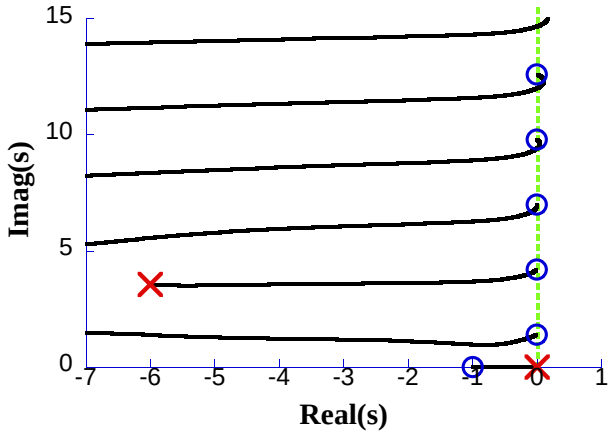

Figure 3.8: PD Hand-Motion Controller Root Loci of the Feedback Loop

transfer function is rearranged in a way such that two points lying on opposite sides of the root locus have opposite signs in the imaginary domain (in the "K-plane"). The entire root loci can be determined by first constructing a fine grid (in the real and imaginary S-plane) in the region of interest. Then, test the sign of the imaginary component (in the K-plane) of each point. If the sign changes between two neighboring points, then the root locus passes between those points.

The next challenge is to form the linearized open-loop transfer function (of the feedback system) and remove (or approximate) all nonlinearities. For example, neglecting the effects of real-world sensor noise, the deadzone can be removed such that $e_0 = 0$. Also, assuming the operator is always within e_{100} from the trolley,[3] the saturator in the PD hand-motion controller of Figure 3.7 can be ignored. Then, the open-loop transfer function of the PD hand-motion controller is:[4]

$$G_{OL} = \overbrace{\frac{100\%}{e_{100}}}^{\text{e to V Converter}} \underbrace{K_{PD}(1+s)}_{\text{PD element}} \underbrace{(A_1 + A_2 e^{-st_2})}_{\text{ZV Shaper}} \underbrace{\frac{\omega_t^2}{s^2 + 2\zeta_t\omega_t s + \omega_t^2}}_{\text{Trolley}} \overbrace{\frac{1}{s}}^{\text{Integrator}} \tag{3.9}$$

The PD gains are collapsed into one term, K_{PD}. A_1, A_2, and t_2 are the amplitudes and time of a ZV shaper. The trolley is a mass controlled by the motor drive (which has its own feedback loop control) that is approximated by a second-order model with natural frequency ω_t and damping ratio ζ_t.[5]

An example hand-motion root-loci is plotted in Figure 3.8. Note that only the positive imaginary components are plotted. Also note the ZV shaper creates an infinite column of zeros along the imaginary axis. Therefore, the closed-loop poles of CLSS systems are *always* oscillatory. The range of stable gains (K_{PD} in this case) can be obtained by tracing along the root loci and locating the point at which poles cross the imaginary axis.

Because it requires broad, linearizing assumptions, the root-loci method can only yield the approximate range of stable hand-motion PD gains. In practice, the actual gains need to be manually refined, using the range obtained from root-loci only as a guide. Because the closed-loop poles are always oscillatory, the refined gains must make essential compromises between stability and responsiveness (higher gains have faster rise times but are more prone to instability/oscillation/longer

[3]This assumption is valid because 1) the operator will be moving crane while inside e_{100} for the majority of the time, and 2) instability such as limit cycling occurs when e is close to zero, which is well within e_{100} and the linear range of the saturator.

[4]The HiBay crane motor drive also contains a nonlinear rate-limiter that is also ignored in this analysis[103].

[5]These are **not** the payload oscillation natural frequency and damping ratio.

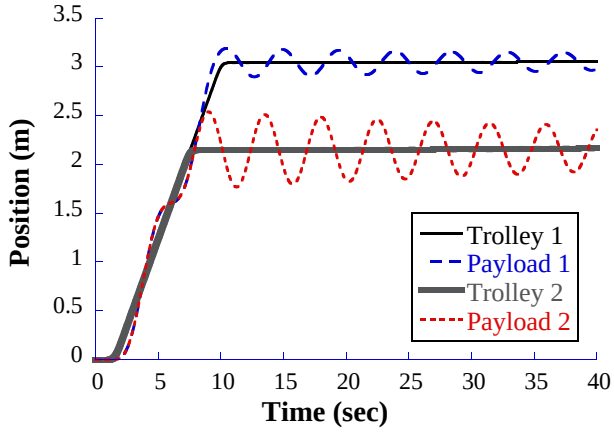

Figure 3.9: Standard Push-Button Pendent Controller Responses

settling times). Furthermore, note that if the input shaper is modified (for instance, to carry double-pendulum payloads with different natural frequencies to be suppressed), then the PD gains must be re-selected.

3.3.2 Controller Performance

As a baseline for comparisons, computer simulated responses for point-to-point movements of approximately 2 and 3 meters using the a standard push-button pendent (no input shaping) are shown in Figure 3.9. Pressing a button for a certain amount of time issues a trapezoidal velocity profile to the motors, which moves the trolley. Due to the pendulum-like nature of the payload, this type of trolley movement will usually induce significant payload oscillations.

The PD hand-motion controller performance was assessed in 2 meter point-to-point (PTP) moves. Four controller parameters were preselected, which produced satisfactory performance in terms of rise time and settling time. These parameters were $e_0 = 0m$, $e_{100} = 3m$, $K_p = 15$, and $K_d = 10$. The ZV input shaper was designed to cancel payload oscillations based on the natural frequency and damping ratio of the resulting payload swing.

Figure 3.10(a) shows the computer simulated trolley and payload response for the PD hand-motion controller. Figure 3.10(b) shows the corresponding experimental results (vision-based hand-motion control, i.e. the wand/glove, was used). Note the wand/glove solid black line disappears when the user wishes to stop the crane by lowering the wand/glove to make it undetectable by the camera. This action deactivates hand-motion control. Clearly, the trolley response was fast (it accelerated and traveled at its maximum speed in the first 5 seconds), yet it induced very little residual payload oscillations. Figures 3.10(a) and 3.10(b) show that hand-motion control is effective at moving the payload quickly without inducing oscillations [69, 72, 75, 114, 74, 71].

3.3.3 Effects of Sensor Noise

There is noise with the laser sensors that measure trolley position. However, this noise is much lower, due to the high accuracy (±5-10mm) of the laser sensors. Furthermore, the laser sensor's high bandwidth (1ms refresh rate, compared to the 35ms PLC cycle time) allows the signals to be filtered without much detriment to performance. This is because the bandwidth of the heavy crane is orders of magnitude lower.

The location accuracy with the camera is relatively high with vision-based hand-motion control. The camera's image pixel size is 1024x768, and has a resolution of 1690.8 pixels/radian [27]. Because the camera is mounted on the trolley approximately 6m high, this translates to around a 3.5mm discernible resolution on objects placed on the floor. Even with the slow speed (140ms refresh rate)

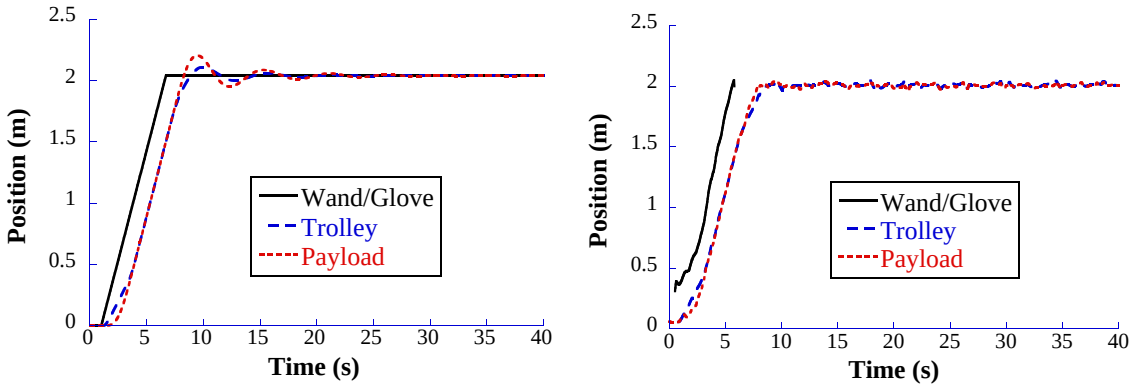

(a) Simulation (b) Experiment

Figure 3.10: Point-to-Point Motion Response Using Vision-Based, PD Hand-Motion Control

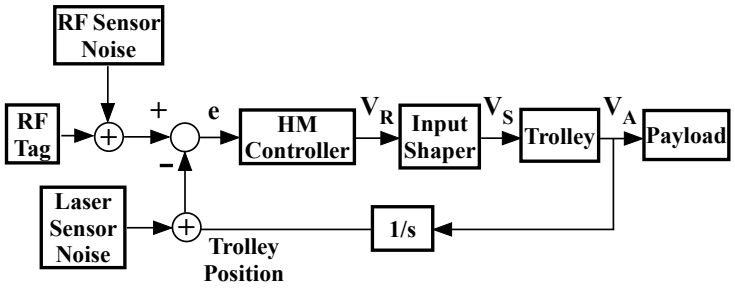

Figure 3.11: Signal Noise in the RF-Based Hand-Motion Control Feedback Loop

of communication between the camera and the PLC, the signals from the camera do not need to be filtered to obtain a high-quality clean signal. Because of this, the signal noise of the wand/glove position is relatively small. Therefore, with vision-based hand-motion, the error signal is used to drive the crane in the feedback loop, has relatively low levels of signal noise.

However, with RF-based systems, the location accuracy is much lower ($\pm$0.2m, see Section 2.3), and therefore the noise effects of the input signals must be considered. The primary sources of signal noise, RF and laser sensors, in RF-based hand-motion control are shown in the block diagram of Figure 3.11.

Figure 3.12(a) shows the positions of the trolley, payload, and tag for a 2 meter PTP movement using RF-based hand-motion control. Note that an operator physically moved the tag, so the movement is not exactly 2m for all trials. At approximately 10 seconds, hand-motion was deactivated (operator stopped pressing the activate button). Clearly, the input shaper was effective at reducing the amplitude of residual payload oscillations.

However, due to signal noise in the tag location, the error signal, e, was very noisy. Noise is amplified by the derivative component of the PD controller. As a result, the shaped velocity command (that is sent to the motor drives), V_S, contained high frequency spikes, as seen in Figure 3.12(b). High frequency components are undesirable because they may excite unmodeled higher modes, such as the trolley rocking phenomenon that was observed on the HiBay crane [28]. Trolley rock was also responsible for the small amount of residual payload sway that can be seen in Figure 3.12(a). Large spikes in the command are also undesirable because the crane would not travel at the maximum speed (approximately $0.3m/s$). Therefore, the full capabilities of the crane are not being utilized. Furthermore, rapidly changing commands can cause excessive actuator wear.

Fortunately, the actual trolley velocity, V_A, in Figure 3.12(b) shows that the crane was physically incapable of following the fast changing velocity commands. This is because the crane acts like

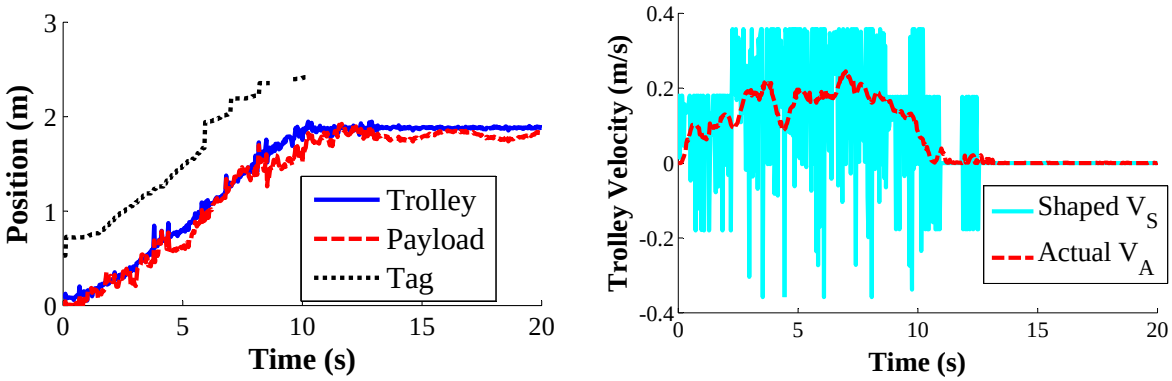

(a) Positions (b) Trolley Velocities

Figure 3.12: Point-to-Point Motion Response Using RF-Based, PD Hand-Motion Control

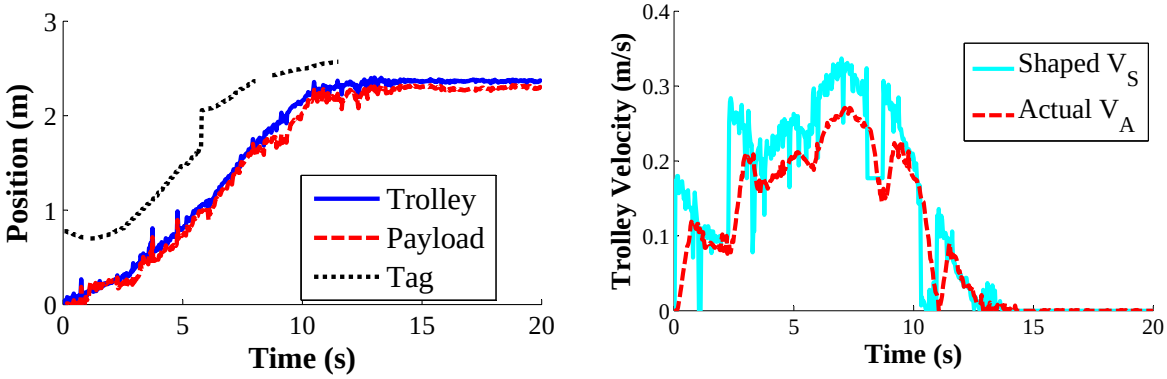

(a) Positions (b) Trolley Velocities

Figure 3.13: Point-to-Point Motion Response Using RF-Based, P Hand-Motion Control

a low-pass filter, due to its inertia. This is a benefit because if the crane was able to follow the reference commands, then dangerous levels of structural vibration might result.

3.3.4 Removing the Derivative Component

To reduce the effects of signal noise, the derivative component of the PD controller was set to zero, while keeping all other control parameters the same. This effectively reduced the PD to a proportional (P) controller. Figure 3.13(a) shows the positions of the trolley, payload, and tag for a 2 meter PTP movement. It took just under 10 seconds to travel the desired distance. Residual payload oscillation was less than with the PD controller because there was less trolley rocking. The shaped velocity command, shown in Figure 3.13(b), was also smoother, albeit still with some noise. Furthermore, the actual trolley velocity data shows that the crane never reached the maximum velocity of $0.3m/s$.

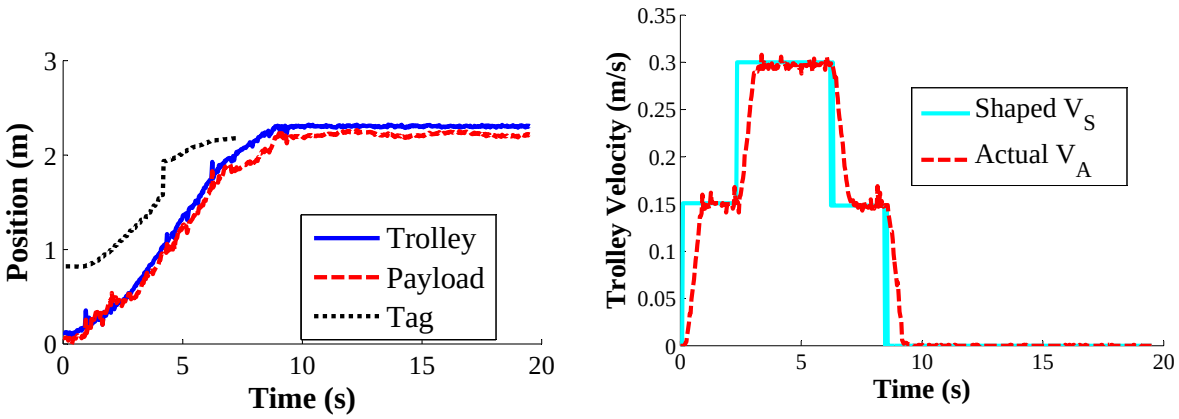

(a) Positions

(b) Trolley Velocities

Figure 3.14: Point-to-Point Motion Response Using RF-Based, On-Off Hand-Motion Control

3.4 On-Off Controller

To further reduce the effects of noise, and to simplify controller design, the On-Off controller was developed. Its behavior is similar to a relay deadzone and is described by:[6]

$$V_R = \begin{cases} 0\% & : |e| \leq e_0 \\ 100\% \times \text{sign}(e) & : |e| > e_0 \end{cases} \tag{3.10}$$

Where e_0 is the deadzone size and is chosen by the designer. Recall that deadzones are necessary to prevent chattering caused by sensor noise.

The controller performance was tested using a 2 meter PTP movement. The parameter e_0 was set to $0.4m$. The choice of e_0 was based on the distance it took for the crane to decelerate from maximum velocity. Figure 3.14(a) shows the tag, trolley, and payload positions using the On-Off controller. It took approximately 9 seconds (1 second faster than the PD and P controllers) to travel 2 meters. Residual payload oscillation was negligible. It is evident from the velocity profiles in Figure 3.14(b) that noise was virtually eliminated from the shaped command. Because of this, the actual velocity of the trolley was able to reach maximum velocity of 0.3m/s, which explains the faster completion time.

3.4.1 Selecting the Deadzone Size, e_0

As mentioned above, the choice of e_0 is based on the crane's stopping distance, d_{stop}, from its maximum velocity. The stopping distance of the crane while using hand-motion controller can be determined by considering the simplified hand-motion control block diagram in Figure 3.15. A pulse of amplitude V_{pulse} and length t_{pulse} is used as the reference velocity command, V_R. The command is input shaped to produce V_S, which drives the trolley to produce the actual trolley velocity, V_A. This is then integrated to produce the trolley position. Note that V_A also goes to the payload block; however, the payload is irrelevant here, because it is assumed that the payload does not back-drive the trolley.

To determine d_{stop}, V_{pulse} is set to 100% and t_{pulse} set to a length that gives the crane ample time to accelerate to its maximum velocity. Then, d_{stop} is the distance traveled by the trolley after the driving pulse has ended at t_{pulse}. Clearly, d_{stop} is dependent on a number of factors:

- The choice of input shaper. Generally, a longer duration shaper[7] results in longer stopping

[6] For the On-Off controller, (3.10) describes the "HM Controller" block in the augmented hand-motion control block diagram of Figure 3.6

[7] Assuming positive impulses.

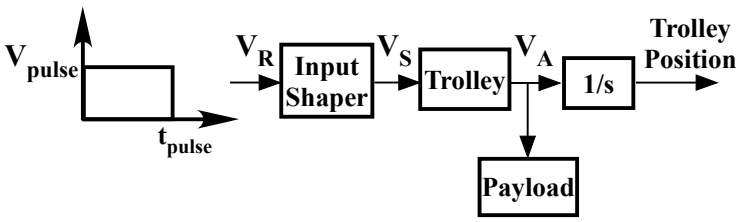

Figure 3.15: Block Diagram for Determining the Stopping Distance

distances.

- The trolley block. Generally, if the trolley (and bridge assembly) has larger inertia, or if the motor drives are configured conservatively (i.e. slow acceleration/deceleration), then the stopping distance will be greater.
- The amplitude of the command, V_{pulse}.

The ideal deadzone size is selected by:

$$e_0 = d_{stop}. \tag{3.11}$$

This choice is justified by considering the following. If e_0 is too small, then the response of the trolley may be oscillatory (or even exhibit perpetual limit cycles - this will be discussed in Section 3.5). This phenomenon is illustrated in Figure 3.16(a), where the positions of the RF tag (set constant at 2m) and the trolley are plotted over time. The limits of the deadzone are shown by the dashed-dotted lines. The trolley oscillates because it overtravels beyond the far-side deadzone while slowing down. Then, the trolley reverses and the process repeats for a few more cycles. If e_0 is increased to remove this oscillation, but $e_0 < d_{stop}$, then the trolley will still overtravel the tag, as shown in Figure 3.16(b).

On the other hand, if $e_0 > d_{stop}$, then the trolley (and therefore the payload) will stop short of the desired location, as shown in Figure 3.16(c). Furthermore, large deadzones are cumbersome to operate and may lead to additional perceived controller lag. This is because users need to move further distances to move the HM device out of the deadzone in order to move the crane.

If $e_0 = d_{stop}$, then the trolley and payload will stop exactly over the tag, as shown in Figure 3.16(d). In practice, however, e_0 is usually chosen to be slightly larger than d_{stop}. This is because many operators do not feel comfortable having the crane and payload approach so closely to them. The larger e_0 adds a buffer distance between the operator and the approaching payload.

Note the above procedure chooses e_0 based on the crane's stopping distance *from maximum speed*. This is the worst case scenario where the stopping distance is the greatest. If, during operation, the crane is not at maximum speed when it enters the deadzone, then it will stop short of the tag, similar to the situation in Figure 3.16(c). However, this is still more preferable than overshooting the tag and potentially hitting the operator or an obstacle beyond the desired location.

In the case of the HiBay crane, the size of d_{stop} is greater than the range of unstable, i.e. limit cycling, e_0's. The topic of On-Off controller stability will be covered in Section 3.5. Therefore, the design choice in (3.11) also avoids instability issues. However, if the application was on a different crane, and d_{stop} is smaller than the range of unstable e_0's, then e_0 should be chosen based on controller stability and not on the stopping distance.

3.4.2 Comparison with the PD/P Controllers

Although it is possible to design high-performance filters that reduce signal noise before passing to the P and PD controllers, adding extra components increases the design and implementation

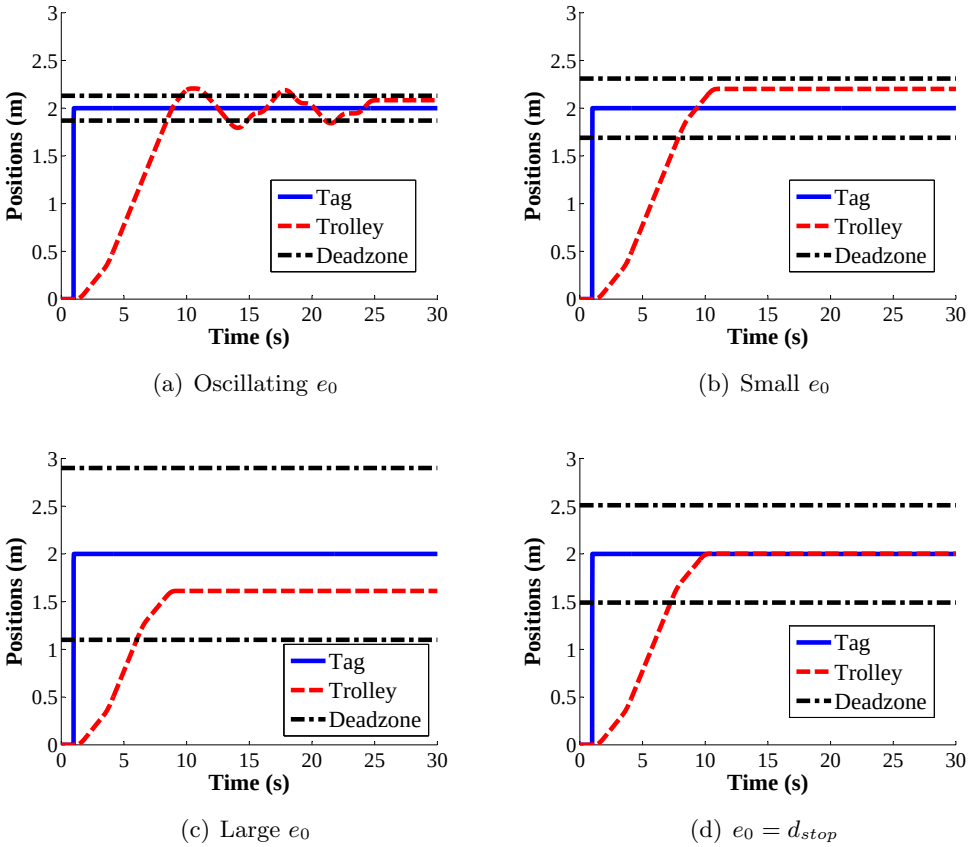

(a) Oscillating e_0

(b) Small e_0

(c) Large e_0

(d) $e_0 = d_{stop}$

Figure 3.16: Choice of e_0 Sizes for the On-Off Controller, Simulation Responses

complexity. For example, implementing N-point filters adds $2 \times N$ more computations per cycle. Furthermore, longer filters increase lag and slow the controller responsiveness. Extra design considerations also have to be given to filter parameters such as cut-off frequency, filter order, etc.

The On-Off controller avoids many of the problems associated with signal noise, while still being relatively easy to design. It only has two design parameters: e_0 and the input shaper. Whereas the P or PD controller need at least four or more design parameters: P, D, e_0, e_{100}, input shaper, and possibly more parameters for the noise filter.

Compared with the PD/P controllers, the On-Off controller utilizes the capabilities of the crane more efficiently because on average, it produces higher crane velocities. This is because the reference velocity commands saturate to 100% when $e > e_0$. In contrast, the PD/P controller scale the reference velocity commands based on e. Furthermore, if no filters are used, then the signal noise is enough to prevent the PD/P controller from sending maximum velocity commands. On-Off control is also simpler to operate, because pushing the button on the tag tells the crane to "go" (with 100% velocity). With PD/P controllers, the operator needs to learn an additional interface action. They need to adjust the distance between the trolley and the tag to set the speed of the crane.

However, the P controller is not without its benefits, because it has the ability to make slower movements that are more suitable for precise positioning. Furthermore, rather than being chosen based on the crane's stopping distance like with the On-Off controller, the P controller's deadzone is chosen based on the HM device location accuracy. Generally, this allows the P controller's deadzone to be smaller than that of the On-Off controller.[8]

[8] e.g. In Figure 3.13(a), $e_0 = 0.25m$ for the P controller; In Figure 3.14(a), $e_0 = 0.4m$ for the On-Off controller.

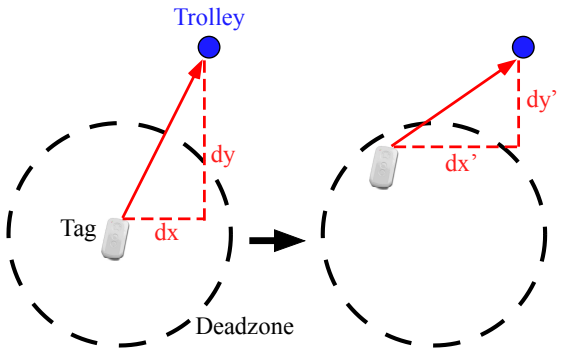

Figure 3.17: Detrimental Effects of Large Deadzones in FRP Mode

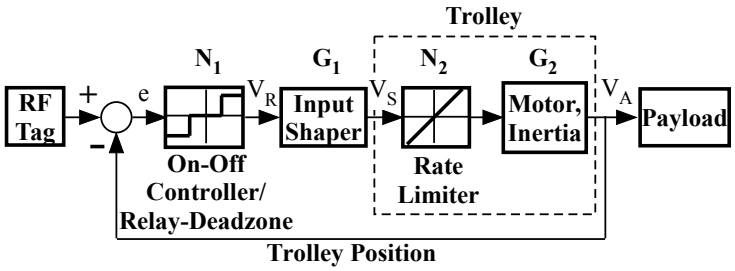

Figure 3.18: On-Off Hand-Motion Controller Implemented on the HiBay Crane

Large deadzones are particularly detrimental to the fixed-relative-positioning (FRP) mode that was discussed in Section 2.5. To illustrate this, the left side of Figure 3.17 shows an overhead view of the RF-tag, a blue circle representing the trolley, and a dashed circle that represents the deadzone around the tag when FRP mode is first activated. The relative positions between the tag and trolley in this initial configuration is described by dx and dy. The right side of Figure 3.17 shows the tag moving to a different position within the deadzone. Because the tag is still inside the initial deadzone, velocity commands are zero, and the crane does not move. Yet the relative position between tag and trolley has changed to dx' and dy'. This non-response by the crane could frustrate the human operator. Clearly, good FRP performance requires smaller deadzones. This makes the P controller (without the noise-amplifying derivative component) a better choice for the FRP mode than the On-Off controller.

The pros and cons of the PD/P and On-Off hand-motion controllers are summarized in Table 3.1.

3.5 Stability Analysis of the On-Off Controller Using Describing Functions

While the approximate stability of the PD/P hand-motion controller can be determined using root-loci (by ignoring nonlinearities), the same technique cannot be applied to the On-Off controller, due to its inherent hard nonlinearity. In this section, the describing function (DF) method is used to analyze the stability of the feedback loop, as well as help the designer choose the size of e_0. Again, note that although the operator can always choose to deactivate hand-motion control (as in Figure 3.6) to stop the crane in cases of controller instability or emergencies. However, it is still important for the designer to know how to pick controller parameters that do not lead to unstable behaviors.

Figure 3.18 is a block diagram of the feedback loop of the On-Off hand-motion controller implemented on the HiBay crane. The On-Off controller is effectively a relay-deadzone nonlinearity, and is labeled N_1. For the purposes of this analysis, a ZV shaper with impulse amplitudes A_1 and

Table 3.1: Pros and Cons of PD/P vs. On-Off Controllers

Pros	Cons
PD/P • PD feedback controllers are well understood and commonly used. • Stability of linearized PD and shaper in the loop CLSS systems have been studied extensively [33, 31]. • Good for precise trolley (and payload) positioning [103], due to small deadzone and ability to move the crane slowly.	• Linearized techniques from [33, 31] yields approximate range of stable gains. In practice, gains need to be manually modified. • Linear CLSS systems inherently have oscillatory closed-loop poles. • Gains are optimized with respect to the input shaper and trolley. New gains must be selected if the shaper changes. • Several parameters to select: e_0, e_{100}, K_p, K_d, and input shaper. • Motor commands can chatter due to sensitivity to sensor noise. Can result in slower move speeds and excessive wear.
On-Off • Simple and few design parameters: e_0 and input shaper. • Less susceptible to sensor noise. Motor commands do not chatter. • Faster movement speeds because reference commands are always maximum velocity.	• Challenging for small movements because the reference command is always maximum velocity, and the deadzone is relatively large. • If the input shaper changes, then e_0 needs to be re-selected.

A_2, and the second impulse time of t_2 is used. The linear element G_1 consists of the ZV shaper multiplied by a constant that scales percentage velocity commands to actual velocities (in m/s):

$$G_1 = (A_1 + A_2 e^{-st_2}) \frac{V_{max}}{100}, \tag{3.12}$$

where V_{max} is the maximum velocity of the trolley.

An accurate model of the HiBay trolley is represented by the elements inside the dashed box. First, there is a rate limiter [103], labeled N_2. The rate-limiter is a common nonlinearity that exists inherently or by design (usually to prevent over-speeding or over-loading) in electro-mechanical components (in the HiBay crane, this is a feature of the motor drives). The output of a rate-limiter attempts to follow the input but with the constraint that the slope of the output is bounded by $\pm m$ [25]. The second block in the trolley is a linear transfer function, G_2, that captures the movement characteristics of the trolley (i.e. motor behavior and inertia):

$$G_2 = \frac{\omega_T^2}{s^2 + 2\zeta_T \omega_T s + \omega_T^2} \left(\frac{1}{s}\right), \tag{3.13}$$

where ω_T and ζ_T are the trolley's natural frequency and damping ratio, respectively. Note the integrator, $\frac{1}{s}$, that converts V_A into trolley position, is included in G_2.

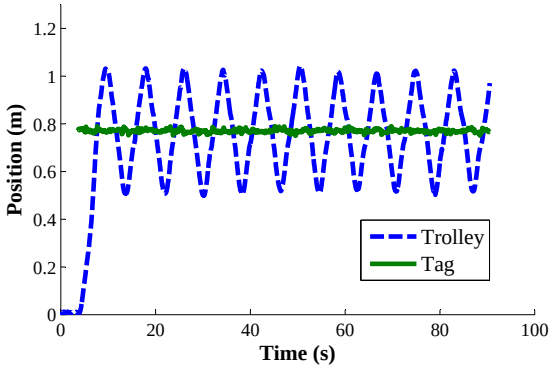

Figure 3.19: Limit Cycling on the HiBay Crane, $e_0 = 0.15m$

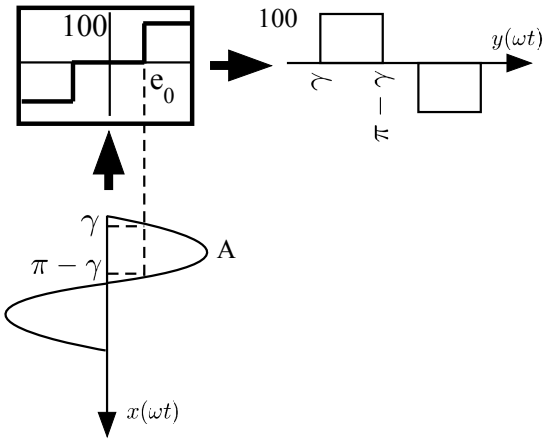

Figure 3.20: Relay-Deadzone Response

The On-Off hand-motion feedback loop in Figure 3.18 was experimentally tested on the HiBay crane. The input shaper was a ZV shaper designed for a nominal length (5m) single pendulum payload. The deadzone size, e_0, was varied to obtain the range of values that yielded self sustaining limit cycles. Note that smaller deadzones are more likely to limit cycle. Figure 3.19 shows the trolley movements when the On-Off controller was limit cycling. Note the tag was used to initiate trolley movement, but was constant throughout the experiment. The deadzone size was $e_0 = 0.15m$, and is the largest value at which self-sustaining limit cycles were observed.

The first step in the DF stability analysis of the On-Off hand-motion controller feedback loop is to obtain the describing functions for the two nonlinearities in Figure 3.18. Recall that a describing function is a quasi-linear approximation for the behavior of a nonlinearity, when the input signal is a sinusoid. The describing function, $N(A, \omega)$ is a function of the input amplitude, A, and frequency, ω, and was defined in (3.1). It is the complex ratio of the fundamental component of the output, $y(t)$ in Figure 3.2(a), to the input sinusoid, $x(t)$ in Figure 3.2(a).

3.5.1 Relay-Deadzone Describing Function

The right side of Figure 3.20 shows the pulse wave-like output, $y(\omega t)$, of the relay-deadzone when subjected to an input sinusoid, $x(t) = Asin(\omega t)$. Note that $A > e_0$ is assumed. If $A \leq e_0$, i.e. $x(t) \leq e_0$, then the input signal is never greater than the deadzone, and therefore the output is always zero. Also, e_0 is the size of the deadzone. The point in the cycle where $x(t) > e_0$ is $\gamma = sin^{-1}\left(\frac{e_0}{A}\right)$. The describing function of the relay-deadzone is a function of the input amplitude.

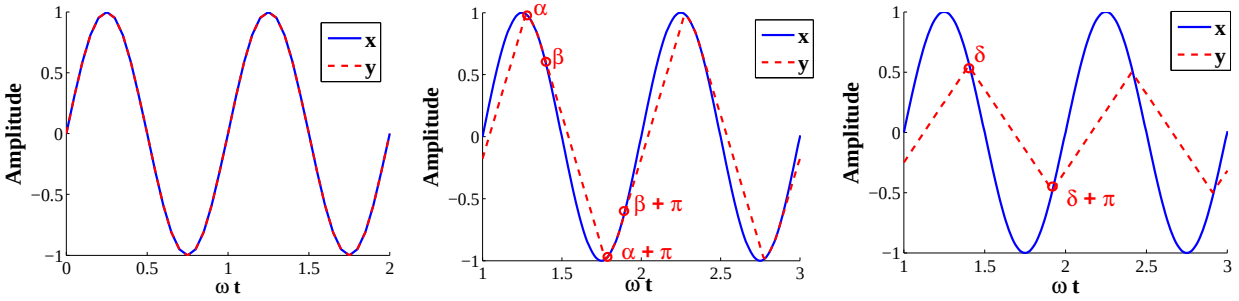

(a) Mode A (b) Mode B (c) Mode C

Figure 3.21: Rate-Limiter Response

It has two qualitatively different modes depending on the size of A [22]:

$$N(A) = \begin{cases} 0 & : A \leq e_0 \\ \frac{400}{A\pi}\sqrt{1-\left(\frac{e_0}{A}\right)^2} & : A > e_0 \end{cases} \tag{3.14}$$

3.5.2 Rate-Limiter Describing Function

Depending on the amplitude and frequency of the input sinusoid, the output of the rate-limiter can be separated into three qualitatively different modes [79]. The output, y, in mode A is plotted against the input sinusoid, x, in Figure 3.21(a). The rate of change of the input is slow compared to the maximum rate allowed by the rate-limiter. Therefore, the output follows the input exactly. For mode B, shown in Figure 3.21(b), the output is able to follow the input sinusoid for certain parts of the cycle, between α and β, where $\beta = cos^{-1}\left(-\frac{m}{A\omega}\right) > \frac{\pi}{2}$, and $sin(\alpha) + sin(\beta) = \frac{m}{A\omega}(\alpha + \pi - \beta)$. At other parts of the cycle, the output always changes at the maximum rate of $\pm m$. For mode C, shown in Figure 3.21(c), the output is unable to follow the input for all parts of the cycle. The output takes the form of a sawtooth wave with rising and falling slew rates equal to $\pm m$. It intersects the input at $\delta = sin^{-1}\frac{\pi m}{2A\omega}$. The conditions and describing functions for the rate-limiter in modes A, B, and C are summarized in Table 3.2 [79].

Table 3.2: Rate-Limiter Describing Functions

Mode	Condition	$N(A,\omega)$
A	$0 < \frac{A\omega}{m} \leq 1$	1
B	$1 < \frac{A\omega}{m} < \sqrt{(\frac{pi^2}{4}+1)}$	$Real = 2m\frac{sin(\alpha)+sin(\beta)}{\pi A\omega} + \frac{sin(\beta)cos(\beta)-sin(\alpha)cos(\alpha)+\beta-\alpha}{\pi}$ $Imag = 2m\frac{cos(\alpha)+cos(\beta)}{\pi A\omega} + \frac{sin(\alpha)^2-sin(\beta)^2}{\pi}$
C	$\frac{A\omega}{m} \geq \sqrt{(\frac{pi^2}{4}+1)}$	$\frac{4m}{\pi A\omega}\left(sin(\delta) + jcos(\delta)\right)$

3.5.3 Limit Cycle Predictions: Ignoring the Rate-Limiter

First, a simplified version of the feedback loop from Figure 3.18 that ignores the rate-limiter is considered. The block diagram of this version is shown in Figure 3.22, where N_1 is the relay-deadzone, G_1 represents the input shaper in (3.12), and G_2 is the linear component of the trolley in (3.13). This system resembles the nonlinear system in Figure 3.2(a), where the forward loop consists of a nonlinearity followed by a linear element (combined from G_1 and G_2). Here, the linear element G_2 is a sufficient low-pass filter, so the application of the DF analysis is justified.

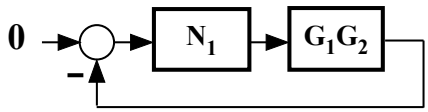

Figure 3.22: Feedback Loop Without the Rate-Limiter

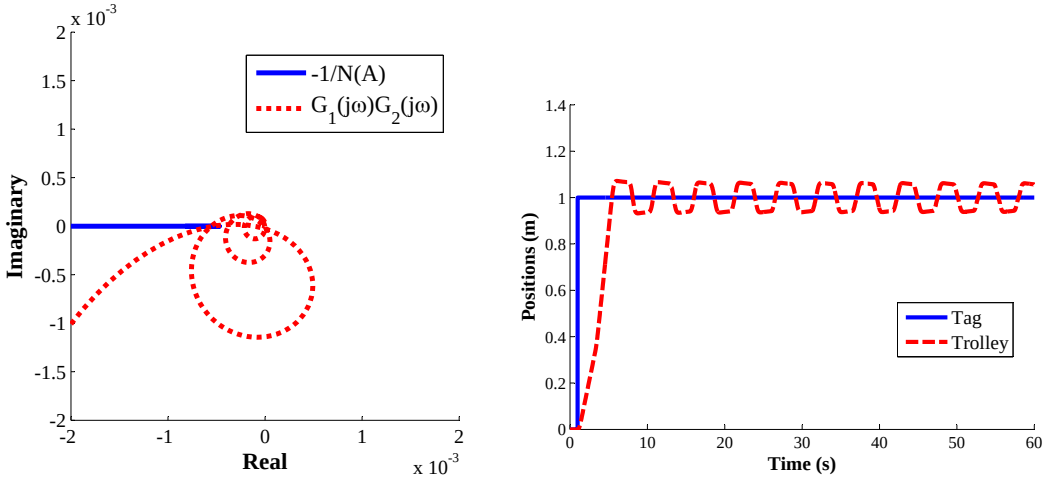

(a) DF Limit Cycle Plot

(b) Simulation Response

Figure 3.23: Predicting Limit Cycles, Ignoring Rate-Limiter. $e_0 = 0.03m$

To predict the existence of limit cycles, a number of values for e_0 were tested. For each e_0, $-1/N(A)$ was plotted against $G_1(j\omega)G_2(j\omega)$ by varying A and ω. Figure 3.23(a) shows the plots for the largest value of e_0 (0.03m) where an intersection between $-1/N(A)$ and $G_1(j\omega)G_2(j\omega)$ is visible. Therefore, the DF analysis predicts $e_0 = 0.03m$ is the largest deadzone for which limit cycles will occur. This is confirmed by computer simulations of the system (without the rate-limiter) in Figure 3.23(b), which clearly shows the trolley oscillating. In this simulation, $e_0 = 0.03m$. If $e_0 > 0.03m$, then the simulations do not show limit cycling.

Although the limit cycle prediction using the DF method matched well with computer simulations, the largest limit cycling deadzone on the HiBay crane was actually 0.15m, as shown in Figure 3.19. This suggests that the rate-limiter plays a significant role in the dynamics of the HiBay crane.

3.5.4 Limit Cycle Predictions: Including the Rate-Limiter

The block diagram with the rate-limiter, N_2, is shown in Figure 3.24. Note that this system contains multiple nonlinearities. To predict limit cycles, it is simpler to plot the open-loop transfer function, $N_1(A)G_1(j\omega)N_2(A,\omega)G_2(j\omega)$, for a range of amplitudes, frequencies, and e_0's. If the plots pass through -1+0j, then limit cycles are predicted.

Using this method, the plots for $e_0 = 0.03m$ are shown in Figure 3.25(a). Each line represents the value of the open-loop transfer function for a constant value of A_2 (the amplitude of N_2's input sinusoid), but varying ω. The green cross indicates the location of -1+0j. Figure 3.25(a) indicates that if the deadzone is 0.03m (this is the largest value found using this method), then the system

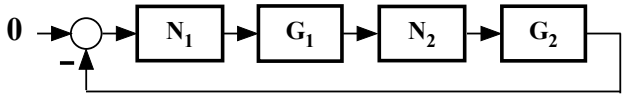

Figure 3.24: Feedback Loop With the Rate-Limiter

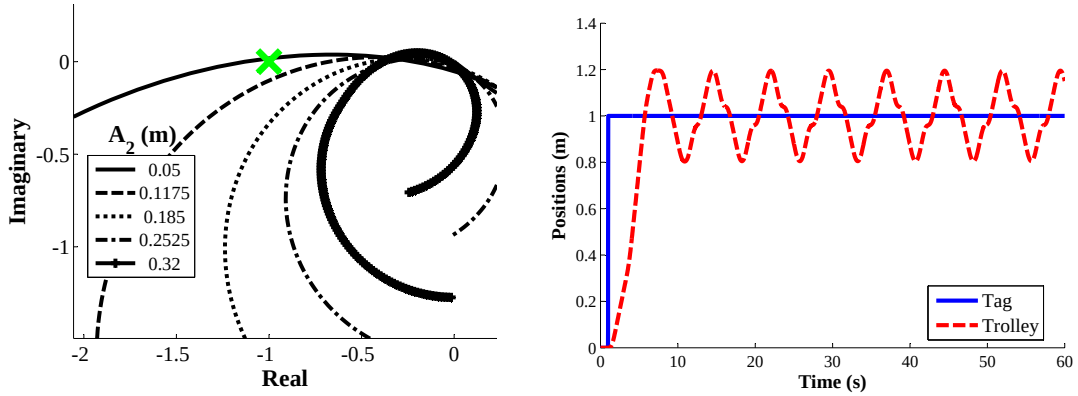

(a) $N_1(A)G_1(j\omega)N_2(A,\omega)G_2(j\omega)$, $e_0 = 0.03m$

(b) Simulation Response, $e_0 = 0.12m$

Figure 3.25: Predicting Limit Cycles, Including the Rate-Limiter

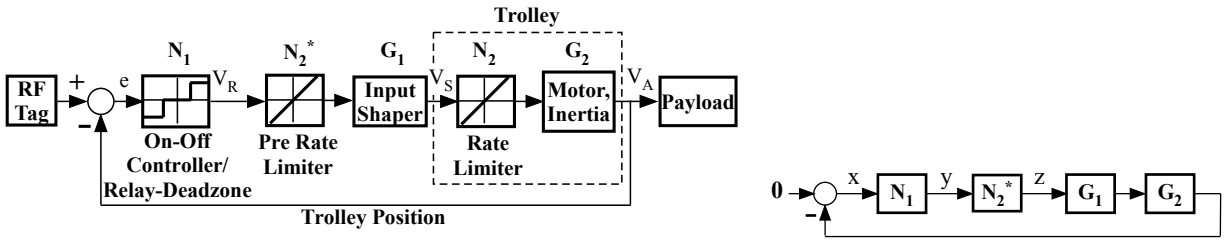

(a) Block Diagram

(b) Effective Feedback Loop Used for DF Analysis

Figure 3.26: On-Off Control with Pre-Rate-Limiter

will exhibit limit cycle behavior with $A_2 \approx 0.05m$.

However, this time the predictions using the DF method did not match the computer simulation results. The largest deadzone found from simulations was $e_0 = 0.12m$. The response is shown in Figure 3.25(b). However, note that the limit cycle prediction using computer simulation is reasonably close to that of the actual HiBay crane ($e_0 = 0.15m$). This indicates the accuracy of the simulation model is quite good.

The DF prediction was inaccurate because the input shaper, G_1, is not a sufficient low-pass filter. Therefore, the fundamental assumption for the DF method was violated.[9] One way to circumvent this problem is with a pre-rate-limiter, which is the topic of the next section.

3.5.5 On-Off Controller with Pre-Rate-Limiter

An alternative On-Off hand-motion controller is to insert a pre-rate-limiter before the input shaper, represented as N_2^* in Figure 3.26(a). A properly designed pre-rate-limiter provides several benefits:

1. It ensures that the shaped command reaches the trolley motors uncorrupted by the rate-limiter (N_2) in the motor drives [100]. In certain cases, a rate-limiter can have adverse effects on the oscillation-reducing properties of an input-shaped signal.

2. It effectively removes the actual rate-limiter from the system. This reduction results in the feedback loop shown in Figure 3.26(b). This is because a pre-rate-limited input-shaped signal

[9] This can be confirmed by replacing G_1 with an appropriate low-pass filter, such as $\frac{0.05}{s+4}$. In this case, the limit cycle predictions using the DF method match the computer simulations.

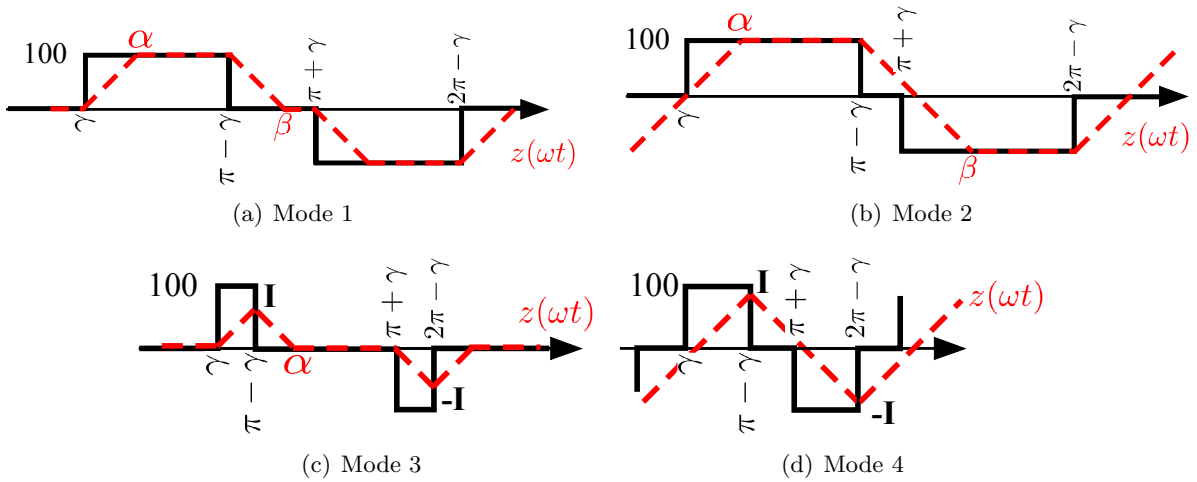

(a) Mode 1

(b) Mode 2

(c) Mode 3

(d) Mode 4

Figure 3.27: Output Modes of Relay-Deadzone Rate-Limiter

never exceeds the bounds of the rate-limiter. Therefore, the rate-limiter always operates in its linear regions, and is effectively removed from the system.

3. The DF method can be used to predict limit cycles accurately for the system in Figure 3.26(b). This is because $N_1 N_2^*$ can be combined into one nonlinearity, and $G_1 G_2$ combined into one linear element, which, despite the input shaper, retains the low-pass filtering properties from G_2. The resulting system resembles the classical single nonlinearity system for DF analysis from Figure 3.2(a). In this manner, the fundamental assumptions of the DF method are valid, and accurate limit cycle predictions can be expected.

The next step is to derive the describing function for the combined relay-deadzone (pre)-rate-limiter, or $N_1 N_2^*$.

3.5.6 Relay-Deadzone Rate-Limiter Describing Function

As labeled in Figure 3.26(b), the input sinusoid to the relay-deadzone, N_1, is x. The behavior of the relay-deadzone was shown in Figure 3.20 and described by (3.14). The relay-deadzone's output is y, which is the input to the rate-limiter. The output of the rate-limiter, $z(\omega t)$, can have one of four qualitatively different behavior modes. These modes are shown in Figure 3.27, where the solid and dashed lines represent $y(\omega t)$ and $z(\omega t)$, respectively. The slope of $z(\omega t)$ is limited to $\pm m$ by the rate-limiter in all modes.

3.5.6.1 Mode 1

In mode 1, shown in Figure 3.27(a), the rate-limiter is fast enough such that $z(\omega t)$ reaches all states (100, 0, -100) produced by the relay-deadzone. The conditions for mode 1 are:

$$\frac{m}{\omega} \geq \frac{H}{\pi - 2\gamma}, \quad \frac{m}{\omega} \geq \frac{H}{2\gamma} \tag{3.15}$$

where $H = 100$ is the amplitude of the relay output. The mode 1 output over one period is:

$$z(\omega t) = \begin{cases} \frac{m}{\omega}(\omega t - \gamma) & \omega t = [\gamma, \alpha) \\ H & \omega t = [\alpha, \pi - \gamma) \\ H - \frac{m}{\omega}(\omega t - (\pi - \gamma)) & \omega t = [\pi - \gamma, \beta) \\ 0 & \omega t = [\beta, \pi + \gamma) \\ -\frac{m}{\omega}(\omega t - (\pi + \gamma)) & \omega t = [\pi + \gamma, \alpha + \pi) \\ -H & \omega t = [\alpha + \pi, 2\pi - \gamma) \\ -H + \frac{m}{\omega}(\omega t - (2\pi - \gamma)) & \omega t = [2\pi - \gamma, \beta + \pi) \\ 0 & \omega t = [\beta + \pi, \gamma + 2\pi) \end{cases} \tag{3.16}$$

Where $\alpha = \frac{H\omega}{m} + \gamma$ and $\beta = \frac{H\omega}{m} + (\pi - \gamma)$.

3.5.6.2 Mode 2

In mode 2, as shown in Figure 3.27(b), the output is such that it can reach the ±100 relay states, but not the 0 state in the middle. The conditions for mode 2 are:

$$\frac{m}{\omega} \geq \frac{2H}{\pi}, \quad \frac{m}{\omega} \leq \frac{H}{2\gamma} \tag{3.17}$$

The mode 2 output over one period is:

$$z(\omega t) = \begin{cases} -H + \frac{m}{\omega}(\omega t + \gamma) & \omega t = [-\gamma, \alpha) \\ H & \omega t = [\alpha, \pi - \gamma) \\ H - \frac{m}{\omega}(\omega t - (\pi - \gamma)) & \omega t = [\pi - \gamma, \beta) \\ -H & \omega t = [\beta, 2\pi - \gamma) \end{cases} \tag{3.18}$$

Where $\alpha = -\gamma + \frac{2H\omega}{m}$ and $\beta = \alpha + \pi$.

3.5.6.3 Mode 3

In mode 3, as shown in Figure 3.27(c), the output is able to reach the 0 state in the middle but unable to reach the ±100 states. The output intersects the falling and rising edges of the input at $\pm I$, where $I = \frac{m}{\omega}(\pi - 2\gamma)$. The conditions for mode 3 are:

$$\frac{m}{\omega} \leq \frac{H}{\pi - 2\gamma}, \quad 1 \geq \frac{\pi - 2\gamma}{2\gamma} \tag{3.19}$$

The mode 3 output over one period is:

$$z(\omega t) = \begin{cases} \frac{m}{\omega}(\omega t - \gamma) & \omega t = [\gamma, \pi - \gamma) \\ I - \frac{m}{\omega}(\omega t - (\pi - \gamma)) & \omega t = [\pi - \gamma, \alpha) \\ 0 & \omega t = [\alpha, \pi + \gamma) \\ -\frac{m}{\omega}(\omega t - (\pi + \gamma)) & \omega t = [\pi + \gamma, 2\pi - \gamma) \\ -I + \frac{m}{\omega}(\omega t - (2\pi - \gamma)) & \omega t = [2\pi - \gamma, \alpha + \pi) \\ 0 & \omega t = [\alpha + \pi, \gamma + 2\pi) \end{cases} \tag{3.20}$$

Where $\alpha = (\pi - \gamma) + \frac{I\omega}{m}$.

3.5.6.4 Mode 4

In mode 4, as shown in Figure 3.27(d), the output cannot reach any constant state and intersects the input at the falling and rising edges. Note that depending on initial conditions, the output may have non-zero offset and may not be symmetrical about the horizontal axis. However, for simplicity, it is assumed here that the mode 4 output is symmetric and intersects the input at $\pm I$, where $I = \frac{m\pi}{\omega 2}$. The conditions for mode 4 are:

$$\frac{m}{\omega} \leq \frac{2H}{\pi}, \quad 1 \leq \frac{\pi}{4\gamma} \tag{3.21}$$

The mode 4 output over one period is:

$$z(\omega t) = \begin{cases} -I + \frac{m}{\omega}(\omega t + \gamma) & \omega t = [-\gamma, \pi - \gamma) \\ I - \frac{m}{\omega}(\omega t - (\pi - \gamma)) & \omega t = [\pi - \gamma, 2\pi - \gamma) \end{cases} \tag{3.22}$$

3.5.6.5 Describing Functions for All Modes

Having described the behavior between the input and output of the relay-deadzone rate-limiter, its describing function can be obtained by evaluating the DF definition, (3.1). If $A \leq e_0$, then $N(A, \omega) = 0$. Otherwise, the following are the describing functions for all four modes, and are applicable when conditions for each mode are satisfied (Equations (3.15), (3.17), (3.19), (3.21) for modes 1-4 respectively):
Mode 1:

$$N(A,\omega) = \frac{4m}{\pi A\omega}\sin\left(\frac{H\omega}{m}\right)\cos(\gamma) + \frac{j4m}{\pi A\omega}\cos(\gamma)\left(-1+\cos\left(\frac{H\omega}{m}\right)\right) \tag{3.23}$$

Mode 2:

$$\begin{aligned} N(A,\omega) = {} & \frac{-4m}{\pi A\omega}\left(-\sin(\gamma)+\sin(\gamma)\left(\cos\left(\frac{H\omega}{m}\right)\right)^2 - \cos(\gamma)\sin\left(\frac{H\omega}{m}\right)\cos\left(\frac{H\omega}{m}\right)\right) + \\ & \frac{-j4m}{\pi A\omega}\left(-\cos(\gamma)+\cos(\gamma)\left(\cos\left(\frac{H\omega}{m}\right)\right)^2 + \sin(\gamma)\sin\left(\frac{H\omega}{m}\right)\cos\left(\frac{H\omega}{m}\right)\right) \end{aligned} \tag{3.24}$$

Mode 3:

$$N(A,\omega) = \frac{8m}{A\pi\omega}\sin(\gamma)\left(\cos(\gamma)\right)^2 - j\left(\cos(\gamma)\right)^3 \tag{3.25}$$

Mode 4:

$$N(A,\omega) = \frac{4m}{A\pi\omega}\left(\sin(\gamma) - j\cos(\gamma)\right) \tag{3.26}$$

3.5.7 Limit Cycle Prediction: On-Off Controller with the Pre-Rate-Limiter

The describing functions for the relay-deadzone rate-limiter were used to plot the On-Off controller's open-loop transfer function, $N_1N_2^*(A, j\omega)G_1(j\omega)G_2(j\omega)$, over a range of A's (the amplitude of the input sinusoid into $N_1N_2^*$), ω's, and e_0's. Recall that plots that intersect -1+0j indicate the existence of limit cycles. Figure 3.28(a) shows the plots for the largest value of e_0 ($= 0.12m$) where $N_1N_2^*(A, j\omega)G_1(j\omega)G_2(j\omega)$ intersect -1+0j (the location is indicated by the green cross). Each line represents the value of the open-loop transfer function for a constant value of A, but varying ω. At the intersection with -1+0j, A and ω are approximately 0.23 m and 0.84 rad/s, respectively.

The predictions from the DF analysis also matched the simulation results from a computer model of the pre-rate-limited feedback loop. Figure 3.28(b) plots the response when $e_0 = 0.12m$,

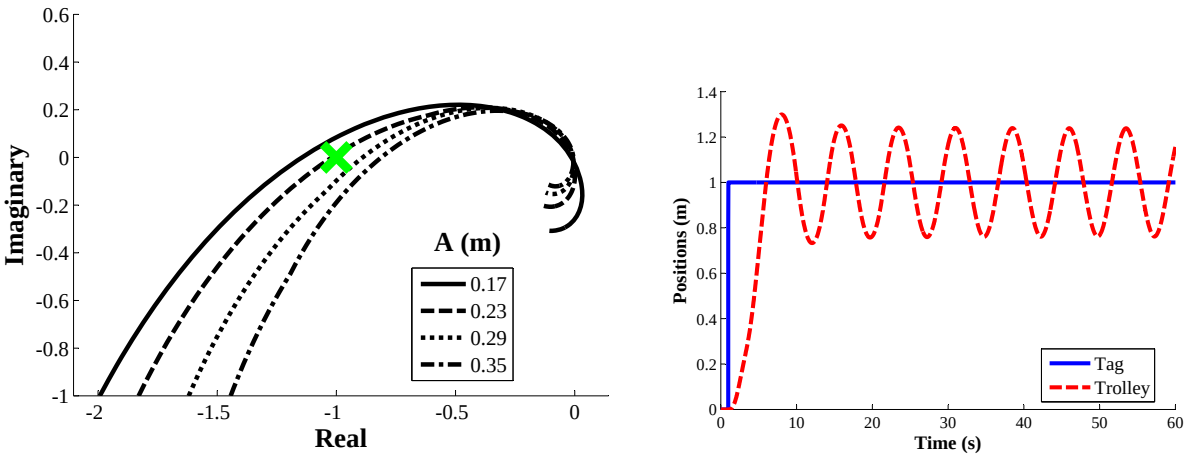

(a) $N_1N_2^*(A, j\omega)G_1(j\omega)G_2(j\omega)$ (b) Simulation Response

Figure 3.28: Predicting Limit Cycles, with Pre-Rate Limiter, $e_0 = 0.12m$

which was the largest value that resulted in limit cycling. The predicted amplitude and frequency of limit cycle also closely matched the simulation results: $A_{sim} = 0.20m$, and $\omega_{sim} = 0.84$ rad/s.

The pre-rate-limited On-Off controller was also implemented on the HiBay crane. Experimental results showed that the largest value of e_0 which caused limit cycles was 0.16m. The limit cycle predictions from the DF analysis, computer simulations, and experimental results are summarized in Table 3.3. Note that both prediction methods were quite close (within 4cm) to the experimental results. Furthermore, both methods accurately predicted the amplitude and frequency of the limit cycle as well.

Table 3.3: Comparison Limit Cycle Predictions and Experimental Results

Method	Largest Limit Cycle e_0 (m)	Amplitude A (m)	Frequency ω (rad/s)
DF Analysis	0.12	0.23	0.84
Computer Simulations	0.12	0.23	0.838
HiBay Crane	0.16	0.271	0.733

Figure 3.29 shows the tag and trolley response on the HiBay crane implementation. Two cases are shown: 1) $e_0 = 0.16$m, which was the largest value of e_0 that caused limit cycles; and 2) $e_0 = 0.6$m, which did not cause limit cycles.

3.6 Brisk On-off Smart Stop (BOSS) Controller

While the On-Off controller improves over the PD/P controller in many aspects, its greatest weakness is in the size of its deadzone. In essence, e_0 alone determines the stability of the feedback loop, as well as the controller performance. Previous discussions of the On-Off controller assumed the deadzone was fixed in size. In Section 3.4.1, this size was determined by the largest crane stopping distance from maximum velocity. This design choice accounts for the worst case scenario, so that the payload does not overshoot and the trolley does not overtravel the desired location.

To understand the weakness of a fixed-sized deadzone, consider the acceleration and deceleration properties of the On-Off controller. When the crane is stopping, it requires a relatively large deadzone so that the it does not overshoot the desired location. However, when the operator wishes to initiate motion, a large deadzone is undesirable, because it increases the operator perceived lag. Therefore, the acceleration of the On-Off controller would benefit from a small deadzone. This

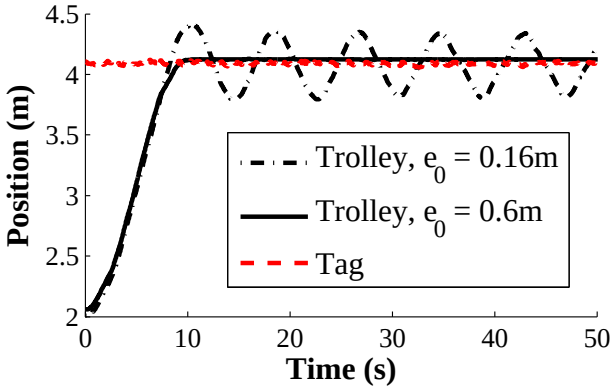

Figure 3.29: On-Off Hand-Motion Controller with Pre-Rate-Limiter, Experimental Response on the HiBay Crane

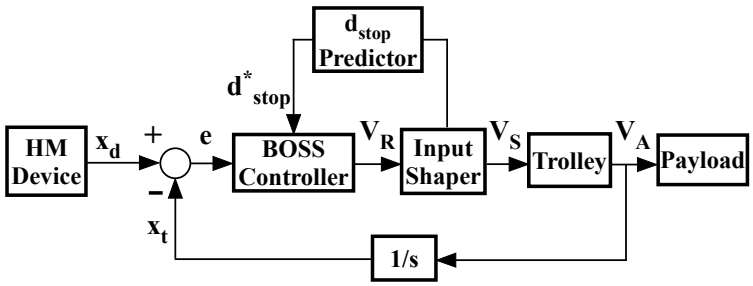

Figure 3.30: Brisk On-off Smart Stop (BOSS) Controller Block Diagram

is the also the reason why small deadzones are desirable for precise positioning, a feature that is crucial for the Fixed Relative Positioning (FRP) mode.[10] In summary, a fixed-sized deadzone needs to compromise between the conflicting requirements during acceleration, and during deceleration. Furthermore, the deceleration properties are not constant. For example, the stopping distance varies with different input shapers, and is reduced if the crane is not decelerating from maximum velocity.

This motivates the design of a new Brisk On-off Smart Stop (BOSS) controller. The nominal deadzone is small so that the operator can briskly initiate crane motions. However, the controller also stops the crane intelligently without trolley overtravel, payload overshoot, or residual oscillations around the desired position.

Figure 3.30 shows the BOSS controller block diagram. It has the same basic architecture as the other hand-motion controllers, but with the following exceptions: 1) the position of the hand-motion (HM) device is x_d; 2) the trolley position (integrated from V_A) is x_t; 3) the BOSS controller takes the place of the HM controller; and 4) the addition of the "d_{stop} Predictor" block. This block takes inputs from the input shaper block, and produces the output signal, d^*_{stop}, which then goes into the BOSS controller.

3.6.1 d_{stop} Predictor

At each digital time step,[11] the d_{stop} predictor calculates an estimate, d^*_{stop}, for the crane's stopping distance, d_{stop}. This distance assumes that a "Stop Now" command was issued at that instant in time, i.e. deactivating hand-motion control as if the operator released the button on the HM device.

[10] Section2.5: Fixed Relative Positioning Mode.

[11] Assuming the controller is implemented on a computational device such as a PLC.

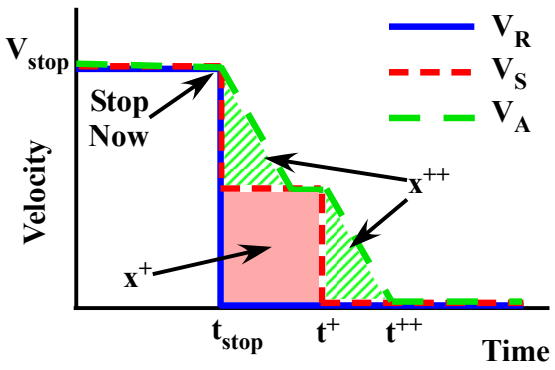

Figure 3.31: Overtravel from Input-Shaped Velocity Commands

Note this stop command effectively sets $e = V_R = 0$.

At this juncture, it is important to note some characteristics of input shaping. In essence, input shapers are partial time delays. Input shaping convolves V_R with delayed shaper impulses. Effectively, at each cycle time, a portion of V_R is used to form the shaped output, V_S. The remaining portion of V_R is saved for future outputs. On digital devices, this input-shaping process is implemented using memory buffers that store the portion of V_R that is executed at later times [86].

Figure 3.31 illustrates how the input-shaping process can create overtravel, and thus affect the calculation of d^*_{stop}. With reference to the block diagram in Figure 3.30, V_R is the reference velocity command; V_S is the input-shaped velocity command; and V_A is the actual trolley velocity. At time t_{stop}, the "Stop Now" command is issued, so V_R is immediately set to zero. However, because there are still unexecuted commands[12] remaining in the input shaper's buffer, V_S continues on for some time, reaching zero velocity at t^+. The red solid filled region is known as the "Overtravel" distance, or x^+ [120]. It represents the distance that the V_S velocity profile travels between t_{stop} and t^+.

In the example shown in Figure 3.31, the effects of the trolley's inertia, motor drives, etc, gives V_A a trapezoidal ramp profile and, therefore, the acceleration is finite. V_A also continues after the "Stop Now" command, finishing at zero velocity at t^{++}. The green hash filled regions are marked by x^{++},[13] and they represent the distance that the V_A velocity profile travels between t_{stop} and t^{++}.

3.6.1.1 Simple Method for Calculating d^*_{stop}

x^+ can be calculated ahead of time by the coarse integration of the shaped velocity command from t_{stop} to t^+, using the shaper impulse times as the integration step size [120]:

$$x^+ = V_{stop} \sum_{i=2}^{n} A_i t_i \tag{3.27}$$

where $V_{stop} = V_R(t_{stop})$, n is the number of impulses in the shaper, and A_i and t_i are the i^{th} shaper impulse amplitude and time location, respectively. x^+ can also be easily calculated by summing all unexecuted commands in the shaping buffer, V_{buffer}, and multiplying by the digital cycle time, t_s:

$$x^+ = t_s \sum V_{\text{buffer}} \tag{3.28}$$

This simple prediction method uses x^+ as the estimate for the trolley stopping distance:

$$d^*_{\text{stop, simple}} = x^+. \tag{3.29}$$

[12] A ZV shaper is used in the example shown here.
[13] Note that x^{++} includes the area denoted by x^+.

If the "Trolley" block in Figure 3.30 is unity, i.e. the dynamics of the trolley and motors can be ignored such that $V_S = V_A$, then the prediction is exact, i.e. $d^*_{\text{stop, simple}} = d_{stop}$. Often, even in cases where the trolley block is not unity, (3.29) can still provide a good estimate of the actual stopping distance. This issue will be discussed further in Section 3.6.5.

3.6.1.2 Advanced Method for Calculating d^*_{stop}

A more accurate prediction of the actual stopping distance accounts for the trolley dynamics, i.e. calculates the value of x^{++}. This value can be found by integrating V_A from t_{stop} to t^{++}. However, V_A is the actual trolley velocity. Although V_A can be measured in real-time by sensors in the motor drives or encoders, these sensors measurements cannot be used to predict V_A ahead of time. Therefore, a prediction method is required.

One way to do this is to perform a coarse simulation of the Trolley block, which, for this discussion, is represented by a linear model with impulse response $G_T(t)$. Note that $G_T(t)$ should also include the integrator between V_A and x_t, shown in Figure 3.30. Then, the input to $G_T(t)$ is the V_S velocity profile after t_{stop}, i.e. $V_S|_{[t_{stop},t^+]}$. Note that at $t = t_{stop}$, this velocity profile is completely known, and can therefore be used for predictions:

$$V_S|_{[t_{stop},t^+]} = A_i V_{stop} \quad : t_{stop} + t_{i-1} \leq t < t_{stop} + t_i, \quad \text{for } i = 2, \ldots, n \tag{3.30}$$

where n is the number of impulses in the shaper, and A_i and t_i are the i^{th} shaper impulse amplitude and time location, respectively. Note that $t^+ = t_{stop} + t_n$.

The input profile V_S can be approximated as a finite sum of N pulses, by breaking (3.30) into pulses of width Δ so that:

$$V_S(t) \approx \sum_{j=0}^{N} V_S(j\Delta)\delta(t - j\Delta)\Delta, \tag{3.31}$$

where $\delta(t-j\Delta)$ is the unit pulse function delayed by $j\Delta$, and $N = \text{Round}(t_n/\Delta)$. Then, at $t = t_{stop}$, x^{++} can be calculated by multiplying the V_S pulses with the trolley impulse response, $G_T(t)$, and summing the result:

$$x^{++} = \sum_{j=0}^{N} V_S(j\Delta) \times G_T(t - j\Delta) \times \Delta. \tag{3.32}$$

Therefore, a more accurate prediction of d_{stop} is:

$$d^*_{\text{stop, adv.}} = x^{++}. \tag{3.33}$$

The above method assumes the trolley and motor drives can be modeled by the impulse response, $G_T(t)$. If, however, nonlinearities must be accounted for (e.g. rate-limiter in the HiBay crane motor drives), then x^{++} can still be predicted by performing numerical simulations.

One caveat to using (3.33) is that the designer must account for the computational complexities. This is because a d^*_{stop} prediction must be made at *every* digital cycle. For example, even if the trolley and motor drives are modeled as a linear second-order plant, $G_T(t)$ is an exponentially decaying sinusoid, which contain hard-to-compute terms such as square roots and exponentials. Those terms need to be multiplied and summed as per (3.33). Furthermore, if Δ is small, more summations need to be executed. Obviously, predicting x^{++} using numerical simulations is even more computationally expensive.

3.6.2 BOSS Controller Algorithm

Knowing where the crane will stop is a powerful tool that can be used to directly address the weaknesses of the On-Off controller. Firstly, the nominal deadzone size can be lowered significantly,

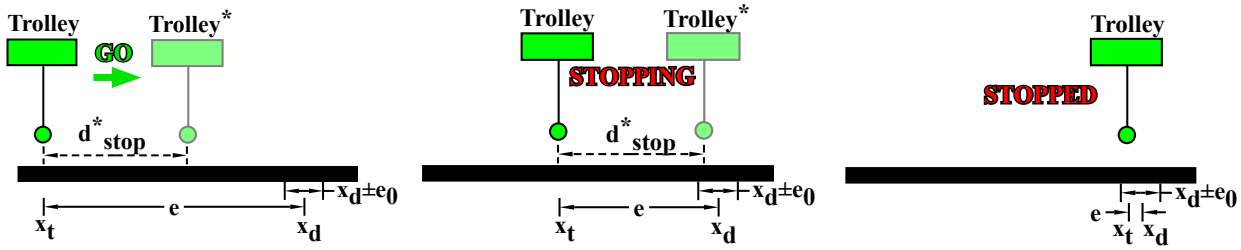

(a) Going (b) Stopping (c) Stopped

Figure 3.32: Behavior of the BOSS Controller

which is beneficial for initiating crane motion and for brisk acceleration. Secondly, the d^*_{stop} prediction can be used to intelligently stop the crane near the desired HM device position, x_d, and also to prevent the trolley from overtraveling beyond x_d. The BOSS control algorithm is essentially an On-Off controller that accounts for d^*_{stop}:

$$V_R = \begin{cases} 0\% & : |e| \leq e_0 \text{ OR } d^*_{stop} > |e| - e_0 \\ 100\% \times \text{sign}(e) & : |e| > e_0 \end{cases} \tag{3.34}$$

Recall that $e = x_d - x_t$, where x_t is the position of the trolley. The behavior of the BOSS controller is illustrated in Figure 3.32. In Figure 3.32(a), the trolley is initially a distance e away from the desired position, x_d. Therefore, the BOSS controller issues full-velocity commands to move the trolley rightwards. The predictor calculates the position where the trolley will stop, if a stop command is issued at that instant. The predicted position is pictorially represented by $Trolley^*$. The position of $Trolley^*$ is d^*_{stop} distance away from x_t.

In Figure 3.32(b), the predictor calculates that $Trolley^*$ will overtravel the near-side deadzone boundary. Therefore, the BOSS controller issues a stop command at this instant, and the trolley begins to decelerate. In Figure 3.32(c), the trolley has stopped at the predicted position within the deadzone.

By observing the behavior of the BOSS controller, it can be seen that e_0 is effectively the acceptable tolerance of the trolley position from the desired position. If d^*_{stop} predictions are accurate, then the trolley is guaranteed to stop within e_0 distance from x_d.

3.6.3 Performance Comparisons to PD and On-Off Controllers

To compare the performance of the BOSS controller to previous controllers, simulations of the HiBay crane with various controllers were performed. Note the HiBay trolley is modeled as a nonlinear rate-limiter combined with a linear second-order plant. Various types of Hand-Motion (HM) device input motions are used as examples to demonstrate the strengths and weaknesses of each controller.

3.6.3.1 Point-to-Point (PTP) Step Moves

Figure 3.33(a) shows the response using a PD controller with $e_0 = 0m$, $e_{100} = 3m$, $K_p = 15$. Plotted are the positions of the HM device (held constant at 2m, and HM control was activated after 1s), trolley, hook, and the boundaries of the deadzone. The plot for the deadzone boundaries overlap the position of the HM device because $e_0 = 0$. Although in practice, e_0 is usually not chosen to be zero for PD controllers, it is done so in this case in order to accentuate PD characteristics. This will in turn, help in the comparisons with the On-Off and BOSS controllers. Also, note that unlike the experimental hand-motion control responses shown in Figures 3.12(a), 3.13(a), and 3.14(a), hand-motion control is not deactivated by a human operator when the trolley approaches the desired

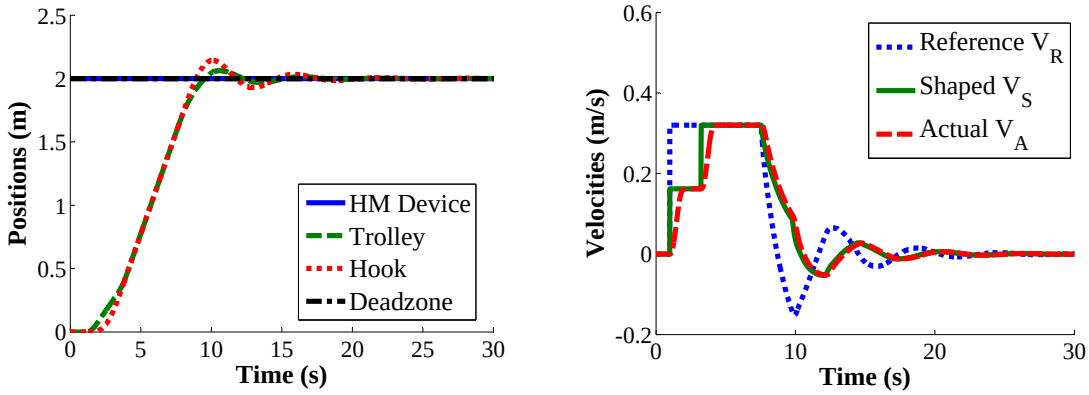

(a) Positions (b) Velocities

Figure 3.33: Aggressive Rise Time Gains PD, $e_0 = 0m$, $e_{100} = 3m$, $K_p = 15$, $K_d = 10$

position in the results shown here. Hand-motion control remains activated during the entire trial for the purpose of comparing controller performance.

To reiterate, the advantages of the PD controller is that the deadzone may be set very low, and it is good for making precise movements. However, it is beset by weaknesses: 1) at least four control parameters need to be selected; 2) it does not perform well with real-world sensor noise;[14] and 3) the inherent oscillatory nature of the closed-loop poles require tuning the gains to compromise between overshoot/overtravel, settling time, and rise time.

For example, the response in Figure 3.33(a) was tuned to have aggressive rise times (the trolley reached 2m for the first time at 9.54s). However, the down side is that the response exhibits hook overshoot, a maximum trolley overtravel of 0.062m, and oscillatory behavior around the desired position. Because of the oscillations, the trolley 2% settling time is relatively slow at 11.46s.

Figure 3.33(b) shows the reference command, V_R, shaped command, V_S, and the actual trolley velocity, V_A. Note the shape of V_R is a step during the acceleration phase, which produces the fastest possible acceleration. However, during deceleration, V_R is a gradual decay, and then oscillated around 0, sending forward and reverse commands when the trolley is oscillating around the HM device. Clearly, this is not the fastest nor the most efficient way of decelerating.

If less overtravel is desired, then the controller gains must be decreased to $K_p = 10$ from $K_p = 15$. This response is shown in Figure 3.34(a). Obviously, less aggressive gains increase the rise time. The time it took for the trolley to reach 2m for the first time was 10.39s, or 0.85s slower than that of the aggressive gains PD. However, because overtravel was less, the 2% settling time is 9.7s, or 1.76s faster than the aggressive PD. Note the trolley still exhibits small oscillatory behaviors after reaching 2m. Figure 3.34(b) shows the velocities. Again, the shape of V_R is a step during acceleration, but decays gradually during deceleration, and still oscillates after reaching the desired position.

Figure 3.35(a) shows the response of an On-Off controller with $e_0 = 0.49m$. The size of the deadzone was chosen to match the crane's stopping distance from maximum velocity. Because of this, the trolley and hook stopped almost exactly at the desired position of the HM device. The speed of the response is virtually identical to that of the no-overtravel PD. The trolley reached its final position (2.019m) at 10.34s, or 0.05s faster than the no-overtravel PD. The 2% settling time was 9.77s, or 0.07s slower than the no-overtravel PD. However, unlike the PD, the On-Off controller did not exhibit overtravel nor oscillatory behaviors.

Advantages of the the On-Off controller are: 1) simple to design, as only one parameter, e_0,

[14] Sensor noise is not shown in these simulations

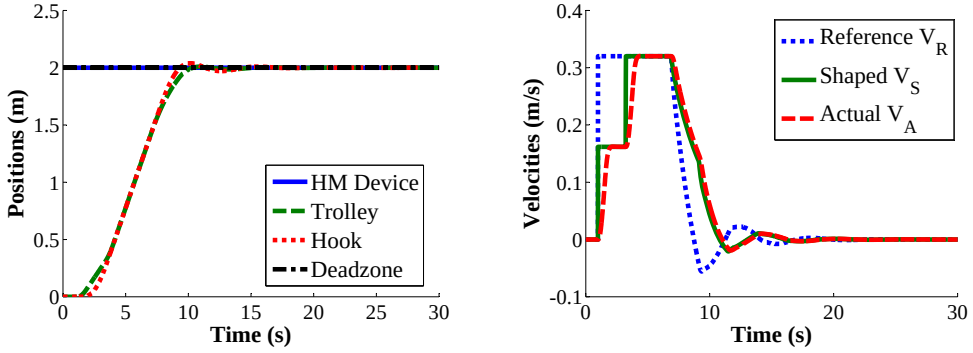

(a) Positions (b) Velocities

Figure 3.34: No-Overtravel Gains PD, $e_0 = 0m$, $e_{100} = 3m$, $K_p = 10$, $K_d = 10$

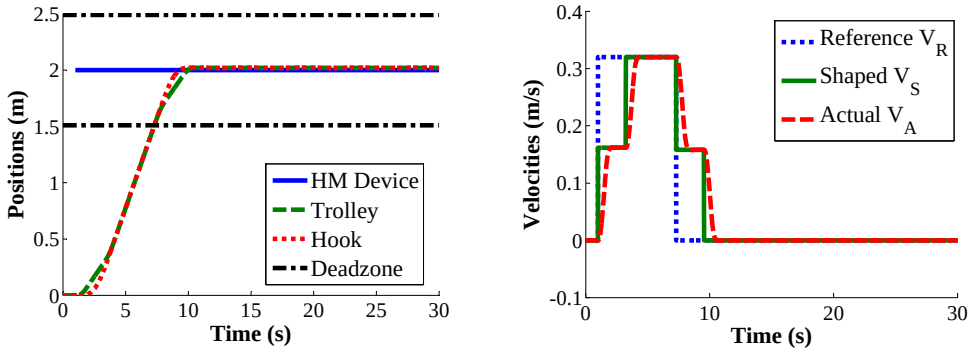

(a) Positions (b) Velocities

Figure 3.35: On-Off, $e_0 = 0.49m$

needs to be chosen; 2) less susceptible to real-world sensor noise;[15] and 3) because the controller only outputs 100% or 0% V_R commands, movements are generally faster. This can be seen in Figure 3.35(b). The shape of V_R are steps during acceleration *and* deceleration. In general, given a fixed input shaper, step reference velocity commands are the fastest way of moving a system without residual oscillations or overshoot.

Figure 3.36(a) shows the response using the BOSS controller, with e_0 set to a smaller distance, 0.15m. The response is virtually identical to that of the On-Off controller. Note that $d^*_{stop} \neq d_{stop}$ because the simple prediction method in (3.29) was used.[16] Figure 3.36(b) shows that the BOSS V_R commands are also virtually identical (steps in acceleration and deceleration) to that of the On-Off controller.

To illustrate the superior deceleration behavior of the On-Off and BOSS controllers over the PD controller, point-to-point moves with varying step sizes were conducted. In the simulation trials, the PD controller parameters were chosen to minimize trolley overtravel and were $e_0 = 0m$, $e_{100} = 3m$, $K_p = 10$, $K_d = 10$. The On-Off e_0 was 0.49m, and the BOSS e_0 was 0.15m.

Figure 3.37(a) plots the maximum trolley overtravel (defined as the difference between the maximum trolley position and the final trolley position) versus the step size. With the PD controller, the trolley consistently overtravels, while the On-Off and BOSS controllers do not. Even though the PD overtravel distances are generally small (2.5cm), it emphasizes the point that PD CLSS

[15] Sensor noise is not shown in these simulations

[16] Robustness to d^*_{stop} prediction errors will be discussed in Section 3.6.5

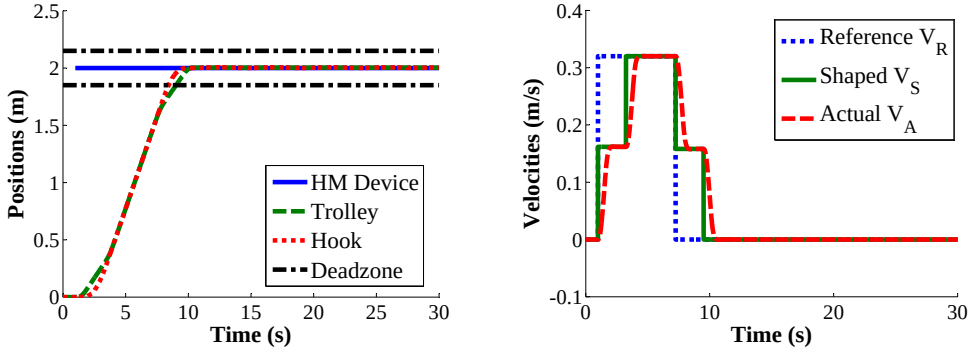

(a) Positions (b) Velocities

Figure 3.36: BOSS, $e_0 = 0.15m$

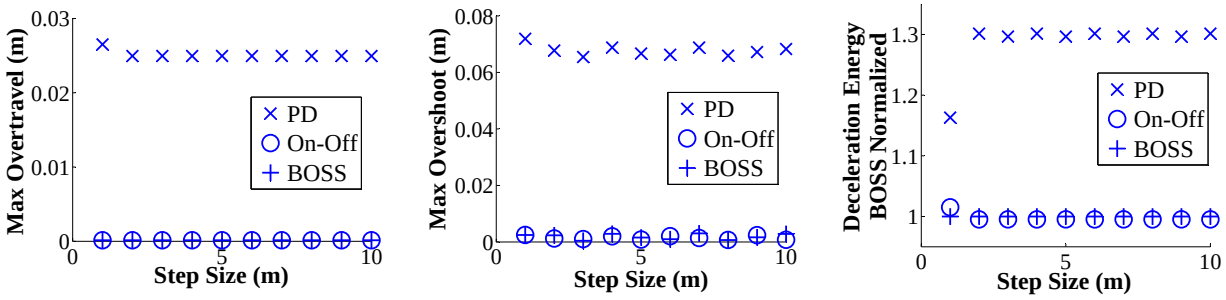

(a) Maximum Trolley Overtravel (b) Maximum Hook Overshoot (c) Deceleration Energy

Figure 3.37: Controller Performance Comparisons to PTP Inputs

controllers are inherently oscillatory. Figure 3.37(b) shows similar results for the maximum hook overshoot, defined as the difference between the maximum hook position and the final hook position. The PD controller consistently overshoots by about 7cm, while the On-Off and BOSS controllers show very little overshoot. Note that hook overshoots are undesirable because it can potentially hit obstacles or the operator beyond the desired position.

The energy usage is one way to measure the inefficient and oscillatory movements of the PD controller during deceleration. The energy usage is approximated as the integral of the square of the actual trolley velocity, V_A, after the crane begins to decelerate at $t = t_{decel}$:

$$E_{decel} = \int_{t_{decel}}^{t_f} (V_A(t))^2 \, dt, \tag{3.35}$$

where t_f is the trial's final time. Figure 3.37(c) plots the energy use, normalized to that of the BOSS controller, for all controllers versus step size. The plots show that the PD controller consistently expends about 30% more energy than the On-Off and BOSS controllers. For a step size = 1m, the PD controller only uses about 15% more energy because the trolley did not reach maximum velocity before decelerating.

Experimental point-to-point moves were conducted on the HiBay crane. Figure 3.38(a) plots the maximum trolley overtravel for step sizes ranging from 1-5m. With the On-Off and BOSS controllers, overtravel was virtually zero, while with the PD controller, overtravel was approximately 4 to 8cms. Figure 3.38(b) plots the maximum hook overshoot over the same range of step sizes. With the On-Off and BOSS controllers, overshoot was small (< 4cm), while with the PD controller, overshoot was at least 6cm or more. Figure 3.38(c) plots the BOSS-normalized deceleration energy

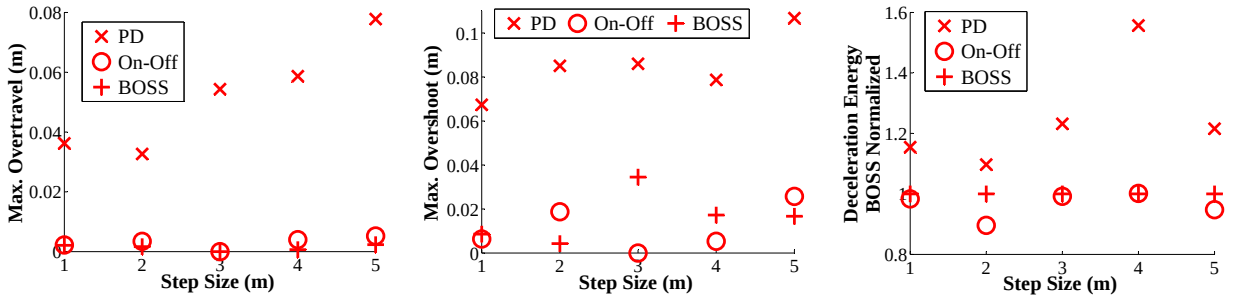

(a) Maximum Trolley Overtravel (b) Maximum Hook Overshoot (c) Deceleration Energy

Figure 3.38: Controller Performance Comparisons to PTP Inputs, Experimental Results

versus step size. The On-Off and BOSS controllers used about the same amount of energy during deceleration, except for the 2m step size, where the On-Off controller used around 10% less. The PD controller used about 20% more energy than the BOSS controller, except for the 2m step size where it was around 10% more, and the 4m step size, where it was around 60% more. Note these experimental results were subjected to measurement noise, so not all data points are consistent with the general trend. Nevertheless, the same trends from simulations are observed in the experiments: the On-Off and BOSS controllers produce less overtravel and overshoot, and uses less energy during deceleration than the PD controller.

The results shown here have demonstrated that the PD controller's deceleration behaviors are inferior to that of the On-Off and BOSS controllers. Furthermore, when the e_0 of an On-Off controller is chosen correctly, its performance is virtually identical to the BOSS controller. However, the On-Off controller performance degrades for certain inputs, which will be discussed next.

3.6.3.2 Pulse-Like Backtracking Moves

Figure 3.39(a) shows the HM device making pulse-like backtracking movements, i.e. go forward, and then reverse backwards through the deadzone. This demonstrate two previously mentioned weaknesses of the On-Off controller. The first weakness pertains to the On-Off controller's fixed-size deadzone, and its dependency on the velocity of the crane as it enters the deadzone just before decelerating. This is illustrated by the movements from 0-10s. The trolley and hook stopped well short of, rather than exactly on the HM device, like previously shown in Figure 3.35(a). This is because when the trolley entered the deadzone around 2s, it was not traveling at maximum velocity. The On-Off controller deadzone is sized to match the crane's stopping distance from maximum velocity, so entering the deadzone at a lower velocity causes the trolley to undertravel.

The second weakness pertains to the detrimental effects of the On-Off controller's relatively large deadzone. This is illustrated by the data from 10-30s. Because the deadzone is $\pm$0.49m, the HM device can be moved anywhere inside a 0.98m range without causing the trolley to move. In contrast, PD controllers with small/no deadzones can follow the backtracking movements, albeit with some overshoot and oscillations. This behavior is shown in Figure 3.39(b) for the same HM device movement. Note the deadzone was set to 0, so the deadzone boundaries are not plotted. The PD controller is also more suitable than On-Off for making precise movements, because it can command a range of velocities between 0% and 100%, rather than saturating the command on every move. Because of this, the PD was found to be more suitable for the Fixed Relative Positioning (FRP) mode.

The two weaknesses of the On-Off controller described above are exacerbated when the crane's stopping distance increases. This may be caused by: 1) heavier trolley inertia, 2) more conservative motor drive parameters, and 3) longer duration shapers.

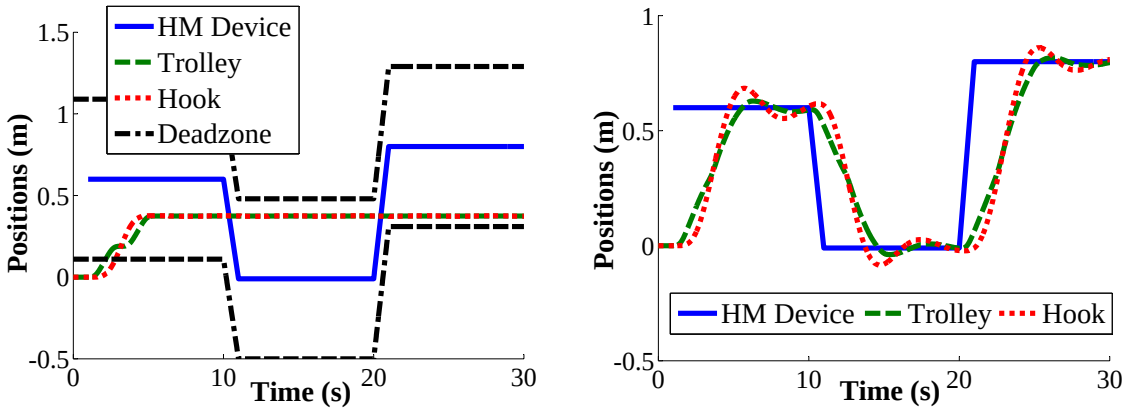

(a) On-Off, $e_0 = 0.49m$

(b) PD, $e_0 = 0m$, $e_{100} = 3m$, $K_p = 10$, $K_d = 10$

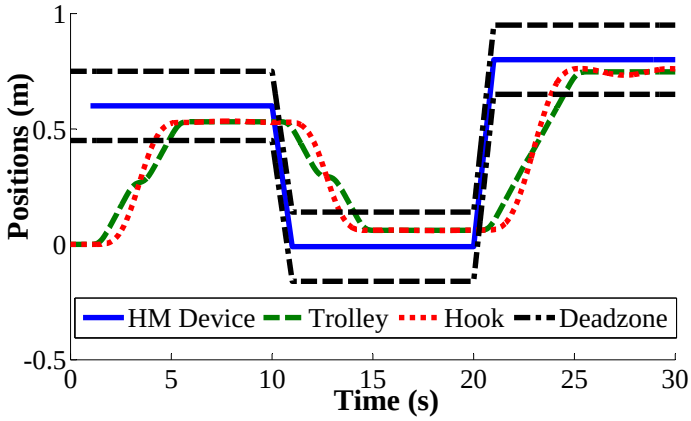

(c) BOSS, $e_0 = 0.15m$

Figure 3.39: Backtracking Pulse-Like Movements

Figure 3.39(c) shows the response of the BOSS controller to the same HM device movements used in Figures 3.39(a) and 3.39(b). The BOSS controller overcomes the two weaknesses of the On-Off controller. First, in the movements from 0-10s, its deceleration behavior results in much better positioning accuracy. Second, in the movements from 10-30s, the smaller deadzone allows the BOSS controller to follow the backtracking motions of the HM device. However, the trolley does not overtravel nor oscillate around the desired positions like the PD controller in Figure 3.39(b).

The controllers were tested in trials where the hand-motion device was moved such that its position over time resembles rectangular pulse waves, with step sizes (amplitudes) varying from 0.2 to 1.0m. The pulse duration was constant at 10s. In the simulation trials, the PD controller parameters were chosen to minimize trolley overtravel and were $e_0 = 0m$, $e_{100} = 3m$, $K_p = 10$, $K_d = 10$. The On-Off e_0 was 0.49m, and the BOSS e_0 was 0.15m.

For each trial, tracking errors were used to quantify the performance of the controllers for backtracking pulse inputs. The tracking error is the difference between the HM device position, x_d, and the trolley or hook positions, $x_{t/h}$, integrated over the duration of the trial, t_f:

$$Error = \int_0^{t_f} |x_d - x_{t/h}| dt. \tag{3.36}$$

Figure 3.40 shows each controller's trolley and hook tracking errors, normalized against the BOSS controller, plotted as a function of the pulse step size. When the step size is small, i.e.

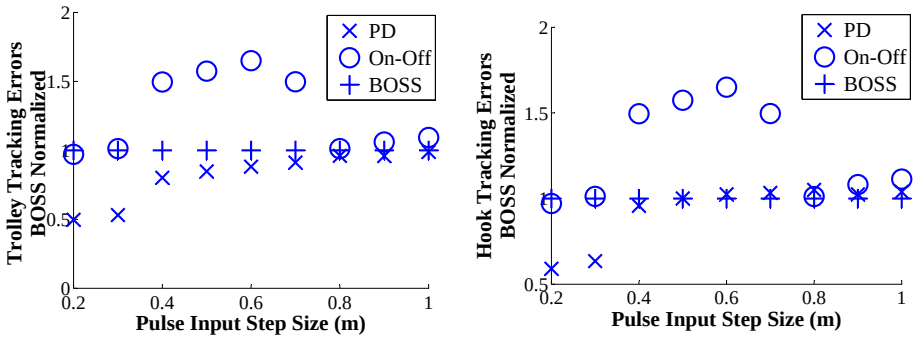

(a) Trolley (b) Hook

Figure 3.40: Tracking Errors for Backtracking Pulse Inputs

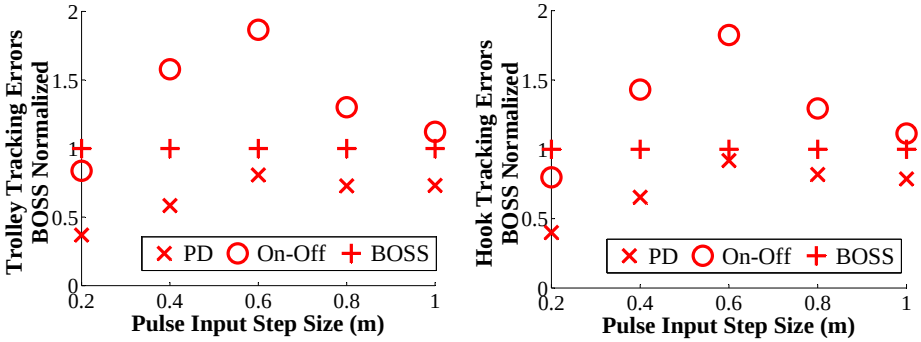

(a) Trolley (b) Hook

Figure 3.41: Tracking Errors for Backtracking Pulse Inputs, Experimental Results

0.2-0.3m, the BOSS and On-Off controllers' tracking errors are 50% larger than that of the PD controller. This is because $e_0 = 0m$ for the PD controller, while $e_0 = 0.15m$ for the BOSS controller, and $e_0 = 0.49m$ for the On-Off controller. The BOSS and On-Off controllers cannot track input pulse amplitudes that are only slightly larger, or smaller than their deadzones.

However, as the step sizes increase beyond 0.4m, the tracking errors between the PD and BOSS controllers converge. This is because the amplitude is now much larger than the BOSS controller's deadzone, resulting in greater tracking accuracy. Step sizes from 0.4-0.7m are still too small relative to the On-Off controller's deadzone, which results in around 50% larger tracking errors than the BOSS controller. The tracking errors of all three controllers converge only when the input pulse amplitude is above 0.8m.

Figure 3.41 shows similar results from experiments on the HiBay crane. Note the HM device was manually moved to produce pulse-like motions. Therefore, command input signals to each controller are slightly different. The PD controller trolley and hook tracking errors were less than that of the BOSS controller for the 0.2 and 0.4m pulse input step sizes. However, for step sizes larger than 0.6m, the BOSS and PD controllers' tracking errors converge. The tracking errors for the On-Off controller was around the same as that of the BOSS controller for the 0.2m step size, larger for the 0.4 and 0.6m step sizes, and begins converge with that of the BOSS controller for the 0.8 and 1.0m step sizes. Note that the On-Off e_0 was 0.6m for these experiments. In the simulation results shown in Figure 3.40, the On-Off e_0 was 0.49m.

Figures 3.40 and 3.41 illustrate the obvious fact that the BOSS and On-Off controllers are not able to track the HM device if it does not move significantly out of their deadzones. However, if the HM device movement is large, then both controllers track as well as the PD controller. The

advantage of the BOSS controller is that its deadzone can be set much lower than the On-Off controller, thereby increasing its tracking performance even for small movements.

The PD controller has better tracking performance than the BOSS controller for small amplitude movements that are less than the BOSS e_0. However, this is inconsequential, because as stated before, the BOSS e_0 effectively represents the acceptable tolerance around the desired position. Therefore, the BOSS controller is *intentionally designed* to ignore HM device movements that are smaller than e_0. If the design intent was to track smaller movements, then the size of the BOSS e_0 can simply be decreased.

The examples shown in this section demonstrate the BOSS controller possesses *both* the precise movement capabilities of the PD controller, *and* the speed, efficiency, no-overtravel, and non-oscillatory response behaviors of the On-Off controller.

3.6.4 Stability

The discrete logic rules of the BOSS controller in (3.34), when combined with the continuous dynamic nature of the physical crane, form a relatively new control paradigm, known as hybrid switched control systems [52, 117]. This field is relatively immature, and mathematically proving the stability of this type of systems is quite involved. Therefore, this section will demonstrate BOSS controller stability by using the responses from a large number of practical exemplary cases.

Trials were conducted using a BOSS controller with $e_0 = 0.15m$, and using the simple d^*_{stop} prediction method. For the simulations, the nonlinear rate-limiter combined with the linear second-order plant was used as the HiBay crane trolley. Therefore, this stability analysis also accounts for the inaccuracies of the simplified d^*_{stop} prediction method. Note the nonlinear rate-limiter will also reduce the oscillation-reduction properties of input shapers. The crane carries two types of loads: a single-pendulum hook of hoist length 6m; and a double-pendulum setup with a 80kg hook and a 27kg point-mass payload. The hoist length (trolley to hook) and rigging length (hook to payload) are both 3m. Various input shapers were used in the simulations. For the single-pendulum hook, single-mode shapers (ZV, ZVD, EI with 5% insensitivity, and UMZV) were used. For the double-pendulum payload, two-mode shapers (ZV2, ZVD2, and SI2 with 5% insensitivity around both natural frequencies) were used.

Figure 3.42(a) plots the residual peak-to-peak trolley oscillations for step input sizes ranging from 1-10m. All shapers with the BOSS controller did not produce trolley oscillations. Therefore, limit cycles were not induced, which indicates controller stability. Figure 3.42(b) plots the residual peak-to-peak hook oscillations for the same step inputs. All oscillations were below 0.2m, with the UMZV shaper incurring the largest amplitudes. This is because the oscillation-reduction properties of rapid-changing UMZV-shaped signals are corrupted more by the rate-limiter in the trolley plant. Figure 3.42(c) shows the residual payload oscillations for the double-pendulum payload and two-mode shapers. Again, oscillations are quite small, all under 0.05m.

Figures 3.43(a) plots the residual trolley oscillations versus step size for point-to-point moves on the HiBay crane. Due to space limitations, only step sizes from 1-5m were tested, and a subset of the shapers from the simulations were used here. For all tested cases, there were virtually no trolley oscillations, which indicates controller stability. Figures 3.43(b) and 3.43(c) plots the residual hook and payload oscillations. All oscillations were less than 0.5m, which shows the oscillation-reduction properties of the input shapers were effective. In some cases, such as the hook oscillation for UMZV shaper and 5m step size, the amplitude was unusually larger than other cases. However these are the result of 1) measurement noise, 2) parameter estimation errors (such as the cable lengths, hook and payload masses for the two-mode shaper payloads, and 3) real-world nonlinearities in the motor drives and drivetrain.

Figure 3.44 shows the peak-to-peak trolley, hook, and payload oscillations for sinusoidal inputs of 2m peak-to-peak amplitude, and periods ranging from 1-10s. This range of periods and amplitudes produces hand-motion device velocities that vary approximately from 0.4m/s (very slow walk) to

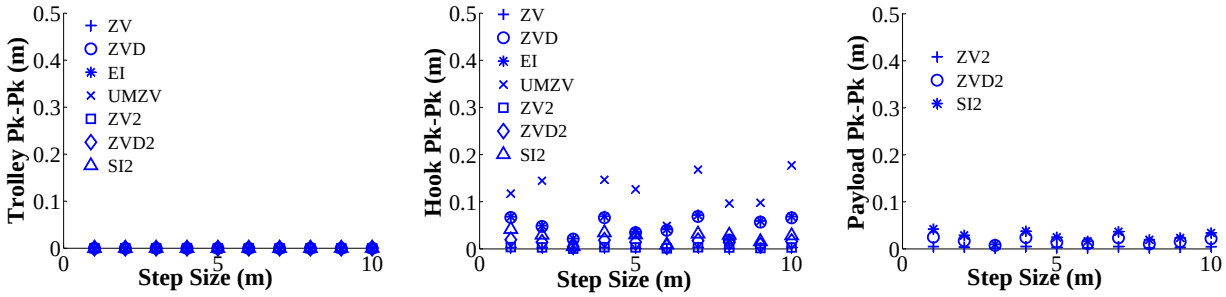

(a) Trolley (b) Hook (c) Payload

Figure 3.42: BOSS $e_0 = 0.15m$, Step Inputs, Residual Peak-to-Peak Oscillations

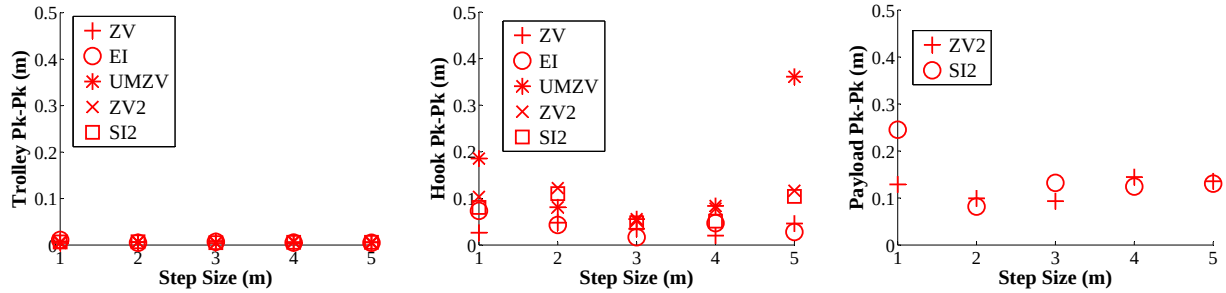

(a) Trolley (b) Hook (c) Payload

Figure 3.43: BOSS $e_0 = 0.15m$, Step Inputs, Residual Peak-to-Peak Oscillations, Experimental Results

4m/s (running). This type of sinusoidal input simulates an operator moving back and forth at the slow and fast human speeds. Note the upper limit on the vertical axis is 2m, corresponding to the peak-to-peak amplitude of the input sinusoid. Plots that exceed this limit indicate instability, where the output is amplified by the system to levels beyond the input amplitude, possibly indicating resonance. However, all three plots in Figure 3.44 are lower than this limit, thereby indicating bounded-input-bounded-output (BIBO) stability for the cases tested.

Note that smaller periods indicate higher frequency (and therefore faster) hand-motion (HM) device movements. At these speeds, the trolley, hook, and payload oscillation amplitudes are lower, because the crane is not physically capable of moving fast enough to follow the HM device. However, the crane can follow the slower HM device movements of longer input periods. Therefore, in those cases, the trolley, hook, and payload oscillation amplitudes are increased.

Figure 3.45 shows the peak-to-peak trolley, hook, and payload oscillations for sinusoidal inputs of 10m peak-to-peak amplitude, and periods ranging from 4-24s. This range of periods and amplitudes produces hand-motion device velocities that vary approximately from 0.83-5m/s. Again, the response amplitudes are small for shorter (faster move speeds) input periods, and increase with longer periods, but do not exceed the vertical axis limit of 10m. Note the spread in hook and payload oscillations for each shaper are less in Figure 3.45 than in 3.44. This is because the larger amplitude of the input signal is proportionally larger than the oscillations resulting from corrupted shaped commands.

Figure 3.46 shows the peak-to-peak trolley, hook, and payload oscillations for sinusoidal inputs of 20m peak-to-peak amplitude, and periods ranging from 10-42s. This range of periods and amplitudes produces hand-motion device velocities that vary approximately from 0.95-4m/s. Again, the response amplitudes are small for shorter (faster move speeds) input periods, and increase with longer periods, but do not exceed the vertical axis limit of 20m.

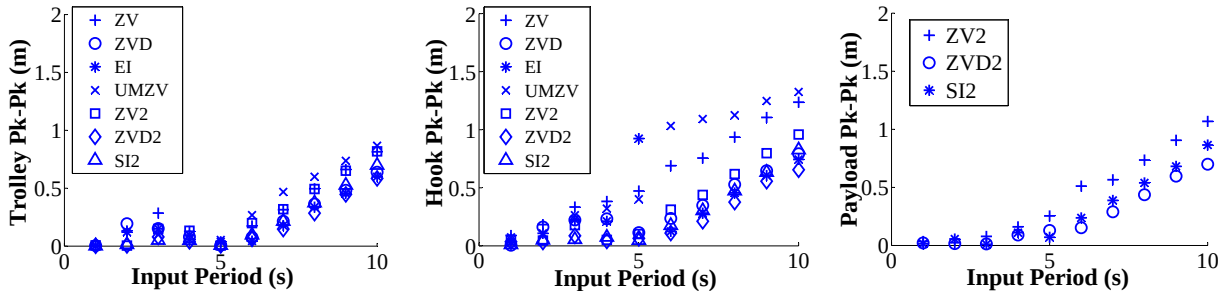

(a) Trolley (b) Hook (c) Payload

Figure 3.44: BOSS $e_0 = 0.15m$, 2m Peak-to-Peak Sinusoidal Inputs, Peak-to-Peak Oscillations

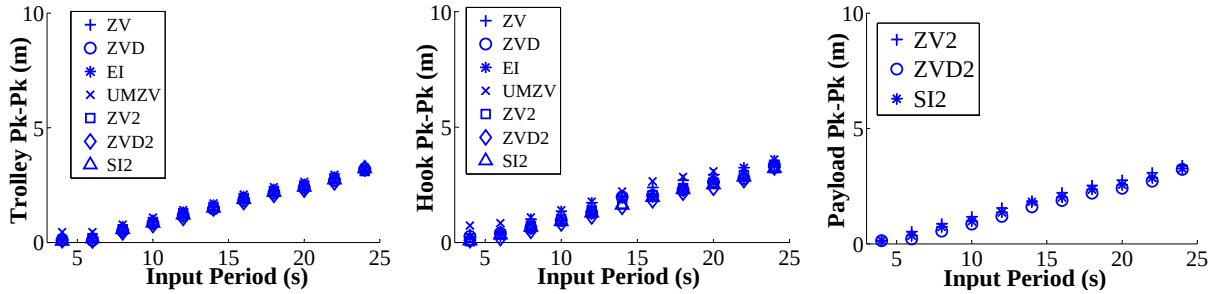

(a) Trolley (b) Hook (c) Payload

Figure 3.45: BOSS $e_0 = 0.15m$, 10m Peak-to-Peak Sinusoidal Inputs, Peak-to-Peak Oscillations

3.6.5 Effects of d^*_{stop} Prediction Inaccuracies

Because the performance of the BOSS controller depends on the accuracy of the stopping distance prediction, d^*_{stop}, simulation trials were conducted to investigate the effects of varying the predictor's accuracy.

For comparison purposes, the trolley plant is modeled as unity, i.e. the shaped command to the motors is equal to the actual trolley velocity, or $V_S = V_A$. In such cases, predictions using the simple method are exactly equivalent to the actual trolley stopping distance, d_{stop}. Then, for different trials, the prediction is modified by an adjustment factor, K, such that $d^*_{stop} = K d_{stop}$ to investigate how controller performance is affected by underestimating or overestimating d_{stop}.

The simulated trolley has a maximum velocity of 0.32m/s, and a ZV shaper was used to to cancel the oscillations of a 6m length suspended hook. With these parameters, the trolley stopping

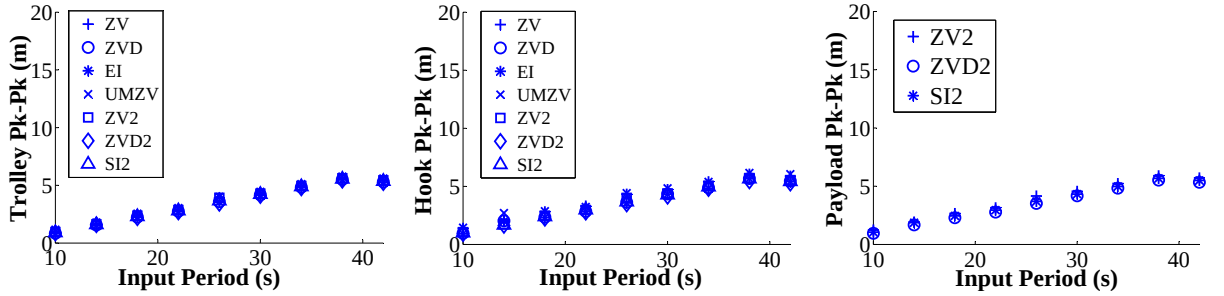

(a) Trolley (b) Hook (c) Payload

Figure 3.46: BOSS $e_0 = 0.15m$, 20m Peak-to-Peak Sinusoidal Inputs, Peak-to-Peak Oscillations

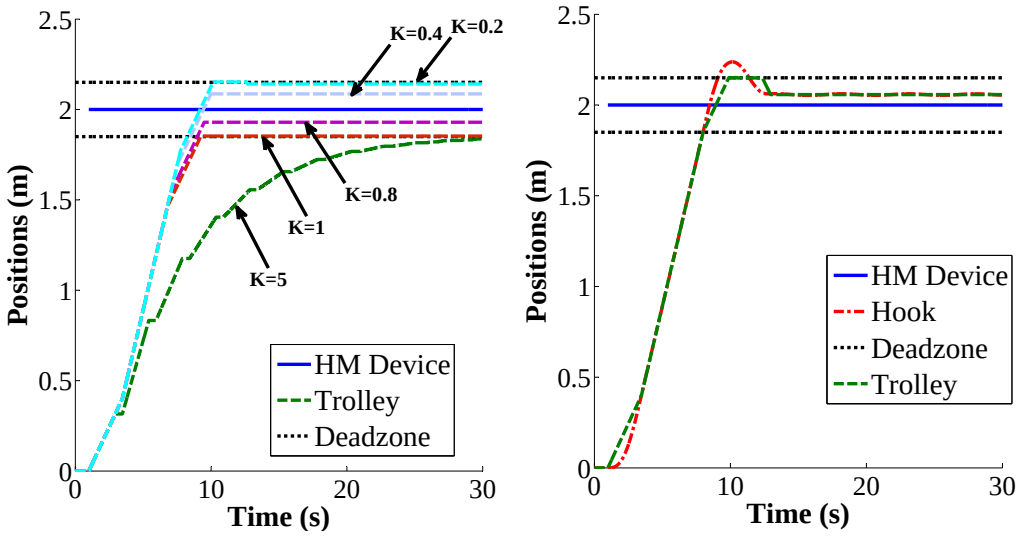

(a) K=0.2 to K=5 (b) K=0

Figure 3.47: Effects of K on Trolley Movements, $e_0 = 0.15m$

distance from maximum velocity is $d_{stop} = 0.39m$. The input hand-motion (HM) device position was constant at 2m for each trial.

Figure 3.47(a) shows the effects on the trolley movement of varying K from 0.2-5 , for $e_0 = 0.15m$. When K=5, the predictor overestimates d_{stop}. The behavior of the BOSS controller is conservative, and approaches the deadzone slowly. This is because the predictor sends numerous overriding stop commands, much before the trolley comes close to the deadzone. When K=1, the prediction is exact, therefore the trolley stops exactly on the near-side deadzone boundary. When $K < 1$, the predictor is less conservative and underestimates d_{stop}. Therefore, the trolley stops further into the deadzone. At K=0.2, the trolley stopped on the far-side deadzone boundary. If the prediction is underestimated even more, then the trolley overtravels beyond the deadzone, reverses, and stops inside the deadzone. This is illustrated in Figure 3.47(b) for K=0. Note that if K=0, then the BOSS controller essentially reduces to an On-Off controller. This can be seen by substituting $d^*_{stop} = 0$ into the BOSS algorithm of (3.34).

Figure 3.48(a) plots the maximum trolley position, $max(x_t)$, less the desired HM device position, x_d, on the vertical axis. Note that a positive value indicates trolley overtravel, and a negative value indicates trolley undertravel. The horizontal axis is the predictor error, represented by K. Five plots are shown, each corresponding to different sized deadzones, ranging from $e_0 = 0.1$ to 0.5m. The plots show that if $K \geq 1$, i.e. the d^*_{stop} is exact or overestimated, then the trolley always undertravels and stops on the near-side deadzone boundary. Conservatively overestimating the stopping distance is desirable for hand-motion control, because this prevents the payload from overshooting beyond x_d, which can potentially hit operators or obstacles.

If $K < 1$, then the d^*_{stop} prediction is underestimated, and the trolley travels further into the deadzone before stopping. The stopping distance inside the deadzone is inversely proportional to K. The trolley will overtravel beyond x_d if:

$$\begin{aligned} d_{stop} - d^*_{stop} &\geq e_0 \\ d_{stop} - K d_{stop} &\geq e_0 \\ K &\leq 1 - \frac{e_0}{d_{stop}} \end{aligned} \tag{3.37}$$

For example, using an $e_0 = 0.15m$ BOSS controller on this crane, if $K < 0.62$ (or d^*_{stop} is underestimated by more than 38%), then the trolley will overtravel beyond the hand-motion device. If

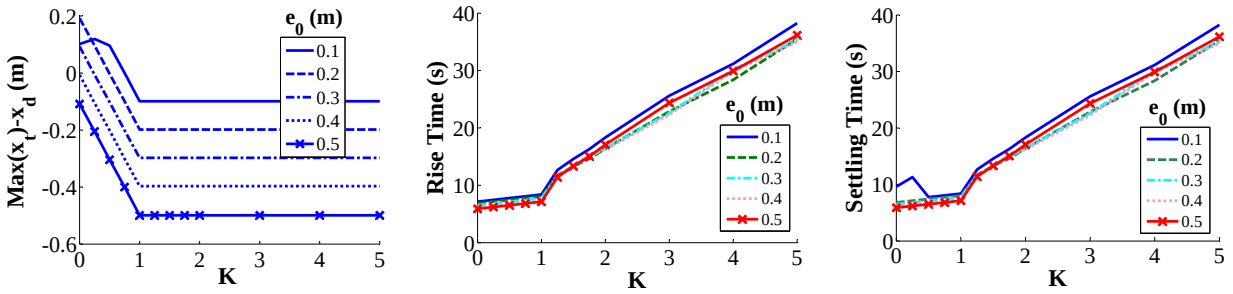

(a) Effects of K on Trolley Overtravel (b) Effects of K on Rise Time (c) Effects of K on Settling Time

Figure 3.48: Effects of d_{stop} Estimation Inaccuracies, K

the trolley overtravels beyond the far-side deadzone boundary, then the crane will reverse, similar to the situation in Figure 3.47(b). The condition for the trolley overtraveling beyond the far-side deadzone boundary is:

$$K \leq 1 - \frac{2e_0}{d_{stop}} \tag{3.38}$$

Figure 3.48(b) plots rise times versus K for various e_0's. In this case, the rise time is defined as the time when the trolley first enters the deadzone. From K=0 to K=1, rise time increases linearly with K, but with a very slight gradient. Rise times in this range are otherwise very similar. As K is increased beyond 1, there is an initial jump in rise time, after which rise times increase linearly with K. Overestimating d_{stop} increases the rise time because the crane approaches the deadzone slowly and conservatively, as was shown by the case of K=5 in Figure 3.47(a).

Figure 3.48(c) plots the settling times versus K for various e_0's. In this case, the settling time is defined as the time when the trolley remains inside the deadzone indefinitely. The trends are virtually identical to the rise times in Figure 3.48(b), because in most cases, the trolley remains inside the deadzone after entering. The exception is in the cases of $e_0 = 0.1m$, K=0, 0.25, in which the trolley overtravels beyond the far-side deadzone and reverses.

3.6.5.1 Reducing the Detrimental Effects of d^*_{stop} Prediction Inaccuracies

Ideally, the predictor would be completely accurate, so that the predicted stopping distance exactly matches the actual stopping distance. Then, e_0 can be set to the lowest possible value, which is usually dictated by the location accuracy of the hand-motion device. However, in reality, the simple prediction method will always underestimate the actual stopping distance. One way to circumvent this issue is to multiply the predicted d^*_{stop} by an adjustment factor, K^*, so that the product is closer to the actual d_{stop}. Such factor(s) can be found by comparing d^*_{stop} to d_{stop}, under a variety of common scenarios that the crane may experience.[17] A static value of K^* can then be found by averaging these scenarios. Alternatively, one can design K^* to adapt to changing conditions.

Fundamentally, there is a tradeoff between under- and overestimating d^*_{stop}. If d^*_{stop} is conservatively overestimated, then the performance is adversely affected by rapid increases in rise time and settling time. However, the upside is that it guarantees the trolley will never overtravel beyond the near-side deadzone boundary. Conversely, aggressively underestimating d^*_{stop} results in fast rise time and fast settling time. The trolley will also overtravel beyond the near-side deadzone boundary. However, this situation may still be acceptable, as long as (3.37) is not satisfied, and the trolley does not overtravel beyond x_d. Therefore, in practice, it is desirable to underestimate

[17] For example, stopping from different velocities and using different shapers.

d^*_{stop}, and select e_0 such that the discrepancies between d^*_{stop} and d_{stop} satisfy the following:

$$1 - \frac{e_0}{d_{stop}} \leq \frac{d^*_{stop}}{d_{stop}} \leq 1 \tag{3.39}$$

Note that only an approximate estimate of d_{stop} is required for this purpose.

3.6.6 Summary

It is well known that input shapers reduce vibrations by slightly increasing the acceleration and deceleration durations of the original reference command. Vaughan et al. have addressed such issues by 1) using a Reduced-Overtravel shaper that automatically reverses the trolley when a "stop now" command is detected [120]; and 2) using a predictive GUI element that shows the operator where the crane will stop when he/she issues a "stop now" command [119]. However, the crucial difference is that in Vaughan's work, operators use traditional interfaces such as joysticks and push-button pendents to specify *velocity* reference commands. Operators using the BOSS hand-motion controller specify the desired *position*, which is a measure that is ultimately more relevant to crane control.[18]

Because the desired setpoint of the system is a *position*, and the crane is driven by *velocity* commands, there is an inherent integrator in the feedback loop that converts velocity into position. Then, because the input shaper is essentially a partial time delay, the shaping buffer's unexecuted velocity commands can also be integrated to predict the future trolley position, i.e. d^*_{stop}. This prediction is exploited by the BOSS controller to make decisions *ahead of time*.

Because it considers all available information stored in the shaping buffer, the BOSS controller has an inherent advantage over other closed-loop signal shaping (CLSS) feedback controllers. While it can be argued that the derivative component of a PD controller also has a predictive element, the derivative acts on the error signal, which is inherently a *reactive* measure.

Other notable features of the Brisk On-off Smart Stop (BOSS) controller are:

- For a given input shaper and an acceptable tolerance from the desired position, the BOSS controller moves a shaper-and-integrator-in-the-loop system in the shortest possible time without overtravel (assuming the d_{stop} predictor is accurate). This is because the BOSS controller always issues time-optimal V_R commands, i.e. step in acceleration and step in deceleration.

- The BOSS controller is very simple to design. The input shaper is designed to cancel payload oscillations, and e_0 is set to the lowest possible value. Usually this value is dictated by the location accuracy of the hand-motion device. More importantly, however, is that unlike PD or On-Off controllers, the choice for e_0 and input shaper are effectively independent. Changing the input shaper does not necessitate selecting a new e_0.

- The BOSS controller possesses both the precise movement capabilities of the PD controller, as well as the speed, efficiency, no-overtravel, and non-oscillatory behaviors of the On-Off controller.

- The BOSS controller's small e_0 allows it to accelerate briskly, and its d_{stop} predictor smartly stops the trolley near the desired position.

- In the PD/P and On-Off experimental movements shown in Figures 3.10(b), 3.12(a), 3.13(a), and 3.14(a), the human operator deactivated hand-motion control well before the trolley reached the desired 2m position. The operator did this because he knew the approximate

[18] Crane operators care more about positioning the payload than its velocity.

distance it would take for the crane to stop. This behavior is captured in the block diagram in Figure 3.6, where the operator forms the outermost feedback loop. With the BOSS controller, the d_{stop} predictor automatically calculates this stopping distance and essentially performs the same function of deactivating hand-motion control, i.e. stopping the crane. Therefore, the BOSS controller further increases hand-motion control's ease of use, because it reduces the operator's mental load.

CHAPTER IV

HAND-MOTION CRANE CONTROL USAGE TESTS

In collaboration with Konecranes, many hand-motion operating modes were developed and tested. Some of these ideas were eliminated early in the development process. Other ideas progressed further, where operator studies were eventually conducted. The studies quantitatively and qualitatively evaluated the merits of hand-motion control in comparison to standard crane control interfaces.

4.1 Wand/Glove Hand-Motion Control Usage Studies[1]

This section presents the results an operator study that was conducted to compare crane control using a standard push-button pendent versus hand-motion control. Operators used the glove and wand in Come-Here mode, and a PD with input shaping controller was used. The goal was to move the payload (represented by the hook) from start to finish as quickly as possible without collisions with obstacles. The nominal path around the obstacle course in this study is shown in Figure 4.1(a). The start and end zones are indicated by the rectangle and circle, respectively. Ten novice operators completed the obstacle course using the following control interfaces:

1. Standard push-button pendent.
2. Glove interface with PD controller (high gains, Come-Here mode) and ZV input shaper.
3. Wand interface with PD controller (high gains, Come-Here mode) and ZV input shaper.

Figure 4.1(b) shows an overhead view of typical payload responses for a single operator using the pendent and glove. Compared to using the pendent, using the glove significantly reduced the payload swing and allowed the operator to move the payload more efficiently.

Figure 4.2(a) shows the course completion times for each operator. The average completion time using the pendent was 77 s. The average completion times using the glove was 24 s (68.8% improvement over the pendent), and using the wand was 30 s (61% improvement over the pendent).

[1] ***This work was performed with the assistance of Joe Bhaumik.***

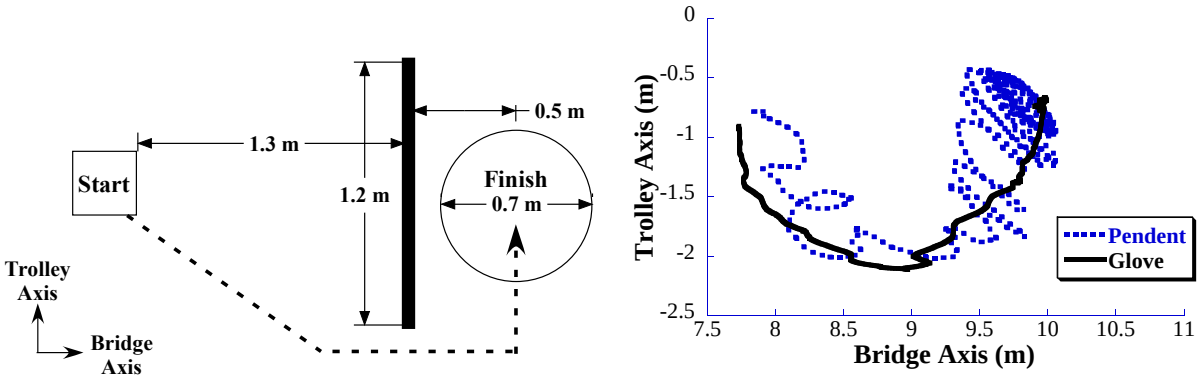

(a) Overhead View and Nominal Path

(b) Exemplary Payload Responses

Figure 4.1: PD Controller and ZV Shaper Obstacle Course

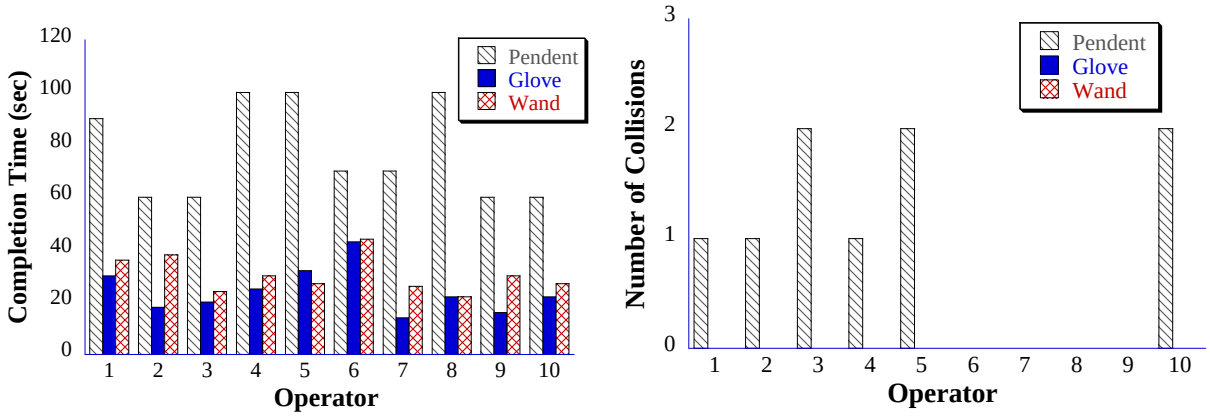

(a) Completion Times

(b) Collisions

Figure 4.2: PD Controller and ZV Shaper Obstacle Course Results

A one-way repeated measures ANOVA test indicated there were statistically significant differences in the completion times of the three control methods, $F = 63.88, P < .0001$. A 95% confidence interval Tukey's test indicated there were statistically significant differences between the pendent and wand ($P < .0001$), and between the pendent and glove ($P < .0001$). However, there was no significant difference between the wand and the glove ($P = 0.46$).

Figure 4.2(b) plots the number of collisions that occurred during each trial. Using pendent control, many operators collided the payload with the obstacle. The average number of collisions per trial was 0.9. However, all operators were able to avoid the obstacle using the glove and wand, corresponding to 100% improvements over the pendent. A one-way repeated measures ANOVA test indicates that there were statistically significant differences in the number of collisions using the three control methods $F = 10.57, P = 0.00092$. A 95% confidence interval Tukey's test indicated there were statistically significant differences between the pendent and wand ($P = 0.0024$), and between the pendent and glove ($P < 0.0024$).

4.1.1 Summary

Two types of controllers were investigated: 1) Standard pendent control (for baseline comparisons), and 2) Hand-motion control. An operator study based on driving the crane through an obstacle course was conducted. The study compared pendent control to PD and input shaping hand-motion control. Using the wand and glove, operators demonstrated better than 60% improvements in completion time, and 100% improvements in avoiding obstacles than using the pendent.

4.2 Glove Control and Double-Pendulum Payloads[2]

This section presents an investigation of using the vision-based, glove hand-motion control (in Come-Here mode) to move double-pendulum payloads. Point-to-point (PTP) straight line moves and L-shaped moves were conducted using the push-button pendent and the On-Off controller with different multi-mode shapers.

Figure 4.3(a) illustrates the experimental setup. The camera is used to track the hook (to gauge the effectiveness of oscillation control) and the glove. The hoist cable length (between the trolley and hook) and the rigging length (between the hook and payload) are L_1 and L_2, respectively. Figure 4.3(b) depicts the experimental setup and the relative size of the payload.

[2] ***This work was performed with the assistance of Sirri Sunay Gurleyuk.***

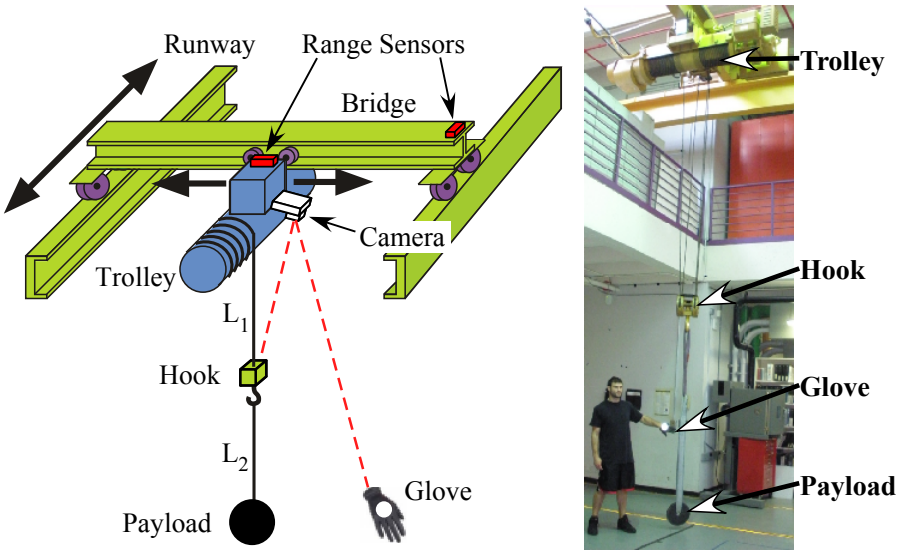

(a) Schematic (b) Photo

Figure 4.3: Double-Pendulum Hand-Motion Crane Control

Table 4.1: Hook and Payload Parameters

L_1	3.35 m
L_2	2.65 m
Hook Mass	50 kg
Payload Mass	11.3 kg

The approximate parameters for the double-pendulum payload are summarized in Table 4.1. Because these parameters are only approximate, the natural frequencies and damping ratios of the system were experimentally measured by observing the oscillatory response of the hook and payload to an external disturbance. The natural frequencies and damping ratios are listed in Table 4.2.

4.2.1 Shapers for the Double-Pendulum

A trade-off with using input shapers is that it increases the rise time of the command, which can be perceived by an operator using hand-motion control as increased lag. In general, the duration of an input shaper increases if multiple modes are suppressed, or if the desired shaper robustness to modeling error is increased [87]. To minimize shaper duration, SNA shapers (described in Section 1.1.7) were used. SNA shapers contain negative impulses that can significantly reduce the shaper duration. However, compared to positive impulse shapers, the negative shapers are typically less robust to modeling errors.

Two-mode SNA shapers with varying negativity (the amplitude of the negative impulses) were used for the experiments. These shapers were designed to induce zero vibration at the modeled

Table 4.2: Double-Pendulum Natural Frequencies and Damping Ratios

ω_1	1.4 rad/s
ω_2	1.8 rad/s
ζ_1	0.01
ζ_2	0

Table 4.3: Two-Mode SNA Shapers

Shaper	Negativity	$\begin{bmatrix} A_i \\ t_i(sec) \end{bmatrix}$
A	0	$\begin{bmatrix} 0.269 & 0.214 & 0.256 & 0.261 \\ 0 & 1.917 & 1.919 & 3.845 \end{bmatrix}$
B	0.5	$\begin{bmatrix} 0.623 & -0.50 & 0.764 & -0.50 & 0.613 \\ 0 & 0.484 & 1.561 & 2.642 & 3.122 \end{bmatrix}$
C	1	$\begin{bmatrix} 1 & -1 & 1 & -1 & 1 \\ 0 & 0.374 & 1.409 & 2.463 & 2.826 \end{bmatrix}$

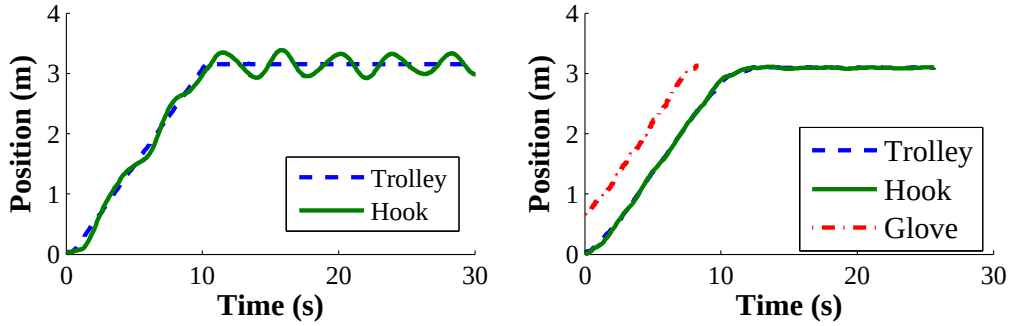

(a) Push-Button Pendent

(b) Hand-Motion, Shaper A

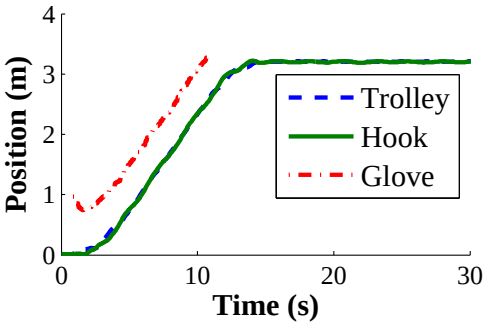

(c) Hand-Motion, Shaper B

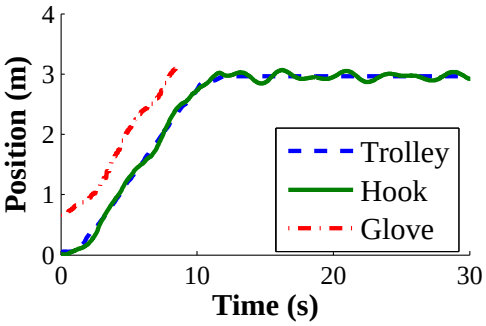

(d) Hand-Motion, Shaper C

Figure 4.4: Point-to-Point Moves

natural frequencies and damping ratios listed in Table 4.2. The shaper impulse amplitudes and times are listed in Table 4.3, in order of increasing negativity and/or decreasing shaper duration. Shaper C is more than 1s or 36% faster than shaper A, and shaper B is 0.72s or 23% faster than shaper A. Shapers with larger negativity are more aggressive due to their shorter durations, but are more sensitive to parameter (e.g. frequency, damping ratio) estimation errors.

4.2.2 Point-to-Point Moves

Figure 4.4(a) shows the trolley and hook response when the pendent was used to move the double-pendulum payload approximately 3 meters in a straight line. Note the large-amplitude (approximately 0.4 m peak to peak) hook oscillations. The payload (not recorded by the camera) oscillated with an amplitude of approximately 0.9 m. This distance was gauged by eyeball using a measurement tape placed underneath the oscillating payload.

Figure 4.4(b) shows the results from a similar move using hand-motion control and shaper A. Operators initiated motion by revealing the glove to the camera at some horizontal distance away

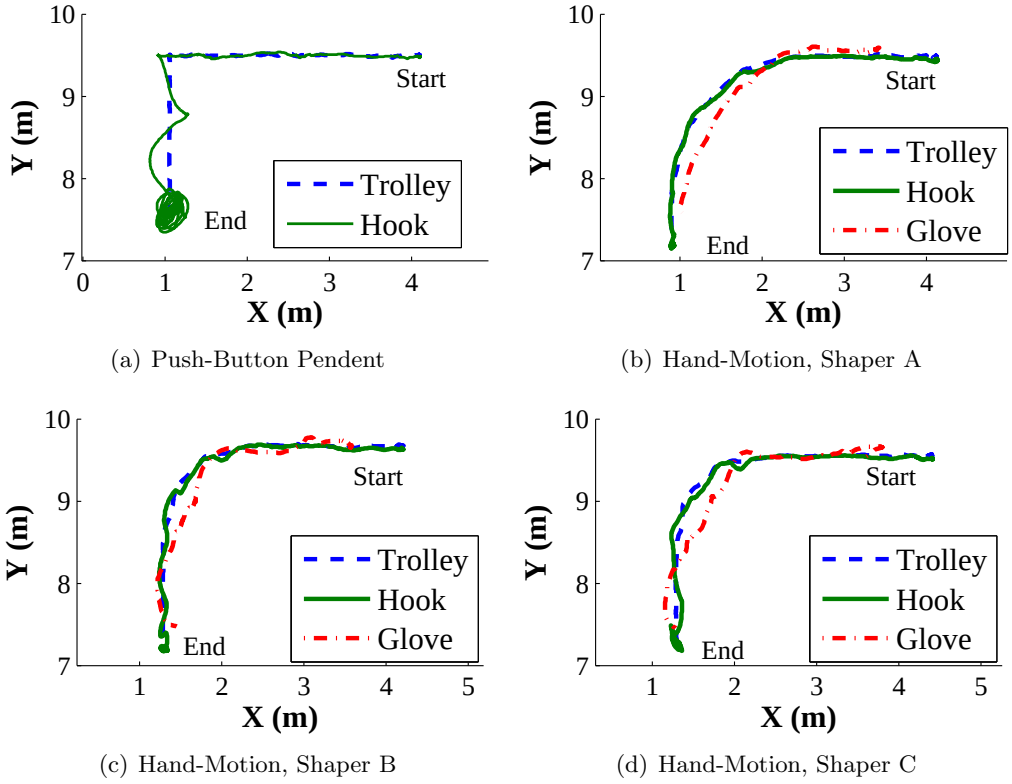

(a) Push-Button Pendent

(b) Hand-Motion, Shaper A

(c) Hand-Motion, Shaper B

(d) Hand-Motion, Shaper C

Figure 4.5: L-Shaped Moves

from the trolley. To stop, operators simply dropped their hand (or hid the glove from the camera view). Figure 4.4(b) shows that there was virtually no residual hook oscillation. There was also virtually no residual payload oscillations.

Figures 4.4(c) and 4.4(d) show the response when using shapers B and C. Shaper C's move time was 11.7 s, significantly faster than Shaper A's 12.3 s. However, there are also visible hook oscillations (max peak to peak amplitude was approximately 0.22m) for shaper C. Nevertheless, this amplitude is still about 50% smaller than the pendent control in Figure 4.4(a).

4.2.3 L-Shaped Moves

Figure 4.5(a) shows the positions of the trolley and hook during an L-shaped move using the pendent. The L trajectory traversed 3 m in the negative X direction, followed by 2 m in the negative Y direction. Clearly, it is difficult to reduce oscillation with pendent control. The peak-to-peak hook and payload oscillations are approximately 0.5 m and 1 m, respectively.

Figure 4.5(b) shows the results from a similar move using hand-motion and shaper A. In contrast to pendent control, residual hook and payload oscillations were not an issue. However, due to the long duration of shaper A, the actual trajectory did not follow the sharp corner of the desired path [95].

Figures 4.5(c) and 4.5(d) show the results using shapers B and C. Because these shapers have shorter durations (shaper B and C are 0.72 and 1 sec shorter than shaper A, respectively), there was less rounding of the corner. Hook and payload oscillations were still significantly less than using pendent control. However, as Figure 4.6 shows, the time response in the Y-axis for shaper C reveals peak-to-peak residual hook oscillation was 0.2 m. This is because shapers with high values of negativity are more susceptible to modeling errors, which caused the shaper to be slightly less effective at reducing oscillations.

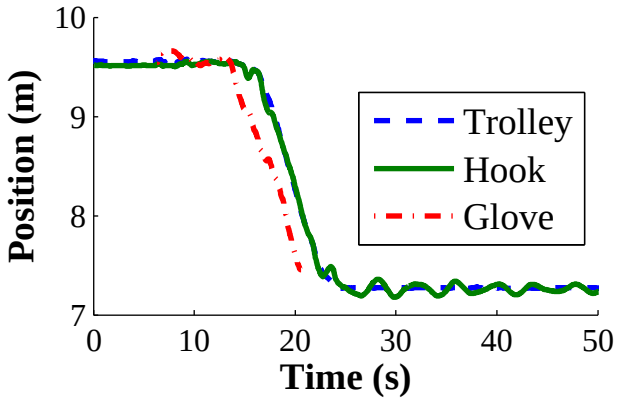

Figure 4.6: L-Move Using Hand-Motion, Shaper C, Y Axis

4.2.4 Summary

Tests showed that hand-motion control was more effective than the push-button pendent at moving double-pendulum payloads in straight-line and L-shaped trajectories. There is a notable trade-off between shaper duration and robustness. Longer shapers increase operator-perceived lag and degrade tracking of the desired trajectory. This can be alleviated by using shorter-duration shapers that contain negative impulses. However, these shapers usually have less effective oscillation-reduction properties in the presence of modeling errors. Nevertheless, the results demonstrated that hand-motion control is effective with multi-mode payloads using multi-mode shapers.

4.3 Operator Study on the Effects of On-Off Controller Deadzone Size[3]

A study was conducted to investigate the effects of varying the deadzone size for the On-Off hand-motion controller (in Come-Here mode). The deadzone is necessary for On-Off control in order to eliminate motor chatter due to RF-RTLS sensor noise. The deadzone also forms a region of zero-commanded velocity around the operator, which helps prevent the payload from colliding with the operator (when using Come-Here mode). The deadzone should be increased for heavy payloads and/or heavy cranes, because it would take a longer distance for the crane to come to a complete stop. Another goal of this study was to gauge the level of operator comfort to how close the payload approaches them as the crane comes to a stop.

Nine novice and moderately-experienced crane operators were tasked with driving the crane through a simple obstacle course illustrated in Figure 4.7. Operators moved the hook from the start into the finish circle as quickly as possible, without colliding with the obstacle. The hook (which has relatively small physical dimensions) is used to represent a point-mass single-pendulum payload. The On-Off controller in Come-Here mode was used for all hand-motion control modes. Each operator completed the course using four different control methods:

1. Standard push-button pendent **with** input shaping
2. RF-based hand-motion with small (0.4m) deadzone
3. RF-based hand-motion with medium (0.8m) deadzone
4. RF-based hand-motion with large (1.2m) deadzone

The deadzone size determines how far from the tag the hook will be stopped after the crane decelerates. With a small deadzone, the hook will almost be touching the tag after it stops.

[3] ***This work was performed with the assistance of Nathan Knight.***

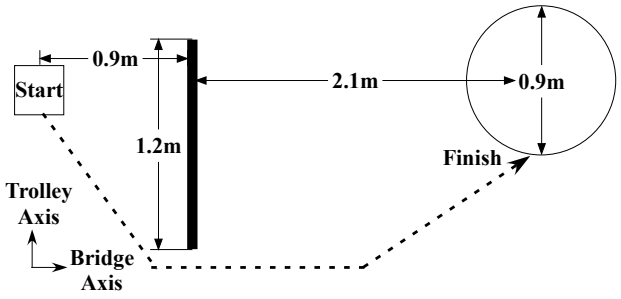

Figure 4.7: Obstacle Course

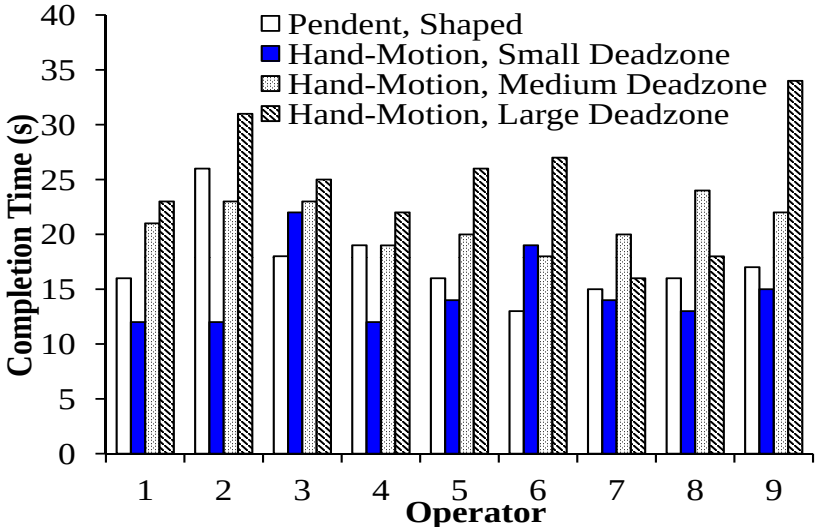

Figure 4.8: Obstacle Course Completion Times

However, the operator will be able to initiate crane movement by moving the tag only a small distance. With a large deadzone, the hook will stop further from the tag, but the operator will need to move the tag further distances to initiate crane movements.

As input shaping was used in all modes, operators were freed from the burden of manually controlling hook oscillations. Coupled with the fact that the relatively simple course was wide and spacious, most operators did not have collisions with the obstacle. Figure 4.8 shows the course completion times. The results showed that for the 9 operators tested, hand-motion control with the small deadzone was the fastest with an average completion time of 14.8s. Shaped pendent control was second fastest with an average time of 17.3s, followed by hand-motion with medium deadzone of 21.1s and hand-motion with large deadzone of 24.7s.

A one-way repeated measures ANOVA test indicates there were statistically significant differences (F=12.29, $P < 0.0001$) in the completion times of all four control methods. However, a 95% confidence interval Tukey's test indicated that the difference between the pendent and hand-motion small deadzone was *statistically insignificant*. Tukey's tests concluded that the only statistically significant pairwise differences were between: 1) Hand-motion large and small deadzones ($P < 0.0001$), 2) Hand-motion large deadzone and the pendent (P=0.0017), and 3) hand-motion medium and small deadzones (P=0.0069). These results indicate that hand-motion with medium and large deadzones were statistically slower than the other two control methods. This can be explained by the fact that operators need to move further to initiate crane motion with larger deadzones.

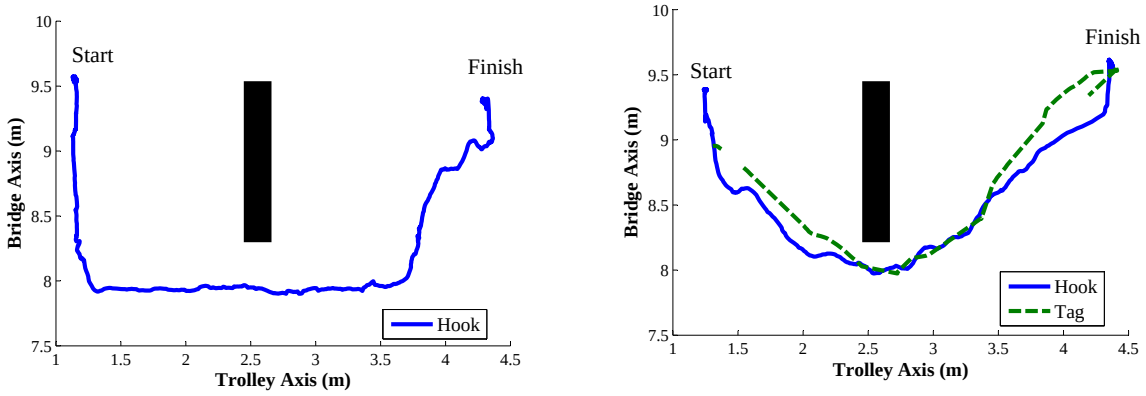

(a) Pendent, Shaped

(b) Hand-Motion, Small Deadzone

Figure 4.9: Recorded Examples of Operators Completing the Obstacle Course

To understand why small-deadzone hand-motion control is faster on average than shaped pendent control, consider Figure 4.9(a), which shows the overhead view of the hook path for an example of an operator using the push-button pendent with shaping. Note the 90 degree turns in the path. This is because the operator was pushing one button (that moves the crane in one direction of one axis) at a time. To make diagonal movements, the operator must be more adept and press two buttons simultaneously.

In contrast, Figure 4.9(b) shows an example of the hook and tag path for an operator using hand-motion control with small deadzone. Note the plot for tag position is not a contiguous line because the operator activated and deactivated hand-motion control (by pressing a button) at various times. The operator is able to take a shorter route around the obstacle, because it is easy to move the crane in both axes simultaneously. Furthermore, note that the hook follows more or less the desired path that was traced out using the tag by the operator.

Before the conclusion of each test, operators were asked a series of questions on their preferences and level of comfort. When asked whether they preferred hand-motion control or pendent control, all but one operator preferred hand-motion. Several participants commented that the large, bulky drop-down pendent felt cumbersome to use, in comparison to the relatively small and nimble RF tag. When asked which hand-motion controller deadzone size was most preferable, all but one preferred the small deadzone.

4.3.1 Summary

The results from this study suggest 1) Hand-motion control is more preferable and faster on average than the standard push-button pendent, and 2) Operators preferred smaller deadzones with On-Off hand-motion control.

4.4 Usage Study of Hand-Motion Control in a Practical Application[4]

The goal of this operator study was to study the performance of hand-motion control in a practical crane application. With consideration to the limitations of hand-motion control (e.g. vertical and inching movements in Sections 2.6 and 2.7, respectively), the application was designed to contain tasks that are suitable for hand-motion control. An assembly-line-like application was studied and contains the following basic tasks:

1. The operator summons the crane, which is at a remote location. A typical scenario is when the

[4] ***This work was performed with the assistance of Ranj Saeed.***

operator stands by the payload to be picked up, and summons the crane to his/her location. When summoned, the crane should travel to the operator as fast as possible.

2. Hoisting and lowering the hook. Considering that hand-motion control is not suitable for vertical motions (See Section 2.6), operators hoist/lower the hook by pressing buttons.

3. Manually attaching and detaching the payload (using rigging straps) from the hook.

4. Transport the payload to the destination. Typically, the operator is required to be in close proximity or at least be closely monitoring the payload during the transport phase.

4.4.1 Step by Step Tasks in the Application

Due to the space restrictions, the floorspace available for experiments using the HiBay crane was a 6m x 3m rectangle. Figure 4.10(a) is an overhead plan view of the floorspace, and the starting configuration of the crane, payloads 1 (150lbs) and 2 (60lbs), dividing barriers, and the table, which serves as the payload destinations.[5] Figure 4.10(b) shows the starting configuration. In step 1, the operator moves the crane to payload 1, and hook the rigging straps up to the hook. Note the hook starts at an elevated height, so the operator must change the hook height to pick up the payloads.

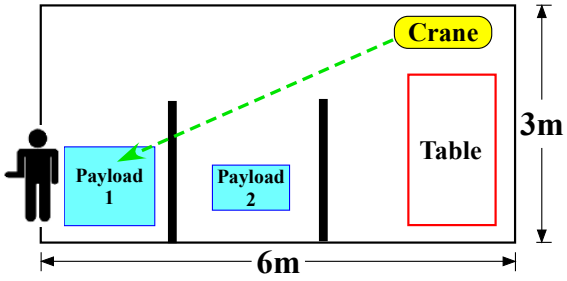

(a) Practical Application Step 1, Plan View

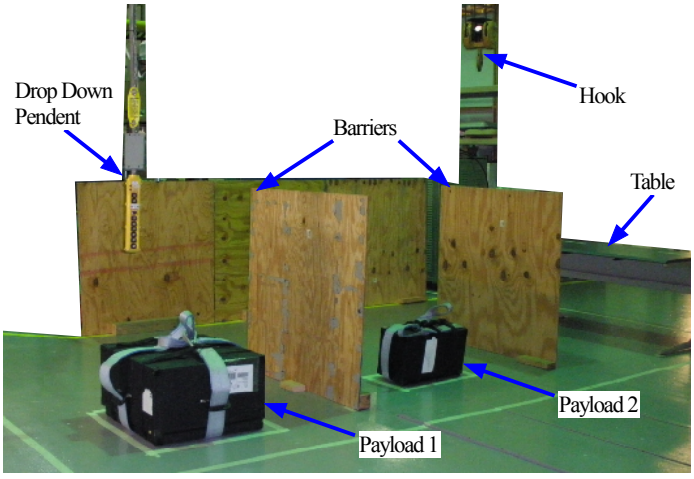

(b) Start Configuration

Figure 4.10: Practical Application Step 1 Photos

In step 2, illustrated in Figure 4.11, payload 1 is lifted to chest height and moved around the barriers to the table, where it is placed and detached from the hook.

[5]The table simulates a workbench or elevated assembly table.

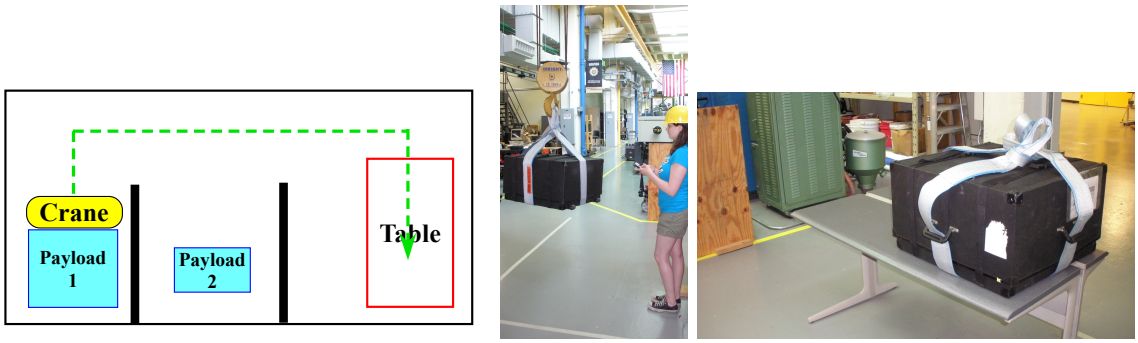

(a) Plan View (b) Payload 1 Lifted (c) Payload 1 on Table

Figure 4.11: Practical Application Step 2

In step 3, illustrated in Figure 4.12, the crane is maneuvered (the hook can be hoisted over barriers) to payload 2, where it is rigged up and lifted to chest height. Then, payload 2 is maneuvered around the barrier and placed on the table.

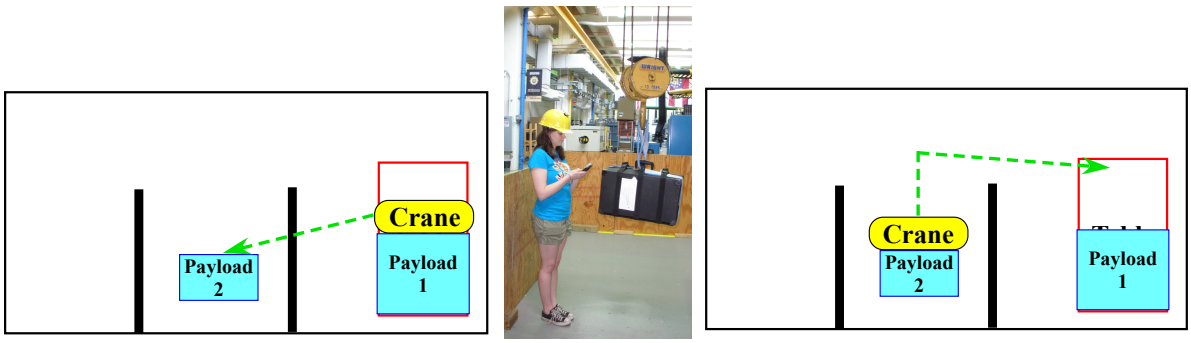

(a) Move to Payload 2 (b) Payload 2 Lifted (c) Move Payload 2 to Table

Figure 4.12: Practical Application Step 3

The finish configuration is shown in Figure 4.13, where both payloads have been placed on the table.

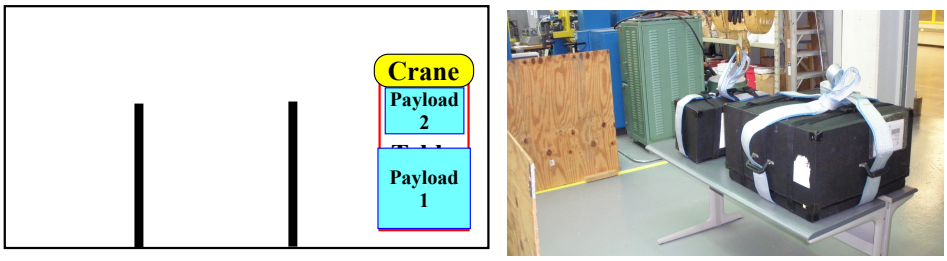

(a) Finish Configuration (b) Payloads 1 and 2 on Table

Figure 4.13: Practical Application Step 4

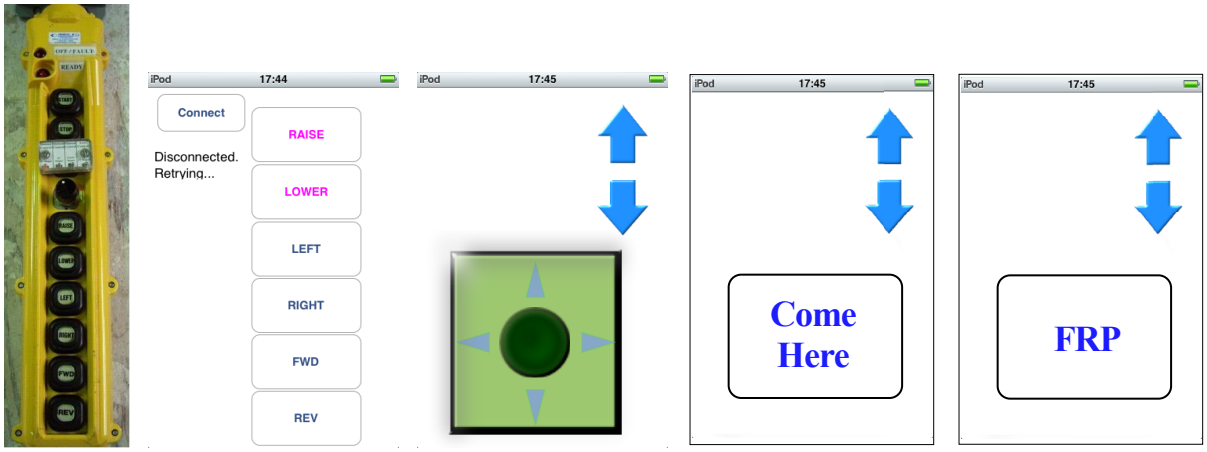

(a) Pendent (b) iOS Pendent (c) iOS Joystick (d) HM Come Here (e) HM FRP

Figure 4.14: Control Interfaces Used in the Study

4.4.2 Control Interfaces

Eleven (4 females and 7 males) novice to moderately-experienced crane operators were recruited for the study. Each operator performed the tasks using various interfaces and controllers:

- Push-button drop-down pendent, shown in Figure 4.14(a), **without** input shaping. This is the existing baseline crane control interface.
- iOS Pendent implemented on a touchscreen device (iPod) **with** input shaping. The GUI is illustrated in Figure 4.14(b). Past operator studies earlier in this chapter have shown that the drop-down pendent is severely disadvantaged due to its form factor. Physically, it is large and unwieldy. It is also tethered to the trolley, which restricts operator movements.

  In order to more clearly ascertain the advantages of hand-motion control over traditional interfaces, all other factors, such as the physical form of the interface, are held constant. The iOS pendent is implemented on the auxiliary touchscreen device that is also used in hand-motion control. Additionally, the layout of the buttons are similar to that of the drop-down pendent.
- iOS Joystick implemented on a touchscreen device (iPod) **with** input shaping. The GUI is illustrated in Figure 4.14(c). The operator touches the virtual joystick (dark green circle) and slides in different directions inside the green square to move the crane. This mode is included so that another industry standard interface can also be compared to hand-motion control in the same form factor. The blue arrows hoists and lowers the hook.
- Hand-motion control in Come-Here mode, and using the On-Off controller. The RF tag is used to track the operator's hand, supplemented with the iPod touchscreen device. Figure 4.14(d) shows the GUI. The blue arrows hoists and lowers the hook.
- Hand-motion control in Fixed Relative Positioning (FRP) mode (Section 2.5) and using the P controller. Figure 4.14(e) shows the GUI. The blue arrows hoists and lowers the hook.

4.4.3 Data Collection

Operators were given a few minutes to familiarize themselves with each interface. The following data were recorded for each trial:

- Completion time
- The motion of the crane trolley and hook. The total distance that the crane traveled can be used as an indication of the efficiency of commanded movements, as well as the total energy expenditure.
- Measures to gauge the level of operator effort:
  - Number of interface actions (button presses or joystick movements).
  - The displacement of the operator's body (tracked by an additional RF-tag mounted to the hard hat worn by the operator).
- Video recording
- Exit questionnaire

Because input shaping was used in four of the five modes, operators did not need to manually control the payload oscillation, and therefore easily avoided the barriers. Furthermore, operators were instructed to move the payloads as if they were in a real assembly plant, i.e. very carefully without damaging the payloads. For each trial, the number of collisions with the barriers were recorded. However, in almost all trials, this number was zero, even when operators were using the drop-down pendent *without* input shaping.[6]

4.4.4 Study Results - Performance Measures

Figure 4.15(a) plots the averaged completion times for all control methods. Hand-motion Come-Here mode was the fastest with an average completion time of 3.33 min. This was followed by the iOS pendent and joystick with 3.79 and 3.82 min, respectively. Even though on average, Come-Here was faster than iOS joystick and pendent by approximately 14%, the differences were not large enough (due to large spreads) to be statistically significant to pass 95% confidence Tukey tests. The slowest interfaces were Hand-motion FRP mode and the drop-down pendent with average times of 4.93 min and 6.10 min, respectively. 95% confidence pairwise Tukey tests indicate the differences between FRP and all other modes, and the differences between the drop-down pendent and all other modes, were statistically significant.

Figure 4.15(b) plots the average distance traveled by the cranefor all control methods. Using hand-motion Come-Here mode, the crane trolley traveled the shortest average distance of 26.4 m. This was followed by the iOS pendent and joystick with 29.4 and 29.6 m, respectively. Even though on average, the crane traveled less in Come-Here mode than iOS joystick and pendent by approximately 11%, the differences were not large enough to be statistically significant. An explanation for this is that in Come-Here mode, it is easier than the iOS modes for the crane to make more direct, straight-line movements. This phenomenon was illustrated in Figure 4.9(b) of the previous section. The crane traveled the furthermost distance with the drop-down pendent and FRP with average distances of 31.6 and 35.4 m, respectively. Tukey tests indicate the differences between FRP and Come-Here, FRP and iOS joystick, and FRP and iOS pendent, were statistically significant. One explanation to why FRP made less efficient motions is that it is more complicated to use, leading to many differences between the actual crane behavior and operator expectations.

Figure 4.15(c) plots the average number of interface actions (i.e. button presses and joystick movements) for all interfaces. Note the drop-down pendent averaged 284 presses, and extends beyond the range of the plot. Come-Here averaged the fewest button presses, with 29.6, followed by FRP with 33.8, iOS pendent with 41.9, and iOS joystick with 42.4. With Come-Here, operators pressed buttons approximately 41.9% less than iOS joystick and pendent. However, due to large

[6] In this mode, each operator moved the crane very slowly or simply waited for payload swing to die down.

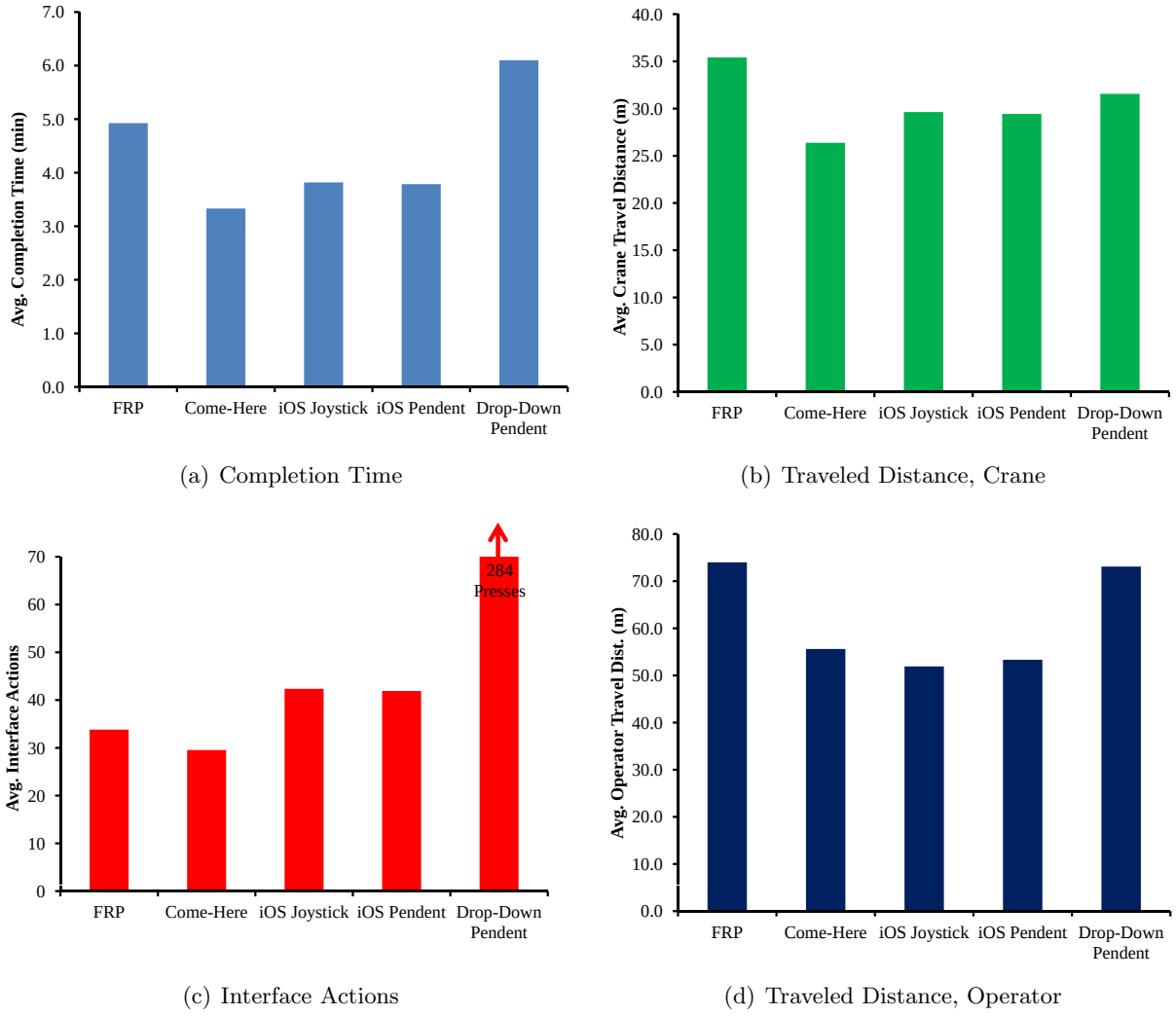

(a) Completion Time

(b) Traveled Distance, Crane

(c) Interface Actions

(d) Traveled Distance, Operator

Figure 4.15: Averaged Performance Measures

spreads, the differences between Come-Here, FRP, iOS pendent, and iOS joystick were not large enough to be statistically significant.

The number of interface actions measures only one aspect of operator effort. This is because with the hand-motion modes, the movement of the operator's body is a significant part of commanding the crane. Figure 4.15(d) plots the average distance traveled by operators for all interfaces. The interfaces in order from least to most distance traveled are: iOS joystick with 51.9m, iOS pendent with 53.3m, Come-Here with 55.6m, drop-down pendent with 73.1m, and FRP with 74m. In Come-Here mode, operators only walked further by approximately 5.9% than the iOS modes. The differences between the two longest traveled interfaces (Fixed Relative Positioning mode and drop-down pendent) and the three least traveled interfaces (iOS joystick, iOS pendent, Come-Here) were statistically significant. However, the differences amongst the three least traveled interfaces were not statistically significant.

Operators required the least amount of interface actions with Come-Here, and walked slightly more than the iOS modes. Together, these indicate Come-Here mode requires very little effort from operators. Even though operators in FRP mode required less interface actions than with the iOS modes, they still needed to travel significantly greater distances, because FRP inherently requires operators to physically move in order to command the crane. With iOS modes or Come-Here, operators can stand in one place to move the crane. Finally, the drop-down pendent requires

significantly more effort from operators (in both interface actions and distance walked).

4.4.5 Study Results - Questionnaire Responses

After the tests were completed, the operators answered questions to gauge their subjective thoughts on each interface. Figures 4.16(a) - 4.16(f) plots the averaged responses to the following questions (in order):

1. "On a scale from 1 to 10, 1 being the easiest, how easy was it to control the crane?".
2. "On a scale from 1 to 10, 1 being the safest, how safe did you feel while using this control method?".
3. "On a scale from 1 to 10, 1 being most intuitive, how natural did the controls feel?".
4. "At any point did you feel as if the payload was too close to you?".
5. "At any point did you feel as if you lost total control of the payload/crane?".
6. "If hired today as a crane operator, would you feel comfortable using this control method?"

Note that for Figures 4.16(a)-4.16(e), lower bars are better. For Figure 4.16(f), higher bars are better.

The plots in Figure 4.16 indicate that the Fixed Relative Positioning (FRP) and the drop-down pendent were generally the least preferred interfaces. Come-Here, iOS joystick, and iOS pendent were generally more preferred by operators. The general comments made by all operators were that the drop-down pendent, because it did not have input-shaping, was the most difficult interface. One suggestion made by some operators was that the iOS joystick and pendent interfaces should reorient themselves to match the orientation of the operator. For example, pushing forward should always move the crane in the direction that the operator is facing. This can be implemented using accelerometer, gyroscope, or compass sensors available on many mobile devices. This suggestion was integrated into the master's thesis of Arto Kivila.

Some operators commented that FRP was too difficult to familiarize in a short amount of time. The test conductor noticed that many operators were unaware of whether they were holding the FRP button, and thus the crane did not behave as expected, leading to operator frustration. Furthermore, operators consistently stated that too much thought was required when using FRP, because operators needed to be constantly aware of their initial position relative to the payload, which may be change every time they deactivate and activate FRP. Some operators recognized that FRP would be very useful in certain situations. However, as learning anything new takes time, the efficiency of using FRP obviously depends on the operator's level of training. The concept of FRP is inherently foreign to most operators. In contrast, concepts of joysticks and push-buttons are already familiar to most operators (skeuomorphism). Conversely, Come-Here was very popular amongst operators. Many felt Come-Here was the most intuitive interface with the lowest learning curve, because they did not need to think much about driving the crane.

4.4.6 Summary

Operators performed tasks in a practical, assembly-line-like application (picking up, moving, and dropping off payloads) using five different control methods. The industry-standard drop-down pendent, due to its lack of input shaping to suppress oscillations, was least preferred by operators. Furthermore, it performed the worst in terms of average completion times, and required the highest levels of operator effort.

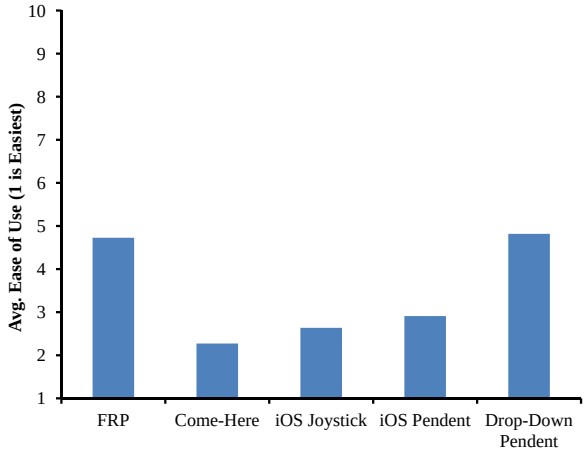

(a) Ease of Use (1 is Easiest)

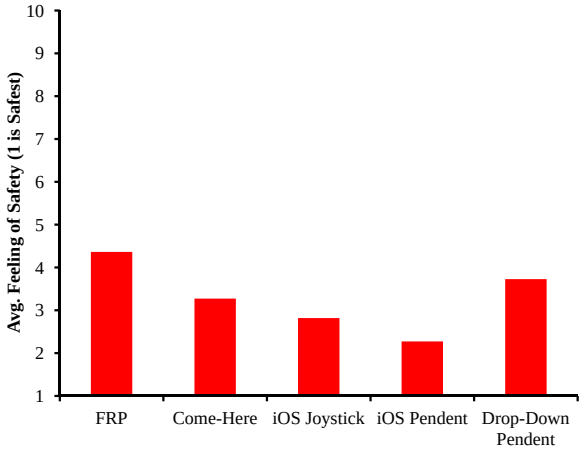

(b) Feeling of Safety (1 is Safest)

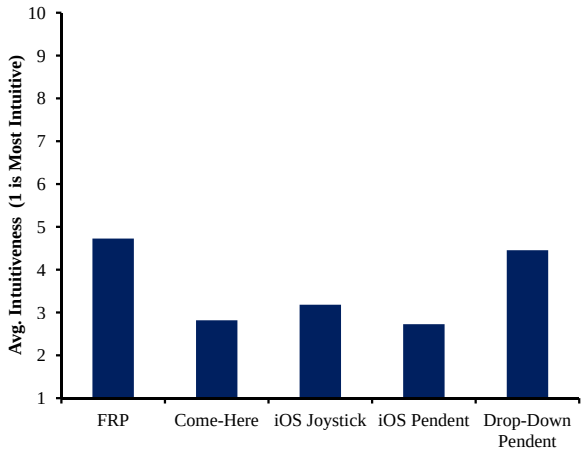

(c) Feeling of Intuitiveness (1 is Most Intuitive)

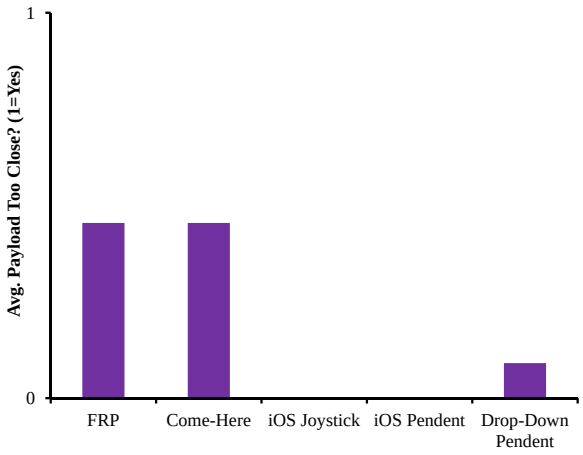

(d) Did the Payload Come Too Close? (1=Yes)

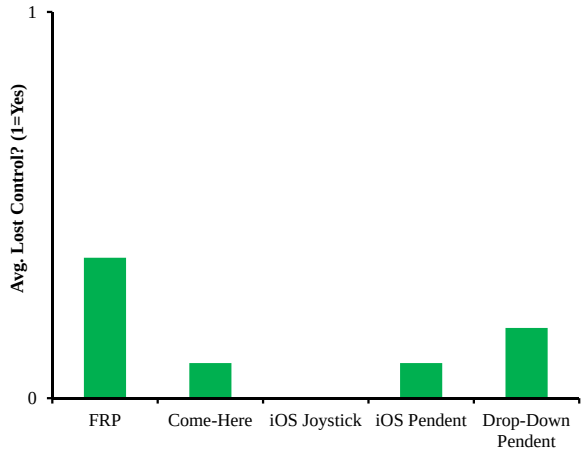

(e) Did Operator Lose Control? (1=Yes)

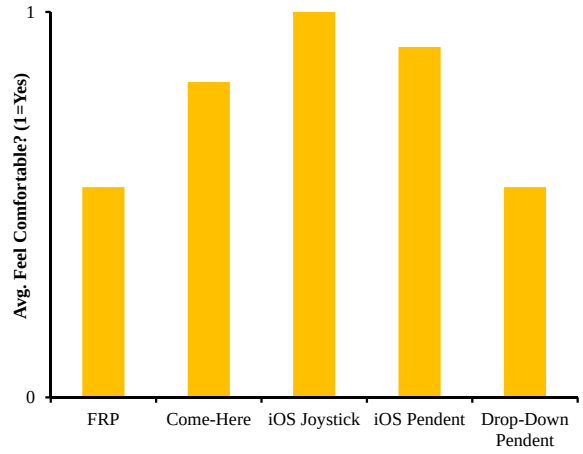

(f) Feel Comfortable If Hired as Real Crane Operator? (1=Yes)

Figure 4.16: Averaged Responses From Exit Questionnaires

The iOS pendent and iOS joystick produced very similar results in all four performance measures. These interfaces represent traditional interfaces, but in the same form-factor as the hand-motion interfaces. They also had input shaping for the purpose of better isolating the effects of the

hand-motion interface. Operators generally liked these two interfaces.

The Fixed Relative Positioning (FRP) mode was generally disliked by most operators. This is because the FRP was a foreign concept to most operators. It also required an extra layer of thought process (i.e. remembering the initial relative position) to use. Therefore, it is not surprising that FRP yielded worse levels of performance compared to the iOS interfaces, in terms of completion time and effort exerted. It also produced the least efficient crane motion out of all interfaces. However, as with learning anything new, some operators commented that they could be efficient with FRP in certain situations, if given more training time.

The Come-Here mode was also generally liked by most operators. It also yielded the fastest average completion time (approximately 14% faster than the iOS interfaces), the most efficient crane motions (approximately 11% less crane distance traveled than the iOS interfaces),[7] while still being one of the least effort-exerted interfaces. Come-Here performed better than the drop-down pendent in all aspects.

[7]However, these differences are not large enough to be statistically significant (95% confidence Tukey tests)

CHAPTER V

OFF-CENTERED LIFTS

Cranes can fail, sometimes catastrophically, in a number of ways. One generally accepted list of 13 failure modes in cranes was put forth by MacCollum [56]. Of these, "side pull" is one of the most common causes of crane-related injuries and fatalities [63]. The United States Department of Labor, Occupational Safety & Health Administration defines side pull as: "the portion of the hoist pull acting horizontally when the hoist lines are not operated vertically" [115].

In the vast majority of cases, side pull is considered extremely dangerous and should be avoided. Some typical problems associated with side pull include: 1) The cables may come out of the grooves on the hoist drum and rub against the remaining cables or drum, resulting in damaged cables; 2) Side pull may cause unintended stress on certain crane components; 3) Dangerous and unpredictable payload sliding and swinging.[1]

Many different situations can be classified as having side pull. For example, the topic of Chapter 6 is the laying down of long payloads, which can potentially put the hoist cable at extreme angles. However, this chapter investigates the specific situation of lifting a payload off the ground when the payload is not properly centered beneath the hoist (an off-centered lift). In a typical lift, the hook is suspended from the trolley by hoist cable(s) and attached to the payload on the ground with an arrangement of rigging cable(s).

In an off-centered lift, the payload center is horizontally offset from the hoist by some distance. This situation is shown schematically in Figure 5.1(a). If the crane hoists in this configuration, then the payload may slide across underneath the trolley, and swing in the air when it comes off the ground. Clearly, this presents an undesirable and potentially fatal dynamic effect.

While there is no accurate source of crane accident statistics[2], a significant portion of injuries and fatalities were caused by being struck by the payload [9]. With near certainty, a subset of these incidents can be attributed to off-centered lifts. The author has also received anecdotal evidence of two fatal incidents in a General Motors plant during the past year where the crane operators were struck by the unexpected horizontal movement of large casting dies when they were lifted from the ground.

The correct and recommended procedure for lifting payloads is to position the hoist over the center of the payload [21], as shown in Figure 5.1(b). This lifts the payload vertically upwards, which eliminates dangerous payload sliding and swinging. Obviously, centering the hoist over the payload before lifting is by far the most effective preventative measure against off-centered lifts. However, this may be challenging for the crane operator to perform because the position of the hoist may be difficult to judge if it is very high off the ground. Thus, it is important to study off-centered lifts and develop solutions to this dangerous problem.

First, situations that result in dangerous levels of sliding and swinging should be determined. To this end, two theoretical dynamic models were derived: 1) point-mass hook and point-mass payload, and 2) point-mass hook and rigid-body payload. These models were used to quickly and efficiently produce simulation responses, from which, situations that lead to dangerous levels of sliding and swinging can be identified. The knowledge obtained from the theoretical models are used to intelligently design auto-centering techniques to assist crane operators during lifts.

[1] In fact, the HiBay crane was involved in one such incident, which resulted in the loss of a large and expensive piece of equipment.

[2] This is due to the fact that crane-related incidents are not well documented, and that the definitions of "accident" or even "crane" are not universal.

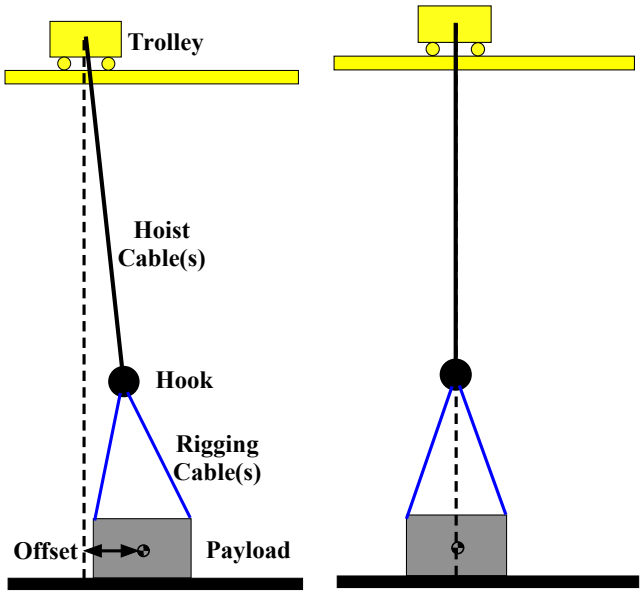

(a) Off-Centered (b) Centered

Figure 5.1: Payload Liftup Situations

5.1 Background

Barrett and Hrudey investigated lifting payloads off the ground from initial conditions that differed in hoist cable tensions [8]. However, their work focused on the dynamic forces exerted on the structural components of the crane, rather than the motion of the payload. There are no other known prior work related to the lifting up of payloads from the ground. In nearly all crane-related academic publications, the focus was on modeling a payload swinging in the air while payload interaction with the ground was largely ignored. The most popular choice to model the swinging payload is the lumped-mass single pendulum [1]. Some prior work used more complex models to address specific situations such as varying the hoist cable length [92, 106], double pendulums [2, 45], and distributed loads [58].

Modeling the interaction between the payload and ground is a crucial part of understanding the dynamics of off-centered lifts. For this reason, the importance of contact dynamics and friction modeling are apparent. A number of contact modes can exist between payload and ground: stiction (zero relative tangential velocity between contact surfaces), sliding/slipping (non-zero relative velocity), and separation of contact (non-zero normal velocity) [59]. The choice of friction model is important for determining the mode of contact.

The fundamental forces that contribute to dry friction between two solid surfaces is highly complex. Although there are more precise models available, this dissertation uses Coulomb's law to model friction. Coulomb's law is an empirically-derived approximation that captures much of the aggregate behavior of friction. Its combination of simplicity and accuracy is often the best choice in many applications. Simply stated, it relates the tangential friction force to the normal force between two contact surfaces under stiction and sliding conditions:

$$\begin{array}{ll} |f_f| & \leq \mu_s \, |f_N| \quad : \text{stiction} \\ |f_f| & = \mu_k \, |f_N| \quad : \text{sliding} \end{array} \tag{5.1}$$

where f_f and f_N are the tangential friction and normal forces, respectively; and μ_s and μ_k are the static and kinetic coefficients of friction, respectively.

The stiction described in (5.1) leads to the interesting and well-known Painlevé's paradox [5,

59, 7, 107]. The paradox arises between what some refer to as the inconsistency between Newtonian mechanics and the unilateral constraint of the friction force during stiction (that it can take any value up to a limit). Many authors illustrate the paradox using the example of a rigid rod falling and sliding on a horizontal surface. The choice of parameters may lead to contradictory situations with no solutions (e.g. if the coefficient of friction is high [5]), or to indeterminate situations with multiple solutions.

One way to resolve this issue is to allow impact/impulse forces (i.e. removing the restriction that all forces are bounded) [7, 107]. Because cranes move relatively slowly, this dissertation ignores impact forces and assumes that Painlevé's paradox do not appear in the cases studied here. Moreover, due to the inherently approximate nature of friction models, and that the goal is to obtain a general trend over the aggregate behavior of off-centered lifts, it will be shown that the simplified methods presented here are sufficient.

It should be noted that modeling dynamic behavior with Coulomb friction is highly complex, even for seemingly simple problems. This is largely because during stiction, (5.1) does not give the friction force as a function of state. Rather, it only imposes a unilateral constraint on the force. Moreover, the complexity increases when the *direction* of forces and velocities are taken into account. The result is a circularity - accelerations are determined by forces, which are now determined partly by accelerations (and velocities). This dissertation takes the systematic approach suggested by Mason [59]:

1. Enumerate the contact modes: stiction, sliding (including direction), separation/contact
2. Solve the mechanics problems associated with each contact mode to obtain velocities and accelerations at each contact point/surface
3. Discard the solution(s) if the contact velocities and accelerations are inconsistent with the hypothesized contact mode

Practical issues arise when there are many contact modes. The problem complexity grows for multiple contact points/surfaces, and for multiple bodies. To address this, Pfeiffer and Glocker framed the task of solving for the friction forces and accelerations as a Linear Complementarity Problem (LCP). This method exploits the complementary nature between properly formed acceleration and friction vectors, and then solves the problem using efficient LCP techniques. This method avoids the tedious solving and checking for each contact mode in multi-contact/bodies problems, as in Mason's approach outlined above.

Modeling the transitions between contact modes (e.g. from stiction to sliding and vice versa) is important. A contact point has zero initial velocity when it transitions from stiction to sliding. Because of this, the initial direction of the kinetic/sliding friction is ambiguous (friction opposes velocity) because it involves the division of zero in its calculation. To address this, Mitiguy et al. proposed a simple method using an arbitrary small number, ϵ and a continuous function that bridges the discontinuous transition between stiction and sliding [60]. This technique is useful when the contact point/surface moves in a 2-D plane, where it is important to determine the direction of friction.

Finally, the computer program, Autolev [38], was used extensively in this chapter to obtain the Newton-Euler dynamic equations [23].

5.2 Point-Mass Hook and Point-Mass Payload

In this model, the hook and payload are two point masses, H and P, as shown in Figure 5.2. The hoist cable is modeled as a massless rigid rod of length L, which is a known function of time. The hoist cable's rate of change, $\dot{L}$, is also known, and assumed constant during hoisting (i.e. $\ddot{L} = 0$). Hoisting begins at time $t = 0$, and is stopped after the payload is lifted to a predetermined height

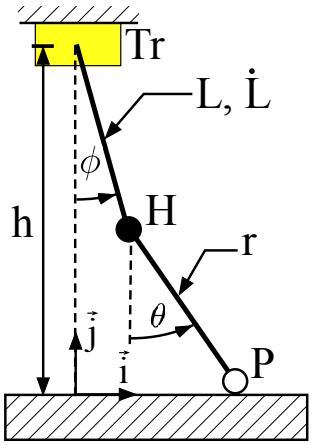

Figure 5.2: Model with Separate Point-Masses for the Hook and Payload

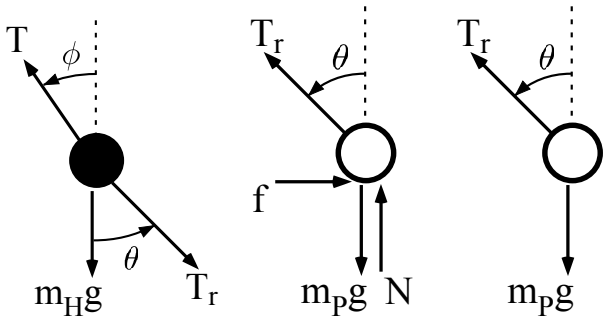

(a) H (b) P, Stiction and Sliding (c) P, Swinging

Figure 5.3: Point-Masses Hook and Payload: Free Body Diagrams

off the ground. The hoist cable, which has an angle from vertical of ϕ, connects H to the trolley, Tr, which is h meters above the ground. Also shown is the origin of the inertial frame, with $\vec{i}$ and $\vec{j}$ being the unit vectors in horizontal and vertical directions, respectively. There is also a rigging cable of constant length r connecting H to P, and its angle from vertical is θ. The position of P in the $\vec{i}$ and $\vec{j}$ directions are x and y, respectively.

Three modes are possible: 1) stiction on the ground, 2) sliding on the ground, and 3) swinging in the air. The free body diagrams of H and P are shown in Figure 5.3. Three forces act on the hook: hoist cable tension, T, rigging cable tension, T_r, and gravity, which is given by the hook mass, m_H, multiplied by g. When the payload is on the ground, four forces act on it: rigging cable tension, T_r; friction force parallel with the ground, f; gravity (the payload mass is m_P); and the normal reaction force from the ground, N. Two forces act on the payload when it is swinging in the air: rigging cable tension and gravity.

Figure 5.4 illustrates the transitions between each mode. The starting mode is stiction, where P is stationary. The following describes each transition, indicated by numbers in the diagram:

1. During stiction, if the friction force resisting movement exceeds $\mu_S|N|$, then the dynamics transition to sliding.

2. During sliding, if the payload velocity, $|\dot{x}|$, becomes zero, then the dynamics transition to stiction.

3. If the normal force becomes less than zero during stiction or sliding, then the dynamics

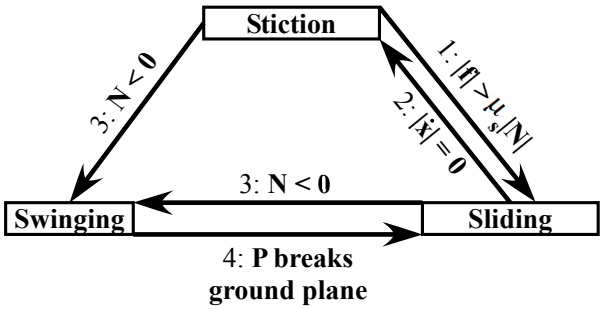

Figure 5.4: Point-Masses Hook and Payload: Mode Transitions

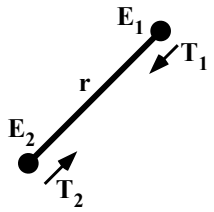

Figure 5.5: Spring Rigging Cable Model

transition to swinging.

4. If P hits the ground during swinging, then the dynamics transition to sliding.

The next subsection describes modeling the rigging cable as a spring (rather than a stiff rod like the hoist cable), followed by subsections that detail each dynamic mode of this model.

5.2.1 Modeling the Rigging Cable as a Spring

The hoist cable is modeled as a massless stiff rod, because it is assumed to always be in tension. This is a good assumption because the weight of the hook prevents it from slacking in almost all situations. Rigging cables, however, can be slack, which presents some difficulties. The problem with the stiff rod model for the rigging cable is that it imposes strict geometric constraints on the system. This makes the dynamic equations difficult to solve. Also, if the cable loses tension, then the geometric constraints disappear completely. This condition requires solving a completely new set of dynamic equations.

Kyle et al. modeled ropes and chains as N segments, where each segment is a point mass connected to other segments by springs and dampers [48]. Spring models introduce additional flexibility to the system[3]. However, difficulties with the strict geometric constraints of the stiff-rod assumption are averted.

In this dissertation, the rigging cable (of length r) is modeled as a massless spring between the two connection endpoints, E_1 and E_2. The rigging cable effectively exists as two equal and opposite forces, T_1 and T_2 acting on E_1 and E_2, respectively. This is illustrated in Figure 5.5. The direction and magnitude of these forces can be calculated easily from the position vectors of the endpoints, $\vec{E_1}$ and $\vec{E_2}$. The rigging cable length r and a unit vector between the two endpoints are defined as:

$$r = \|\vec{E_1} - \vec{E_2}\| \tag{5.2}$$

$$\vec{u_r} = \frac{\vec{E_1} - \vec{E_2}}{r}, \tag{5.3}$$

[3]Flexibility is kept to a minimum as the spring constant for rigging cable is usually very large.

where $\vec{u_r}$ is the unit vector that points from E_2 to E_1. If r is longer than the unstretched length of rigging cable, r_u, then the tension in the cable is T_r, and forces are exerted on the end points. Otherwise, the cable is slack and no forces are exerted. These conditions can be stated as:

$$\begin{aligned} &\text{if } r > r_u, \quad \text{then} \\ &\vec{T_1} = -K_r\,(r - r_u)\,\vec{u_r} && (5.4)\\ &\vec{T_2} = -\vec{T_1} && (5.5)\\ &T_r = |T_1| = |T_2| && (5.6)\\ &\text{else} \\ &T_r = \vec{T_1} = \vec{T_2} = 0 && (5.7) \end{aligned}$$

where K_r is the spring constant, and T_r is the tension force in the rigging cable as shown in Figure 5.3.

5.2.2 Stiction

Stiction is the default starting mode for the dynamic analysis. Because the payload is assumed stationary during this mode, there is only one degree of freedom, which is represented by ϕ. The differential equation describing motion is:

$$\ddot{\phi} = \frac{r x_{stic} T_r \cos(\phi) - \sin(\phi)(g m_H + \frac{H T_r}{r}) - 2 m_H \dot{L} \dot{\phi}}{m_H L}, \tag{5.8}$$

where x_{stic} is the horizontal (stationary) position of P during this mode, T_r is the rigging cable tension calculated using the spring-model method described in Section 5.2.1, and r is the rigging cable length given by:

$$r = \sqrt{h^2 + x_{stic}^2 + L^2 - 2hL\cos(\phi) - 2x_{stic} L \sin(\phi)}. \tag{5.9}$$

The motion of the hook, H, is easily calculated from ϕ and L (Note that L is a specified and known function of time). Knowing the hook position and the rigging cable length allows the calculation of the forces acting on the payload. With reference to Figure 5.3(b), the normal and friction forces with the ground are:

$$N = g m_P - T_r \frac{h - L\cos(\phi)}{r} \tag{5.10}$$

$$f = T_r \frac{x_{stic} - L\sin(\phi)}{r} \tag{5.11}$$

Note that $x = x_{stic}$ and $\dot{x} = y = \dot{y} = 0$ while the system is in this mode.

5.2.3 Sliding

There are two degrees of freedom during sliding: ϕ and x, and the differential equations of motion are:

$$\ddot{\phi} = \frac{\frac{1}{r} T_r x \cos(\phi) - \sin(\phi)(g m_H + \frac{h T_r}{r}) - 2 m_H \dot{L} \dot{\phi}}{m_H L} \tag{5.12}$$

$$\ddot{x} = \frac{f - \frac{T_r}{r}(x - L\sin(\phi))}{m_P}, \tag{5.13}$$

where r is given by:

$$r = \sqrt{h^2 + x^2 + L^2 - 2hL\cos(\phi) - 2xL\sin(\phi)}. \tag{5.14}$$

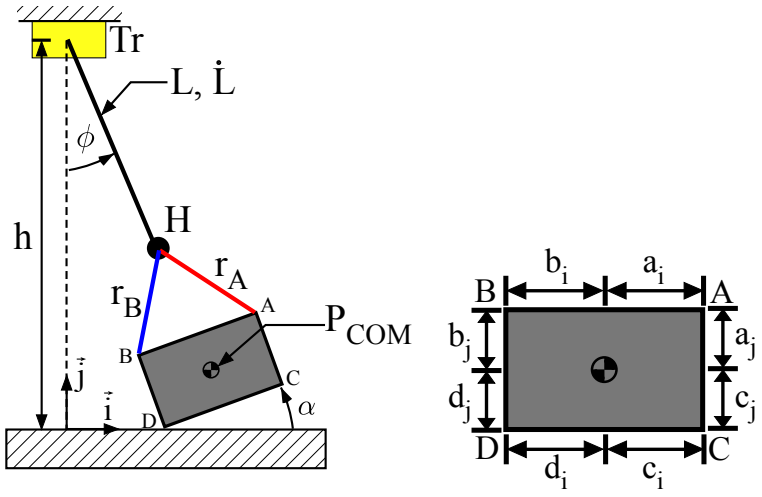

(a) Schematic (b) Payload

Figure 5.6: Point-Mass Hook and Rigid-Body Payload Model

The forces acting on the payload, which are needed for determining mode transitions, are given by:

$$N = gm_P - \frac{T_r(h - L\cos(\phi))}{r} \tag{5.15}$$

$$f = \mu_K N \tag{5.16}$$

Note that $y = \dot{y} = 0$ in this mode.

5.2.4 Swinging

There are three degrees of freedom in the swinging mode: ϕ, x, and y, and the differential equations of motion are:

$$\ddot{\phi} = \frac{\frac{T_r x}{r}\cos(\phi) - \sin(\phi)(gm_H + \frac{T_r}{r}(h - y)) - 2m_H\dot{L}\dot{\phi}}{m_H L} \tag{5.17}$$

$$\ddot{x} = \frac{-T_r(x - L\sin(\phi))}{m_P r} \tag{5.18}$$

$$\ddot{y} = \frac{T_r(h - y - L\cos(\phi))}{m_P r} - g \tag{5.19}$$

5.3 Point-Mass Hook and Rigid-Body Payload

As most payloads are not point masses, a more realistic model is required to capture some important dynamic effects. Figure 5.6 illustrates a model where the hook, H, is a point mass, and the payload, P, is a rectangular rigid body. The position of the payload center of mass (COM) in the $\vec{i}$ and $\vec{j}$ inertial frame directions are x and y, respectively. The payload's rotation from horizontal is α, and its rotational inertia is I. There are now two rigging cables, r_A and r_B, attached to two points on P: A and B. The bottom corners of P are indicated by C and D. The positions from the COM to: i) A is $a_i\vec{i} + a_j\vec{j}$; ii) B is $-b_i\vec{i} + b_j\vec{j}$; iii) C is $c_i\vec{i} + -_j\vec{j}$; iv) D is $-d_i\vec{i} - d_j\vec{j}$.

This dissertation will focus on symmetrical riggings and uniform rectangular payloads, so that $a_i = b_i$, $c_i = d_i$, $a_j = b_j$, and $c_j = d_j$. However, the equations presented here are also applicable to payloads that have different dimensions, as well as different rigging arrangements.

Seven dynamic modes are possible: 1) Planar (i.e. $\alpha = 0$) stiction, 2) Stiction on C, 3) Stiction on D, 4) Planar (i.e. $\alpha = 0$) sliding, 5) Sliding on C, 6) Sliding on D, and 7) Swinging. There are

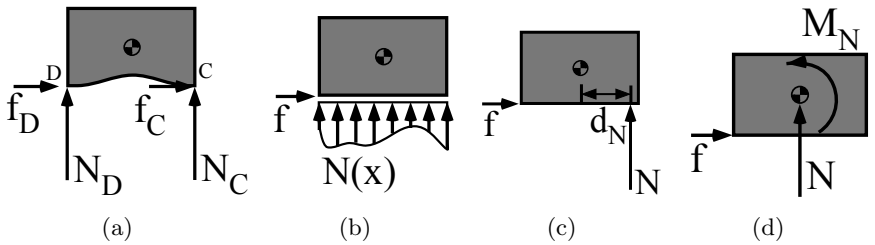

Figure 5.7: Modeling Normal Forces on the Bottom Surface of P

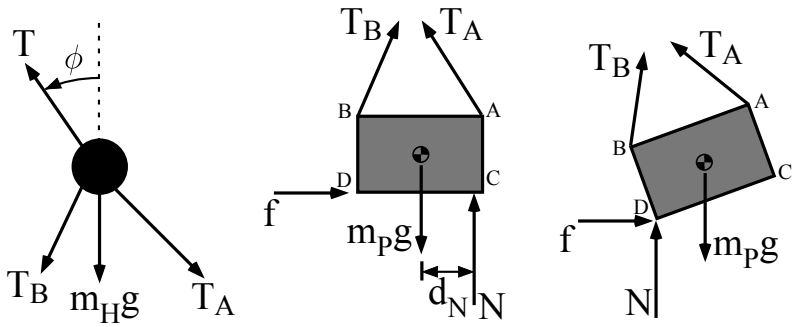

Figure 5.8: Point-Mass Hook and Rigid-Body Payload: Free Body Diagrams

a number of ways to model the the contact forces on the bottom surface of P in the planar modes. A common way is shown in Figure 5.7(a), which assumes the bottom surface is slightly concave, so only C and D are touching the ground. However, using this method is problematic in the planar stiction mode because the forces are statically indeterminate. Furthermore, they are complicated by two sets of friction and normal forces.

More realistically, the bottom surface is acted on by a normal force distribution, $N(x)$, and a resultant friction force, f, as shown in Figure 5.7(b). This can also be represented by equivalent models shown in Figures 5.7(c) (resultant N acting at a distance d_N from the COM) and 5.7(d) (resultant N acting at COM coupled with a moment M_N). In this dissertation, the model in Figure 5.7(d) was used to obtain the dynamic equations. This model is simpler to deal with as the forces act at fixed locations rather than at variable locations like in Figure 5.7(c). Then, the equations were converted to the equivalent model in Figure 5.7(c) (i.e. obtain d_N from M_N). This is more convenient for determining transitions between planar modes and modes where the payload is tipping on C or D.

In all modes, four forces act on the hook, H, as shown in Figure 5.8(a): hoist cable tension, T; rigging cable tensions T_A and T_B; and gravity, m_Hg. Figure 5.8(b) shows the forces acting on the payload while it is in planar (i.e. $\alpha = 0$) stiction and sliding. The contributing forces are: rigging cable tensions T_A and T_B; the horizontal friction force with the ground, f; gravity, m_Pg; and the net normal force, N, which acts at some horizontal distance, d_N, from the COM. The net normal force is equivalent to the distribution of forces acting on the bottom surface from C to D. Figure 5.8(c) is the stiction and sliding FBD of P while it is tipping (i.e. $\alpha \neq 0$) on corner C or D. The notable feature here is that f and N act on the tipping corner.

Figure 5.9 illustrates the transitions between each dynamic mode. The starting mode is planar stiction, where P is stationary. This mode is shown at the top center of the diagram.

The following describes each transition, indicated by numbers in the diagram:

1. During planar stiction, if the friction force at the contact point resisting movement exceeds

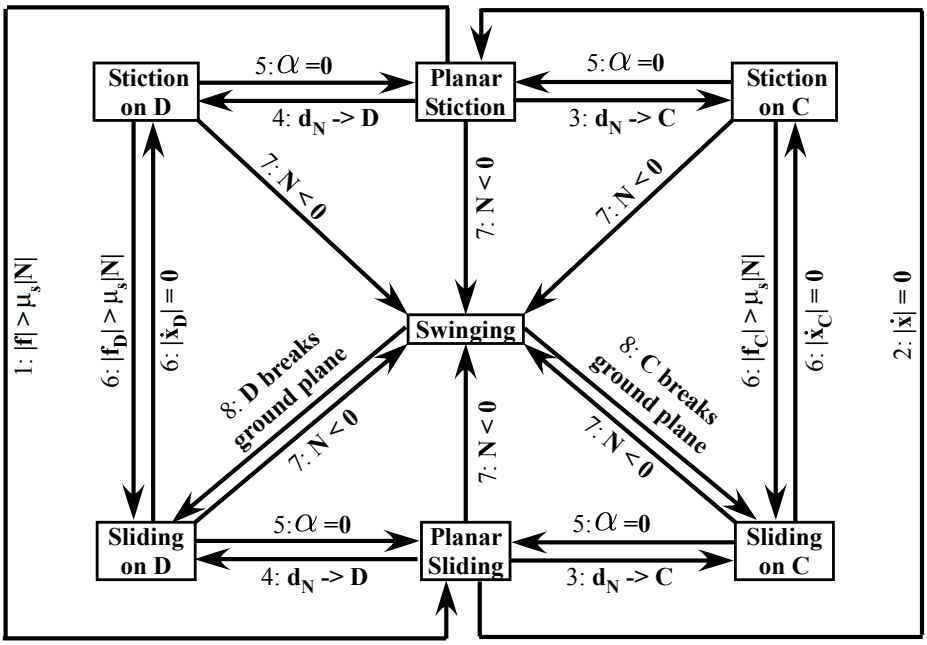

Figure 5.9: Point-Mass Hook and Rigid-Body Payload: Mode Transitions

$\mu_S|N|$, then the dynamics transition to planar sliding. Planar sliding is the block at the bottom center of the diagram.

2. During planar sliding, if the velocity of the contact point, in this case it is equivalent to $|\dot{x}|$ becomes zero, then the dynamics transition to planar stiction.

3. During planar stiction or sliding, if d_N reaches corner C (i.e. the net normal force, N acts on C), then the dynamics transition to stiction or sliding on C (i.e. the payload begins to tip onto C).

4. There is a similar transition for tipping on to corner D.

5. If the payload rotation angle, α, goes to zero while tipped on C or D, then the dynamics transition back to the corresponding planar mode.

6. The transitions between stiction and sliding when the payload is tipped on C or D are similar to the planar cases (steps 1 and 2).

7. If the normal force goes to zero while the payload is still touching the ground, then the dynamics transition to swinging.

8. If the payload hits the ground while swinging, then the dynamics transition to sliding on C or D depending on which corner touches the ground.

The following subsections gives details for each dynamic mode.

5.3.1 Planar Stiction

Planar stiction is the default starting mode. Because the payload is assumed stationary, there is only one degree of freedom: the hoist cable angle, ϕ. The differential equation describing motion

is:

$$\ddot{\phi} = \frac{1}{m_H L}\left(x_{stic}\cos(\phi)\left(\frac{T_A}{r_A}+\frac{T_B}{r_B}\right)+\sin(\phi)\left(a_j\frac{T_A}{r_A}+b_j\frac{T_B}{r_B}\right)+\cos(\phi)\left(a_i\frac{T_A}{r_A}-b_i\frac{T_B}{r_B}\right)\right.$$
$$\left.-\sin(\phi)\left(gm_H-(d_j-h)\left(\frac{T_A}{r_A}+\frac{T_B}{r_B}\right)\right)-2m_H\dot{L}\dot{\phi}\right), \quad (5.20)$$

where x_{stic} is the horizontal (stationary) position of the COM of P, T_A and T_B are the tensions in the rigging cables calculated using the method in Section 5.2.1, and the rigging cable lengths r_A and r_B are:

$$r_A = (a_i^2+a_j^2+x_{stic}^2+2a_ix_{stic}+(d_j-h)^2+2a_j(d_j-h)+L^2+2a_jL\cos(\phi)$$
$$+2(d_j-h)L\cos(\phi)-2a_iL\sin(\phi)-2x_{stic}L\sin(\phi))^{0.5} \quad (5.21)$$
$$r_B = (b_i^2+b_j^2+x_{stic}^2+(d_j-h)^2+2b_j(d_j-h)+L^2+2b_iL\sin(\phi)+2b_jL\cos(\phi)$$
$$+2(d_j-h)L\cos(\phi)-2b_ix_{stic}-2x_{stic}L\sin(\phi))^{0.5}. \quad (5.22)$$

Knowing the hook position and the rigging cable lengths allows for the calculation of the forces on the payload that are required to determine dynamic mode transitions. With reference to Figure 5.8(b), f, N, and d_N are:

$$f = \frac{T_A}{r_A}(a_i+x_{stic}-L\sin(\phi))+\frac{T_B}{r_B}(x_{stic}-b_i-L\sin(\phi)) \quad (5.23)$$
$$N = gmP-\frac{T_A}{r_A}(h-a_j-d_j-L\cos(\phi))-\frac{T_B}{r_B}(h-b_j-d_j-L\cos(\phi)) \quad (5.24)$$
$$d_N = \left(-d_j(x_{stic}-L\sin(\phi))(T_A/r_A+T_B/r_B)-\frac{T_A}{r_A}(a_ih+a_jx_{stic}-a_iL\cos(\phi)\right.$$
$$\left.-a_jL\sin(\phi))-\frac{T_B}{r_B}(b_jx_stic+b_iL\cos(\phi)-b_ih-b_jL\sin(\phi))\right)\frac{1}{N} \quad (5.25)$$

Note that $x = x_{stic}$ and $\dot{x} = y = \dot{y} = \alpha = \dot{\alpha} = 0$ in this mode.

5.3.2 Stiction on C

When the payload experiences stiction on corner C, it is now free to rotate about the corner. There are now two degrees of freedom in this mode: ϕ and α. The differential equations describing the motion are:

$$\ddot{\phi} = (x_{cstic}\cos(\phi)(T_A/r_A+T_B/r_B)-\sin(\phi)(gm_H+h(T_A/r_A+T_B/r_B))$$
$$-\sin(\alpha-\phi)((a_j+c_j)T_A/r_A+(b_j+c_j)T_B/r_B)-\cos(\alpha-\phi)((b_i+c_i)T_B/r_B$$
$$-(a_i-c_i)T_A/r_A)-2m_H\dot{L}\dot{\phi})/(m_HL) \quad (5.26)$$
$$\ddot{\alpha} = -(T_B(h(b_i+c_i)\cos(\alpha)+h(b_j+c_j)\sin(\alpha)+x_{cstic}(b_i+c_i)\sin(\alpha)$$
$$-x_{cstic}(b_j+c_j)\cos(\alpha)-(b_i+c_i)L\cos(\alpha-\phi)-(b_j+c_j)L\sin(\alpha-\phi))/r_B$$
$$-gm_P(c_i\cos(\alpha)+c_j\sin(\alpha))-T_A(x_{cstic}(a_j+c_j)\cos(\alpha)+h(a_i-c_i)\cos(\alpha)+$$
$$x_{cstic}(a_i-c_i)\sin(\alpha)+(a_j+c_j)L\sin(\alpha-\phi)-h(a_j+c_j)\sin(\alpha)$$
$$-(a_i-c_i)L\cos(\alpha-\phi))/r_A)/(I+m_P(c_i^2+c_j^2)), \quad (5.27)$$

where x_{cstic} is the horizontal position of corner C on the ground, and r_A and r_B are given by:

$$r_A = (h^2+x_{cstic}^2+(a_j+c_j)^2+(a_i-c_i)^2+L^2+2x_{cstic}(a_i-c_i)\cos(\alpha)$$
$$+2(a_j+c_j)L\cos(\alpha-\phi)+2(a_i-c_i)L\sin(\alpha-\phi)-2hL\cos(\phi)$$
$$-2x_{cstic}L\sin(\phi)-2h(a_j+c_j)\cos(\alpha)-2x_{cstic}(a_j+c_j)\sin(\alpha)$$
$$-2h(a_i-c_i)\sin(\alpha))^{0.5} \quad (5.28)$$

$$
\begin{aligned}
r_B &= (h^2 + x_{cstic}^2 + (b_i + c_i)^2 + (b_j + c_j)^2 + L^2 + 2h(b_i + c_i)\sin(\alpha) \\
&\quad +2(b_j + c_j)L\cos(\alpha - \phi) - 2hL\cos(\phi) - 2x_{cstic}L\sin(\phi) - 2h(b_j + c_j)\cos(\alpha) \\
&\quad -2x_{cstic}(b_i + c_i)\cos(\alpha) - 2x_{cstic}(b_j + c_j)\sin(\alpha) - 2(b_i + c_i)L\sin(\alpha - \phi))^{0.5} \quad (5.29)
\end{aligned}
$$

The forces needed to determine mode transitions are given by:

$$
\begin{aligned}
f &= T_B(x_{cstic} - L\sin(\phi) - (b_i + c_i)\cos(\alpha) - (b_j + c_j)\sin(\alpha))/r_B + m_P((c_i\cos(\alpha) \\
&\quad +c_j\sin(\alpha))\dot{\alpha}^2 + (c_i\sin(\alpha) - c_j\cos(\alpha))\ddot{\alpha}) - T_A(L\sin(\phi) + (a_j + c_j)\sin(\alpha) \\
&\quad -x_{cstic} - (a_i - c_i)\cos(\alpha))/r_A \quad (5.30) \\
N &= gm_P + m_P((c_i\sin(\alpha) - c_j\cos(\alpha))\dot{\alpha}^2 - (c_i\cos(\alpha) + c_j\sin(\alpha))\ddot{\alpha}) \\
&\quad -T_B(h + (b_i + c_i)\sin(\alpha) - L\cos(\phi) - (b_j + c_j)\cos(\alpha))/r_B \\
&\quad -T_A(h - L\cos(\phi) - (a_j + c_j)\cos(\alpha) - (a_i - c_i)\sin(\alpha))/r_A, \quad (5.31)
\end{aligned}
$$

and the motion of P's COM is given by:

$$
\begin{aligned}
x &= x_{cstic} - c_i\cos(\alpha) - c_j\sin(\alpha) \quad (5.32) \\
\dot{x} &= c_i\sin(\alpha)\dot{\alpha} - c_j\cos(\alpha)\dot{\alpha} \quad (5.33) \\
y &= c_j\cos(\alpha) - c_i\sin(\alpha) \quad (5.34) \\
\dot{y} &= -c_i\cos(\alpha)\dot{\alpha} - c_j\sin(\alpha)\dot{\alpha} \quad (5.35)
\end{aligned}
$$

5.3.3 Stiction on D

Stiction on corner D is very similar to stiction on C. The differential equations describing motion are:

$$
\begin{aligned}
\ddot{\phi} &= (x_{dstic}\cos(\phi)(T_A/r_A + T_B/r_B) + \cos(\alpha - \phi)((a_i + d_i)T_A/r_A - (b_i - d_i)T_B/r_B) \\
&\quad -\sin(\phi)(gm_H + h(T_A/r_A + T_B/r_B)) - \sin(\alpha - \phi)((a_j + d_j)T_A/r_A \\
&\quad +(b_j + d_j)T_B/r_B) - 2m_H\dot{L}\dot{\phi})/(m_H L) \quad (5.36) \\
\ddot{\alpha} &= -(gm_P(d_i\cos(\alpha) - d_j\sin(\alpha)) + T_A(h(a_j + d_j)\sin(\alpha) + (a_i + d_i)L\cos(\alpha - \phi) \\
&\quad -h(a_i + d_i)\cos(\alpha) - x_{dstic}(a_i + d_i)\sin(\alpha) - x_{dstic}(a_j + d_j)\cos(\alpha) \\
&\quad -(a_j + d_j)L\sin(\alpha - \phi))/r_A + T_B(h(b_j + d_j)\sin(\alpha) + h(b_i - d_i)\cos(\alpha) \\
&\quad +x_{dstic}(b_i - d_i)\sin(\alpha) - x_{dstic}(b_j + d_j)\cos(\alpha) - (b_j + d_j)L\sin(\alpha - \phi) \\
&\quad -(b_i - d_i)L\cos(\alpha - \phi))/r_B)/(I + m_P(d_i^2 + d_j^2)) \quad (5.37)
\end{aligned}
$$

where x_{dstic} is the horizontal position of corner D on the ground, and r_A and r_B are given by:

$$
\begin{aligned}
r_A &= (h^2 + x_{dstic}^2 + (a_i + d_i)^2 + (a_j + d_j)^2 + L^2 + 2x_{dstic}(a_i + d_i)\cos(\alpha) \\
&\quad +2(a_i + d_i)L\sin(\alpha - \phi) + 2(a_j + d_j)L\cos(\alpha - \phi) - 2hL\cos(\phi) - 2x_{dstic}L\sin(\phi) \\
&\quad -2h(a_i + d_i)\sin(\alpha) - 2h(a_j + d_j)\cos(\alpha) - 2x_{dstic}(a_j + d_j)\sin(\alpha))^{0.5} \quad (5.38) \\
r_B &= (h^2 + x_{dstic}^2 + (b_j + d_j)^2 + (b_i - d_i)^2 + L^2 + 2h(b_i - d_i)\sin(\alpha) \\
&\quad +2(b_j + d_j)L\cos(\alpha - \phi) - 2hL\cos(\phi) - 2x_{dstic}L\sin(\phi) - 2h(b_j + d_j)\cos(\alpha) \\
&\quad -2x_{dstic}(b_j + d_j)\sin(\alpha) - 2x_{dstic}(b_i - d_i)\cos(\alpha) \\
&\quad -2(b_i - d_i)L\sin(\alpha - \phi))^{0.5} \quad (5.39)
\end{aligned}
$$

The forces needed to determine mode transitions are given by:

$$
\begin{aligned}
f &= T_A(x_{dstic} + (a_i + d_i)\cos(\alpha) - L\sin(\phi) - (a_j + d_j)\sin(\alpha))/r_A \\
&\quad +T_B(x_{dstic} - L\sin(\phi) - (b_j + d_j)\sin(\alpha) - (b_i - d_i)\cos(\alpha))/r_B \\
&\quad -m_P((d_i\cos(\alpha) - d_j\sin(\alpha))\dot{\alpha}^2 + (d_i\sin(\alpha) + d_j\cos(\alpha))\ddot{\alpha}) \quad (5.40)
\end{aligned}
$$

$$
\begin{aligned}
N &= gm_P + T_B(L\cos(\phi) + (b_j + d_j)\cos(\alpha) - h - (b_i - d_i)\sin(\alpha))/r_B \\
&\quad -T_A(h - L\cos(\phi) - (a_i + d_i)\sin(\alpha) - (a_j + d_j)\cos(\alpha))/r_A \\
&\quad -m_P((d_i\sin(\alpha) + d_j\cos(\alpha))\dot{\alpha}^2 - (d_i\cos(\alpha) - d_j\sin(\alpha))\ddot{\alpha}) \qquad (5.41)
\end{aligned}
$$

and the motion of the payload's COM is given by:

$$
\begin{aligned}
x &= x_{dstic} + d_i\cos(\alpha) - d_j\sin(\alpha) \qquad (5.42)\\
\dot{x} &= -d_i\sin(\alpha)\dot{\alpha} - d_j\cos(\alpha)\dot{\alpha} \qquad (5.43)\\
y &= d_i\sin(\alpha) + d_j\cos(\alpha) \qquad (5.44)\\
\dot{y} &= d_i\cos(\alpha)\dot{\alpha} - d_j\sin(\alpha)\dot{\alpha} \qquad (5.45)
\end{aligned}
$$

5.3.4 Planar Sliding

When the payload experiences planar sliding, it translates horizontally across the ground. It has two degrees of freedom, ϕ and x. The differential equations of motion are:

$$
\begin{aligned}
\ddot{\phi} &= (x\cos(\phi)(T_A/r_A + T_B/r_B) + \sin(\phi)(a_jT_A/r_A + b_jT_B/r_B) + \cos(\phi)(a_iT_A/r_A \\
&\quad -b_iT_B/r_B) - \sin(\phi)(gm_H - (d_j - h)(T_A/r_A + T_B/r_B)) - 2m_H\dot{L}\dot{\phi})/(m_HL) \qquad (5.46)\\
\ddot{x} &= (f - T_A(a_i + x - L\sin(\phi))/r_A - T_B(x - b_i - L\sin(\phi))/r_B)/m_P \qquad (5.47)
\end{aligned}
$$

where r_A and r_B are given by:

$$
\begin{aligned}
r_A &= (a_i^2 + a_j^2 + (d_j - h)^2 + 2a_j(d_j - h) + L^2 + x^2 + 2a_ix + 2a_jL\cos(\phi) \\
&\quad +2(d_j - h)L\cos(\phi) - 2a_iL\sin(\phi) - 2Lx\sin(\phi))^{0.5} \qquad (5.48)\\
r_B &= (b_i^2 + b_j^2 + (d_j - h)^2 + 2b_j(d_j - h) + L^2 + x^2 + 2b_iL\sin(\phi) + 2b_jL\cos(\phi) \\
&\quad +2(d_j - h)L\cos(\phi) - 2b_ix - 2Lx\sin(\phi))^{0.5} \qquad (5.49)
\end{aligned}
$$

The forces and d_N needed to determine mode transitions are given by:

$$
\begin{aligned}
N &= gm_P - T_A(h - a_j - d_j - L\cos(\phi))/r_A - T_B(h - b_j - d_j - L\cos(\phi))/r_B \qquad (5.50)\\
f &= \mu_K N \qquad (5.51)\\
d_N &= (-d_jf - T_B(b_i(d_j - h) + b_jx + b_iL\cos(\phi) - b_jL\sin(\phi))/r_B - T_A(a_jx \\
&\quad -a_i(d_j - h) - a_iL\cos(\phi) - a_jL\sin(\phi))/r_A)/N \qquad (5.52)
\end{aligned}
$$

Note that $y = c_j$ and $\dot{y} = \alpha = \dot{\alpha} = 0$ in this mode.

5.3.5 Sliding on C

When the payload is sliding on corner C, the situation is similar to planar sliding; however there is an added degree of freedom in rotation. The differential equations of motion are:

$$
\begin{aligned}
\ddot{\phi} &= (x\cos(\phi)(T_A/r_A + T_B/r_B) + \cos(\alpha - \phi)(a_iT_A/r_A - b_iT_B/r_B) \\
&\quad -\sin(\alpha - \phi)(a_jT_A/r_A + b_jT_B/r_B) - \sin(\phi)(gm_H + (h - y)(T_A/r_A + T_B/r_B)) \\
&\quad -2m_H\dot{L}\dot{\phi})/(m_HL) \qquad (5.53)
\end{aligned}
$$

$$
\begin{aligned}
\ddot{\alpha} &= (gm_P(c_i\cos(\alpha)+c_j\sin(\alpha))+T_A(a_ix\sin(\alpha)+a_jx\cos(\alpha)+a_jL\sin(\alpha-\phi)\\
&+a_i\cos(\alpha)(h-y)+a_i\sin(\alpha)(c_i\cos(\alpha)+c_j\sin(\alpha))+a_j\cos(\alpha)(c_i\cos(\alpha)+c_j\sin(\alpha))\\
&+L\cos(\phi)(c_i\cos(\alpha)+c_j\sin(\alpha))-a_iL\cos(\alpha-\phi)-a_j\sin(\alpha)(h-y)-(h-y)(c_i\cos(\alpha)\\
&+c_j\sin(\alpha)))/r_A+T_B(b_jx\cos(\alpha)+b_iL\cos(\alpha-\phi)+b_jL\sin(\alpha-\phi)+b_j\cos(\alpha)(c_i\cos(\alpha)\\
&+c_j\sin(\alpha))+L\cos(\phi)(c_i\cos(\alpha)+c_j\sin(\alpha))-b_ix\sin(\alpha)-b_i\cos(\alpha)(h-y)\\
&-b_j\sin(\alpha)(h-y)-b_i\sin(\alpha)(c_i\cos(\alpha)+c_j\sin(\alpha))-(h-y)(c_i\cos(\alpha)+c_j\sin(\alpha)))/r_B\\
&+m_P(c_i\cos(\alpha)+c_j\sin(\alpha))(c_i\sin(\alpha)-c_j\cos(\alpha))\dot{\alpha}^2+\mu_K(c_i\sin(\alpha)-c_j\cos(\alpha))(T_B(h\\
&+b_i\sin(\alpha)-y-b_j\cos(\alpha)-L\cos(\phi))/r_B+T_A(h-y-a_i\sin(\alpha)-a_j\cos(\alpha)\\
&-L\cos(\phi))/r_A-gm_P-m_P(c_i\sin(\alpha)-c_j\cos(\alpha))\dot{\alpha}^2))/(I+m_P(c_i\cos(\alpha)+c_j\sin(\alpha))^2\\
&-m_P\mu_K(c_i\cos(\alpha)+c_j\sin(\alpha))(c_i\sin(\alpha)-c_j\cos(\alpha))) \qquad (5.54)
\end{aligned}
$$

$$
\begin{aligned}
\ddot{x} &= -(T_A(x+a_i\cos(\alpha)-a_j\sin(\alpha)-L\sin(\phi))/r_A+T_B(x-b_i\cos(\alpha)-b_j\sin(\alpha)\\
&-L\sin(\phi))/r_B+\mu_K(T_B(h+b_i\sin(\alpha)-y-b_j\cos(\alpha)-L\cos(\phi))/r_B+T_A(h-y\\
&-a_i\sin(\alpha)-a_j\cos(\alpha)-L\cos(\phi))/r_A-gm_P-m_P(c_i\sin(\alpha)-c_j\cos(\alpha))\dot{\alpha}^2))/m_P\\
&-\mu_K(c_i\cos(\alpha)+c_j\sin(\alpha))(gm_P(c_i\cos(\alpha)+c_j\sin(\alpha))+T_A(a_ix\sin(\alpha)+a_jx\cos(\alpha)\\
&+a_jL\sin(\alpha-\phi)+a_i\cos(\alpha)(h-y)+a_i\sin(\alpha)(c_i\cos(\alpha)+c_j\sin(\alpha))\\
&+a_j\cos(\alpha)(c_i\cos(\alpha)+c_j\sin(\alpha))+L\cos(\phi)(c_i\cos(\alpha)+c_j\sin(\alpha))-a_iL\cos(\alpha-\phi)\\
&-a_j\sin(\alpha)(h-y)-(h-y)(c_i\cos(\alpha)+c_j\sin(\alpha)))/r_A+T_B(b_jx\cos(\alpha)+b_iL\cos(\alpha-\phi)\\
&+b_jL\sin(\alpha-\phi)+b_j\cos(\alpha)(c_i\cos(\alpha)+c_j\sin(\alpha))+L\cos(\phi)(c_i\cos(\alpha)+c_j\sin(\alpha))\\
&-b_ix\sin(\alpha)-b_i\cos(\alpha)(h-y)-b_j\sin(\alpha)(h-y)-b_i\sin(\alpha)(c_i\cos(\alpha)+c_j\sin(\alpha))\\
&-(h-y)(c_i\cos(\alpha)+c_j\sin(\alpha)))/r_B+m_P(c_i\cos(\alpha)+c_j\sin(\alpha))(c_i\sin(\alpha)-c_j\cos(\alpha))\dot{\alpha}^2\\
&+\mu_K(c_i\sin(\alpha)-c_j\cos(\alpha))(T_B(h+b_i\sin(\alpha)-y-b_j\cos(\alpha)-L\cos(\phi))/r_B+T_A(h\\
&-y-a_i\sin(\alpha)-a_j\cos(\alpha)-L\cos(\phi))/r_A-gm_P-m_P(c_i\sin(\alpha)-c_j\cos(\alpha))\dot{\alpha}^2))/(I\\
&+m_P(c_i\cos(\alpha)+c_j\sin(\alpha))^2-m_P\mu_K(c_i\cos(\alpha)+c_j\sin(\alpha))(c_i\sin(\alpha)-c_j\cos(\alpha))) \qquad (5.55)
\end{aligned}
$$

where r_A and r_B are given by:

$$
\begin{aligned}
r_A &= (a_i^2+a_j^2+L^2+x^2+(h-y)^2+2a_ix\cos(\alpha)+2a_iL\sin(\alpha-\phi)\\
&+2a_jL\cos(\alpha-\phi)-2a_jx\sin(\alpha)-2Lx\sin(\phi)-2a_i\sin(\alpha)(h-y)\\
&-2a_j\cos(\alpha)(h-y)-2L\cos(\phi)(h-y))^{0.5} \qquad (5.56)\\
r_B &= (b_i^2+b_j^2+L^2+x^2+(h-y)^2+2b_jL\cos(\alpha-\phi)+2b_i\sin(\alpha)(h-y)\\
&-2b_ix\cos(\alpha)-2b_jx\sin(\alpha)-2Lx\sin(\phi)-2b_iL\sin(\alpha-\phi)\\
&-2b_j\cos(\alpha)(h-y)-2L\cos(\phi)(h-y))^{0.5} \qquad (5.57)
\end{aligned}
$$

The forces needed to determine mode transitions are given by:

$$
\begin{aligned}
N &= gm_P+m_P((c_i\sin(\alpha)-c_j\cos(\alpha))\dot{\alpha}^2-(c_i\cos(\alpha)+c_j\sin(\alpha))\ddot{\alpha})\\
&-T_B(h+b_i\sin(\alpha)-y-b_j\cos(\alpha)-L\cos(\phi))/r_B\\
&-T_A(h-y-a_i\sin(\alpha)-a_j\cos(\alpha)-L\cos(\phi))/r_A \qquad (5.58)\\
f &= \mu_KN \qquad (5.59)
\end{aligned}
$$

The vertical motion of the payload's COM is:

$$
\begin{aligned}
y &= c_j\cos(\alpha)-c_i\sin(\alpha) \qquad (5.60)\\
\dot{y} &= -(c_i\cos(\alpha)+c_j\sin(\alpha))\dot{\alpha} \qquad (5.61)
\end{aligned}
$$

5.3.6 Sliding on D

Sliding on corner D is similar to sliding on C. The differential equations of motion are:

$$\begin{aligned}\ddot{\phi} &= (x\cos(\phi)(T_A/r_A + T_B/r_B) + \cos(\alpha-\phi)(a_iT_A/r_A - b_iT_B/r_B)\\ &\quad -\sin(\alpha-\phi)(a_jT_A/r_A + b_jT_B/r_B) - \sin(\phi)(gm_H + (h-y)(T_A/r_A + T_B/r_B))\\ &\quad -2m_H\dot{L}\dot{\phi})/(m_HL) \qquad (5.62)\end{aligned}$$

$$\begin{aligned}\ddot{\alpha} &= -(gm_P(d_i\cos(\alpha) - d_j\sin(\alpha)) + T_A(a_iL\cos(\alpha-\phi) + a_j\sin(\alpha)(h-y)\\ &\quad +a_i\sin(\alpha)(d_i\cos(\alpha) - d_j\sin(\alpha)) + a_j\cos(\alpha)(d_i\cos(\alpha) - d_j\sin(\alpha)) + L\cos(\phi)(d_i\cos(\alpha)\\ &\quad -d_j\sin(\alpha)) - a_ix\sin(\alpha) - a_jx\cos(\alpha) - a_jL\sin(\alpha-\phi) - a_i\cos(\alpha)(h-y)\\ &\quad -(h-y)(d_i\cos(\alpha) - d_j\sin(\alpha)))/r_A + T_B(b_ix\sin(\alpha) + b_i\cos(\alpha)(h-y)\\ &\quad +b_j\sin(\alpha)(h-y) + b_j\cos(\alpha)(d_i\cos(\alpha) - d_j\sin(\alpha)) + L\cos(\phi)(d_i\cos(\alpha) - d_j\sin(\alpha))\\ &\quad -b_jx\cos(\alpha) - b_iL\cos(\alpha-\phi) - b_jL\sin(\alpha-\phi) - b_i\sin(\alpha)(d_i\cos(\alpha) - d_j\sin(\alpha))\\ &\quad -(h-y)(d_i\cos(\alpha) - d_j\sin(\alpha)))/r_B - m_P(d_i\sin(\alpha) + d_j\cos(\alpha))(d_i\cos(\alpha) - d_j\sin(\alpha))\dot{\alpha}^2\\ &\quad -\mu_K(d_i\sin(\alpha) + d_j\cos(\alpha))(gm_P - T_B(h + b_i\sin(\alpha) - y - b_j\cos(\alpha) - L\cos(\phi))/r_B\\ &\quad -T_A(h - y - a_i\sin(\alpha) - a_j\cos(\alpha) - L\cos(\phi))/r_A - m_P(d_i\sin(\alpha) + d_j\cos(\alpha))\dot{\alpha}^2))/(I\\ &\quad +m_P(d_i\cos(\alpha) - d_j\sin(\alpha))^2 - m_P\mu_K(d_i\sin(\alpha) + d_j\cos(\alpha))(d_i\cos(\alpha) - d_j\sin(\alpha))) \qquad (5.63)\end{aligned}$$

$$\begin{aligned}\ddot{x} &= -(T_A(x + a_i\cos(\alpha) - a_j\sin(\alpha) - L\sin(\phi))/r_A + T_B(x - b_i\cos(\alpha) - b_j\sin(\alpha)\\ &\quad -L\sin(\phi))/r_B - \mu_K(gm_P - T_B(h + b_i\sin(\alpha) - y - b_j\cos(\alpha) - L\cos(\phi))/r_B\\ &\quad -T_A(h - y - a_i\sin(\alpha) - a_j\cos(\alpha) - L\cos(\phi))/r_A - m_P(d_i\sin(\alpha) + d_j\cos(\alpha))\dot{\alpha}^2))/m_P\\ &\quad -\mu_K(d_i\cos(\alpha) - d_j\sin(\alpha))(gm_P(d_i\cos(\alpha) - d_j\sin(\alpha)) + T_A(a_iL\cos(\alpha-\phi)\\ &\quad +a_j\sin(\alpha)(h-y) + a_i\sin(\alpha)(d_i\cos(\alpha) - d_j\sin(\alpha)) + a_j\cos(\alpha)(d_i\cos(\alpha) - d_j\sin(\alpha))\\ &\quad +L\cos(\phi)(d_i\cos(\alpha) - d_j\sin(\alpha)) - a_ix\sin(\alpha) - a_jx\cos(\alpha) - a_jL\sin(\alpha-\phi)\\ &\quad -a_i\cos(\alpha)(h-y) - (h-y)(d_i\cos(\alpha) - d_j\sin(\alpha)))/r_A + T_B(b_ix\sin(\alpha)\\ &\quad +b_i\cos(\alpha)(h-y) + b_j\sin(\alpha)(h-y) + b_j\cos(\alpha)(d_i\cos(\alpha) - d_j\sin(\alpha))\\ &\quad +L\cos(\phi)(d_i\cos(\alpha) - d_j\sin(\alpha)) - b_jx\cos(\alpha) - b_iL\cos(\alpha-\phi) - b_jL\sin(\alpha-\phi)\\ &\quad -b_i\sin(\alpha)(d_i\cos(\alpha) - d_j\sin(\alpha)) - (h-y)(d_i\cos(\alpha) - d_j\sin(\alpha)))/r_B - m_P(d_i\sin(\alpha)\\ &\quad +d_j\cos(\alpha))(d_i\cos(\alpha) - d_j\sin(\alpha))\dot{\alpha}^2 - \mu_K(d_i\sin(\alpha) + d_j\cos(\alpha))(gm_P - T_B(h + b_i\sin(\alpha)\\ &\quad -y - b_j\cos(\alpha) - L\cos(\phi))/r_B - T_A(h - y - a_i\sin(\alpha) - a_j\cos(\alpha) - L\cos(\phi))/r_A\\ &\quad -m_P(d_i\sin(\alpha) + d_j\cos(\alpha))\dot{\alpha}^2))/(I + m_P(d_i\cos(\alpha) - d_j\sin(\alpha))^2 - m_P\mu_K(d_i\sin(\alpha)\\ &\quad +d_j\cos(\alpha))(d_i\cos(\alpha) - d_j\sin(\alpha))) \qquad (5.64)\end{aligned}$$

where r_A and r_B are given by:

$$\begin{aligned}r_A &= (a_i^2 + a_j^2 + L^2 + x^2 + (h-y)^2 + 2a_ix\cos(\alpha) + 2a_iL\sin(\alpha-\phi)\\ &\quad +2a_jL\cos(\alpha-\phi) - 2a_jx\sin(\alpha) - 2Lx\sin(\phi) - 2a_i\sin(\alpha)(h-y)\\ &\quad -2a_j\cos(\alpha)(h-y) - 2L\cos(\phi)(h-y))^{0.5} \qquad (5.65)\\ r_B &= (b_i^2 + b_j^2 + L^2 + x^2 + (h-y)^2 + 2b_jL\cos(\alpha-\phi) + 2b_i\sin(\alpha)(h-y)\\ &\quad -2b_ix\cos(\alpha) - 2b_jx\sin(\alpha) - 2Lx\sin(\phi) - 2b_iL\sin(\alpha-\phi)\\ &\quad -2b_j\cos(\alpha)(h-y) - 2L\cos(\phi)(h-y))^{0.5} \qquad (5.66)\end{aligned}$$

The forces needed to determine mode transitions are given by:

$$\begin{aligned}N &= gm_P - T_B(h + b_i\sin(\alpha) - y - b_j\cos(\alpha) - L\cos(\phi))/r_B\\ &\quad -T_A(h - y - a_i\sin(\alpha) - a_j\cos(\alpha) - L\cos(\phi))/r_A - m_P((d_i\sin(\alpha)\\ &\quad +d_j\cos(\alpha))\dot{\alpha}^2 - (d_i\cos(\alpha) - d_j\sin(\alpha))\ddot{\alpha}) \qquad (5.67)\end{aligned}$$

$$f = \mu_K N \tag{5.68}$$

The vertical motion of the payload's COM is:

$$y = d_i \sin(\alpha) + d_j \cos(\alpha) \tag{5.69}$$
$$\dot{y} = (d_i \cos(\alpha) - d_j \sin(\alpha))\dot{\alpha} \tag{5.70}$$

5.3.7 Swinging

There are four degrees of freedom in the swinging mode. The differential equations of motion are:

$$\begin{aligned}\ddot{\phi} = {} & (x\cos(\phi)(T_A/r_A + T_B/r_B) + \cos(\alpha-\phi)(a_i T_A/r_A - b_i T_B/r_B) \\ & - \sin(\alpha-\phi)(a_j T_A/r_A + b_j T_B/r_B) - \sin(\phi)(g m_H + (h-y)(T_A/r_A + T_B/r_B)) \\ & -2m_H \dot{L}\dot{\phi})/(m_H L)\end{aligned} \tag{5.71}$$

$$\begin{aligned}\ddot{\alpha} = {} & (T_A(a_i x\sin(\alpha) + a_j x\cos(\alpha) + a_j L\sin(\alpha-\phi) + a_i\cos(\alpha)(h-y) - a_i L\cos(\alpha-\phi) \\ & -a_j\sin(\alpha)(h-y))/r_A + T_B(b_j x\cos(\alpha) + b_i L\cos(\alpha-\phi) + b_j L\sin(\alpha-\phi) \\ & -b_i x\sin(\alpha) - b_i\cos(\alpha)(h-y) - b_j\sin(\alpha)(h-y))/r_B)/I\end{aligned} \tag{5.72}$$

$$\begin{aligned}\ddot{x} = {} & -(T_A(x + a_i\cos(\alpha) - a_j\sin(\alpha) - L\sin(\phi))/r_A + T_B(x - b_i\cos(\alpha) - b_j\sin(\alpha) \\ & -L\sin(\phi))/r_B)/m_P\end{aligned} \tag{5.73}$$

$$\begin{aligned}\ddot{y} = {} & (T_B(h + b_i\sin(\alpha) - y - b_j\cos(\alpha) - L\cos(\phi))/r_B + T_A(h - y - a_i\sin(\alpha) \\ & -a_j\cos(\alpha) - L\cos(\phi))/r_A)/m_P - g\end{aligned} \tag{5.74}$$

where r_A and r_B are given by:

$$\begin{aligned}r_A = {} & (a_i^2 + a_j^2 + L^2 + x^2 + (h-y)^2 + 2a_i x\cos(\alpha) + 2a_i L\sin(\alpha-\phi) + 2a_j L\cos(\alpha-\phi) \\ & -2a_j x\sin(\alpha) - 2Lx\sin(\phi) - 2a_i\sin(\alpha)(h-y) - 2a_j\cos(\alpha)(h-y) \\ & -2L\cos(\phi)(h-y))^{0.5}\end{aligned} \tag{5.75}$$

$$\begin{aligned}r_B = {} & (b_i^2 + b_j^2 + L^2 + x^2 + (h-y)^2 + 2b_j L\cos(\alpha-\phi) + 2b_i\sin(\alpha)(h-y) - 2b_i x\cos(\alpha) \\ & -2b_j x\sin(\alpha) - 2Lx\sin(\phi) - 2b_i L\sin(\alpha-\phi) - 2b_j\cos(\alpha)(h-y) \\ & -2L\cos(\phi)(h-y))^{0.5}\end{aligned} \tag{5.76}$$

5.4 Model Verifications

The models presented in Sections 5.2 and 5.3 were simulated in Matlab and then verified by experiments on the HiBay crane. The differential equations describing the dynamics were numerically integrated using `ode45`. The most difficult part of the simulation effort was correctly detecting transitions between modes. This was achieved using the `events` function, which detects zero-crossings and terminates ODE integration.

However, as `events` can only detect when values cross zero, transitions can be erroneously reported/undetected in certain cases, such as when a value initializes at zero in the beginning of a mode. For example, the velocity, $\dot{x}$, is initially zero after it transitions from stiction to sliding. The solution is to add or subtract `eps` (the smallest difference between two numbers that Matlab can detect) to the value, and intelligently detect the direction of zero-crossing. That way, values never initialize at zero and are guaranteed to be triggered by zero-crossings that occur in the correct direction.

As only 1-D sliding cases are examined here (as opposed to general planar sliding examined in [60]), friction can only be in the $+i$ or $-i$ directions. The direction of the friction force is determined by the following: a) if transitioning from swinging or other sliding modes, then the friction force direction will be opposite to the direction of the impending contact point's velocity prior to the

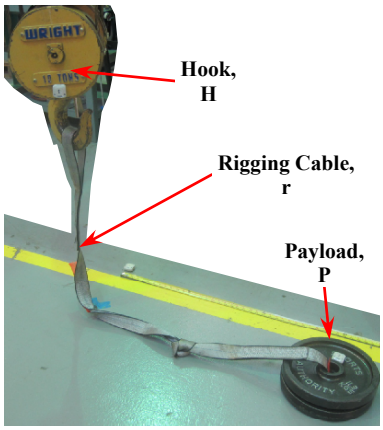

Figure 5.10: Weight Plates Payload Experimental Setup

Table 5.1: Point-Mass Payload Experimental Parameter Values

Parameter	Value(s)	Parameter	Value(s)
m_H (kg)	59	m_P (kg)	11.3, 22.7, 34.0, 45.4
h (m)	6.37	x_{init} (m)	0.3, 0.6, 0.9, 1.2
r_U (m)	1.65	K_r (N/m)	924000
μ_S	0.33	μ_K	0.28
$\dot{L}$ (m/s)	-0.117		

transition; b) if transitioning from stiction modes, then the friction force direction is the same as that of the stiction friction prior to the transition.

The following sections detail the experimental setups. Despite sensor limitations, the experimental results generally matched quite well with the simulations.

5.4.1 Point-Mass Hook and Point-Mass Payload

Figure 5.10 shows the experimental setup and components corresponding to various parts of the model. The parameters for the experiment are listed in Table 5.1. Stacks of 25lbs (11.3kg) weight plates were used to approximate point-mass payloads. The payload was attached to the hook by a standard 2" wide polyester lifting straps (rigging cable). The payload was placed on the ground, off-centered from the trolley by various distances (approximately, $x_{init} = 0.3, 0.6, 0.9, 1.2$ meters). Then, the hook was hoisted at a constant velocity until the payload was no longer touching the ground. The positions of the hook and payload were recorded by a combination of a trolley-mounted camera and 3-D radio frequency tag location system.

Figure 5.11 shows the experimental and simulated horizontal deflections of the hook and a 50lbs payload, when the trolley was off centered by 1.2m. Clearly, the simulations match quite well with the experimental data. The period of oscillations were accurately predicted by the simulations. However, the simulations tended to overestimate the amplitude (by around 0.15m) of oscillations for the cases shown here. There are two main sources of experimental error: 1) The stacked plates have real dimensions (each are 12" diameter and 1.5" thick) and are not point-masses. This means the plates do not have point-contact with the ground, and behave more closely to the rigid-body model, which can tip and slide on the edges. This behavior allows the plates to maintain physical contact with the ground for longer durations, thereby reducing the amplitude of swing in the air. 2) The RF-tag location system is only accurate to approximately $\pm$ 0.15m. Figures 5.12 and 5.13 show similar results for the 75 and 100lbs payloads off-centered by 1.2m.

Figure 5.14 compares the swing amplitudes between simulation and experimental results for all

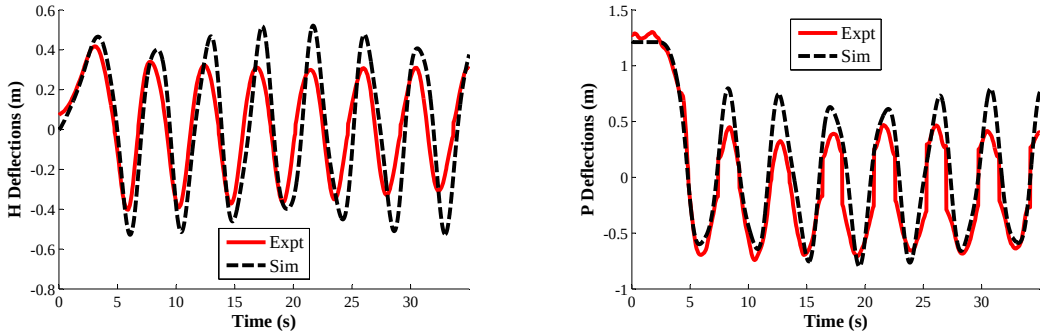

(a) Hook (b) Payload

Figure 5.11: Lift-Up of Point-Mass Payload [m_P = 50lbs, x_{init}=1.2m]

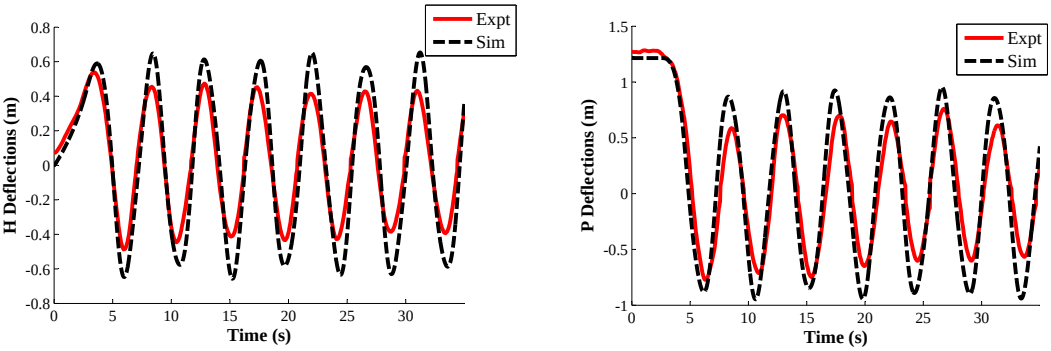

(a) Hook (b) Payload

Figure 5.12: Lift-Up of Point-Mass Payload [m_P = 75lbs, x_{init}=1.2m]

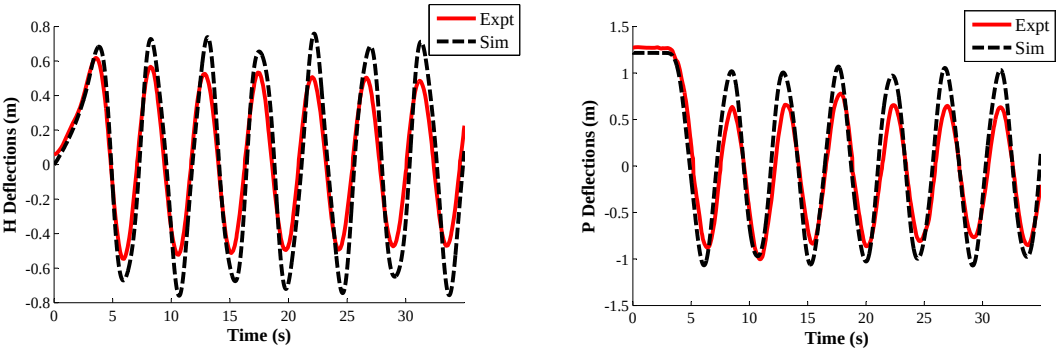

(a) Hook (b) Payload

Figure 5.13: Lift-Up of Point-Mass Payload [m_P = 100lbs, x_{init}=1.2m]

tested cases. The simulation results generally follow that of the experiments. Obviously, larger x_{init} results in larger swing amplitudes. Given the small offset of $x_{init} = 0.3m$, all payloads regardless of weight lifted off the ground at the starting position, without sliding. This is the reason why the simulations predicted swing amplitudes that are close to $x_{init} = 0.3m$. The experimental results showed swing amplitudes that were slightly larger than x_{init}. This is most likely due to sensor noise

Table 5.2: Plastic-Box Payload Experimental Parameter Values

Parameter	Value(s)	Parameter	Value(s)
m_H (kg)	59	m_P (kg)	68.0
h (m)	6.37	x_{init} (m)	0.6, 0.9, 1.2
r_U (m)	0.787	K_r (N/m)	2903225
μ_S	0.37	μ_K	0.33
$\dot{L}$ (m/s)	-0.117	I (kg m^2)	2.51
$a_i = b_i = c_i = d_i$ (m)	0.65	$a_j = b_j = c_j = d_j$ (m)	0.38

and model simplifications.

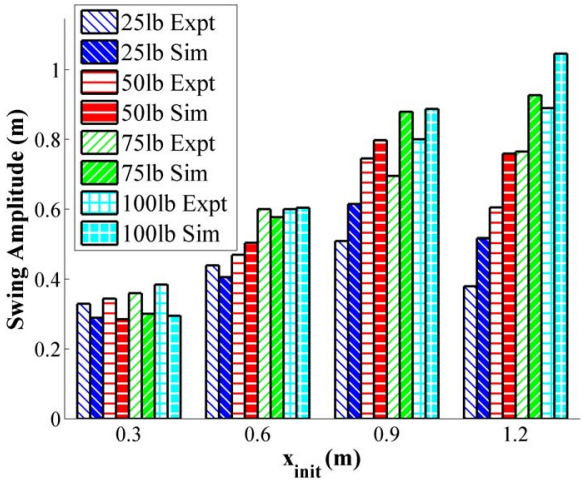

Figure 5.14: Summary of Swing Amplitudes, Experimental vs. Simulated

As x_{init} increased to 0.6m, only the heavier 75 and 100lbs payloads had swing amplitudes that were close to x_{init} - this indicates no sliding occurred. The lighter 25lb and 50lbs payloads had swing amplitudes that were noticeably less than the value of x_{init}, which indicates sliding occurred before the payload lifted off the ground. When x_{init} increases further to 1.2m, all payloads slid before lifting off. The lighter payloads slid more than the heavier payloads. The average discrepancy between the simulation and experimental swing amplitudes for all cases tested was 15.8%.

5.4.2 Point-Mass Hook and Rigid-Body Payload

Two payloads, a black plastic box and a large wooden box, were used to verify the point-mass hook and rigid-body payload model. Figure 5.15 shows the experimental setups for both payloads. For the black-box, r_A and r_B are each represented by two segments of 3" wide lifting straps. For the wooden-box, the rigging attachment points on the payload, A and B, are not on the edge of the box. Instead, they are approximately 7" towards the payload center. Additionally, the RF tags used to track the payload position were mounted at points A' and B', which are on box edges. Tables 5.2 and 5.3 list the parameter values for the plastic-box and wooden-box experiments, respectively.

Figure 5.16 shows the experimental and simulation results for the horizontal deflections of H, points A and B, for the black-box payload off-centered by x_{init}=0.6m. The plots clearly show that the experimental results were accurately predicted by simulations. The motions of points A and B match the simulation predictions especially well. Figures 5.17 and 5.18 show the simulated and experimental data for x_{init}=0.9m and 1.2m, respectively.

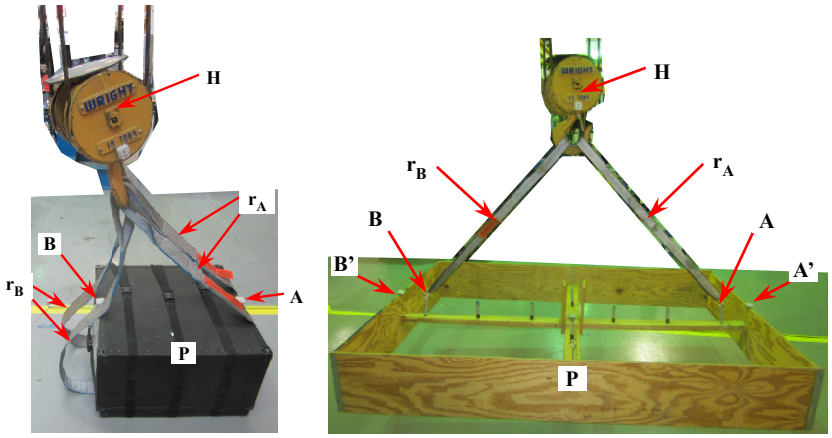

(a) Plastic-Box (b) Wooden-Box

Figure 5.15: Rigid-Body Payload Experimental Setups

Table 5.3: Wooden-Box Payload Experimental Parameter Values

Parameter	Value(s)	Parameter	Value(s)
m_H (kg)	59	m_P (kg)	33.6
h (m)	6.37	x_{init} (m)	0.6, 0.9, 1.2
r_U (m)	1.22	K_r (N/m)	1250000
μ_S	0.34	μ_K	0.24
$\dot{L}$ (m/s)	-0.117	I (kg m^2)	40.09
$a'_i = b'_i = c_i = d_i$ (m)	1.08	$a'_j = a_j = b'_j = b_j = c_j = d_j$ (m)	0.146
$a_i = b_i$ (m)	0.902		

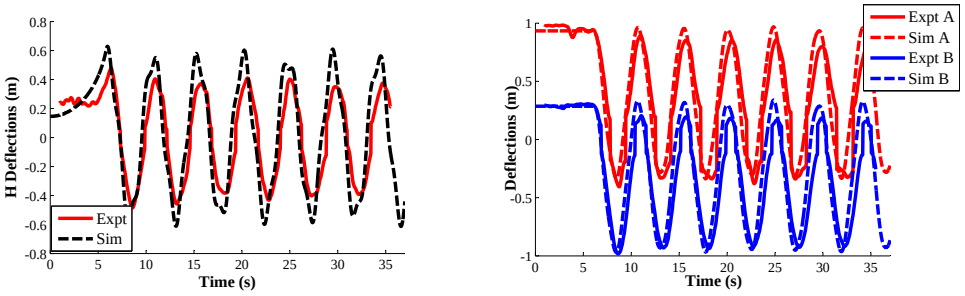

(a) Hook (b) Payload Sides A & B

Figure 5.16: Lift-Up of Plastic-Box Payload [x_{init}=0.6m]

Simulations were less accurate in predicting the hook positions. This can be attributed to two model assumptions that deviate from the experiments: 1) The hook is not physically a point mass - it consists of a sheave block and the hook itself. 2) The arrangement of the hoist cables in the sheave block is more similar to two cables wrapped around two pulleys (which can be seen in Figure 5.15), rather than a single hoist cable attached to a point mass, as in Figure 5.6.

Furthermore, in the experimental cases shown here, due to the payload offsets, the hook does not begin at 0 deflection. Instead, the hook is pulled by the rigging cables, and the entire hook assembly is tilted about its sheave. This can affect hook measurements because the hook is tracked using a flat plate of reflective markers mounted on top of the hook assembly. Tilting the hook also

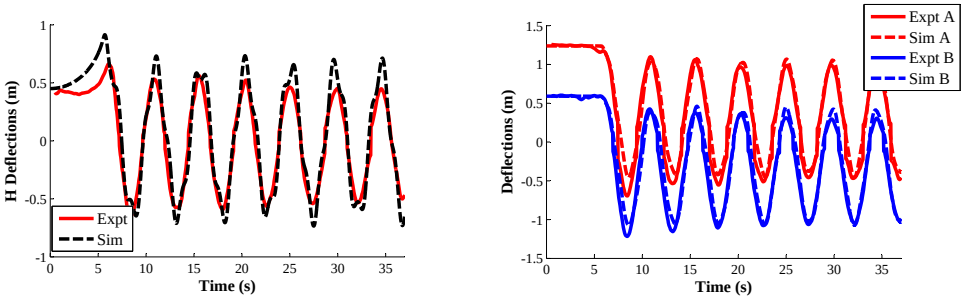

(a) Hook (b) Payload Sides A & B

Figure 5.17: Lift-Up of Plastic-Box Payload [x_{init}=0.9m]

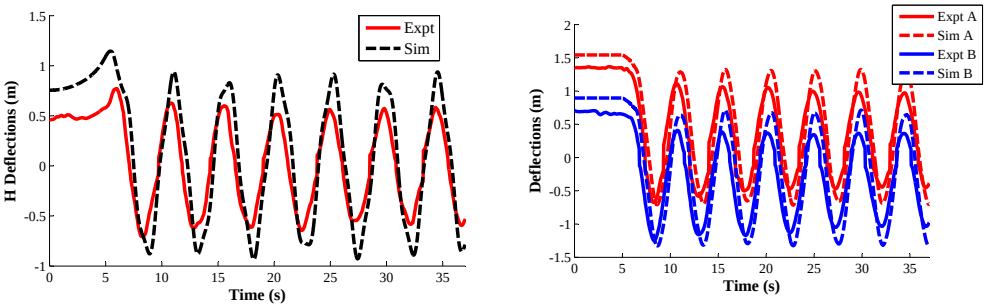

(a) Hook (b) Payload Sides A & B

Figure 5.18: Lift-Up of Plastic-Box Payload [x_{init}=1.2m]

tilts the plate. In the view of the trolley-mounted camera, the tilted reflective markers appear to converge in the direction of zero-deflection. measurements. Because of this, the experimental hook deflections are less than that of simulations at the start of these experiments.

Figure 5.19 shows the experimental and simulation results for the wooden-box payload, off-centered by 0.6m. Again, the plots indicate that the simulation models predicted the experimental results quite accurately. Figures 5.20 and 5.21 show similar data for x_{init} = 0.9, and 1.2m, respectively.

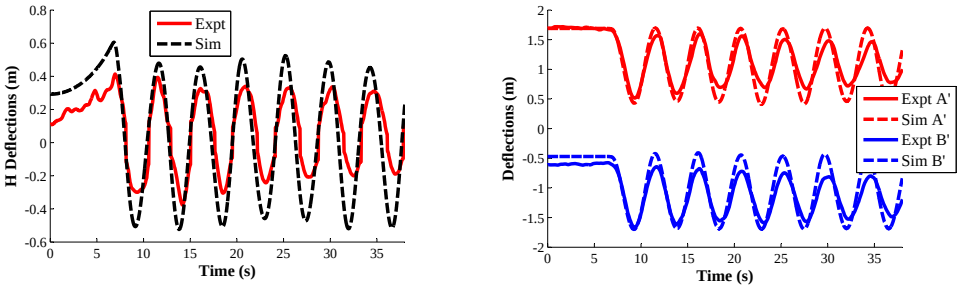

(a) Hook (b) Payload Sides A' & B'

Figure 5.19: Lift-Up of Wooden-Box Payload [x_{init}=0.6m]

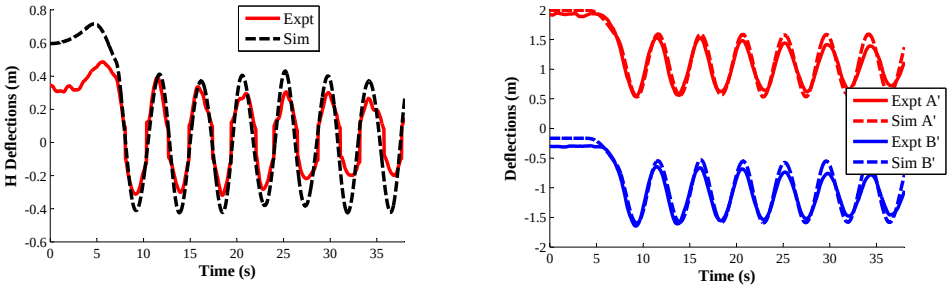

(a) Hook (b) Payload Sides A' & B'

Figure 5.20: Lift-Up of Wooden-Box Payload [x_{init}=0.9m]

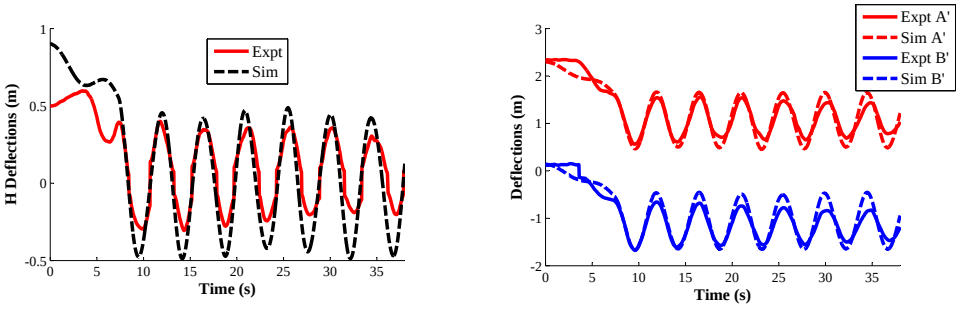

(a) Hook (b) Payload Sides A' & B'

Figure 5.21: Lift-Up of Wooden-Box Payload [x_{init}=1.2m]

5.5 Trends in Off-Centered Lifts

Section 5.4 established the point-mass and rigid-body payload models were reasonably accurate, as their simulation responses matched well with that from experiments. In this section, the models will be used to simulate under a wide variety of parameters to investigate trends in off-centered lifts. Unless otherwise specified, the HiBay crane parameters listed in Table 5.4 will be used.

5.5.1 Point-Mass Payloads and the HiBay Crane

In this subsection, the payload mass, m_P, is varied from 50 to 950 kg; the unstretched rigging length, r_U, is varied from 0.3 to 3 m; and the initial offset, x_{init}, is varied from 0.3 to 1.2 m. The ranges or r_U and m_P were sized to match the dimensions and lifting capacity of the crane. The range of offsets were selected based on the height of the crane and on realistic offsets that can be seen during operational lifts. When the offset distance is $x_{init} = 1.2m$, the angle of the hoist cable

Table 5.4: Nominal HiBay Crane Parameters

Parameter	Value(s)	Parameter	Value(s)
m_H (kg)	59	K_r (N/m)	924000
h (m)	6.37	$\dot{L}$ (m/s)	-0.117
μ_S	0.33	μ_K	0.28
r_U (m)	1.65		

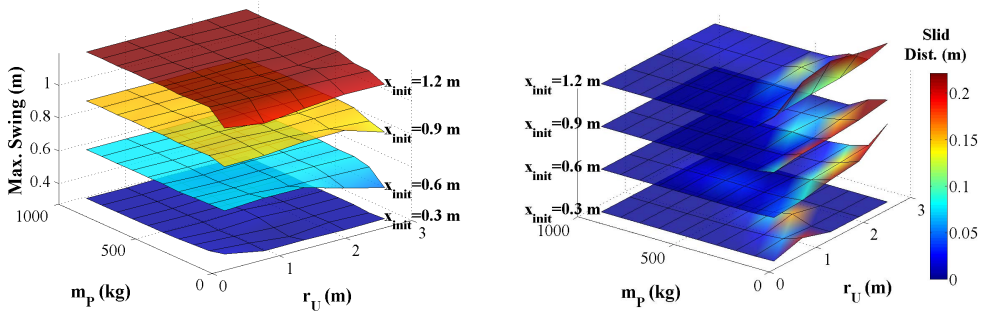

(a) Maximum Payload Swing

(b) Payload Slid Distance

Figure 5.22: Point-Mass Payloads, HiBay Crane

is approximately 10°. For a crane of this height (6.37m), this is an extreme angle that is highly noticeable to a human operator. It is unlikely that the operator will inadvertently lift a payload that is offset at larger distances. Therefore, $x_{init} = 1.2m$ is the upper limit to the range of offsets being investigated.

Figure 5.22(a) plots the maximum payload swing amplitude (after the payload has permanently left the ground) on the vertical axis, over the range of payload masses and rigging cables on the horizontal axes. Each surface in the plot represents a different initial offset, as indicated. Several trends are noteworthy:

- Obviously, the larger the initial offset, the larger the payload will swing.
- The maximum swing amplitude is upper-bounded by the initial offset. In the majority of tested cases, the maximum swing amplitude was only slightly less than the initial offset.
- The rigging cable length does not have a noticeable effect on the swing amplitude.
- For the majority of tested parameters, the payload mass also does not have a noticeable effect on the swing amplitude. However, for very light payloads, e.g. $m_P = 50kg$, the swing amplitudes are slightly less. This trend is observable for $x_{init} = 0.6, 0.9, 1.2m$.

Lighter payloads swing less because they tend to slide greater distances towards the trolley (and thus reducing the offset) before losing contact with the ground. This trend can be clearly seen in Figure 5.22(b), which plots the payload slid distance before leaving the ground, over m_P and r_U. The colors of the surfaces indicate the distance that the payload slid. Each surface represents a different initial offset, as indicated on the plot. Lighter payloads have a greater tendency to slide due to smaller normal reaction forces from the ground. This results in smaller forces that are required to overcome the resistance to sliding, i.e. the value of $\mu_S N$ is small for light payloads.

The swing amplitude is an important measure of the level of danger in an off-centered swing. Obviously, the larger the swing, the more potential the payload has to collide with objects and people. Furthermore, larger swings also have greater peak velocities.[4] This trend is shown in Figure 5.23(a), which plots the maximum horizontal payload velocity during swinging on the vertical axis, over m_P and r_U on the horizontal axes. Each surface represents a different initial offset, as indicated on the plot. Note that at $x_{init} = 1.2m$, the max payload velocity ($> 1.5m/s$) exceeds the human walking speed of $\approx 1.4m/s$. These situations are particularly dangerous, because it is more difficult for humans avoid faster moving payloads.

Higher payload velocity also indicates potentially higher levels of damage and danger, especially for heavy payloads that have greater momentums. For example, suppose the heaviest payload tested

[4]Typically, for systems that resemble single-pendulums, the maximum velocities during swinging occur when the payload is directly underneath the trolley.

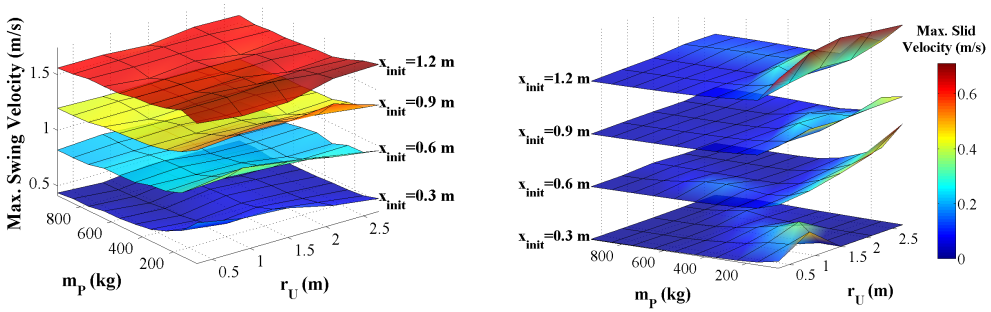

(a) During Swinging (b) During Sliding

Figure 5.23: Point-Mass Payloads, HiBay Crane, Maximum Horizontal Payload Velocities

here, $m_P = 950kg$, was lifted from an offset distance of 0.6m. Then, the maximum velocity of the swinging payload is $\approx 0.8m/s$, which is relatively slow compared to human speed. However, the swinging payload after it leaves the ground has a maximum momentum of 760 kgm/s. To put that into context, that level of momentum is approximately equal to a 100kg football linebacker charging at full speed.

Figure 5.23(b) plots similar information for the maximum payload velocity during sliding. For each surface, the magnitude of the maximum velocity is represented by color. For the cases tested, the velocities during sliding (the largest value was 0.7m/s, slower than the human walking speed) were significantly slower than during swinging. Combined with the fact that in most cases, the payload slid very small distances, it can be concluded that it is more critical, in terms of the potential levels of detriment, to consider the payload during swinging than during sliding.

In general, the swing amplitude is largely dependent on the offset distance at which the payload permanently lifts off the ground. This distance, x_{lift}, is an important measure, because it essentially determines the swing amplitude, which in turn, is a direct indication on the level of potential damages and dangers. If the maximum swing amplitude is similar in magnitude to the initial offset, then this indicates the payload did not slide (or slid a very small distance), and broke contact with the ground at (or near) the initial offset position, i.e. $x_{lift} \approx x_{init}$. Most of the cases tested in this subsection fit under this scenario.

Even though the point-mass hook and point-mass payload system is technically a double-pendulum during swinging motion, in certain conditions, it can be approximated by a single-pendulum model. The conditions where this is valid are: 1) when the payload mass is at least greater than two-times the hook mass;[5] 2) when the rigging length, r_U, is very short relative to the hoist cable length, L, such that $L/r_U > 3$; or 3) when the rigging length is very long relative to the hoist cable length, such that the ratio $L/r_U \ll 1$ [91].

Using the single-pendulum model to approximate swing motion, the relationships between x_{lift} and the maximum swing amplitude and maximum swing velocity can be established. Because the payload lifts off the ground at x_{lift}, the horizontal swing displacement,d_{swing}, is essentially a sinusoidal function in time:[6]

$$d_{swing}(t) = x_{lift}\cos(\omega t) \tag{5.77}$$

where $\omega = \sqrt{\frac{g}{L_{total}}}$ is the swing frequency, and $L_{total} = r_U + L(t_{lift})$ is the combined rigging and hoist cable length at the time of lift-off. Thus, the maximum swing amplitude is $\max(d_{swing}) = x_{lift}$. The swing velocity, v_{swing}, is the derivative of 5.77 in time:

$$v_{swing}(t) = -\omega x_{lift}\sin(\omega t) \tag{5.78}$$

[5]In almost all crane lifts, the payload is much heavier than the hook.
[6]Note that damping and phase shift are ignored.

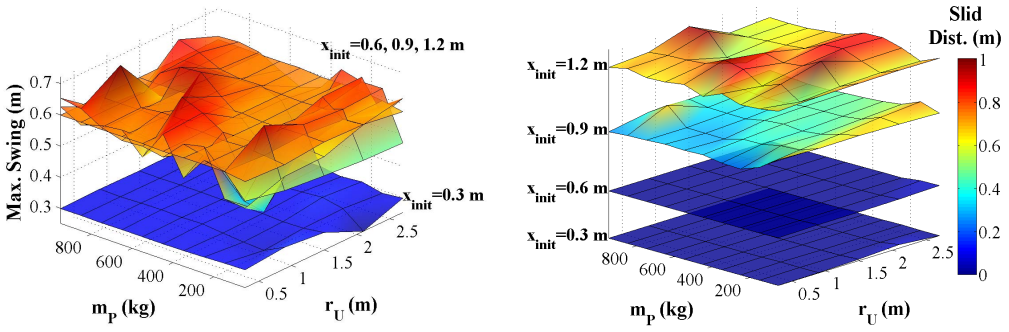

(a) Maximum Payload Swing

(b) Payload Slid Distance

Figure 5.24: Point-Mass Payloads, Slow Hoist

Thus, the maximum swing velocity is $\max(v_{swing}) = \omega x_{lift}$. By setting $x_{lift} = x_{init}$, the prediction for maximum swing velocity matches the data in Figure 5.23(a).

5.5.2 Point-Mass Payloads and Hoist Speeds

In this subsection, a very slow hoist speed, $\dot{L} = -0.04m/s$, is used. This is approximately one third of the HiBay crane hoist speed ($\dot{L} = -0.117m/s$). Figure 5.24(a) plots the maximum payload swing amplitude over the range of payload masses and rigging cables. The data for initial offset $x_{init} = 0.3m$ is represented by the bottom surface, and the data for $x_{init} = 0.6$, 0.9, 1.2m are represented by three overlapping surfaces that occupy the vertical space around maximum swing = 0.6m.

By hoisting slowly, the maximum swing amplitudes for large initial offsets are significantly reduced. This is because even if the payload begins to lift off the ground, it has more time to slide underneath the trolley and reestablish ground contact at a position that has less offset. In essence, slower hoist speeds reduce the swing amplitude by decreasing the offset distance at which the final lift-off point occurs, i.e. x_{lift} is reduced. Furthermore, this reduction effect is applicable only when the initial offset, x_{init}, is larger than a critical value, x^*_{lift}. If $x_{init} > x^*_{lift}$, then the lift-off position is reduced to $x_{lift} \approx x^*_{lift}$. By applying the single-pendulum swing model in (5.77), the maximum swing amplitude is also reduced to around $\max(d_{swing}) \approx x^*_{lift}$. If $x_{init} \leq x^*_{lift}$, then there is no reduction. For the cases tested here, $x^*_{lift} \approx$0.6m, and the maximum payload swing amplitudes for $x_{init} = 0.9$ and 1.2m were reduced to around the same value. However, there was no reduction effect for $x_{init} = 0.3$ and 0.6m.

The absence of reduction for smaller offsets can be clearly seen in Figure 5.24(b), which plots the payload slid distance, over m_P and r_U. The colors of the surfaces indicate the distance that the payload slid. Each surface represents a different initial offset, as indicated on the plot. For $x_{init} =$ 0.3 and 0.6m, the payloads virtually lifted off the ground at their initial positions, i.e. $x_{lift} \approx x_{init}$. However, for $x_{init} = 0.9$ and 1.2m, the payload slid significantly larger distances from x_{init} to x^*_{lift} before lifting off the ground.

5.5.3 Rigid-Body Payloads and the HiBay Crane

From this subsection on, rigid-body payloads will be investigated. Payloads are uniform, aluminum (density = $2700kg/m^3$) rectangular cuboids. Initial offsets ranging from 0.3 to 1.2m are investigated, and the widths and heights of the payloads are varied from 0.5 to 2m. With reference to the schematic diagrams in Figure 5.6, the payload width, P_{width}, is equal to $2a_i$, and the payload

height, P_{height}, is equal to $2a_j$.[7] The payload depth (into the page in Figure 5.6), is constant at 0.5m. Note by varying the payload size, its mass also changes proportionally to its volume. The rotational inertia also changes according to the payload geometry.

The friction coefficients used with the rigid-body payloads are: $\mu_S = 0.37$ and $\mu_K = 0.33$. Because different sized payloads are investigated, the rigging lengths change with the payload width. The rigging lengths are sized such that when the trolley is centered above the payload, the tight rigging cables are 60° from horizontal, i.e. with reference to Figure 5.6, points H, A, and B form an equilateral triangle. This is the recommended rigging length size, so that tension forces in the rigging are properly distributed and do not exceed the designed limits [21]. Additionally, because the rigging lengths may change with the payload, the rigging spring constant, K_r, also changes.[8] However, the rigging cable stiffness is always very high, so its variations do not have significant effects on the results.

With the exception of K_r, μ_S, μ_K, and r_U, the nominal HiBay crane parameter values in Table 5.4 are used in the simulations the rigid-body payloads. Figure 5.25(a) plots the maximum horizontal swing amplitude of the payload mass center, P_{COM}, over P_{width} and P_{height}. Each surface corresponds to a different offset distance, as indicated in the plot. Figure 5.25(b) shows similar information, but for $x_{init} = 1.2$m. The following are noteworthy:

- Swing amplitudes are upper bounded by the offset distance. In general, larger offsets generally result in larger swings.
- For lower offsets, i.e. $x_{init} = 0.3$ and 0.6m, the swing amplitudes are mostly uniform across all tested payload dimensions. Also, the swing amplitudes for these cases are only slightly less than the offset distance, which indicates the payloads were lifted off the ground near their initial positions.
- For larger offsets, i.e. $x_{init} = 0.9$ and 1.2m, the swing amplitude is affected by the payload size in two ways:[9]
  - For low and wide payloads, the swing amplitudes are significantly reduced, as indicated in Figure 5.25(b) in the region labeled "Wide Payloads". This is because their large widths allow them to slide and scrape (breaking and reestablishing ground contact repetitively) along the ground as it is being lifted. This effectively reduces x_{lift}, the offset distance at which the payload permanently breaks contact with the ground. The effect is only apparent for low and wide payloads, but not for tall and wide payloads.
  - For tall and narrow payloads the swing amplitudes are also reduced, as indicated in Figure 5.25(b) in the region labeled "Tall Payloads". This is because when the offset is large, tall and narrow payloads are easily tipped over, as illustrated in Figure 5.25(c). The payload tips over when the horizontal position of the payload mass center, P_{COM}, is no longer situated between the bottom corners of the payload - these are points C and D in Figure 5.6. When the payload is tipped over, it also has a greater tendency to slide and scrape, which reduces x_{lift} and the swing amplitude. However, tipping over the payload can be quite dangerous, and is almost always avoided.

Figure 5.26 plots the slid distance, represented by color, over the payload widths and heights. Each surface represents a different offset distance, as indicated on the plot. Figure 5.26 shows that payloads did not slide for smaller offsets, $x_{init} = 0.3$ and 0.6m. However, for larger offsets, $x_{init} = 0.9$ and 1.2m, the surfaces show increased sliding distances for low and wide payloads, and for tall and narrow payloads.

[7] Only symmetric, rectangular payloads are investigated here. Therefore, $a_i = b_i = c_i = d_i$, and $a_j = b_j = c_j = d_j$.

[8] Steel cables (Young's Modulus $E = 200 \times 10^9$) with circular cross sectional area, A, (2cm radius) were used. This information, with the rigging length, can be used to calculate the spring constant, using $K_r = EA/r$.

[9] These effects are more evident for x_{init}=1.2m than x_{init}=0.9m.

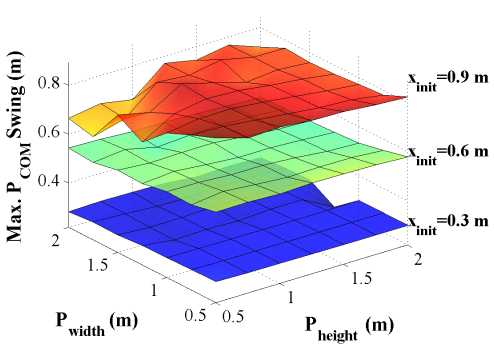

(a) x_{init}=0.3, 0.6, 0.9m

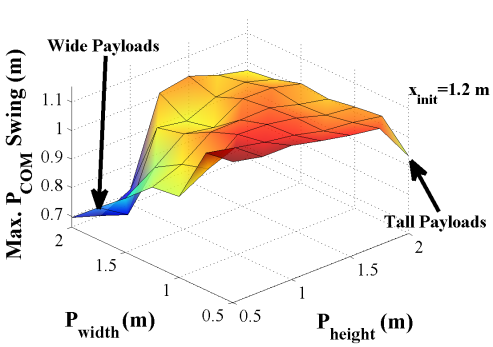

(b) x_{init}=1.2m

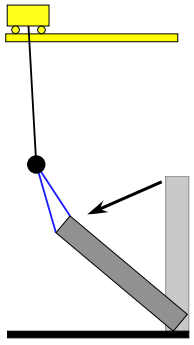

(c) Tall Payload Tipped Over

Figure 5.25: Maximum Swing, Rigid-Body Payloads, HiBay Crane

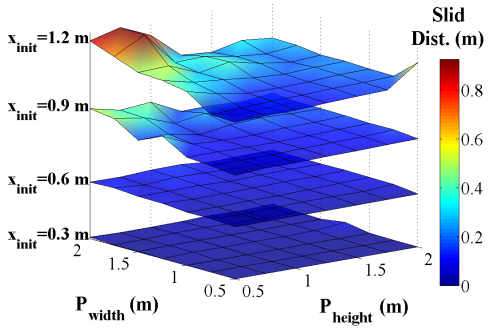

Figure 5.26: Slid Distance, Rigid-Body Payloads, HiBay Crane

Figure 5.27(a) plots the maximum horizontal velocity during swinging. Qualitatively, the surfaces are similar to the maximum swing amplitude surfaces in Figures 5.25(a) and 5.25(b). This is because larger swings also tend to have greater maximum velocities. Also, for cases where the system behaves like a single-pendulum during swing, and for cases where the payload does not slide very much, i.e. that $x_{lift} \approx x_{init}$, (5.77) and (5.78) can be used to predict the maximum swing amplitudes and velocities.

Figure 5.27(b) plots the maximum horizontal slid velocities. The magnitude of slid velocity is represented by color. Note the slid velocities are always less than swing velocities. This is because a free swinging payload moves faster than a sliding payload that is impeded by the ground.

5.5.4 Rigid-Body Payloads and Crane Heights

In this subsection, the crane height is increased to $h = 24m$, which is representative of a very tall and large-lifting-capacity crane. The range of payload sizes was also increased, with P_{width} and P_{height} ranging from 1 to 9m. The offset distances were also increased and ranged from 0.9 to 4.5m. Figure 5.28(a) plots the maximum swing amplitudes, over P_{width} and P_{height}, for x_{init}=0.9, 1.8, and 2.7m. Each surface represents different offsets, as indicated on the plot. Figure 5.28(b) shows similar data for the larger offsets, x_{init}=3.6, 4.5m. The surfaces are separated vertically for clarity, and the surface color represents the swing amplitude.

Figures 5.28(a) and 5.28(b) show the trends observed previously in Figures 5.25(a) and 5.25(b) with the HiBay crane continues for larger payloads and higher cranes, albeit at an increased scale. These trends are: 1) for small offsets (relative to the size of the crane and payload), the payload width and height have virtually no effect on the swing amplitude; and 2) for larger offsets, swing

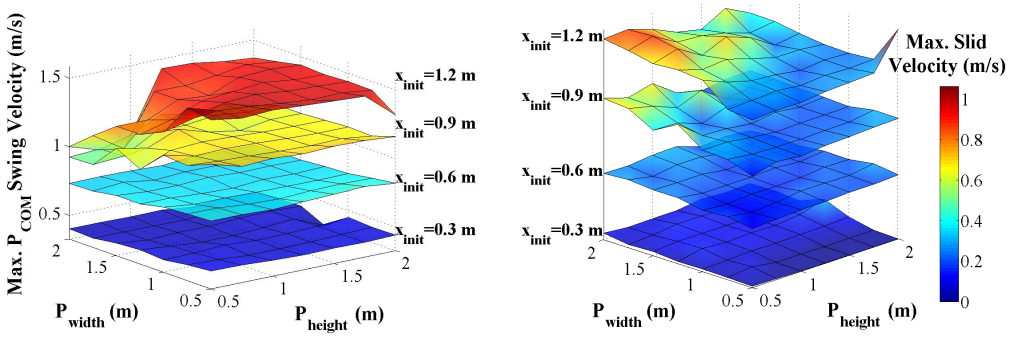

(a) During Swinging (b) During Sliding

Figure 5.27: Rigid-Body Payloads, HiBay Crane, Maximum P_{COM} Horizontal Velocities

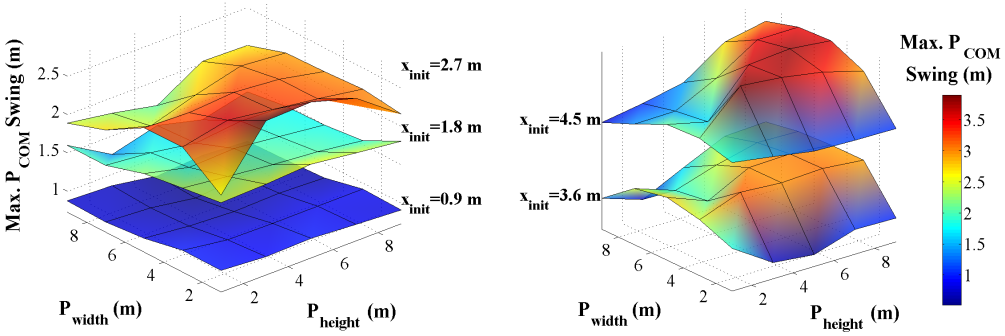

(a) x_{init}=0.9, 1.8, 2.7m (b) x_{init}=3.6, 4.5m

Figure 5.28: Maximum Swing, Rigid-Body Payloads, 24m High Crane

amplitudes are significantly decreased for low and wide payloads, and for tall and narrow payloads. Note that in Figure 5.28(b), all payloads with $P_{width} = 1m$ exhibit the tipping-over phenomenon.

5.5.5 Rigid-Body Payloads and Hoist Speeds

In this subsection, the nominal hoist speed of the HiBay crane ($\dot{L} = -0.117m/s$) was increased nearly three times to $\dot{L} = 0.3m/s$. Figure 5.29(a) plots the maximum swing amplitude over the range of payload widths and heights. Each surface represents different offsets, as indicated on the plot. All surfaces are virtually flat, with swing amplitudes approximately equal in magnitude to x_{init}. This is because in general, with fast hoist speeds, payloads are lifted from the ground near the initial position, i.e. $x_{lift} \approx x_{init}$, regardless of its size. This result conforms with the point-mass payload and slow hoist speed results in Section 5.5.2: payload swing is reduced for slow hoist speeds, but increased for fast hoist speeds.

5.6 Auto-Centering Techniques

Essentially, all off-centered lifts are detrimental. They result in undesirable payload sliding and swinging. Therefore, all mitigation techniques must address this issue directly by reducing the payload offset as much as possible before lifting, i.e. reduce x_{lift}. The ideal case was shown in Figure 5.1(b), where the positions of the trolley, hook, and payload center all lie on a vertical line. Presented in this section are two types of auto-centering techniques: 1) passive, which relies on configuring the lift so that the payload self-centers as it is being lifted; and 2) active, which uses sensors and feedback controllers to move the crane in order to reduce the payload offset. However,

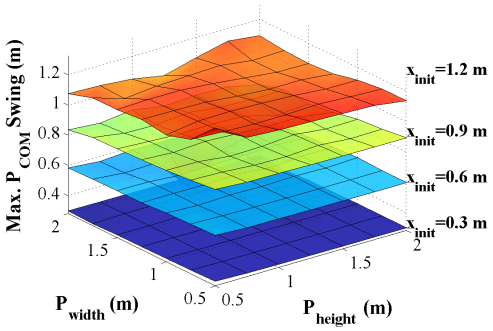

(a) Maximum P_{COM} Swing Amplitude

Figure 5.29: Rigid-Body Payloads, Fast Hoist Speed

the most important factor is still the human operator, who is the first and foremost mitigator to the detrimental effects of off-centered lifts.

5.6.1 Human Factors in Manual-Centering

The human operator is the primary method of preventing or mitigating off-centered lifts. Ultimately, it is the operator who makes the final decisions in commanding motions to the crane. In all lifts, the operator's goal is to manually center the trolley and hook over the payload before lifting. There are several "offset-distance" indicators that operators can use to gauge the size of the offset, including: 1) the angle of the hoist cable; 2) the relative positions of the trolley, hook, and the payload center, P_{COM}; 3) the geometries of the riggings, e.g. for symmetrical rigging arrangements, the operator would look for symmetric geometries formed by the rigging cables. In the following scenarios, because the quality of offset-distance indicators are reduced, the ability for an operator to manually center the trolley is compromised. Therefore, these scenarios are good candidates to implement auto-centering techniques:

- If the payload is very large, or its geometry is highly irregular, it may be difficult to judge the position of the its center of mass, P_{COM}.
- In many lift scenarios, because the operator is on the ground, he/she may be in a very poor observational view point for centering the trolley and hook. The optimal view point is one that is "zoomed-out", where the operator can see and compare the positions of the trolley, hook, and payload center, simultaneously.
- If the rigging cables are very long, then it can be difficult to judge whether the hook is centered over P_{COM}, due to the large vertical separation.
- If the crane is high, e.g. 24m off the ground like in Section 5.5.4 or with construction tower cranes, then many of the aforementioned offset-distance indicators are compromised:
  - For very high cranes, relatively larger (and therefore more detrimental) offsets are required to produce noticeable offset indicators that can trigger a human operator response. One such indicator is the hoist cable angle.
  - Poor viewing positions. With many construction tower cranes, the operator, who sits in the cab on the jib, cannot see the payload. They rely on either auxiliary cameras or radio assistance from men on the ground.

5.6.2 Passive Self-Centering

To reduce the detrimental effects of payload offsets, the following techniques can be used that configure the lift such that the payload passively self-centers, i.e. reduce x_{lift}:

- Sections 5.5.2 and 5.5.5 showed that slow hoist speeds allow the payload to self-center before lifting off the ground.
- Sections 5.5.3 and 5.5.4 showed that low and wide payloads have a self-centering effect when the offset distance is large. Therefore, placing the payload on wide pallets for example, can reduce swing if the payload is lifted from large offset positions.

Note that in all passive auto-centering techniques, the payload slides/scrapes along the ground to self-center before lifting. Although sliding and scraping is undesirable, it is still a more favorable outcome than large amplitude payload swings. Furthermore, these passive techniques offer only a means by which the detrimental effects of off-centered lifts can be *mitigated*, not eliminated. If sliding and scraping are to be eliminated, then the active auto-centering techniques that follow should be used.

5.6.3 Hook-Based Auto-Centering

One of the more common types of sensors that are equipped on cranes are ones that measure the hook position. In contrast to tracking the position of detachable payloads, tracking the hook (or a "spreader", for dock-side container cranes) is simpler because it is a permanent component of the crane. There are many ways to track the hook position, such as with a trolley-mounted camera [27], hoist cable angle sensors [13], load cells [17], or accelerometers and gyroscopes [46].

Furthermore, there is already much work in literature that uses feedback controllers to control hook swing [80, 3, 67, 65, 62, 40]. The hook is often assumed to be attached to the payload to form a single rigid-body. This simplifies the dynamics as the hook-payload forms a single-pendulum dynamic system beneath the trolley. However, the goal of those works was to reduce the payload swing amplitude while the payload is in the air. Very few efforts have focused specifically on the off-centered lifting of payloads from the ground.

One of those efforts originate from Liftco Industrial Supplies. Liftco uses a device that rigidly attaches to the hoist cable to detect the cable angle. If the angular deflection is too great, then the device cuts off hoisting and trolley travel motions, `http://www.liftcoindsup.com.au/pullprevention.html`. This device can also prevent other side-pull scenarios, such as accidentally snagging the hook or rigging while the trolley is moving. However, because the device is only a preventative measure, it is still up to the operator to manually center the trolley over the payload before lifting.

The auto-centering technique presented here piggybacks on a PD controller that was designed to reduce hook swing resulting from external disturbances [103]. The control block diagram is shown in Figure 5.30. The trolley and hook are modeled as linear, second-order plants, and the hook deflection (relative to the trolley, aka the hoist cable angle) is tracked using a trolley-mounted camera. The PD controller uses the hook deflection as the error signal and sends commands to move the trolley in order to reduce hook swing. The PD gains are chosen such that the closed-loop oscillatory poles are heavily damped [103].

The hook-based auto-centering algorithm uses the PD disturbance rejection controller to reduce hook deflection if it is too large. If the hook deflection is within acceptable limits, then allow the hook to be hoisted up:

while Command is hoist up **do**
  if Hook deflection is excessive **then**
    Stop hoist; reduce hook deflection using the PD disturbance rejection controller

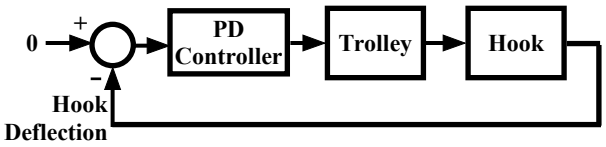

Figure 5.30: PD Disturbance Rejection Controller Block Diagram

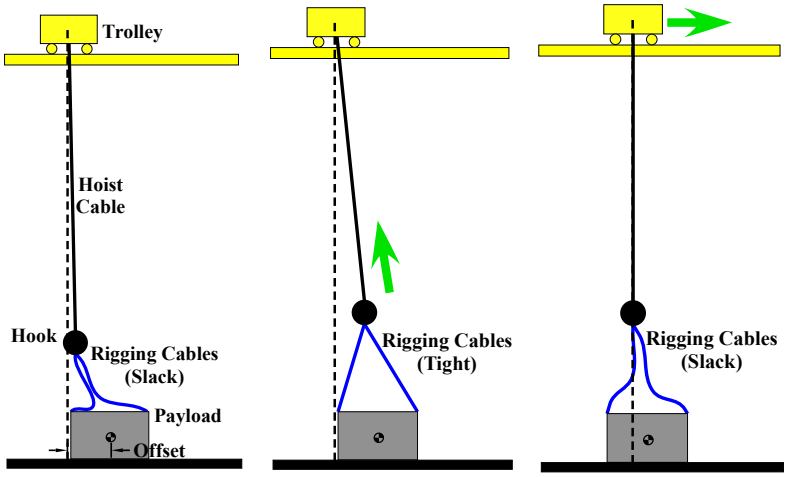

(a) Start (b) Hoisting (c) Reducing Hook Deflections

Figure 5.31: Hook-Based Auto-Centering

else
Hoist up
end if
end while

Note this technique is essentially the same as CAMotion's"Automatic Load Centering" `http://www.camotion.com/SOLUTIONS/CRANECONTROL/CRANEVISION/tabid/504/Default.aspx`. This technique heavily relies on the hook to be deflected as it is being hoisted by an off-centered trolley. For properly-rigged and symmetric payloads, the rigging cables will always deflect the hook until the trolley and hook are aligned over the payload center. However, this may not be the case for improperly-rigged and/or irregularly-shaped payloads. Those situations are beyond the scope of this dissertation.

Figure 5.31(a) illustrates hook-based auto-centering. The trolley starts at a position that is offset from the center of the payload. The hook deflection is relatively small at this point, and the rigging cables are slack. However, as the hook is hoisted, as in Figure 5.31(b), the rigging cables tighten and pull on the hook, increasing the hook deflection. In Figure 5.31(c), the algorithm detects that the hook deflection is excessive, and uses the PD disturbance rejection controller to move the trolley and reduce hook deflections. Typically, the rigging cables are slack after the hook deflection has been reduced. The process in Figures 5.31(b) and 5.31(c) are repeated until the trolley, hook, and payload are aligned. After which, the payload is lifted off the ground.

Hook-based auto-centering was used to pick up the plastic-box payload (Figure 5.15(a)) in off-centered lifts. Figure 5.32(a) plots the the horizontal positions of the trolley, hook, and payload where the trolley was initially offset from the payload by $x_{init} \approx 0.6m$. For comparisons, the responses when no auto-centering was used are also shown, offset above along the vertical axis.

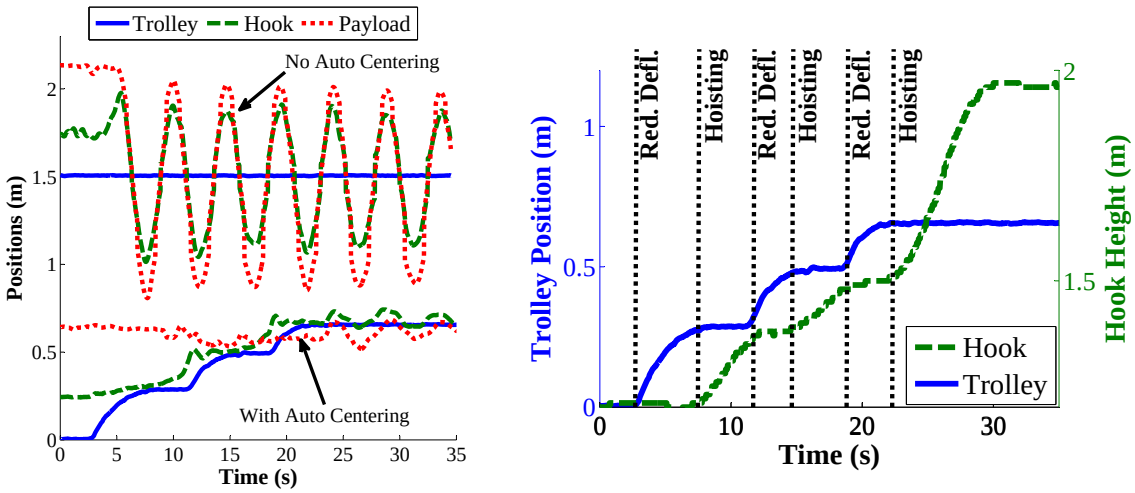

(a) Horizontal Positions

(b) Hoisting and Reducing Hook Deflections

Figure 5.32: Hook-Based Auto-Centering Responses [x_{init} ≈0.6m]

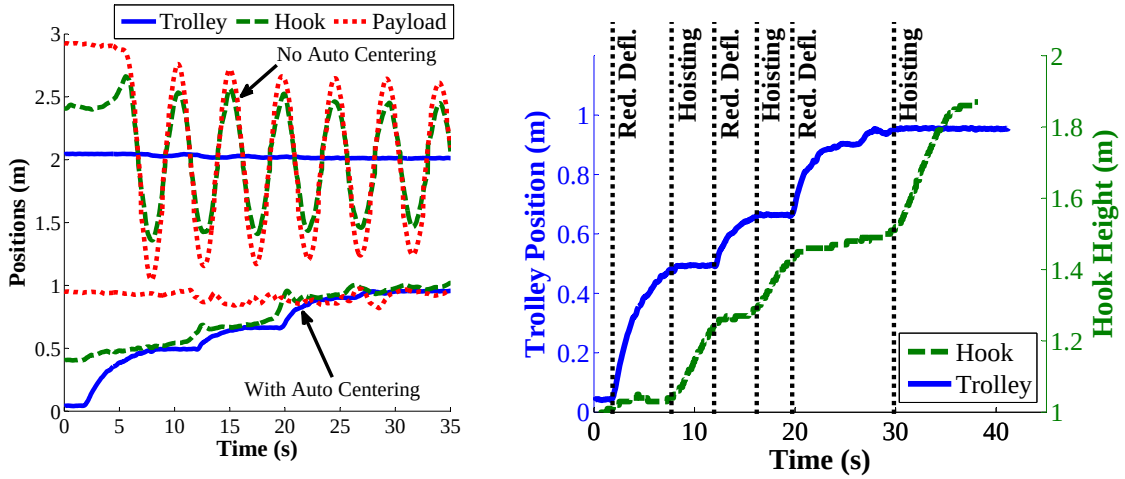

(a) Horizontal Positions

(b) Hoisting and Reducing Hook Deflections

Figure 5.33: Hook-Based Auto-Centering Responses [x_{init} ≈1m]

The peak-to-peak payload oscillation without auto-centering was 1.12m, and only 0.1m with auto-centering, a reduction of 91%. Figure 5.32(b) plots the trolley position (solid line, left vertical axis) and the height of the hook (dashed line, right vertical axis). The figure clearly shows the repetitive process of alternating between hoisting and reducing hook deflections using the PD disturbance rejection controller. When disturbance rejection is active and moving the trolley, the hook height is constant. Conversely, when the hook is being hoisted, the trolley is stationary.

Figure 5.33 shows similar data for $x_{init} \approx 1m$. The peak-to-peak payload oscillation without auto-centering was 1.55m, and only 0.14m with auto-centering, a reduction of 91%. One disadvantage of hook-based auto-centering is its slow speed, due to the repetitive process of hoisting and reducing hook deflections. In the $x_{init} \approx 0.6m$ case, it took approximately 19s for the crane to be centered over the payload before uninterrupted hoisting was allowed. In the $x_{init} \approx 1m$ case, the same process took approximately 28s. The relatively slow speed is inevitable because the controller can only react to hook deflections, which gives indirect information on whether the crane is off-centered from the payload.

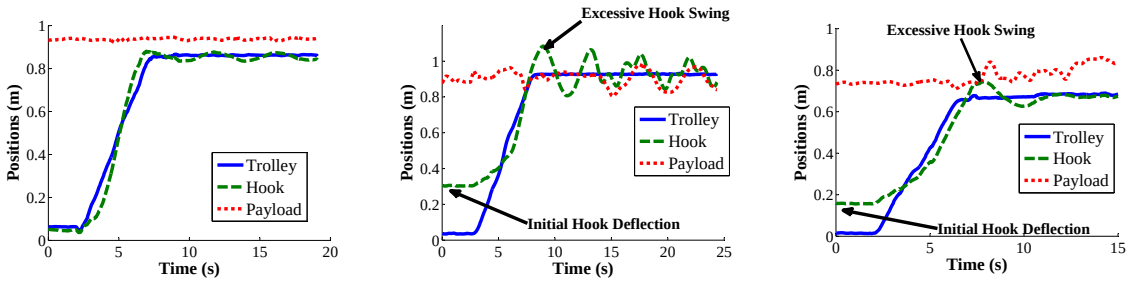

(a) Unrigged, Trolley Positioned Over Payload

(b) Rigged, Trolley Positioned Over Payload and Hoisted

(c) Rigged, Trolley Positioned Over Payload and Waited

Figure 5.34: Excessive Hook Swing Induced by Rigging Cables

5.6.4 Hook and Payload-Based Auto-Centering

By using additional sensors, more information about system states, such as the hook and payload positions, are obtained. Then, faster and more efficient auto-centering movements can be performed. However, additional sensors come with greater costs. The hook position can be tracked with a trolley-mounted camera, or an RF tag, or both. The payload center of mass can be tracked using an RF tag. Alternatively, it may be more convenient to mount RF tags on the outer edges of the payload (if the payload is very large, for example). The position of the payload center can then be calculated from the geometric center of those tags.

Because the position of the payload center is known, the trolley can be centered over the payload immediately. However, even though the hook is attached to the payload, the rigging cables may be slack, which allows the hook to swing freely. Therefore, hook swing induced by trolley motion is still a potential problem. To position the trolley over the payload without inducing significant hook oscillations, PD, On-Off, or BOSS controllers from Chapter 3 can be used.

Another problem to consider is that while the trolley is being positioned over the payload, the rigging cables can potentially cause the hook to swing. To understand this phenomenon, consider the case shown in Figure 5.34(a), which plots the positions of the trolley, hook, and payload. The trolley is being positioned over the payload, which is not rigged to the hook. As expected, the hook does not show any significant residual oscillations.

However, as shown in Figure 5.34(b), if the payload is rigged to the hook, then the rigging cables may be initially tight, and pull on the hook. This causes an initial hook deflection, as indicated in Figure 5.34(b). This situation can happen if the payload offset from the trolley is sufficiently large, and/or the rigging cables are too short, so that the rigging cables are initially tight and pulls on the hook. In Figure 5.34(b), the initial hook deflection resulted in excessive hook swing when the trolley was positioned over the payload. Furthermore, when the payload was hoisted off the ground from this configuration, the level of hook swing was sufficient to induce significant payload swing. Note that even if the rigging cable is not initially tight, and that the initial hook deflection is zero, the weight of the rigging cables and its interaction with the hook can still cause unwanted hook swing while the trolley is moving.

One way to mitigate hook swing induced by rigging cables is to simply wait for the hook swing to damp out. This is shown in Figure 5.34(c), where the trolley was positioned over the payload, and the hook was *not* hoisted.[10] Again, the initial hook deflection caused excessive hook swing after the trolley was positioned over the payload. However, the hook swing was quickly damped out after 10s by its interactions with the rigging cable.

Thus, to avoid hook swing induced by both the rigging cables and trolley motion, the hook and

[10]Note the payload did not actually move from t=7s to t=15s. The drift in the payload position was caused by measurement noise.

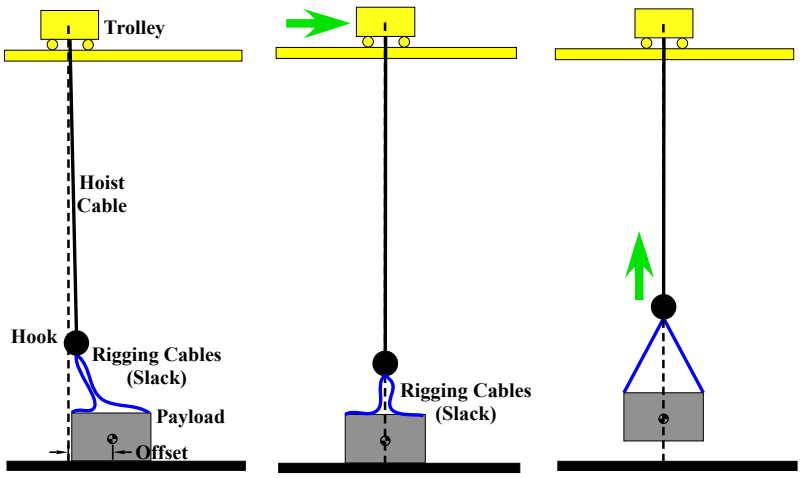

(a) Start (b) Positioning & Waiting (c) Hoisting

Figure 5.35: Hook and Payload-Based Auto-Centering

payload-based auto-centering algorithm is:

while Command is hoist up **do**
  while Trolley is not sufficiently close to the payload center **do**
    Position the trolley over the payload center using the PD, On-Off, or BOSS controllers
  end while
  while Hook swing is excessive **do**
    Wait
  end while
  Hoist up
end while

This auto-centering technique is illustrated by Figure 5.35. The starting offset configuration is shown in Figure 5.35(a). In Figure 5.35(b), the trolley is moved over the payload. Then, if the hook swing is excessive, the controller waits for it to damp out. Finally, the hook and payload are hoisted up in Figure 5.35(c).

For cases where only the payload position is available, and the controller does not have any information on the hook position, then the following methods can be used to reduce hook swing:

- After the controller positions the trolley over the payload, it should always wait for a duration of time for any potential hook swing to damp out before hoisting.
- Hoist at a slow speed after the trolley has been positioned over the payload. The slowly increase in rigging cable tension can damp out hook swing before the payload is lifted from the ground.
- For payloads that are much heavier than the hook, the hook swing has relatively less influence on the payload swing after it lifts off the ground.
- Because a swinging hook is visibly obvious, the crane operator or assistants can manually reduce the hook swing after the trolley has been positioned over the payload.

Hook and payload-based auto-centering was used to pick up the plastic-box payload (Figure 5.15(a)) in off-centered lifts. Figure 5.36(a) plots the the horizontal positions of the trolley, hook, and payload where the trolley was initially offset from the payload by $x_{init} \approx 0.5m$. For comparisons, the responses when no auto-centering was used are also shown, offset above in the direction

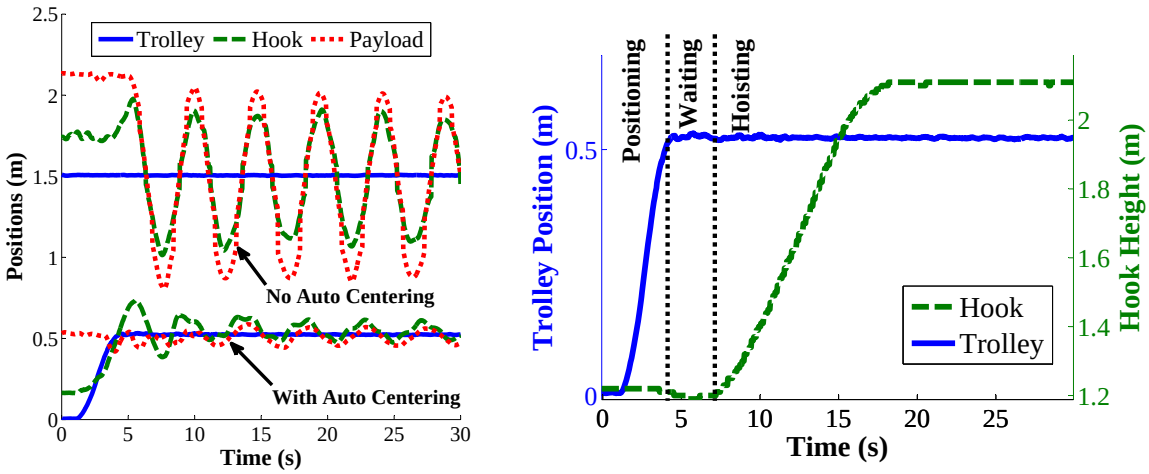

(a) Horizontal Positions

(b) Trolley Adjusting and Hook Hoisting

Figure 5.36: Hook- & Payload-Based Auto-Centering Responses [x_{init} ≈0.5m]

of the vertical axis. The peak-to-peak payload oscillation without auto-centering was 1.12m, and only 0.14m with auto-centering, a reduction of 88%. Figure 5.36(b) plots the trolley position (solid line, left vertical axis) and the height of the hook (dashed line, right vertical axis). The plot clearly shows the three distinct stages in the auto-centering algorithm: 1) the trolley is positioned over the payload, 2) the controller waits for excessive hook swing to damp out, and 3) the hook is hoisted. Figure 5.37 shows similar data for $x_{init} \approx 1m$. The peak-to-peak payload oscillation without auto-centering was 1.55m, and only 0.11m with auto-centering, a reduction of 93%.

The main advantage of the hook and payload-based auto-centering technique over the hook-based auto-centering technique is that the payload position is available to the controller. Thus, the crane is able to be centered over the payload much faster. In the $x_{init} \approx 0.5m$ case, it took approximately 6.2s for the crane to be centered over the payload. In the $x_{init} \approx 1m$ case, the same process took approximately 14.4s. For comparisons, the hook-based auto-centering technique took 19s for $x_{init} \approx 0.6m$ case, and 28s for $x_{init} \approx 1m$.

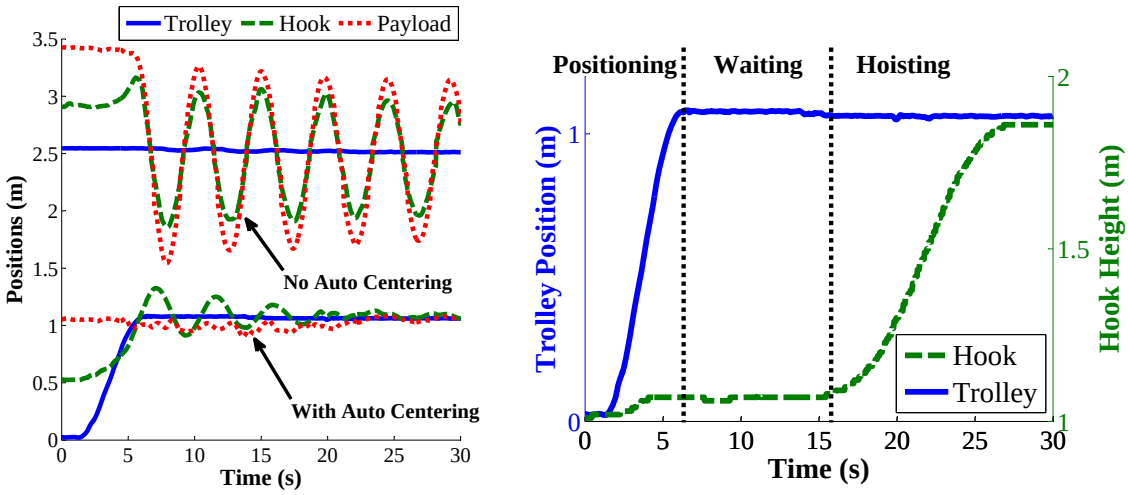

(a) Horizontal Positions

(b) Trolley Adjusting and Hook Hoisting

Figure 5.37: Hook- & Payload-Based Auto-Centering Responses [x_{init} ≈1m]

CHAPTER VI

LAY-DOWN OF LONG PAYLOADS

Lowering a payload down to the ground is typically uneventful, provided that oscillations were eliminated while the payload is suspended in the air. However, in certain situations, it can be very challenging for operators to perform this task. One example is laying down a long, distributed payload from a near-vertical orientation in the air, to a horizontal position on a flat surface. This procedure is known as payload "lay-down".

Figure 6.1 illustrates a four-step lay-down maneuver of a long payload. It is assumed that the payload is attached to the hook and hoist cables and suspended in a vertical position. The crane operator transports the payload to the desired location in step 1. In step 2, the lay-down process begins, wherein the operator establishes a stationary pivot point on the lower end of the payload. During step 3, the operator simultaneously controls the trolley and lowers the hoist cables. The payload then rotates about the pivot, following a quarter circular arc from vertical to horizontal orientation. The lay-down maneuver is complete in step 4, where the payload is lying in a horizontal position.

Several potential problems can occur during the lay-down maneuver (steps 2-4 in Figure 6.1):

1. If the simultaneous movements of the trolley and lowering of the hoist cable are not properly coordinated, then the payload pivot may slip and move suddenly in unintended and unpredictable ways. This is can potentially cause damage, lengthy down-times, and injure people. Due to the level of skill required in making these coordinated movements, highly experienced operators are usually employed.

2. "Side-pull" may occur during steps 2-4. This is when the hoist cable is at a steep angle relative to the hoist drum. Some typical problems associated with side pull include:

   - The cables may come out of the grooves on the hoist drum and rub against the remaining cables or drum, resulting in damaged cables.
   - Side pull may cause unintended stress on certain crane components.

The goal of this chapter is to study the dynamics of lay-down maneuvers. Then, obtain motion-control solutions that aid operators to avoid the problems above. As the process of formulating

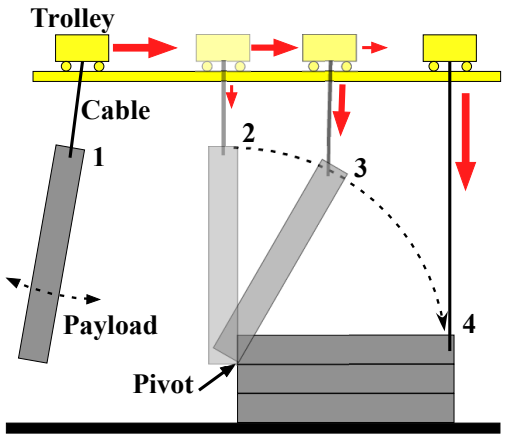

Figure 6.1: Steps in the Lay-Down Process

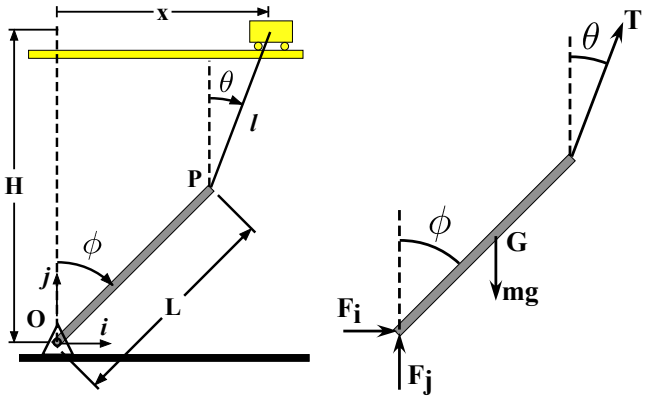

(a) Schematic (b) Free Body Diagram

Figure 6.2: Slender-Beam Payload Lay-Down Model

lay-down dynamic models is similar to that of payload lift-up, the same tools (Autolev [38] and Newton-Euler dynamic equations [23]) were used. Additionally, the Coulomb model of friction, described in Chapter 5 by (5.1), is used to prescribe limit conditions pertaining to the payload pivot.

There is very little past work concerning the lay-down of long payloads. The closest work found was by Hermann et al., who analyzed the dynamics of longitudinal pressure vessels and mobile cranes [29]. The focus of their paper, however, was on the erection of these pressure vessels, rather than the lay-down. Traditionally, two or more mobile cranes are employed in such operations. Erection is difficult due to the complicated maneuvering and high levels of coordination between the cranes. Forces and motions during the process were modeled, which helped the design of an innovative rigging solution that could erect the long payload using only one crane.

One direct application of this work is in the lay-down of 30' (9.1m) aluminum ingots in Alcoa factories. The ingots are lifted vertically from smelting pits, and then transported to a storage area by a crane. The crane stores the ingots by stacking them horizontally using a lay-down procedure similar to Figure 6.1. However, one of the main problems with this procedure is that operators can unintentionally put the crane in side-pull situations, where the hoist cable angle is too large. This is a costly problem for Alcoa due to the frequent down-times that are required to repair the rubbing hoist cables and other crane components.

6.1 Lay-Down Dynamics

Figure 6.2(a) illustrates the dynamic model of the lay-down process and Figure 6.2(b) is the payload's free body diagram. The following describes the model and its assumptions:

1. Establishing the pivot is not considered here. This is a highly-skilled task that is more suitable for manual operation. This is because establishing the pivot involves collisions, sliding, and stiction between surfaces. An automated solution would be impractical, as it would require many expensive sensors or extensive hardware modifications. Therefore, this research considers steps 2-4 in Figure 6.1.

2. The payload has a width (into/out of the page) such that it has sufficient stability in the out of plane direction. Therefore, out of plane movements (e.g. buckling or trolley motions in that direction) are not considered. The payload length is also much greater than its thickness.

3. The pivot point, O, is the origin of the cartesian coordinate reference frame. The frame axes unit vectors are i and j, as indicated in Figure 6.2(a).

4. The payload is modeled as a uniform slender beam of length L, pinned on the lower end at the pivot (assuming the pivot never moves), O. The payload angle from vertical is ϕ.

5. The higher end of the payload, P, is attached to a hoist cable of variable length, l. The angle of the cable relative to vertical is θ.

6. The other end of the hoist cable is attached to the trolley, which is assumed to be a movable point, and is located at a constant height, H, above the ground. The trolley motor controls the horizontal position, x, and its time derivatives, $\dot{x}$, and $\ddot{x}$.

7. The cable is modeled as a massless stiff rod, because it is assumed that the payload mass is much larger than that of the cable. Additionally, the cable must always be in tension. The hoist motor controls the length of the cable, l, and its time derivatives, $\dot{l}$ and $\ddot{l}$.

8. The freebody diagram in Figure 6.2(b) shows four forces acting on the payload: cable tension, T; gravity, mg, acting at the mass center, G; and the reaction forces at O - F_i and F_j.

9. The system has two degrees of freedom. However, there are four generalized coordinates of interest: ϕ, θ, x, and l. Specifying any two coordinates completely determines the configuration of the entire system.[1]

6.1.1 Range of Motions and Coordinate Relationships

The range of payload angles, ϕ, that are considered in this investigation is from 5° (nearly vertical position, after the operator has manually established the pivot) to 90° (horizontal position):

$$5^\circ < \phi < 90^\circ \tag{6.1}$$

The range of hoist cable angles, θ, that are considered is:

$$-90^\circ < \theta < \phi \tag{6.2}$$

The configuration specified by the lower bound indicates that x would be $-\infty$, which is physically impossible. The hoist cable angle upper-bound is ϕ, because as Figure 6.3(a) shows, a configuration with $\theta > \phi$ is physically unstable. In these cases, the payload rotates under gravity to a more stable configuration, such that $\theta < \phi$, as shown in Figure 6.3(b). Note that the position of the trolley, x, and the cable length, l, is the same in both configurations.

The following are positional constraints in the i and j directions that give the relationship between all four coordinates of interest: ϕ, θ, x, and l.

$$L\cos\phi + l\cos\theta - H = 0 \tag{6.3}$$

$$L\sin\phi + l\sin\theta - x = 0 \tag{6.4}$$

6.1.2 Equations of Motion

The derivation of the dynamic equations of motion for the payload begins with the position vector from the pivot, O, to the payload mass center, G:

$$\overline{r}_{G/O} = \frac{L}{2}(\sin\phi\overline{i} + \cos\phi\overline{j}) \tag{6.5}$$

[1] If x and l are specified, then there are two possibilities for θ and ϕ. However, it will be shown that one of these possibilities is physically unstable.

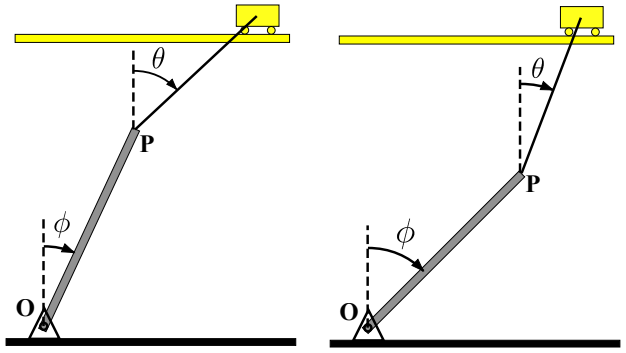

(a) Unstable (b) Stable

Figure 6.3: Unstable and Stable ϕ θ Configurations

The acceleration of G is found by differentiating with respect to time:

$$\begin{aligned}\overline{a}_G &= -\ddot{\phi}\overline{k} \times \overline{r}_{G/O} - \dot{\phi}\overline{k} \times (-\dot{\phi}\overline{k} \times \overline{r}_{G/O}) \\ &= \frac{L}{2}\left((\ddot{\phi}\cos\phi - \dot{\phi}^2\sin\phi)\overline{i} + (-\ddot{\phi}\sin\phi - \dot{\phi}^2\cos\phi)\overline{j}\right) \end{aligned} \tag{6.6}$$

Given $\overline{a}_G$, the equations of motion can be derived in terms of ϕ and θ. First, the sum of moments about point O is:

$$\begin{aligned}\sum M_O &= -I\ddot{\phi} \\ \Rightarrow TL(\cos\theta\sin\phi - \sin\theta\cos\phi) - \frac{1}{2}mgL\sin\phi &= -I\ddot{\phi}\end{aligned} \tag{6.7}$$

where $I = \frac{1}{3}mL^2$ is the payload moment of inertia about O. Next, the sum of forces in $\overline{i}$ is:

$$\begin{aligned}\sum F \cdot \overline{i} &= m\overline{a}_G \cdot \overline{i} \\ \Rightarrow F_i + T\sin\theta &= \frac{1}{2}mL(\ddot{\phi}\cos\phi - \dot{\phi}^2\sin\phi)\end{aligned} \tag{6.8}$$

And the sum of forces in $\overline{j}$ is:

$$\begin{aligned}\sum F \cdot \overline{j} &= m\overline{a}_G \cdot \overline{j} \\ \Rightarrow F_j + T\cos\theta - mg &= \frac{1}{2}mL(-\ddot{\phi}\sin\phi - \dot{\phi}^2\cos\phi)\end{aligned} \tag{6.9}$$

6.1.3 Successful Lay-Down Conditions: Force Constraints

The primary condition for a successful lay-down maneuver, i.e. if the motion is stable in the dynamic sense, is that the pivot must not slip:

$$\left|\frac{F_i}{F_j}\right| \leq \mu_{static} \tag{6.10}$$

where μ_{static} is the dry static coefficient of friction between the payload and the ground. Additionally, the payload must always maintain contact with the surface at the pivot:

$$F_j \geq 0 \tag{6.11}$$

and the cable must always be in tension:

$$T \geq 0 \tag{6.12}$$

Collectively, the above conditions are known as force constraints.

6.2 Allowable Static Configurations

To determine how to best lay down the payload, it is important to know bounds at which the system configuration becomes unstable. The first step in this investigation is to consider only the static case. That is, accelerations and velocities are set to zero such that the equations of motion are reduced to equations that balance forces and moments in static equilibrium:

$$\begin{aligned} TL(\cos\theta\sin\phi - \sin\theta\cos\phi) - \frac{1}{2}mgL\sin\phi = 0 \\ F_i + T\sin\theta = 0 \\ F_j + T\cos\theta - mg = 0 \end{aligned}$$

The above equations can be rearranged to explicitly show T, F_i, and F_j:

$$T = \frac{mg\sin\phi}{2\sin(\phi-\theta)} \tag{6.13}$$

$$F_i = -\frac{mg\sin\theta\sin\phi}{2\sin(\phi-\theta)} \tag{6.14}$$

$$F_j = \frac{mg(\sin\phi\cos\theta - 2\cos\phi\sin\theta)}{2\sin(\phi-\theta)} \tag{6.15}$$

Then, for each ϕ and θ in the range of payload and hoist cable angles being considered, it can be determined whether the configuration is statically allowable, i.e. if the force constraints in (6.10), (6.11), and (6.12) are satisfied. The range of statically stable and allowable configurations can then be determined.

6.2.1 Constraint on Cable Tension

By inspection, (6.13) is always positive, because $\sin\phi > 0$ for the range of ϕ being considered in (6.1); and $\sin(\phi-\theta) > 0$ because $\phi > \theta$ at all times due to (6.2). Therefore, the constraint on the cable always being in tension, (6.12), is always satisfied.

6.2.2 Constraint on Pivot Contact

The equation for F_j in (6.15), is used to determine whether the constraint on pivot contact with the surface, (6.11), is satisfied. By inspection, $\sin\phi\cos\theta - 2\cos\phi\sin\theta \geq 0$ needs to be true in order to satisfy this constraint. Therefore, the condition on θ for pivot contact is:

$$\theta \leq \theta_c = \arctan\left(\frac{1}{2}\tan\phi\right) \tag{6.16}$$

6.2.3 Constraint on Pivot Slip

To determine the conditions on pivot slip, F_i from (6.15) is divided by F_j from (6.14) to yield:

$$\left|\frac{F_i}{F_j}\right| = \left|\frac{-\sin\phi\sin\theta}{\sin\phi\cos\theta - 2\cos\phi\sin\theta}\right|$$

This is then evaluated with the constraint on pivot slip, (6.10), to determine the range of hoist cable angles where the pivot does not slip. Defining:

$$\theta_{\mu 1} = -\arctan\frac{\mu_{static}\sin\phi}{\sin\phi - 2\mu_{static}\cos\phi}, -\frac{\pi}{2} \leq \theta_{\mu 1} \leq \frac{\pi}{2}$$

$$\theta_{\mu 2} = \arctan\frac{\mu_{static}\sin\phi}{\sin\phi + 2\mu_{static}\cos\phi}, -\frac{\pi}{2} \leq \theta_{\mu 2} \leq \frac{\pi}{2}$$

Table 6.1: Aluminum Ingot Lay-Down Example: Crane and Payload Parameters

Parameter	Value
m	8400 kg
L	10 m
H	12 m
μ_{static}	0.6 (Aluminum and mild steel, dry)

the conditional cases on θ such that the pivot does not slip are:

$$\theta_{\mu 1} \leq \theta \leq \theta_{\mu 2}, \qquad \text{if } \theta_{\mu 1} < \theta_{\mu 2} \tag{6.17}$$

$$\theta \geq \theta_{\mu 1} \text{ OR } \theta \leq \theta_{\mu 2}, \qquad \text{if } \theta_{\mu 1} > \theta_{\mu 2} \tag{6.18}$$

Note that $\theta_{\mu 1} \neq \theta_{\mu 2}$ for the range of ϕ considered in this investigation.

6.2.4 Algorithm for Finding the Range of Allowable Static Configurations

The allowable static configurations are found by evaluating whether the constraints are satisfied by iterating though the entire range of ϕ's θ's:

for $\phi = \phi$'s in the range specified by (6.1) **do**
  for $\theta = \theta$'s in the range specified by (6.2) **do**
    if (6.16) AND (6.17) AND (6.18) are satisfied **then**
      The configuration is statically allowable.
    else
      The configuration is not statically allowable.
    end if
  end for
end for

One insight to be gained from (6.16), (6.17), and (6.18) is that in the static case, the inequalities that describe the allowable configurations are only dependent on ϕ and μ_{static}. Therefore, these constraints are applicable to all payloads regardless of size, L, and mass, m.

6.3 Allowable Static Configurations Example

An example with the crane and payload parameters in Table 6.1 is used to illustrate the process of finding allowable static configurations. These parameters reflect a typical aluminum ingot lay-down application.

Figure 6.4(a) shows the forces, T, F_i, and F_j as a function of θ, for $\phi = 10°$. This is the case when the payload is close to a vertical position near the start of lay-down. Note that if $\theta = -90°$, then the trolley is located at $-\infty$; if $\theta = 0°$, then the trolley is located directly over the upper end of the payload. Figure 6.4(a) shows that as the cable angle approaches 0° from -90°, the cable tension increases, but the vertical pivot force, F_j, decreases. This makes sense, because as the cable angle becomes more vertical, an increasing portion of the payload's weight is supported by the cable tension, rather than the contact at the pivot. The critical angle at which the pivot begins to lose contact with the surface, i.e. when $F_j = 0$, is indicated on the figure as θ_c. In this case, the payload will lose pivot contact when θ increases beyond a few degrees above 0. Also, note that pivot horizontal forces, F_i, are relatively small until θ approaches the value of ϕ (10°).

Figure 6.4(b) shows the ratio of horizontal to vertical pivot force, $\left|\frac{F_i}{F_j}\right|$, for the same range of configurations. In this case, $\theta_{\mu 1} > \theta_{\mu 2}$, so the range of θ's that satisfy the pivot slip constraint is given by (6.18). The figure also shows that $\left|\frac{F_i}{F_j}\right|$ will exceed μ_{static} (i.e. the pivot will slip) in a

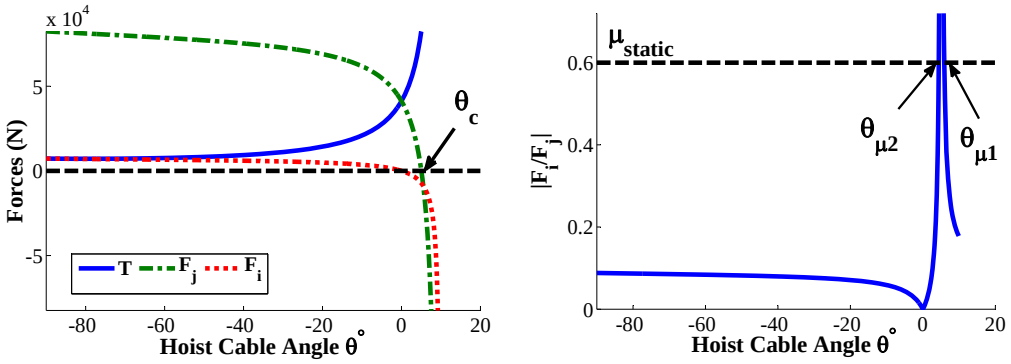

(a) Forces (b) $\left|\frac{F_i}{F_j}\right|$

Figure 6.4: Example Static Case, $\phi = 10°$

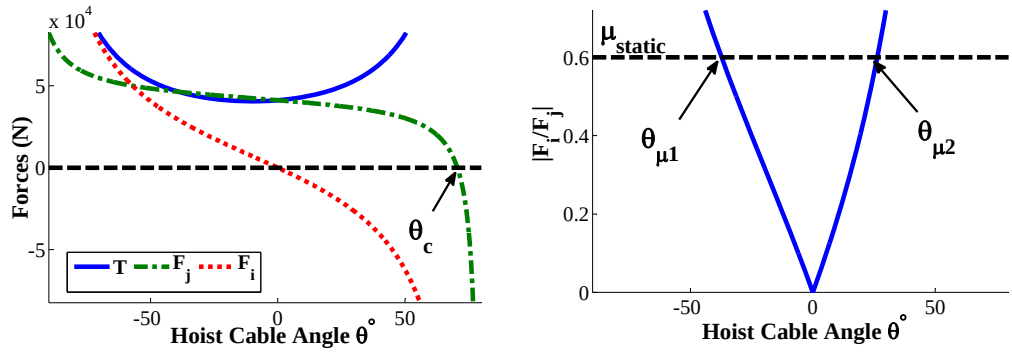

(a) Forces (b) $\left|\frac{F_i}{F_j}\right|$

Figure 6.5: Example Static Case, $\phi = 80°$

narrow range between $\theta_{\mu 1}$ and $\theta_{\mu 2}$. However, note that this may be inconsequential, depending on the location of θ_c in Figure 6.4(a). For example, if $\theta_c < \theta_{\mu 2}$, then the pivot would have already lost contact before it can slip.

Figure 6.5(a) shows similar force information for a payload angle of $\phi = 80°$. This is a case when the payload is close to a horizontal position near the end of lay-down. In contrast to $\phi = 10°$ in Figure 6.4(a), the magnitude of the horizontal pivot force, F_i is significant across the entire range of θ's. Larger horizontal forces create greater propensities for the pivot to slip sideways. The cable tensions are also high across this range of θ's. This indicates the cable plays a significant role in supporting the weight of the payload. Finally, the plot also indicates the location of θ_c, where the pivot will begin to lose contact. Similar to Figure 6.4(a), it is worthy to note that the vertical pivot force, F_j, rapidly decreases and becomes negative only when θ approaches the value of ϕ.

Figure 6.5(b) shows $\left|\frac{F_i}{F_j}\right|$ for the payload angle $\phi = 80°$. In this case, $\theta_{\mu 1} < \theta_{\mu 2}$, so the range of θ's that satisfy the pivot slip constraint is given by (6.17). The figure shows that $\left|\frac{F_i}{F_j}\right|$ will exceed μ_{static} (i.e. the pivot will slip) if $\theta < \theta_{\mu 1}$ or $\theta > \theta_{\mu 2}$.

6.3.1 Allowable Configurations for All Payload Angles, ϕ

Figure 6.6(a) shows the allowable static configurations, indicated by area between the boundaries, across the entire range of payload angles (ϕ) and hoist cable angles (θ). The boundaries are found by

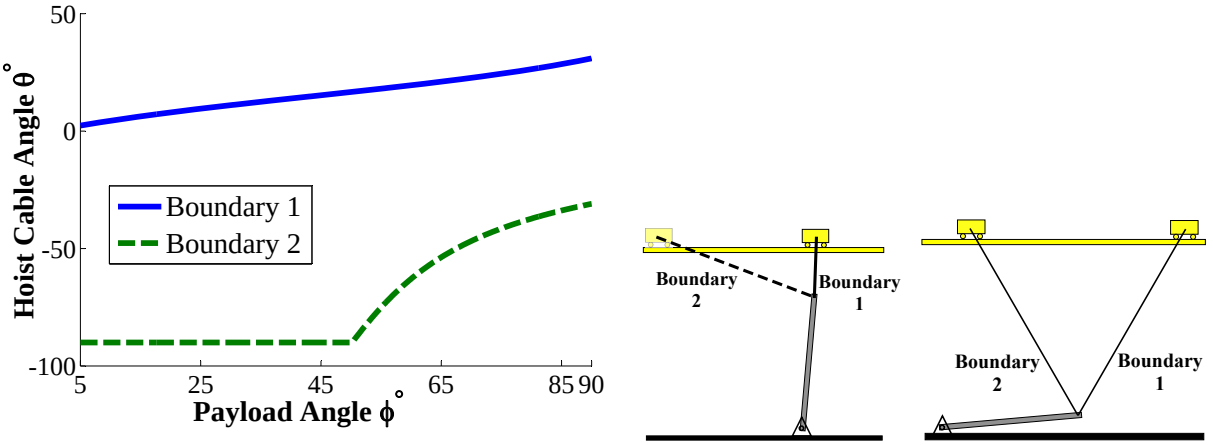

(a) Payload Angle, ϕ, vs. Cable Angle, θ (b) $\phi = 5°$ (c) $\phi = 85°$

Figure 6.6: Allowable Static Configurations

applying the algorithm in Section 6.2.4. For each ϕ, the boundaries indicate the θ's that satisfy all constraints, namely, (6.16), (6.17), and (6.18). Figure 6.6(a) shows the range of allowable θ's begins to narrow as ϕ is increased beyond 50°. This is because the constraint on pivot slip transitions from (6.18) to (6.17), which eliminates a larger range of θ's. One noteworthy feature is that boundary 1 increases in an almost linear fashion from $\theta = 0°$ to $\theta \approx 30°$.

When ϕ is below 50°, boundary 2 is $\theta = -90°$. This is effectively a non-existent boundary, because it means the trolley is allowed to be very far behind the payload, at $-\infty$, and the hoist cable would be at infinite length. This is illustrated in Figure 6.6(b), which shows the boundary configurations when the payload angle is $\phi = 5°$. Note that the trolley is transparent and the hoist cable is dashed to indicate that boundary 2 does not correlate with finite trolley positions and hoist cable lengths. Also, as the figure illustrates, when the payload is at this angle, having a near vertical hoist cable angle (or alternatively, positioning the trolley directly above the payload) is actually quite close to static instability. Figure 6.6(c) shows the configurations at the boundaries when the payload angle is $\phi = 85°$. In this case, both boundaries correlate to finite trolley positions and hoist cable lengths.

The allowable configurations, specified by boundaries in terms of payload and hoist cable angles from Figure 6.6(a), can also be specified in terms of trolley positions and hoist cable lengths. In this way, the boundaries become more relevant, because only the trolley position and hoist cable lengths can be directly controlled. Figure 6.7(a) plots the boundaries of acceptable configurations in terms of payload angle versus the trolley position. Figure 6.7(b) shows similar information for payload angle versus the hoist cable length. Recall from Figure 6.6(a) that boundary 2 for the hoist cable angle is$\theta = -90°$ at payload angle $\phi = 50°$. Therefore, as ϕ approaches 50°, the boundary 2 trolley position approaches $x = -\infty$ in Figure 6.7(a), and the boundary 2 hoist cable length approaches $l = \infty$ in Figure 6.7(b).

6.3.2 Lay-Down Trajectory

The information from Figures 6.7(a) and 6.7(b) can be combined to show the range of allowable configurations in terms of the payload angle, trolley position, and hoist cable length. This can be accomplished by rearranging and adding the squares of positional constraints in (6.3) and (6.4) to

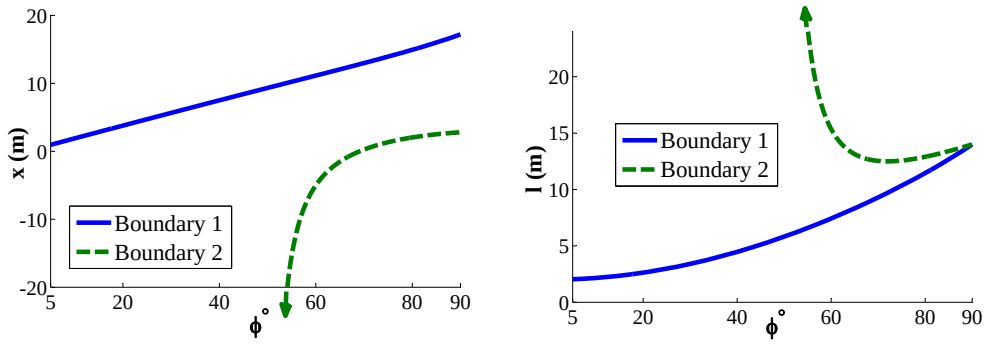

(a) Payload Angle, ϕ, vs. Trolley Position, x (b) Payload Angle, ϕ vs. Hoist Cable Length, l

Figure 6.7: Allowable Static Configurations

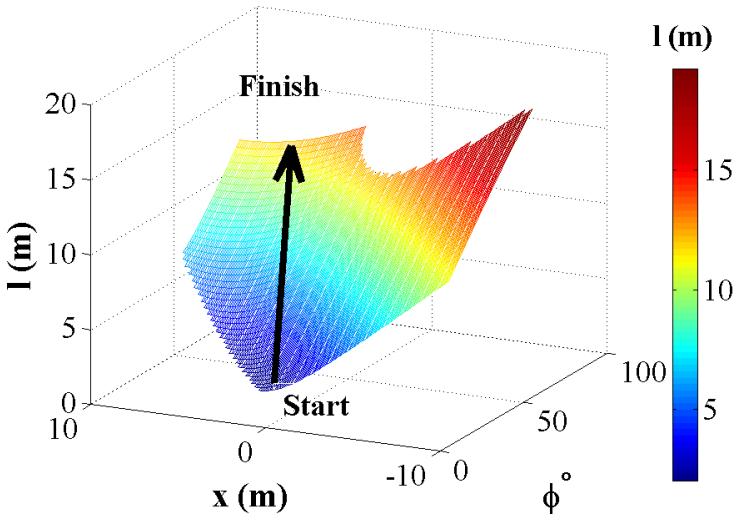

Figure 6.8: Allowable Static Configurations: Payload Angle, ϕ, vs. Trolley Position, x, vs. Hoist Cable Length, l

obtain an equation that eliminates θ and relates ϕ to x and l:

$$\begin{aligned} l^2\cos^2\theta &= (H - L\cos\phi)^2 \\ l^2\sin^2\theta &= (x - L\sin\phi)^2 \\ \Rightarrow l^2 &= H^2 + x^2 + L^2 - 2L(H\cos(\phi) + x\sin(\phi)) \end{aligned} \tag{6.19}$$

where H is the trolley height and L is the payload length. This information is plotted as a surface in Figure 6.8. Note the surface extends to $x = -\infty$ and $l = \infty$, but only the appropriate ranges of x and l are shown. Recall the system only has 2 DOF. Specifying the payload angle and trolley position produces a unique value for the hoist cable length. However, as Figure 6.8 shows, specifying the payload angle and a hoist cable length may produce two non-unique values for the trolley position.

The benefit of visualizing the allowable configurations in this way is that by traversing along the surface, a trajectory from start to finish can be constructed for a lay-down maneuver. For example, such a trajectory is represented by the arrow in Figure 6.8. The trajectory starts at payload angle $\phi = 5°$ and finishes when it is completely laid down at $\phi = 90°$. An automated controller can

execute the lay-down maneuver by positioning the trolley and changing the hoist cable length to follow the trajectory. Furthermore, Figure 6.8 shows the trajectory's proximity to the boundaries of allowable configurations, i.e. the edges of the surface. This information can be used to improve the robustness in the selection of trajectories. For example, robust trajectories would not traverse close to the boundaries.

6.4 Allowable Dynamic Configurations

This investigation can be extended to account for the full dynamic effects captured in (6.7), (6.8), and (6.9). Similar to the static case, the goal is to find system configurations where the force constraints in (6.10), (6.11), and (6.12) are satisfied. However, in the dynamic case, additional motor constraints are applied to limit the velocities and accelerations of the trolley and hoist motors:

$$|\dot{x}| \leq \dot{x}_{max} \tag{6.20}$$

$$|\ddot{x}| \leq \ddot{x}_{max} \tag{6.21}$$

$$|\dot{l}| \leq \dot{l}_{max} \tag{6.22}$$

$$|\ddot{l}| \leq \ddot{l}_{max} \tag{6.23}$$

where $\dot{x}_{max}$ and $\ddot{x}_{max}$ are the maximum trolley velocity and acceleration; and $\dot{l}_{max}$, and $\ddot{l}_{max}$ are the maximum hoist velocity and acceleration. The steps required to find the allowable dynamic configurations are:

1. Incorporate trolley and hoist motor limits using kinematic relationships between x, l, ϕ, and their time derivatives.
2. Do the following steps for all possible configurations to find the range of allowable dynamic configurations:
   (a) For a given configuration, use the motor limits to determine the maximum and minimum values that $\dot{\phi}$ and $\ddot{\phi}$ could have. (It will be clear later that solving for allowable configurations in terms of $\dot{\phi}$ and $\ddot{\phi}$ is a more tractable problem than solving in terms of $\dot{x}, \ddot{x}, \dot{l}, \ddot{l}$.)
   (b) For a given configuration, if the bounds on $\dot{\phi}$ and $\ddot{\phi}$ are known, then the bounds on the forces acting on the payload (T, F_i, F_j) can be determined. This is can be done by using the equations of motion (6.7), (6.8), and (6.9).
   (c) For a given configuration, if the bounds on the forces acting on the payload are known, then it can be ascertained whether the force constraints, (6.10), (6.11), and (6.12), can be violated.

6.4.1 Kinematic Relationships Between x, l, ϕ and Their Time Derivatives

Because no time derivatives of θ appear in the dynamic equations of motion, a kinematic relationship needs to be established between the time derivatives of x, l, and ϕ. This is can be obtained from (6.19). Then, differentiating (6.19) with respect to time twice and rearranging to obtain $\dot{\phi}$ and $\ddot{\phi}$ yields:

$$\dot{\phi} = \frac{l\dot{l} - x\dot{x} + L\dot{x}\sin\phi}{L(H\sin\phi - x\cos\phi)} = f(\dot{x}, \dot{l}) \tag{6.24}$$

$$\ddot{\phi} = \frac{l\ddot{l} - x\ddot{x} + L\left(\ddot{x}\sin\phi + 2\dot{\phi}\dot{x}\cos\phi - H\dot{\phi}^2\cos\phi - \dot{\phi}^2 x\sin\phi\right) + \dot{l}^2 - \dot{x}^2}{L\left(H\sin\phi - x\cos\phi\right)} \tag{6.25}$$

6.4.2 Maximum and Minimum Bounds on $\dot{\phi}$ and $\ddot{\phi}$

For a given configuration (θ, ϕ, x, l are fixed), (6.24) indicates that $\dot{\phi}$ is a linear function of $\dot{x}$ and $\dot{l}$. Therefore, for a given configuration, the maximum and minimum values of $\dot{\phi}$ are:

$$\dot{\phi}_{max} = \max\left(f(\pm\dot{x}_{max}, \pm\dot{l}_{max})\right) \tag{6.26}$$

$$\dot{\phi}_{min} = \min\left(f(\pm\dot{x}_{max}, \pm\dot{l}_{max})\right) \tag{6.27}$$

The equation for $\ddot{\phi}$ is more complicated, and is not linear with respect to $\dot{x}, \ddot{x}, \dot{l}, \ddot{l}$. Therefore, for a given a configuration, the maximum and minimum values of $\ddot{\phi}$ can be found by using an optimization program such as Matlab's 'fmincon'. The objective is to find a vector, $[\dot{x}, \ddot{x}, \dot{l}, \ddot{l}]$ (subjected to motor constraints (6.20) - (6.23)), such that it maximizes or minimizes the value of (6.25).

6.4.3 Forces Acting on the Payload

For a given configuration (ϕ and θ are treated as constants), solving for the cable tension, T, using (6.7) yields a linear function with respect to $\ddot{\phi}$:

$$\begin{aligned} T &= \frac{-I\ddot{\phi} + \frac{1}{2}mgL\sin\phi}{L(\cos\theta\sin\phi - \sin\theta\cos\phi)} \\ &= C_1\ddot{\phi} + C_2 \end{aligned} \tag{6.28}$$

where C_1 and C_2 are constants. Similarly, solving for F_i and F_j from (6.8) and (6.9) yields linear functions in terms of $\ddot{\phi}$ and $\dot{\phi}^2$:

$$\begin{aligned} F_i &= \frac{1}{2}mL(\ddot{\phi}\cos\phi - \dot{\phi}^2\sin\phi) - (C_1\ddot{\phi} + C_2)\sin\theta \\ &= C_3\ddot{\phi} + C_4\dot{\phi}^2 + C_5 \end{aligned} \tag{6.29}$$

$$\begin{aligned} F_j &= \frac{1}{2}mL(-\ddot{\phi}\sin\phi - \dot{\phi}^2\cos\phi) + mg - (C_1\ddot{\phi} + C_2)\cos\theta \\ &= C_6\ddot{\phi} + C_7\dot{\phi}^2 + C_8 \end{aligned} \tag{6.30}$$

6.4.4 Determining if Forces Acting on the Payload Will Violate Constraints

The sets in $\mathbb{R}^2$ that describe the conditions where the force constraints (6.10), (6.11), and (6.12) are ***not satisfied*** are:

$$Q_1 = \left\{\ddot{\phi}, \dot{\phi}^2 : C_6\ddot{\phi} + C_7\dot{\phi}^2 + C_8 < 0\right\} \tag{6.31}$$

$$Q_2 = \left\{\ddot{\phi}, \dot{\phi}^2 : C_1\ddot{\phi} + C_2 < 0\right\} \tag{6.32}$$

$$Q_3 = \left\{\ddot{\phi}, \dot{\phi}^2 : \left|\frac{C_3\ddot{\phi} + C_4\dot{\phi}^2 + C_5}{C_6\ddot{\phi} + C_7\dot{\phi}^2 + C_8}\right| > \mu_{static}\right\} \tag{6.33}$$

Also, trolley and hoist motor limits impose maximum and minimum values on $\ddot{\phi}$ and $\dot{\phi}$:

$$R = \left\{\ddot{\phi}, \dot{\phi}^2 : \ddot{\phi}_{min} \le \phi \le \ddot{\phi}_{max}, 0 \le \dot{\phi}^2 \le \max\left((\dot{\phi}_{max})^2, (\dot{\phi}_{min})^2\right)\right\} \tag{6.34}$$

where $\ddot{\phi}_{min}$ and $\ddot{\phi}_{max}$ are found by the optimization procedure described above, and $\dot{\phi}_{min}$ and $\dot{\phi}_{max}$ are from (6.27) and (6.26).

Given the above information, the following algorithm is used to determine the allowable dynamic configurations:

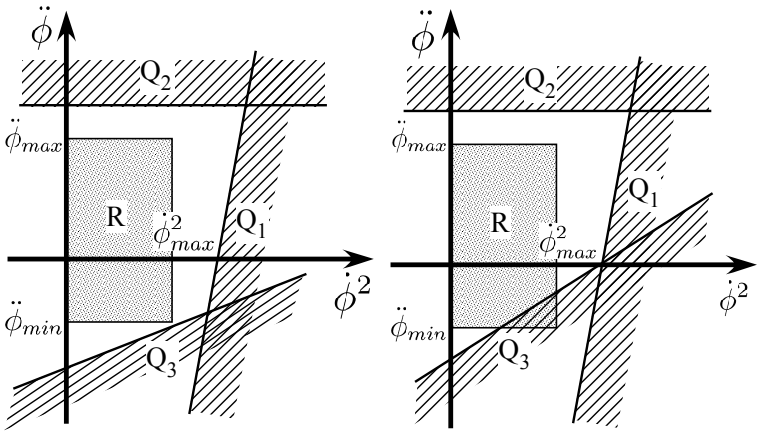

(a) Allowable Configuration (b) Unallowable Configuration

Figure 6.9: Q_i and R regions in the $\ddot{\phi}$ vs. $\dot{\phi}^2$ space

for $\phi = \phi$'s in the range specified by (6.1) **do**
  for $\theta = \theta$'s in the range specified by (6.2) **do**
    if $(Q_1 \cup Q_2 \cup Q_3) \cap R = \varnothing$ **then**
      The configuration is dynamically allowable.
    else
      The configuration is not dynamically allowable.
    end if
  end for
end for

For each configuration, if the algorithm does not find a $[\ddot{\phi}, \dot{\phi}]$ (bounded by motor limits) that can violate any of the force constraints, then the configuration is dynamically allowed; otherwise the configuration is not allowed. The corollary of using the motor limits is that the algorithm assumes the motors operate at maximum velocities and/or accelerations, where the force constraints are most likely to be violated. Therefore, the worst case scenario is always assumed. The benefit of this approach is that the resulting range of allowable dynamic configurations are always guaranteed to be stable.

Note that if a configuration is dynamically unallowable, then it is *possible* to find a set of motor commands that can destabilize the payload. This does not mean the system will *always* destabilize if the system moves to a dynamically unallowable configuration. It is still possible for that configuration to be stable, if the system is moving below the motor limits, for example.

The sets of Q_i and R are depicted over the $\ddot{\phi}$ vs. $\dot{\phi}^2$ space in Figure 6.9. The Q_i sets are represented by linear straight lines, shaded on one side for the inequality. The R set is represented as a rectangle. If no Q_i regions intersect R, as in Figure 6.9a, then the configuration is allowable. Otherwise it is not allowable, as illustrated in Figure 6.9b.

6.4.5 Notes on Implementation

The critical part of the solution algorithm, $(Q_1 \cup Q_2 \cup Q_3) \cap R$, is a challenging problem to solve. Note that the statement is not about finding ***a*** solution within a subspace. Rather, it is strict in the sense that it ascertains whether there are ***any*** solutions that exist within the subspace. The statement is implemented using Matlab's MuPAD symbolic engine, which is capable of evaluating inequalities and set operations.

The choice was made earlier to convert the trolley and hoist motor limits into boundaries on the

Table 6.2: Aluminum Ingot Lay-Down Example: Motor Parameters

Parameter	Value
$\dot{x}_{max}$	0.3 m/s
$\ddot{x}_{max}$	0.2 m/s
$\dot{l}_{max}$	0.2 m/s
$\ddot{l}_{max}$	0.1 m/s

values of $\ddot{\phi}$ and $\dot{\phi}$. The reason for this is that evaluating $(Q_1 \cup Q_2 \cup Q_3) \cap R$ involves relatively simple intersections and unions of linear inequalities in two variables. If the problem was formulated in terms of $[\dot{x}, \ddot{x}, \dot{l}, \ddot{l}]$, then the solution procedure would involve nonlinear inequalities in four variables. This would make the problem much more difficult and increase the solve time beyond acceptable limits.

To save time, rather than iterating through the entire range of hoist cable angle θ's, the lower θ bound of allowable dynamic configurations can instead be found by:

1. For a given payload angle, ϕ, start from the value of the lower θ bound in the static case, e.g. 'Boundary 2' in Figure 6.6(a).

2. Increase θ until an allowable dynamic configuration is found. This value of θ forms the lower bound for the dynamic case.

3. The upper bound for the dynamic case can be found in a similar but reversed manner.

4. Move to the next value of ϕ.

Note that this method does not examine every θ, and assumes that the region of allowable dynamic configurations is contiguous over the θ space, and is bounded on two sides by the lower- and upper-bounds. The justification for iterating up/down from the static lower/upper bounds is that the θ boundaries in the dynamic case are equal to or less than the static case. This is because the forces in the static equations of motion, (6.13), (6.14), and (6.15), are a subset of the forces that can be experienced in the dynamic case.

Another time-saving method is to rewrite (6.33) as two sets. One with $C_3\ddot{\phi} + C_4\dot{\phi}^2 + C_5 > \mu_{static}(C_6\ddot{\phi} + C_7\dot{\phi}^2 + C_8)$ and the second with $-(C_3\ddot{\phi} + C_4\dot{\phi}^2 + C_5) > \mu_{static}(C_6\ddot{\phi} + C_7\dot{\phi}^2 + C_8)$ as the conditional expressions. This decomposition shortens the solve time because it is computationally more complex for the symbolic solver to evaluate inequalities involving absolute functions and fractions.

6.5 Example of Allowable Dynamic Configurations

This example uses the same crane and payload parameters as the ones from the static case in Table 6.1. Trolley and hoist motor limits that are typical for cranes of that size are listed in Table 6.2.

Figure 6.10(a) illustrates the boundaries of allowable dynamic configurations (solid lines) plotted in the θ vs. ϕ space. The boundaries for the static case are also shown in dotted lines. In this case, the difference between the static and dynamic boundaries is not significant. Therefore, the static allowable configurations can be used to build the lay-down trajectory, as was discussed with Figure 6.8.

If the motor limits in Table 6.2 are each increased ten-fold, then the allowable configurations are shown in Figure 6.10(b). Due to greater levels of forces that can be generated by faster motors, the dynamic bounds in this case are noticeably smaller than the static bounds (although the dynamic boundary 2 and static boundary 2 are very similar). Note that no allowable dynamic configurations exist for $\phi < 12°$. This does not mean that the lay-down maneuver is impossible when $\phi < 12°$.

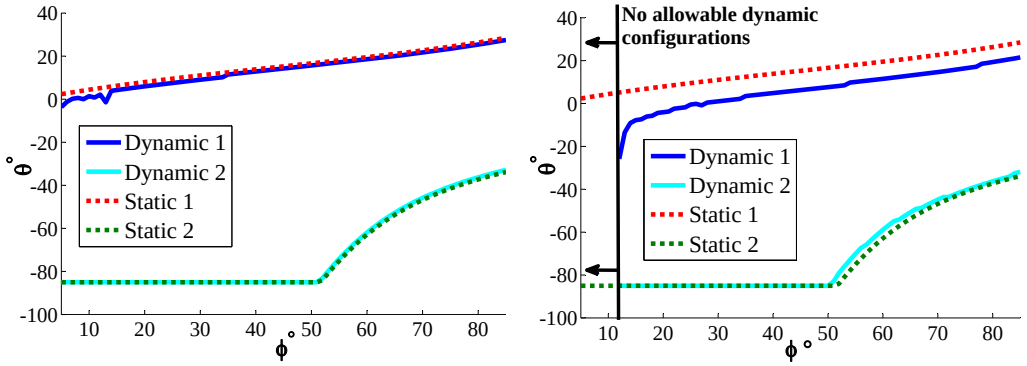

(a) Nominal Motor Limits

(b) Motor Limits ×10

Figure 6.10: Allowable Dynamic Configurations, Payload Angle, ϕ, vs. Cable Angle, θ

Rather, for configurations with $\phi < 12°$, it is possible to find a set of motor commands that violate constraints.

6.6 Including Additional Constraints

So far, the static and dynamic stability have been the main consideration for determining the range of allowable configurations, which can then be used to generate appropriate lay-down trajectories. The criteria for stability are determined by the force constraints, (6.10), (6.11), and (6.12). Considerations for other aspects can also be taken into account by incorporating additional constraints.

6.6.1 Constraint on Limiting Side-Pull

As mentioned in the beginning of this chapter, during lay-down maneuvers, the hoist cable angle may become too large, resulting in the side-pull problem. Preventing side-pull can be incorporated as an extra constraint on the hoist cable angle, θ, (in addition to the existing force constraints) when the range of allowable configurations are determined. This constraint can be formulated as:

$$|\theta| \leq \theta_{max} \tag{6.35}$$

Where θ_{max} is the maximum acceptable hoist cable angle. By revisiting the aluminum ingot example in Sections 6.3 and 6.5, the side-pull constraint can be added by setting the maximum allowed hoist cable angle to $\theta_{max} = 10°$. Recall from Figure 6.10(a) that for this case, the allowable dynamic boundaries are practically identical to the static boundaries. Therefore, the allowable configurations can be adequately determined using the static boundaries alone.

Figure 6.11(a) plots the static boundaries and the side-pull boundaries from (6.35) in the $\phi - \theta$ space. The hashed region represents the allowable configurations that satisfy both sets of boundaries. Notice that the side-pull constraints greatly reduces the range of allowable configurations from the static case.

Figure 6.11(b) shows the narrow range of allowable configurations in the $\phi - x - l$ space. This surface is useful because it shows the allowable configurations in terms of the controllable: trolley position, x, and hoist cable length, l. The curved arrow represents an exemplary lay-down trajectory that moves the payload from the start from $\phi = 5°$ to the finish at $\phi = 90°$. An automated controller can execute the lay-down maneuver while also avoiding side-pull, by positioning the trolley and changing the hoist cable length to follow this trajectory. Note the trajectory runs through the middle of the surface in order to maximize robustness. Also, the range of allowable configurations is quite narrow near the start (indicating less room for movement errors), but broadens towards the finish.

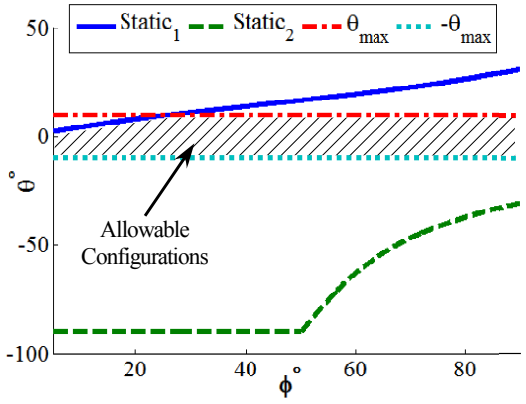

(a) Payload Angle, ϕ, vs. Cable Angle, θ

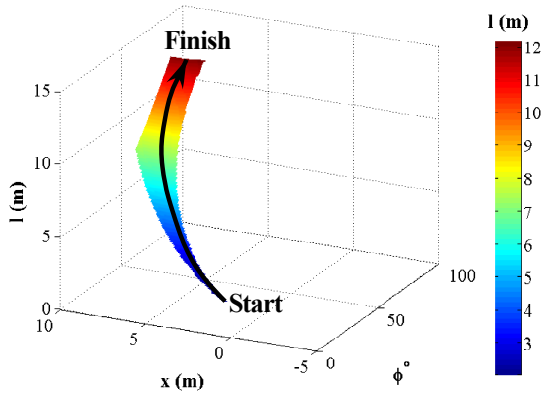

(b) Payload Angle, ϕ, vs. Trolley Position, x, vs. Hoist Cable Length, l

Figure 6.11: Allowable Configurations with Side-Pull Constraint

Table 6.3: Wooden-Box Lay-Down Experimental Parameter Values

Parameter	Value	Parameter	Value
m	33 kg	$\dot{x}_{max}$	0.32 m/s
L	2.16 m	$\ddot{x}_{max}$	0.2 m/s
H	6.37 m	$\dot{l}_{max}$	0.12 m/s
μ_{static}	0.32	$\ddot{l}_{max}$	0.1 m/s

6.6.2 Other Constraints

The methods presented in this chapter determine the range of allowable configurations during a lay-down maneuver. The lay-down maneuver comes from a trajectory that traverses on the surface of allowable configurations, from the starting payload position to the finishing position. However, there are infinite possible trajectories. The selection of the specific trajectory is left to the controller designer, and is beyond the scope of this dissertation. Further constraints and/or optimizations can be incorporated to obtain lay-down trajectories that accomplish different goals, such as:

- Minimizing the move time.
- Maximizing the robustness of the trajectory to errors by maximizing the 'distances' between the trajectory and the boundaries of allowable configurations.

6.7 Example Lay-Down Using the HiBay Crane

The methods proposed in this chapter are demonstrated in an example lay-down maneuver using the HiBay crane and a long wooden box. Figure 6.12(a) is a picture that shows the experimental setup, when the payload is positioned close to upright at the start of the lay-down maneuver. Figure 6.12(b) shows the payload in the finish position. Note there is a hook that connects the hoist cables to the payload. However, for the purpose of this demonstration, the effects of the hook can be neglected. The estimated parameters used to determine the theoretical allowable configurations are listed in Table 6.3.

Figure 6.13(a) shows the static and dynamic boundaries of allowable configurations in the payload angle, $\phi - \theta$ space. Two features are worth noting: 1) compared to the aluminum ingot example, the range of allowable configurations begins to narrow starting at a lower value of $\phi \approx 35°$;

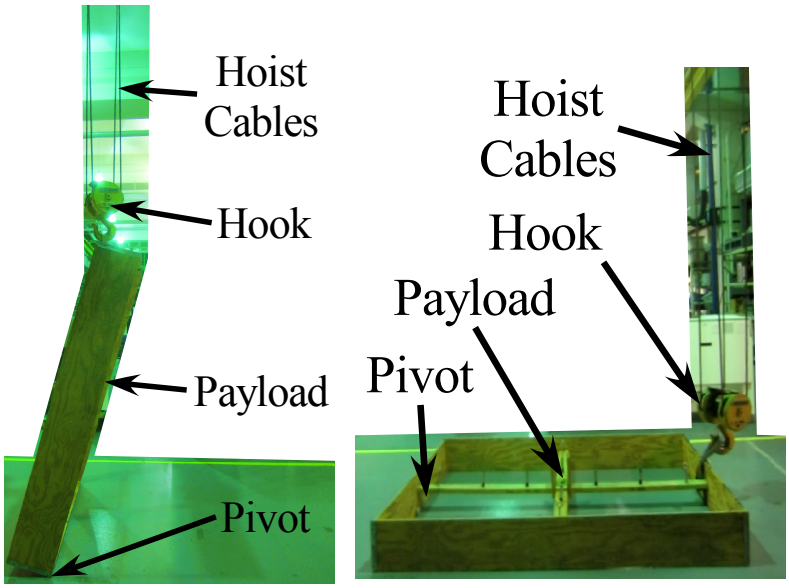

(a) Start Position (b) Finish Position

Figure 6.12: Laying Down the Wooden Box Payload

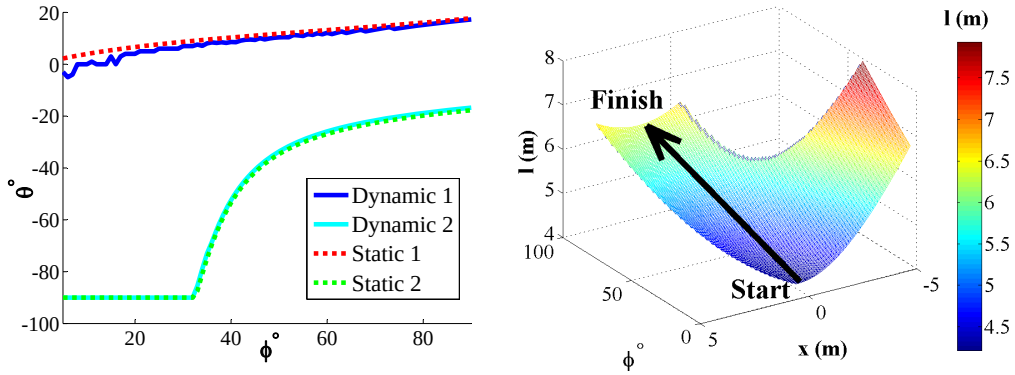

(a) Payload Angle, ϕ, vs. Cable Angle, θ (b) Payload Angle, ϕ, vs. Trolley Position, x, vs. Hoist Cable Length, l

Figure 6.13: Wooden Box Allowable Configurations

and 2) like the aluminum ingot example, the dynamic boundaries are very similar to the static boundaries. Therefore, the static boundaries can be used to determine the lay-down trajectory.

Figure 6.13(b) shows an example trajectory superimposed on the surface of allowable configurations plotted in the $\phi - x - l$ space. The trajectory starts around payload angle $\phi = 5°$, and finishes at $\phi = 90°$. Each point on the trajectory specifies the trolley position, x, and hoist cable length, l.

A few points were selected from the trajectory. Then, trolley and hoist motor velocity command profiles were generated to drive the crane to the selected configurations. The positions of the lower pivot end of the wooden box (point O in the lay-down schematic diagram of Figure 6.2(a)), and the upper end where it is attached to the hook (point P in Figure 6.2(a)), were tracked using RF location tags. Figure 6.14(a) shows the measured tag positions during the execution of the lay-down velocity commands. The upper end follows approximately a quarter circular arc as the payload is laid down from a near-upright position to a horizontal position. Note the fluctuation in position of

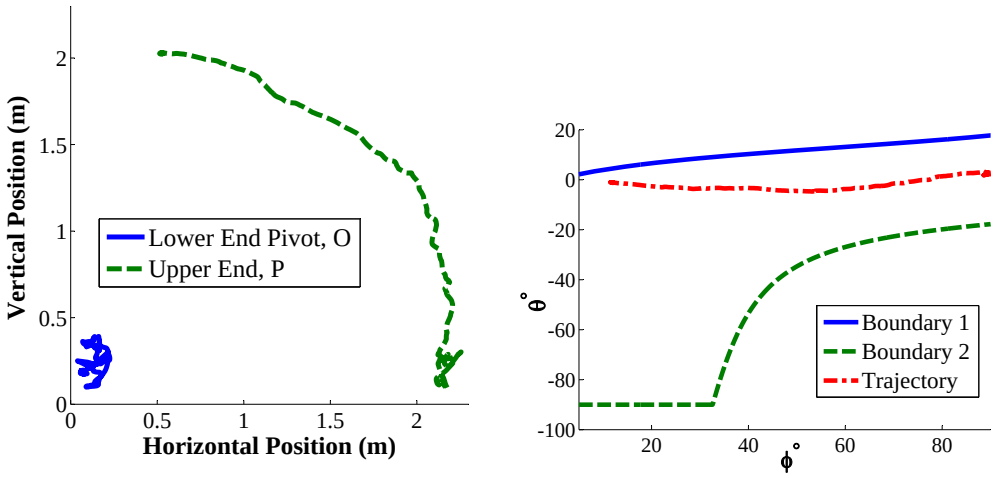

(a) Positions of Lower and Upper Payload Ends (b) Payload Angle, ϕ, vs. Cable Angle, θ

Figure 6.14: Wooden Box Lay-Down Experimental Trajectories

the pivot end was from measurement noise[2] as the pivot did not actually move during the maneuver. Figure 6.14(b) shows the trajectory of the configuration during the lay-down maneuver, plotted in the $\phi - \theta$ space. The trajectory remained well inside the static boundaries throughout the move.

[2]Section 2.3 showed the location accuracy of the RF tag is poor close to the ground.

CHAPTER VII

MINIMAL PAYLOAD OSCILLATION SWITCH-TIMES FOR CRANES WITH NONLINEAR ON-OFF ACTUATORS

Due to their simplicity, ruggedness, and long service life, relay cranes are often found in older factories or in applications where precise crane motions are not a strict requirement. However, with this type of crane controlling payload oscillations is challenging for two reasons: 1) There are only limited actuation actions with on/off relays; and 2) These cranes typically contain nonlinear dynamics. For example, they can accelerate in a manner that is different from their deceleration characteristics. When the relay is turned on, the crane is accelerated by electric motors. When the relay is off, the crane decelerates either by coasting to a stop (brakeless) or by engaging brakes. This characteristic presents an asymmetrical-acceleration nonlinearity in the actuation system.

The behavior of such a crane is illustrated in Figure 7.1. Switching on/off the relay is represented as the command, $r(t)$, and in this case a pulse of length t_p is shown. Typically, the relays are energized by buttons on a control pendent. The command is sent to the nonlinear actuator. When the relay is on, the crane accelerates at a rate of M_a until the velocity saturates at the maximum velocity, V_{max}. When the relay is off, the crane decelerates at $M_d \neq M_a$ until the velocity is zero. The times to accelerate from 0 to V_{max}, and from V_{max} to 0, are T_a and T_d, respectively. In this case, the actuator contains two non-linearities: 1) asymmetrical acceleration and deceleration, $M_d \neq M_a$, and 2) straight-line rate-limiting, where maximum velocity rising and falling rates are limited to M_a and M_d,respectively. The actuator output is the velocity of the trolley, $v(t)$, which is the input to the linear oscillatory dynamics of the swinging payload. This plant can be represented by a second-order damped oscillatory transfer function, and its output is the payload displacement, $y(t)$.

Previous work by Lawrence et al. [49] derived the switch-times in closed-form that partially compensates for the asymmetrical nonlinearity. However, the solution requires the command to reach steady state before the next switch-time, and is only applicable in a limited range of parameters. The numerical optimization method described by Bradley et al. in [12] is similar to the solution technique proposed here. However, their method is computationally expensive, because it requires running a complete time simulation to find the amplitude of payload oscillation at each iteration of optimization. Furthermore, the rate of change in velocity is assumed to be first-order;

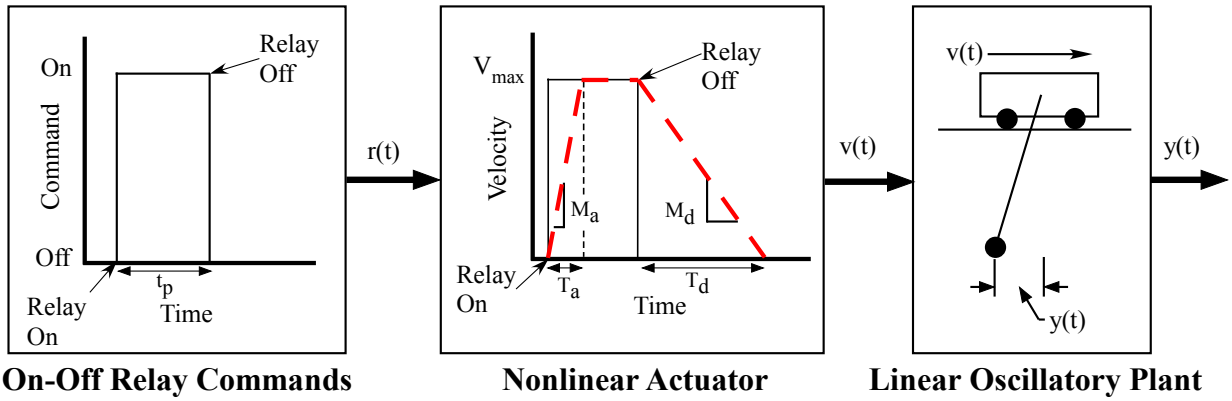

Figure 7.1: Nonlinear Relay Crane Block Diagram

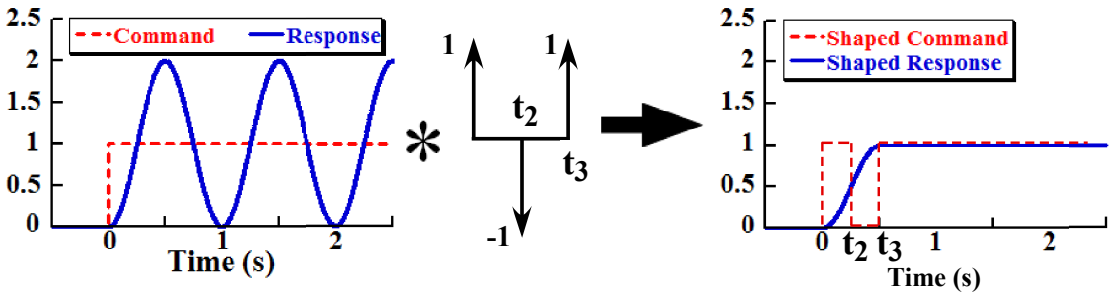

Figure 7.2: System Response to UMZV Shaped and Unshaped Commands.

in cases where the velocity changes differently, numerical optimization may not be able to yield satisfactory solutions (due to multiple local minima).

The solution method presented in this chapter is as follows: First, a closed-form equation is derived to calculate the level of residual oscillation when the linear plant is subjected to arbitrary input velocities. Second, rules and constraints that define the relationship between the trolley velocity and relay switch-times are described. Finally, numerical searches are used to determine minimal-oscillation switch times. Although the examples presented primarily focus on the straight-line asymmetrical-acceleration nonlinearity, the method is also applicable to other types of nonlinearities.

7.1 Input Shaping for On-Off Actuators

As detailed in Chapter 1, input shaping is a technique that reduces vibration in flexible systems by filtering the reference inputs. This is accomplished by convolving a baseline input (such as a step) with a series of impulses referred to as an *input shaper*. The result is a shaped command that can reduce residual vibration. If the impulse amplitudes and time locations are correctly determined, then the residual vibration of a linear system can be entirely eliminated.

One way to produce shaped commands that are compatible with on-off actuators is to constrain the impulse amplitudes of the input shaper to 1 or -1. If the baseline command is a step, then the shaped command consists of on-off pulses. One such *Unity Magnitude Zero Vibration* (UMZV) input shaper may be expressed in terms of impulses (where A_i and t_i represent the amplitude and time of the i^{th} impulse, respectively). It is repeated here for convenience [96]:

$$\begin{bmatrix} A_i \\ t_i \end{bmatrix} = \begin{bmatrix} 1 & -1 & 1 \\ 0 & t_2 & t_3, \end{bmatrix} \tag{7.1}$$

where,

$$\begin{bmatrix} t_2 \\ t_3 \end{bmatrix} \cong \begin{bmatrix} (2\pi/\omega_d)(1/6 + 0.272\zeta + 0.203\zeta^2) \\ (2\pi/\omega_d)(1/3 + 0.005\zeta + 0.179\zeta^2), \end{bmatrix}$$

and ω_d and ζ are the damped natural frequency and damping ratio. The time of the first impulse, t_1, is always set to zero. Note that for undamped systems, $t_2 = T_{period}/6$ and $t_3 = T_{period}/3$, where T_{period} is the period of oscillation. Figure 7.2 shows the convolution of a step command and a UMZV shaper. When the input shaper is correctly designed, the response of the undamped system to a shaped-command is vibration-free, but the response to the step command is oscillatory.

A UMZV-shaped system, without any nonlinearities, will have zero residual vibration. In the presence of the asymmetrical acceleration-deceleration nonlinearity, the performance of UMZV shaped commands is degraded.

For example, consider a set of systems similar to the one in Figure 7.1, but with first-order accelerating/decelerating actuators, where the accelerating time constant is $\tau_a = 0.117s$, and the decelerating time constant, τ_b, is varying. These systems are then subjected to input commands,

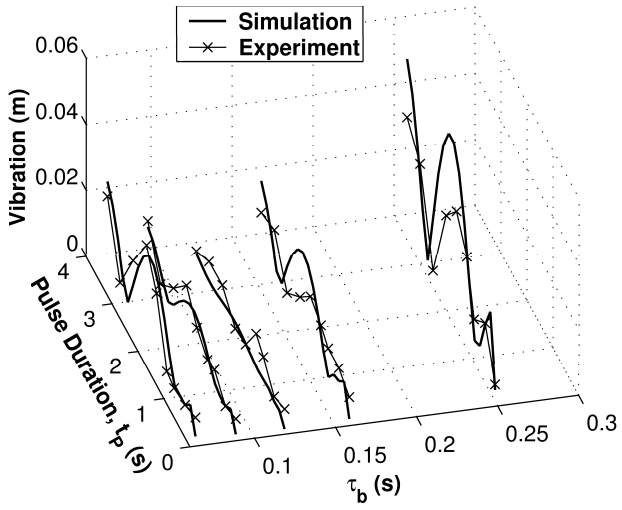

Figure 7.3: Residual Vibration from UMZV Commands on Asymmetrical Actuators [12]

$r(t)$,which are UMZV-shaped pulses of varying length, t_p. Figure 7.3 plots the level of residual payload vibration for these systems as a function of t_p. The plot shows that for most of the tested conditions, there exists significant residual vibration when using UMZV-shaped inputs with nonlinear actuators.

It should be noted that if the asymmetry is removed, i.e. $\tau_b = \tau_a = 0.117s$, then the actuator is linear, and the UMZV shaper function as designed, resulting in residual vibration that is approximately zero. This case is shown in the third data series from the left in Figure 7.3. In the next section, the description of the solution method will begin by deriving an equation for the oscillation of a single-mode oscillatory system subjected to arbitrary inputs.

7.2 Single-Mode Plants

An arbitrary input, $u(t)$, constrained such that $u(t) = 0$ for $t < 0$ and $t \geq t_{end}$, can be approximated as a finite sum of N pulses of width Δ:

$$u(t) \approx \tilde{u}(t) = \sum_{j=0}^{N} u(j\Delta)\delta(t - j\Delta)\Delta, \tag{7.2}$$

where $\delta(t - j\Delta)$ is the unit pulse function delayed by $j\Delta$, and $N = \text{Round}(t_{end}/\Delta)$.

The response of a linear single-mode oscillatory plant to an impulse input is [11]:

$$y(t) = \left[A\frac{\omega}{\sqrt{1-\zeta^2}} e^{-\zeta\omega(t-t_0)} \right] \sin\left(\omega\sqrt{1-\zeta^2}(t-t_0)\right), \tag{7.3}$$

where A is the amplitude of the impulse, ω is the undamped natural frequency of the plant, ζ is the damping ratio, t is time, and t_0 is the time of the impulse input. Because the plant is linear, the response to N impulses can be found by summing (7.3), which yields:

$$\bar{y}(t) = A_{osc} \sin\left(\omega\sqrt{1-\zeta^2}t + \psi\right). \tag{7.4}$$

Here, the phase shift, ψ, is irrelevant to this investigation. The variable of interest is the amplitude of oscillation, A_{osc}.

By choosing a small Δ, $\tilde{u}(t)$ from (7.2), approaches a sum of impulses. Then, if $\tilde{u}(t)$ is input into the plant, then the amplitude of oscillation at $t = t_{end}$ is [84]:

$$A_{osc} = \sqrt{\left(\sum_{j=1}^{N} B_j \cos\phi_j\right)^2 + \left(\sum_{j=1}^{N} B_j \sin\phi_j\right)^2} \tag{7.5}$$
$$B_j = \Delta \frac{A_j \omega}{\sqrt{1-\zeta^2}} e^{-\zeta\omega(t_{end}-t_j)}$$
$$\phi_j = \omega\sqrt{1-\zeta^2} t_j,$$

where $t_j = j\Delta$ and $A_j = u(j\Delta)$ are the time and amplitude of the j^{th} pulse from $\tilde{u}(t)$, respectively.

An alternative approach for calculating the residual oscillation from arbitrary commands in closed-form can be found in [102]. In the next section, the relationship between relay switch-times, the velocity profile, and the payload oscillation will be defined and used to solve for minimal-oscillation switch-times.

7.2.1 Minimal-Oscillation Switch-Times for Straight-Line Asymmetrical-Acceleration Actuator Nonlinearities

Consider the case when both acceleration and deceleration are instantaneous, i.e. $M_a = M_d = \infty$. Then the shape of the minimal-oscillation velocity profile would be identical to a UMZV-shaped step command, as seen in Figure 7.2. The relay switches on at $t_1 = 0$, then off at t_2, and back on at t_3. Previous works have shown that even if the acceleration and deceleration are asymmetric and non-instantaneous, then by modifying the relay switch-times, the generated velocity profile can still result in low payload oscillations [49, 12, 70].

To determine the minimal-oscillation velocity profile, $v(t)$, one simply needs to find two appropriate switch-times, defined as T_2 (relay switch off) and T_3 (relay switch on). The relay is always switched on at zero time, hence $T_1 = 0$. Limited possibilities for actuator actions (can only switch the relay on or off) is advantageous for numerically finding the solution, because it simplifies the dimension of the solution vector to only two entries (T_2 and T_3).

If the switch-times are known, then the resulting velocity profile can be constructed from a set of rules that describe how the actuator behaves. For straight-line asymmetrical-acceleration, the rules are: when the relay is on, velocity increases at rate M_a until V_{max}; when the relay is off, velocity decreases at rate $M_d \neq M_a$ until the velocity reaches zero.

In general, the velocity profile can be classified into $2^{(k-1)}$ archetype shapes, where k is the number of relay switch-times. The archetypes for three-switch commands, shown in Figure 7.4, are differentiated by whether the velocity saturates at V_{max} or 0 at the switch-times. In case a, the velocity does not saturate before both switch-times. In case b, the velocity reaches V_{max} before T_2, but does not reach 0 before T_3. In case c, the velocity does not reach V_{max} before T_2, but reaches 0 before T_3. In case d, the velocity reaches V_{max} before T_2, and reaches 0 before T_3.

Once $v(t)$ is formed, (7.5)[1] is used to calculate A_{osc}, and determines whether the level of payload oscillation, $y(t)$, is minimized. Because (7.5) is closed-form, this calculation can be performed quickly and the optimization is computationally inexpensive. Thus, the solution algorithm using a numerical optimization routine is[2]:

initialize vector X containing relay switch-times

[1] Depending on the vibration equation used, it may be necessary to convert the velocity profile into an acceleration profile to be used in (7.5).

[2] It should be noted that the solution outlined in this section applies to when the crane is moving from 0 to V_{max}. If the switch-times for the stage from V_{max} to 0 are desired, then the velocity profile needs to be created in a 'mirrored' fashion, i.e. by swapping the values of M_a and M_d.

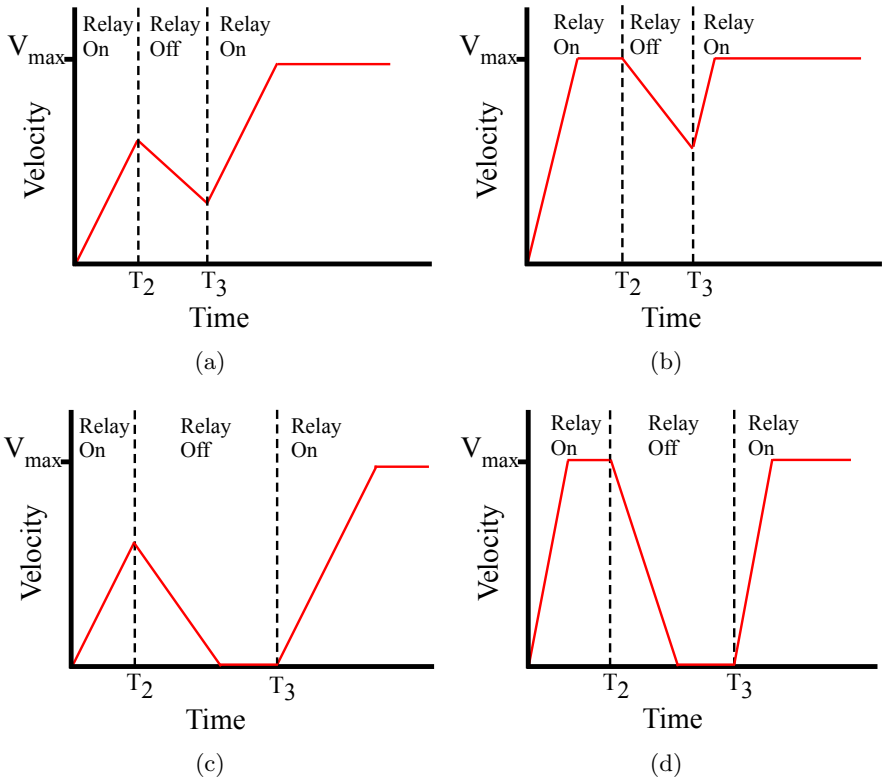

Figure 7.4: Straight-Line Asymmetrical-Acceleration Archetypes for Three-Switch Velocity Profiles

while in numerical optimization routine **do**
  Build velocity profile, $v(t)$, from X
  Calculate residual oscillation A_{osc} from (7.5)
  Modify X
end while
return minimal-oscillation solution, X_{min}

A good initial guess for the vector X is the switch-times from a UMZV shaper. This works well for cases where the severity of the nonlinearity is small (e.g. $M_a \approx M_d$; or if the acceleration and deceleration are nearly instantaneous), because the solution should be close to the UMZV shaper. However, an alternate method is described in the next section that covers more general cases.

7.2.2 Thorough Search

Although numerical optimization is capable of finding a solution quickly, it is quite possible for the optimizer to be stuck in local minima and return unacceptable solutions (where the oscillation is too high). In most cases where the effect of the nonlinearity is significant, the initial guess for vector X typically needs to be close to the actual optimal solution.

A thorough search over a large, but finite, solution space is a viable alternative. This is because A_{osc} can be calculated quickly from closed-form equations. To solve the problem in this way, the solution vector should be defined as the *spacing* between switch-times:

$$X = \begin{bmatrix} X_1 \\ X_2 \end{bmatrix} = \begin{bmatrix} T_2 - T_1 = T_2 \\ T_3 - T_2 \end{bmatrix} \tag{7.6}$$

Next, the bounds for the solution space are defined as:

$$0 \leq X_1 \leq \max(T_a, t_2) \tag{7.7}$$
$$0 \leq X_2 \leq \max(T_d, t_3 - t_2),$$

where T_a and T_d are the acceleration and deceleration times defined in Figure 7.1, and t_2 and t_3 are the UMZV switch-times and defined in (7.1). Clearly, X_1 and X_2 must be lower bounded by 0. The rationale for the upper bound is the following: If the crane acceleration and deceleration are very fast, i.e. $T_a \to 0$, $T_d \to 0$, then the shape of the velocity profile should approach that of a UMZV-shaped command (shown in Figure 7.2). This kind of velocity profile falls into the category shown in Figure 7.4(d), where the velocity saturates at V_{max} and 0 before T_2, and T_3, respectively. In this case, X is upper bounded by the UMZV derived switch-times t_2 and $t_3 - t_2$.

Conversely, if the crane acceleration and deceleration are slow relative to the oscillation period, i.e. $T_a >> T_{osc}$, and $T_d >> T_{osc}$, then the solution velocity profile is hypothesized to be of the type shown in Figure 7.4(a). In this case, there are no saturations before T_2 or T_3, and X is upper bounded by T_a and T_d. Other permutations of T_a and T_d relative to the oscillation period can result in velocity profiles shown in Figure 7.4(b) and 7.4(c), and the upper bounds for these cases are chosen in a similar way.

With the bounds chosen, the solution algorithm is modified from Section 7.2.1 as follows:

define discretized solution space, $\mathbb{X}$, bounded by (7.7)
for $X \in \mathbb{X}$ **do**
    Build velocity profile, $v(t)$
    Calculate residual oscillation, A_{osc}, using (7.5)
end for
find minimal-oscillation solution, $X_{min} \in \mathbb{X}$

This thorough search method typically yields acceptable solutions for most realistic crane parameters. If the parameters are extreme (e.g. a crane with very fast acceleration but very slow deceleration), then it is possible that no acceptable solution is found inside the bounds. In such cases the upper bounds can simply be increased until an acceptable solution is found. Increasing the search space does not significantly increase the computation time. As an example, the time to complete a thorough search over a solution space of > 40000 X candidates was only 5 seconds on a desktop computer. Furthermore, the switch-times for the optimum solution were accurate to within 0.01 seconds, a resolution that is more than adequate for relay cranes.

7.3 Implementation on a Production Crane

The concepts in this chapter were implemented on a decades-old bridge crane that is used for the assembly of aircraft landing gear at a Boeing manufacturing facility in St. Louis, MO, USA [70]. The crane accelerates using AC induction motors that are switched on by relays. To decelerate, the relays de-energize, and the brakeless crane coasts, relying on friction and motor back-EMF to slow down and stop. It was observed that the friction forces that slow the crane varied depending on the crane position *and* the direction of travel. These factors introduced additional nonlinearities to the already challenging problem.

During standard operation, the relays are directly controlled by the buttons on a control pendent corresponding to motions in the North, South, East, and West directions. To implement low-oscillation switch-times, the signals from the pendent are intercepted and modified using a programmable C-VIC module from SEAH Mechatech, shown in Figure 7.5. The modified signals are then sent to the relays that control the motors. First, the crane's behavior during acceleration and deceleration was measured. Then, a model was matched to the actuator nonlinearities. This information was then used to obtain low-oscillation switch-times. Finally, tests were performed to evaluate the effectiveness of the modified crane.

Figure 7.5: Button Pendent and the SEAH Mechatech C-VIC Control Box

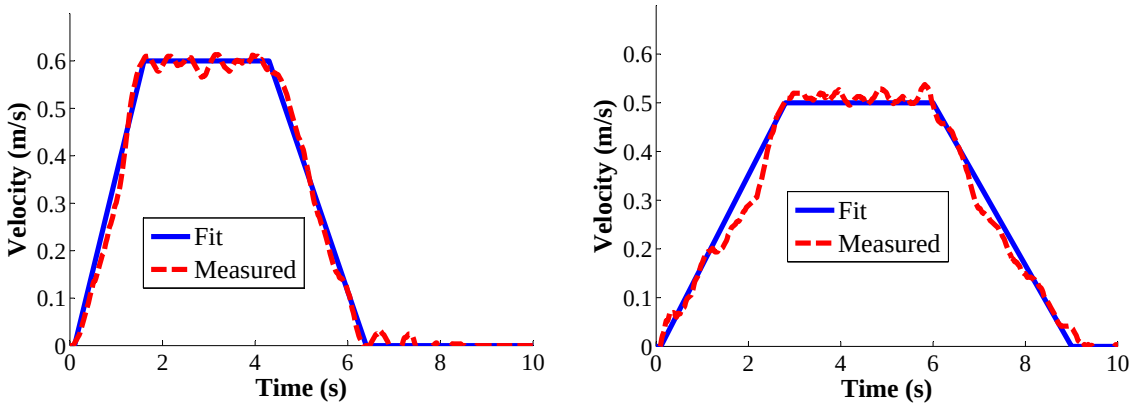

(a) Trolley (b) Bridge

Figure 7.6: Relay Crane Velocity Profiles

7.3.1 Measuring the Acceleration and Deceleration

A laser position sensor was used to measure the trolley motion. The crane was moved in the bridge (East/West) and trolley (North/South) directions. The crane was accelerated from rest to maximum speed and then decelerated until it stopped. This investigation neglected the fact that the crane's acceleration and deceleration varied depending on its position and direction of travel. From repeated measurements, it was found that straight-line accelerating and decelerating models adequately fit the data. Figures 7.6(a) and 7.6(b) show the measured and fitted velocity profiles for the trolley and bridge axes, respectively. The parameters for the model are summarized in Table 7.1.

Table 7.1: Straight-Line Acceleration and Deceleration Fit of the Crane Velocity Profile

	Trolley Axis (North/South)	Bridge Axis (East/West)
V_{max} (m/s)	0.60	0.50
T_a (s)	1.65	2.73
M_a (m/s^2)	0.364	0.183
T_d (s)	2.10	2.93
M_d (m/s^2)	0.286	0.171

Table 7.2: Low-Oscillation Switch-Times

	Trolley Axis (North/South)	Bridge Axis (East/West)
0 to V_{max}		
T_2 (s)	1.13	1.60
T_3 (s)	1.85	2.04
V_{max} to 0		
T_2 (s)	1.38	1.70
T_3 (s)	1.87	2.06

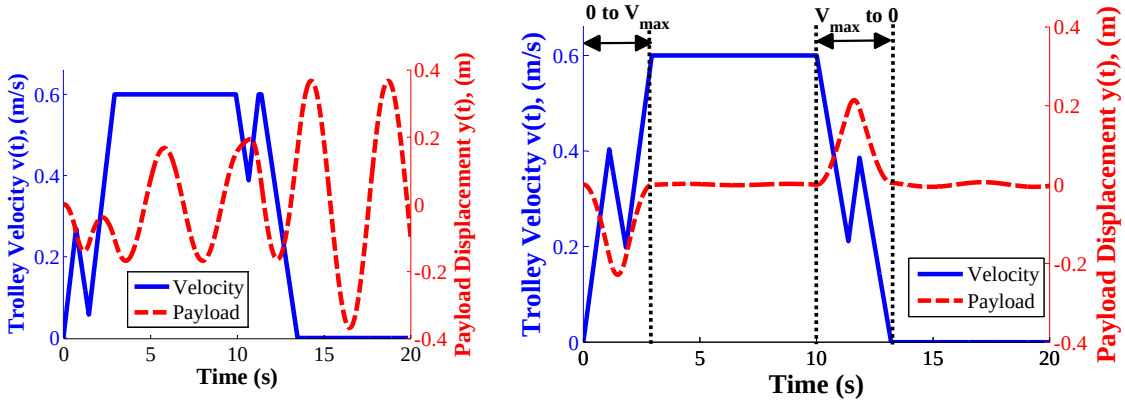

(a) UMZV (b) Minimal-Oscillation

Figure 7.7: Crane Velocity Profiles and Simulated Payload Responses

The maximum velocity of the crane is V_{max}, T_a is the time to accelerate from $0 - V_{max}$, T_d is the time to decelerate from $V_{max} - 0$, and M_a and M_d are the acceleration and deceleration rates, respectively. The bridge axis has lower V_{max} and acceleration/deceleration rates than the trolley axis due to the greater inertia that is moved. The trolley axis has almost a 30% difference between the acceleration and deceleration rates, clearly demonstrating nonlinear behavior. The asymmetry is less significant along the bridge axis, though still enough to warrant a nonlinear controller.

7.3.2 Switch-Times for Reducing Payload Sway

The payload plant was modeled as a 4.9 meters long pendulum, with zero damping. The frequency and period of oscillation were therefore 0.225 Hz and 4.44 s, respectively. Using the algorithm described in Section 7.2.2, minimal-oscillation switch-times were obtained for the stages from 0 to V_{max}, and V_{max} to 0. These are shown in Table 7.2. When a button is pressed and held down, the C-VIC controller turns the relay on/off according to the 0 to V_{max} switch-times. Similarly, when the button is released, the relays are turned on/off according to the V_{max} to 0 switch-times.

If the switch-times ($T_2 = 0.74s$, $T_3 = 1.48s$) from a UMZV shaper designed under the assumption of a linear actuator were used, then the payload would respond with large oscillations. Figure 7.7(a) illustrates this fact by plotting the crane velocity profile and the simulated payload response. On the other hand, Figure 7.7(b) shows the velocity profile using the switch-times in Table 7.2 for the trolley axis. The simulated payload response clearly has very low levels of oscillation. The 0 to V_{max} acceleration and V_{max} to 0 deceleration of the trolley are indicated on the figure. Figure 7.8 show that both stages of the velocity profile have low energy content at the natural frequency of the pendulum, 0.225 Hz, which is indicated by the red vertical line.

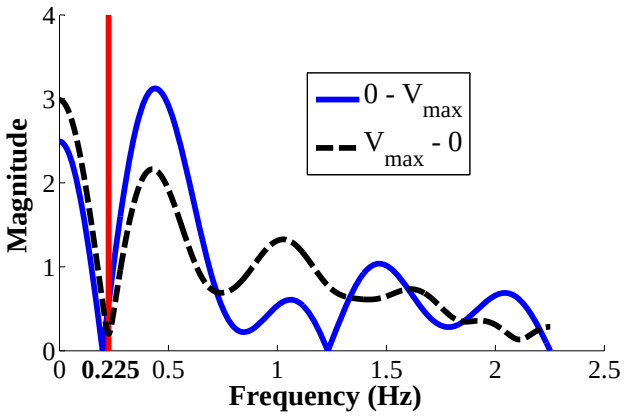

Figure 7.8: Frequency Content of the Minimal-Oscillation Crane Velocity Profile

Table 7.3: Nominal Point to Point Moves

Trial #	Peak-to-peak Payload Sway (m)		Average Sway Ratio: Standard to Optimized
	Optimized	Standard	
Trolley North			4.19
1	0.28	1.27	
2	0.25	0.95	
Trolley South			2.61
1	0.38	1.13	
2	0.45	1.04	
Bridge East			1.75
1	0.25	0.54	
2	0.28	0.39	
Bridge West			3.23
1	0.14	0.50	
2	0.21	0.63	

7.3.3 Experimental Point-to-Point Motion Tests

Point-to-point (PTP) motion tests were conducted to experimentally validate the effectiveness of the modified crane controller. The payload suspension length was set to 4.9 m. PTP motions were performed by manually pushing the pendent buttons such that the crane moved approximately the same distance (1.5 m to 2 m) in each trial. This was repeated in all four directions (North, South, East, West).

Figure 7.9(a) show the payload responses for selected trials in North directions. 'Optimized' trials used the low-oscillation switch times from Table 7.2, implemented by the intercepting C-VIC module. In 'Standard' trials, the pendent buttons directly controlled the relays. It is clear that the optimized switch-times reduce payload oscillation in all four directions. The low levels of oscillation that are still present in the optimized trials can be attributed to the fact that decelerating forces varied depending on crane position and travel direction. This nonlinearity was neglected for this investigation. Figures 7.9(b) to 7.9(d) show similar results in the South, East, and West directions, respectively. Table 7.3 summarizes the results of the PTP tests. The peak-to-peak payload sway with standard control was approximately two to four times greater than with the optimized switch-times.

Table 7.4 shows the results from short move PTP motion tests. In these tests, the pendent-button was pressed for approximately the same duration as T_3, 0-V_{max} from Table 7.2. This action represents the shortest possible distance/duration that the optimized controller is capable

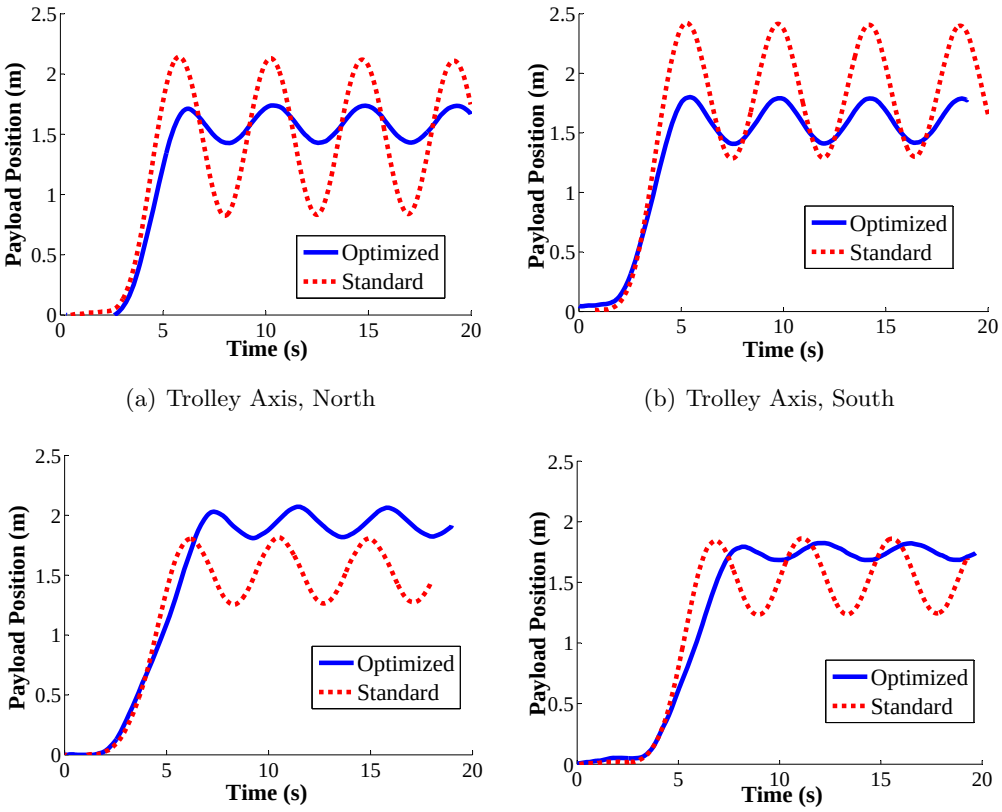

(a) Trolley Axis, North

(b) Trolley Axis, South

(c) Bridge Axis, East

(d) Bridge Axis, West

Figure 7.9: Payload Responses from PTP Experiments

of achieving, while still maintaining low payload oscillations. For comparisons, the button was also pressed for the same duration using standard control. Table 7.4 shows that the optimized controller reduced payload sway over standard control by 4-5 times in the trolley directions, and by 2-3 times in the bridge directions.

Table 7.5 shows the results from long move PTP motion tests. In each trial, the pendent-button was pressed for approximately 5 s and 7 s in the trolley and bridge directions, respectively. Three trials using both control modes were performed in all directions. In the trolley direction, sway-reduction control reduced oscillations by 3-4 times, and in the bridge direction, payload sway was reduced by 5-7 times.

Table 7.4: Short Point to Point Moves

Trial #	Peak-to-peak Payload Sway (m)		Average Sway Ratio: Standard to Optimized
	Optimized	Standard	
Trolley North			4.21
1	0.28	1.18	
Trolley South			5.40
1	0.24	1.27	
Bridge East			2.64
1	0.14	0.37	
Bridge West			3.38
1	0.13	0.44	

Table 7.5: Long Point to Point Moves

Trial #	Peak-to-peak Payload Sway (m)		Average Sway Ratio: Standard to Optimized
	Optimized	Standard	
Trolley North (5 s Moves)			3.36
1	0.22	0.76	
2	0.24	0.75	
3	0.20	0.71	
Trolley South (5 s Moves)			4.46
1	0.19	0.75	
2	0.22	0.69	
3	0.09	0.77	
Bridge East (7 s Moves)			5.04
1	0.06	0.44	
2	0.10	0.50	
3	0.12	0.47	
Bridge West (7 s Moves)			7.11
1	0.05	0.54	
2	0.09	0.54	
3	0.09	0.52	

Table 7.6: Robustness to Changes in Cable Length

Trial #	Peak-to-peak Payload Sway (m)		Average Sway Ratio: Standard to Optimized
	Optimized	Standard	
Bridge East (5.8 m Cable Length)			20.56
1	0.01	0.60	
2	0.03	0.64	
3	0.05	0.61	
Bridge West (5.8 m Cable Length)			11.53
1	0.02	0.66	
2	0.09	0.67	
3	0.06	0.63	
Bridge East (4 m Cable Length)			2.20
1	0.15	0.37	
2	0.13	0.34	
3	0.18	0.30	
Bridge West (4 m Cable Length)			1.85
1	0.14	0.31	
2	0.17	0.34	
3	0.23	0.35	

7.3.4 Robustness Tests

To assess robustness to plant variation, the cable length was varied while keeping the switch-times of the optimized controller constant. The cable was varied from 4 m (0.249 Hz oscillation) to 5.8 m (0.207 Hz oscillation). Then, long move PTP motions were made in the bridge directions (pendent-button pressed for around 7s).

Table 7.6 summarizes the results from the robustness tests. The optimized controller was more effective at 5.8 m cable length (11-20 times reduction in sway) than at the designed length of 4.9 m (5-7 times reduction in sway). At the 4 m cable length, optimized control was less effective. However, the optimized controller still reduced payload sway by approximately two times over standard control.

7.3.5 Operator Study

Five male workers from the Boeing facility were selected for operator testing. The workers had various levels of crane driving experience and aged between 40 and 65. Each worker drove the crane through a course around the production floor with the optimized and standard controllers. Each run recorded 1) the number of times that buttons were pressed (as a measure of operator concentration and effort), 2) the number of minutes it took to complete the course, and 3) the number of times when physical intervention was required to stop the payload (1 minute penalty was added each time this happened) either because the operator gave up or because the payload was going to hit an object.

Table 7.7 summarizes the results from the operator study. On average, the optimized controller significantly reduced 1) the number of button presses (by more than 300%); 2) the completion time (by more than 250%, including the 1 minute penalties); and 3) the number of times that physical intervention was required to physically stop the payload (from several times per operator, to virtually zero). On the whole, operators praised the optimized controller. Some quotes from post-test interviews include: "It's great, made it a lot easier", "It was easier to anticipate stopping, You have to trust it", "Incredible, quickly builds confidence", "It felt much safer", "The stopping distance remains, just limited swing when reached", "Less stress to constantly monitor the load".

Table 7.7: Operator Study Results

		Standard			**Optimized**		
OP	**Crane Experience; Usage Frequency**	**Presses**	**mins**	**Stops**	**Presses**	**mins**	**Stops**
A	Limited; once a week	151 133	11.19 14.35	4 9	36	6.50	0
B	Inexperienced; never	139	17.83	12	25	4.60	0
C	Moderate, used to give crane training; rarely	57	13.98	7	21	3.51	0
D	Inexperienced; never	114	21.61	14	43	6.46	2
E	Nominal, broad knowledge of crane operations and controls; only for testing	91 59	5.74 3.36	0 0	37 37	4.42 3.26	0 0
	Averages	106	12.58	6.57	33	4.79	0.33

7.4 Multi-Mode Plants

To expand the solution method in Section 7.2.1 to multi-mode plants, the first step is to derive an equation similar to (7.5). This will give the oscillation amplitude of multi-mode plants subjected to arbitrary inputs. Then, assuming straight-line asymmetrical-acceleration nonlinearity, the same solutions steps outlined in Section 7.2.1 can be applied in essentially the same way to find low-oscillation switch-times.

A double-pendulum (DP) model, illustrated in Figure 7.10, is used as an example to represent the multi-mode plant. The trolley is subjected to an input acceleration, $u(t)$, and suspends a point mass hook, m_h, from a suspension cable of length L_1. A point mass payload, m_p, is suspended from the hook with a rigging cable of length L_2. The angles that the suspension and rigging cables relative to vertical are θ_1 and θ_2, respectively.

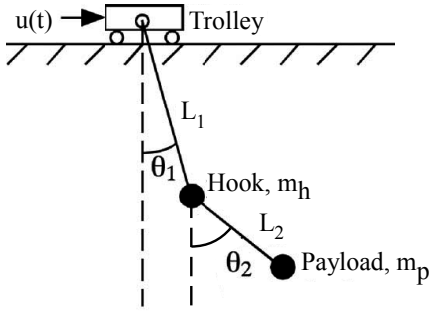

Figure 7.10: Model of Double Pendulum Plant

Using small-angles and zero-damping assumptions, the linearized equations of motion are[3]:

$$\ddot{\theta}_1 = -\theta_1 \frac{g(1+R)}{L_1} + \theta_2 \frac{gR}{L_1} - \frac{u}{L_1} \tag{7.8}$$

$$\ddot{\theta}_2 = -\theta_2 \frac{g(1+R)}{L_2} + \theta_1 \frac{g(1+R)}{L_2}, \tag{7.9}$$

where

$$R = \frac{m_p}{m_h}$$

is the payload to hook mass ratio, and g is the gravitational acceleration. The time responses to an impulse input at t_0 are:

$$\theta_1(t) = G_1 \sin\left(\omega_1(t-t_0)\right) - G_2 \sin\left(\omega_2(t-t_0)\right) \tag{7.10}$$

$$\theta_2(t) = H_1 \sin\left(\omega_1(t-t_0)\right) - H_2 \sin\left(\omega_2(t-t_0)\right), \tag{7.11}$$

where $\omega_{1,2}$ are the natural frequencies:

$$\omega_{1,2} = \sqrt{\frac{g}{2}} \sqrt{(1+R)\left(\frac{1}{L_1} + \frac{1}{L_2}\right) \mp \beta}, \tag{7.12}$$

$$\beta = \sqrt{(1+R)^2 \left(\frac{1}{L_1} + \frac{1}{L_2}\right)^2 - 4\left(\frac{1+R}{L_1 L_2}\right)},$$

and,

$$G_1 = \frac{1}{L_1 L_2} \frac{-L_2\omega_1^2 + g(1+R)}{\omega_1(\omega_1^2 - \omega_2^2)}$$

$$G_2 = \frac{1}{L_1 L_2} \frac{-L_2\omega_2^2 + g(1+R)}{\omega_2(\omega_1^2 - \omega_2^2)}$$

$$H_1 = \frac{1}{L_1 L_2} \frac{g(1+R)}{\omega_1(\omega_1^2 - \omega_2^2)}$$

$$H_2 = \frac{1}{L_1 L_2} \frac{g(1+R)}{\omega_2(\omega_1^2 - \omega_2^2)}.$$

Note that G_1, G_2, H_1, and H_2 are non-zero constants.

It can be seen from (7.10) and (7.11), that the hook and payload responses are linear summations of two modal sine waves. Therefore, the input that minimizes the amplitude of hook oscillation

[3]Similar results are derived in [91]

will also minimize the payload oscillation. However, for the sake of argument, and as the payload is generally more important, (7.11) is used to continue the analysis.

Because of linear assumptions, the response of θ_2 to N impulses can be found by summing (7.11), which yields:

$$\bar{\theta}_2(t) = H_1 \left[A_{osc1} \sin(\omega_1 t + \psi_1)\right] - H_2 \left[A_{osc2} \sin(\omega_2 t + \psi_2)\right] \tag{7.13}$$

Here, the phase shifts ψ_1 and ψ_2 are irrelevant to this investigation. The variables of interest are the amplitudes of oscillation from both modes, A_{osc1} and A_{osc2}.

Recall the arbitrary input, $u(t)$, constrained such that $u(t) = 0$ for $t < 0$ and $t \geq t_{end}$. It was approximated as $\tilde{u}(t)$ by a finite sum of N pulses of width Δ in (7.2). By choosing a small Δ, $\tilde{u}(t)$ approaches a sum of impulses. If $\tilde{u}(t)$ is input into the double-pendulum plant, then θ_2's oscillation amplitudes from both modes at $t = t_{end}$ are:

$$A_{osc1} = \sqrt{\left(\sum_{j=1}^{N} A_j \Delta \cos(\omega_1 t_j)\right)^2 + \left(\sum_{j=1}^{N} A_j \Delta \sin(\omega_1 t_j)\right)^2} \tag{7.14}$$

$$A_{osc2} = \sqrt{\left(\sum_{j=1}^{N} A_j \Delta \cos(\omega_2 t_j)\right)^2 + \left(\sum_{j=1}^{N} A_j \Delta \sin(\omega_2 t_j)\right)^2} \tag{7.15}$$

where A_j and t_j are the amplitudes and times of the j^{th} pulse from $\tilde{u}(t)$, respectively. Due to zero-damping assumptions, and because $\omega_1 \neq \omega_2$, the maximum oscillation amplitude is:

$$A_{osc,1+2} = |H_1 A_{osc1}| + |H_2 A_{osc2}| \tag{7.16}$$

7.4.1 Minimal-Oscillation Switch-Times for Straight-Line Asymmetrical-Acceleration Nonlinearities

The oscillation amplitude of a double-pendulum system can be determined for arbitrary inputs using (7.16). The solution algorithm from Section 7.2.2 needs to be modified slightly to be applicable to multi-mode plants. From input-shaping theory, if the plant contains more modes of oscillation, then the shaper needs more impulses to satisfy additional vibration constraints from the extra modes. For on-off relays, two additional switch-times, T_4 and T_5, are required. This changes the solution vector from (7.6) to:

$$X = \begin{bmatrix} X_1 \\ X_2 \\ X_3 \\ X_4 \end{bmatrix} = \begin{bmatrix} T_2 - T_1 = T_2 \\ T_3 - T_2 \\ T_4 - T_3 \\ T_5 - T_4 \end{bmatrix} \tag{7.17}$$

The relays turn on at T_1, off at T_2, on at T_3, off at T_4, and on at T_5. The velocity profiles are constructed in a similar way as in Figure 7.4, but with two additional switch-times.

Next, the upper bounds on the switch-times values need to be defined. Unlike the single-mode UMZV, there are no clear patterns in the time spacings between the impulses of 5-impulse, two-mode UMZV shapers. This is because the two-mode UMZV shapers dependence on the mode ratio is quite complex. However, it is still possible to make conservative guesses for the upper bounds. Consider two single-mode UMZV shapers that are separately designed for the first and second modes of the double pendulum. Because zero-damping is assumed, the UMZV shapers have the following properties on the time spacing between impulses:

$$t_2 - t_1 = T_{period1,2}/6$$
$$t_3 - t_2 = T_{period1,2}/6$$

Table 7.8: Switch-Times for Double Pendulum Crane

	Two-Mode UMZV	Low-Oscillation Solution
T_2 (s)	0.30	0.64
T_3 (s)	1.08	1.11
T_4 (s)	1.86	2.22
T_5 (s)	2.16	2.69

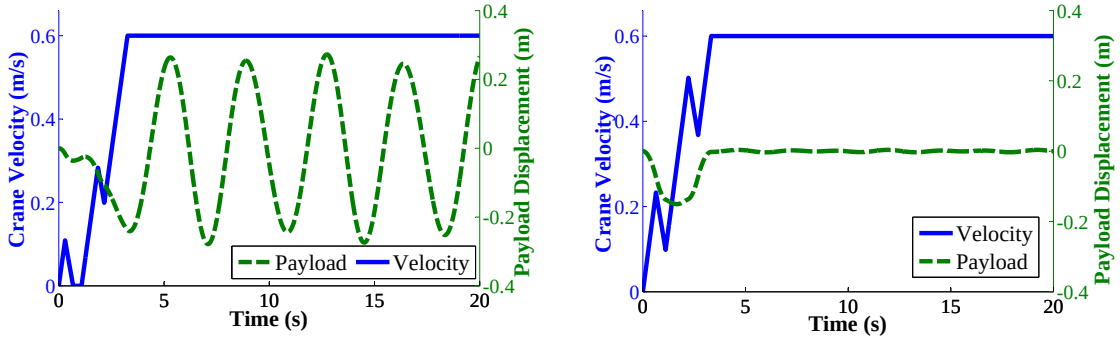

(a) Two-Mode UMZV

(b) Minimal-Oscillation

Figure 7.11: Crane Velocity Profiles and Simulated Payload Responses

where $T_{period1,2}$ represents either the first or second-mode oscillation periods. Thus, these single-mode UMZV shapers are used to estimate the X upper bounds in a manner similar to (7.7):

$$\begin{aligned} 0 \le X_1 &\le \max(T_a, T_{period1}/6, T_{period2}/6) \\ 0 \le X_2 &\le \max(T_d, T_{period1}/6, T_{period2}/6), \\ 0 \le X_3 &\le \max(T_a, T_{period1}/6, T_{period2}/6), \\ 0 \le X_4 &\le \max(T_d, T_{period1}/6, T_{period2}/6), \end{aligned} \tag{7.18}$$

In the rare circumstance that no satisfactory solutions are found, then the X bounds may be increased until an acceptable solution is found. However, the caveat is that the size of the brute-force search space increases exponentially with the number of switch-times. A strategy to reduce the computation time is to start with a coarse discretization over the whole space. After a solution is found, reduce and center a new search space around the solution. Then, find a new solution over the new space with finer discretization. Repeat as necessary.

7.4.2 Example Application

This example uses the actuator parameters of the trolley axis from Table 7.1. The double pendulum parameters are $L_1 = 2.5m$, $L_2 = 2.4m$, and $R = 0.2$. This results in natural frequencies of 0.268 Hz and 0.414 Hz. Table 7.8 contains the switch-times from 1) a two-mode UMZV shaper, and 2) the low-oscillation solution (for the 0 to V_{max} stage) obtained by brute-force search.

Figure 7.11(a) shows the crane velocity profile using the two-mode UMZV shaper and the simulated payload response. Because the shaper does not account for actuator nonlinearities, multi-modal large-amplitude payload oscillations are generated. Figure 7.11(b) shows similar data using the low-oscillation switch-times. The payload responded with almost zero oscillation. Figure 7.12 shows that the frequency content of the solution velocity profile has very low energies at the natural frequencies of the double pendulum plant.

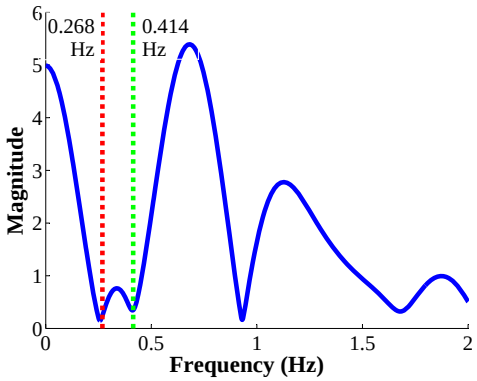

Figure 7.12: Frequency Content of the Minimal-Oscillation Crane Velocity Profile

CHAPTER VIII

CONCLUSIONS

This dissertation developed techniques to improve performance and ease of use in three major aspects of a typical crane operation: 1) moving payloads laterally in the horizontal plane, 2) lifting payloads off the ground, and 3) laying down long payloads to the ground.

For moving payloads laterally, a novel and intuitive hand-motion crane control method was designed. This interface allows operators to drive a crane by simply moving a hand-held device through the desired path. The position of the device, which is tracked by sensors, is used to generate crane-driving command signals. This command is then input-shaped such that payload oscillations are greatly reduced, making it much easier for the operator to drive the crane. Several operating modes were developed to evaluate the hand-motion concept. It was found that the hand-motion concept was unsuitable for making vertical/hoisting and stepping/inching movements. However, in several extensive operator studies where lateral movements were dominant, operators using hand-motion control demonstrated improvements over using standard crane control methods in several quantifiable measures of crane performance.

Three hand-motion control algorithms were developed: PD, On-Off, and the Brisk On-off Smart-Stop (BOSS) controller. To ensure stability, methods based on describing functions were developed to predict limit cycles in a feedback loop containing input shapers and hard nonlinearities. Also, the describing function for a relay-deadzone-rate-limiter was derived. The BOSS controller is a novel concept that exploits the knowledge of unexecuted commands in a feedback system with an input shaper and integrator(s) in the loop. The BOSS controller can move the system to the desired position in minimal time without overshoot or residual oscillations. It is also very simple to design.

For lifting payloads off the ground, Newtonian and Coulomb friction models that focus on the stiction-sliding-separation contact dynamics were derived. The validity of these models were also experimentally verified. Using these models, simulations with parameters that swept over a wide range of realistic values were conducted. From these studies, it was found that most payloads could be approximated as a single-pendulum after lifting off the ground. Because of this, x_{lift}, the offset distance at which payloads left the ground, essentially determined the level of detriment, such as swing amplitude and maximum swing velocity. Additionally, it was found that in many scenarios, x_{lift} was equivalent to x_{init}, the initial payload offset.

In some cases, the payload slides and scrapes along the ground before lifting off the ground. For these cases, x_{lift} is significantly less than x_{init}, as the system is essentially self-centering. These cases are 1) when the hoist speed is slow, 2) when a payload is low and wide, or tall and skinny, and 3) when the payload is very light. These cases were used to produce simple guidelines for passive auto-centering techniques that mitigate the detrimental effects of off-centered lifts. Active auto-centering techniques were also developed. These used sensors to track the positions of the hook and/or payload in order to center the trolley before lifting.

The number one priority in laying down long payloads is to ensure forces do not exceed limits which would cause the pivot to slip. A static model was developed to predict these forces at all possible configurations. Then, boundaries were defined around the acceptable region of the configuration space where force limits were not exceeded. A dynamic model was also derived, and accounted for the maximum velocity and acceleration capabilities of the hoist and trolley motors. From two sets of realistic crane and payload parameters, it was found that the boundaries of acceptable configurations using the dynamic model were not significantly different from that of the static model. Lay-down maneuvers can be executed by following motion trajectories that traverse the space of allowable configurations from the start to end positions. This was demonstrated in an

experimental example.

Finally, a special chapter addressed the topic of oscillation control of nonlinear relay cranes, or systems with on-off nonlinear actuators. Because the linear oscillatory plant is independent from the nonlinear actuators, closed-form equations, which can be calculated quickly and efficiently, were derived to produce the residual plant oscillation amplitude from arbitrary actuator inputs. Then, the relationships between on-off switch-times and the resultant actuator inputs were established. From this, boundaries are defined that limit the range of search space, and a thorough-search or other optimization algorithms can be used to find the optimal set of switch-times that produces minimal oscillations. Results for single- and double-pendulum payloads were shown, as well as the results from extensive testing on a production nonlinear relay crane.

To summarize, the contributions of this dissertation are:

- A novel and intuitive hand-motion control method that improves a crane's ease of use.
- The Brisk On-off Smart-Stop (BOSS) controller. This is a feedback controller designed for systems with an input shaper and integrator in the loop. It is simple to design, and moves the system to the desired position in minimal time without overshoot or residual oscillations.
- Describing function methods for predicting limit cycles in a feedback loop containing input shapers and hard nonlinearities. Also, the describing function for a relay-deadzone-rate-limiter was derived.
- A greater understanding of the motions, dynamics, and forces of lifting payloads off the ground and auto-centering techniques that mitigate the problems associated with off-centered payload lifts.
- A greater understanding of the motions, dynamics, and forces in the lay-down of long payloads. From this, the region of acceptable configurations during lay-down is found. The actual lay-down maneuver can be obtained by traversing this region from the start to finish configurations.
- Methods for obtaining the minimal-oscillation switch-times for nonlinear relay cranes, or systems with on-off nonlinear actuators and one- or two-mode oscillatory plants.

8.1 Future Work

In this dissertation, there were clear limitations in using hand-motion control in certain scenarios, such as hoisting and inching. However, it was mentioned in Section 2.7 that the inching mode can be better implemented by combining with the Come-Here mode. For example, the operator would press button A for the nominal Come-Here mode, but tap button B for the Come-Here mode that inches/steps (or move at snail speed) towards the operator. The same can be implemented for the push mode. Section 2.8 demonstrated proof of concepts for hand-motion path following modes. However, these were not pursued further. The concepts mentioned above are feasible enough to warrant further investigation.

This dissertation has thoroughly explored feasible operating modes of hand-motion control using a *single* hand-motion location device. However, it may be possible to overcome some of these limitations using *multiple* RF-location tags. An example of a multi-tag operation is illustrated in Figure 8.1. The operator uses tag 1 to control the crane using hand-motion. Tag 2 is permanently placed at a remote location, such as a stockpile storage, acting as the target position for the crane to travel to, autonomously. Tag 3 is also permanently located, but at the boundaries of an area where the crane should avoid. An extension to multi-tag operation is hand-motion control with multiple operators. This may have application in coordinated multi-hoist lifts, for example.

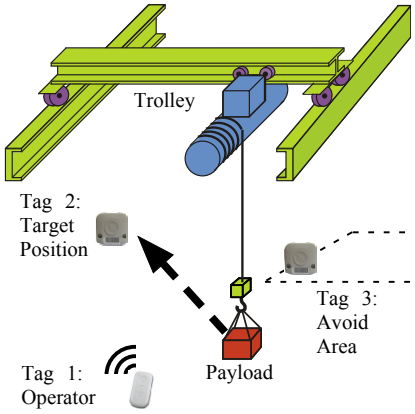

Figure 8.1: Multi-Tag Hand-Motion Crane Control

Future work for off-centered lifts include:

- Extend the 2-D lift-up models to 3-D. Then, more complex and richer motions such as twisting, rotation in multiple axes, and out-of-plane movements can be studied.
- This dissertation considered only symmetric, regularly shaped payloads and symmetric riggings. However, many payload and rigging arrangements do not fit in this category.
- The hook-based auto-centering technique commanded movements in either the trolley or hoist motors, but not both. Faster auto-centering lifts can be achieved by allowing simultaneous movements from both motors. An example algorithm for this type of movements is:
  1. Sense the hook has exceeded the acceptable level of deflection. If the hook is deflected, then at least one rigging cable is in tension.
  2. In general, the hook is deflected towards the direction of the payload. Therefore, the trolley should move in the same direction as the hook deflection. However, this motion will generally slacken the previously tight rigging cable and allow the hook to swing when the trolley moves.
  3. To reduce hook swing and decrease the auto-centering time, simultaneously hoist the hook and move the trolley in a coordinated manner such that tension in the rigging cable is maintained. The hook remains relatively stationary during this motion.
- Components of the simultaneous hoist and trolley motions can also be applied to the hook and payload-based auto-centering method.

Future work for payload lay-down includes:

- Extend the 2-D lay-down analysis to 3-D. Then, more complex and richer motions such as buckling (e.g. for circular cross-section pole payloads that do not have adequate pivot stability in the out-of-plane direction), or the generalized motion of laying down arbitrary payloads in 3-D can be studied.
- In the example shown in this dissertation, the lay-down maneuver was accomplished by executing pre-generated velocity profiles in an open-loop manner. These velocity profiles were generated from a trajectory that approximately traversed over a few points on the surface of allowable configurations. Using sensors that track the payload and hook positions, a more robust feedback controller can be designed to lay-down the payload in a manner that follows the desired trajectory more closely.

- The lay-down algorithm can be optimized with additional conditions such as minimizing the lay-down time, maximizing the robustness to parameter-estimation errors, or maximizing the "distances" from the boundaries of acceptable configurations during the lay-down maneuver.
- Investigate the effects of variations to parameters such as hoist cable length, crane height, friction coefficient, payload mass and dimensions, and motor velocity and acceleration limits.
- Experimentally validate the predicted boundaries of acceptable configurations.

REFERENCES

[1] Abdel-Rahman, E. M., Nayfeh, A. H., and Masoud, Z. N., "Dynamics and control of cranes: A review," *Journal of Vibration and Control*, vol. 9, no. 7, p. 863, 2003.

[2] Ahmad, M. A., Ismail, R. R., Ramli, M. S., Nasir, A. N. K., and Hambali, N., "Feedforward techniques for sway suppression in a double-pendulum-type overhead crane," *Computer Technology and Development, 2009. ICCTD'09. International Conference on*, vol. 1, pp. 173–178, 2009.

[3] Al-Garni, A. Z., Moustafa, K. A. F., and Javeed Nizami, S. S. A. K., "Optimal control of overhead cranes," *Control Engineering Practice*, vol. 3, pp. 1277–1284, Sep 1995.

[4] Amat, J., Frigola, M., and Casals, A., "Human robot interaction from visual perception," IEEE/RSJ Int. Conf. on Intelligent Robots and Systems, (Sendal, Japan), pp. 1997–2002, 2004.

[5] Anh, L. X., *Dynamics of Mechanical Systems with Coulomb Friction*. Computational Fluid and Solid Mechanics, Springer, 2003.

[6] Ballantyne, G. H., "Robotic surgery, telerobotic surgery, telepresence, and telementoring," *Surgical Endoscopy*, vol. 16, no. 10, pp. 1389–1402, 2002.

[7] Baraff, D., "Coping with friction for non-penetrating rigid body simulation," *ACM SIGGRAPH Computer Graphics*, vol. 25, pp. 31–41, 1991.

[8] Barrett, D. A. and Hrudey, T. M., "An investigation of hoist-induced dynamic loads on bridge crane structures," *Canadian Journal of Civil Engineering*, vol. 23, no. 4, pp. 926–939, 1996.

[9] Beavers, J., Moore, J., Rinehart, R., and Schriver, W., "Crane-related fatalities in the construction industry," *Journal of Construction Engineering and Management*, vol. 132, no. 9, pp. 901–910, 2006.

[10] Blackburn, D. F., Singhose, W., Kitchen, J. P., Petrangenaru, V. P., Lawrence, J., Kamoi, T., and Taura, A., "Advanced input shaping algorithm for nonlinear tower crane dynamics," 8th International Conference on Motion and Vibration Control, (Daejeon, Korea), 2006.

[11] Bolz, R. E. and Tuve, G. L., *CRC Handbook of Tables for Applied Engineering Science*. Boca Raton, FL: CRC Press, Inc., 1973.

[12] Bradley, T. H., Danielson, J., Lawrence, J., and Singhose, W., "Command shaping under nonsymmetrical acceleration and braking dynamics," *Journal of Vibration and Acoustics*, vol. 130, no. 5, 2008.

[13] Colgate, J. E., Peshkin, M., and Klostermeyer, S. H., "Intelligent assist devices in industrial applications: a review," *Intelligent Robots and Systems, 2003. (IROS 2003). Proceedings. 2003 IEEE/RSJ International Conference on*, vol. 3, pp. 2516–2521, Oct 2003.

[14] Davison, E. and Constantinescu, D., "A describing function technique for multiple nonlinearities in a single-loop feedback system," *Automatic Control, IEEE Transactions on*, vol. 16, pp. 56–60, Feb 1971.

[15] Drapeau, V. and Wang, D., "Verification of a closed-loop shaped-input controller for a five-bar-linkage manipulator," IEEE Int. Conf. on Robotics and Automation, (Atlanta, GA), 1993.

[16] Dreyfuss, H. and Tilley, A. R., ch. Measure of Man and Woman: Human Factors in Design. Watson-Guptill, 1993.

[17] Ebrahimi, M., Ghayour, M., Madani, S., and Khoobroo, A., "Swing angle estimation for anti-sway overhead crane control using load cell," *International Journal of Control, Automation and Systems*, vol. 9, no. 2, pp. 301–309, 2011.

[18] Fortgang, J., Marquez, J. d. J., and Singhose, W., "Application of input shaping on micro-mills," Japan – USA Symposium on Flexible Automation, (Denver, Colorado), 2004.

[19] Frigola, M., Fernandez, J., and Aranda, J., "Visual human machine interface by gestures," IEEE Int. Conf. on Robotics and Automation, (Taipei, Taiwan), pp. 386–391, 2003.

[20] Fujita, M., Kamata, M., and Miyata, K., "Clarification of cognitive skill in mechanical work and its application," *Int. J. of Human-Computer Interaction*, vol. 18, no. 1, pp. 105–124, 2005.

[21] Garby, R. G., *IPT's Crane and Rigging Handbook*. IPT Publishing and Training Ltd, 2005.

[22] Gelb, A. and Velde, W. E. V., *Multiple-Input Describing Functions and Nonlinear System Design*. McGraw-Hill, 1968.

[23] Ginsberg, J. H., *Engineering dynamics*. Cambridge University Press, 2008.

[24] Golafshani, A. R. and Aplevich, J. D., "Computation of time-optimal trajectories for tower cranes," Control Applications, 1995., Proceedings of the 4th IEEE Conference on, pp. 1134–1139, 1995.

[25] Gordillo, F., Alcalá, I., and Aracil, J., *Dynamics, Bifurcations, and Control*, vol. 273 of *Lecture Notes in Control and Information Sciences*, ch. Bifurcations in Systems with a Rate Limiter, pp. 37–50. Springer Berlin / Heidelberg, 2002.

[26] Guerlain, S., Jamieson, G., Bullemer, P., and Blair, R., "Mpc elucidator: a case study in the design for human-automation interaction," *IEEE Transactions on Systems, Man and Cybernetics, Part A: Systems and Humans*, vol. 32, pp. 25–40, Jan 2002.

[27] Hekman, K., St/"ahell, C., Sorensen, K., and Singhose, W., "Measuring crane payload swing angle through computer vision," pp. 10–12, 2006.

[28] Hekman, K., Sorensen, K., St/"aheli, C., and Singhose, W., "Measuring crane payload swing through computer vision," Int. Symp. on Flexible Automation, (Osaka, Japan), 2006.

[29] Hermann, U. H., Hasan, S., Al-Hussein, M., and Bouferguene, A., "Innovative system for off-the-ground rotation of long objects using mobile cranes," *Journal of Construction Engineering and Management*, vol. 137, no. 7, pp. 478–485, 2011.

[30] Hollnagel, E., *Cognitive Reliability and Error Analysis Method: CREAM*. Oxford: Alden Group, 1998.

[31] Huey, J. R. and Singhose, W., "Trends in the stability properties of clss controllers: A root-locus analysis," *IEEE Trans. on Control Systems Technology*, vol. 18, no. 5, pp. 1044–1056, 2010.

[32] Huey, J., *Intelligent Combination of Input Shaping and PID Feedback Control*. PhD thesis, Georgia Institute of Technology, 2006.

[33] Huey, J. R., Sorensen, K. L., and Singhose, W. E., "Useful applications of closed-loop signal shaping controllers," *Control Engineering Practice*, vol. 16, no. 7, pp. 836–846, 2008.

[34] Hyde, J. and Seering, W., "Using input command pre-shaping to suppress multiple mode vibration," IEEE Int. Conf. on Robotics and Automation, (Sacramento, CA), pp. 2604–2609, 1991.

[35] Incerti, G., "Residual swing suppression of suspended loads using parametric acceleration profiles," Proceedings of the 29th IASTED International Conferencem, Modelling, Identification, and Control, (Innsbruck, Austria), February 15 2010.

[36] Isaacson, W., *Steve Jobs*. Simon & Schuster, 2011.

[37] Jamieson, G. A., "Ecological interface design for petrochemical process control: An empirical assessment," *Systems, Man and Cybernetics, Part A: Systems and Humans, IEEE Transactions on*, vol. 37, no. 6, pp. 906–920, 2007.

[38] Kane, T. R. and Levinson, D. A., *Dynamics, theory and applications*. McGraw Hill, 1985.

[39] Kapila, V., Tzes, A., and Yan, Q., "Closed-loop input shaping for flexible structures using time-delay control," *Journal of Dynamic Systems, Measurement, and Control*, vol. 122, no. 3, pp. 454–460, 2000.

[40] Kar, I. N., Seto, K., and others, "Multimode vibration control of a flexible structure using h infinity-based robust control," *Mechatronics, IEEE/ASME Transactions on*, vol. 5, no. 1, pp. 23–31, 2000.

[41] Kazerooni, H., "The human power amplifier technology at the university of california, berkeley," *Robotics and Autonomous Systems*, vol. 19, no. 2, pp. 179–187, 1996. ICRAM'95.

[42] Kazerooni, H., Fairbanks, D., Chen, A., and Shin, G., "The magic glove," *Robotics and Automation, 2004. Proceedings. ICRA '04. 2004 IEEE International Conference on*, vol. 1, pp. 757–763, Apr 2004.

[43] Kazerooni, H. and Guo, J., "Human extenders," *Journal of Dynamic Systems, Measurement, and Control*, vol. 115, no. 2B, pp. 281–290, 1993.

[44] Khalid, A., Huey, J., Singhose, W., and Lawrence, J., "Human operator performance testing using an input-shaped bridge crane," *ASME J. of Dynamic Systems, Measurement, and Control*, vol. 128, no. 4, pp. 835–841, 2006.

[45] Kim, D. and Singhose, W., "Performance studies of human operators driving double-pendulum bridge cranes," *Control Engineering Practice*, vol. 18, no. 6, pp. 567–576, 2010.

[46] Kim, Y.-S., Yoshihara, H., Fujioka, N., Kasahara, H., Shim, H., and Sul, S.-K., "A new vision-sensorless anti-sway control system for container cranes," vol. 1 of *38th IAS Annual Meeting. Conference Record of the Industrial Applications Conference*, pp. 262–269, 2003.

[47] Ko, C. H., Chiou, J. C., Gau, C. Y., Lee, S. S., and Chang, W. T., "Tower crane vibration supression using generalized input shaping," *International J. of Fuzzy Systems*, vol. 6, no. 1, pp. 38–43, 2004.

[48] Kyle, J. and Costello, M., "Comparison of measured and simulated motion of a scaled dragline excavation system," *Mathematical and Computer Modelling*, vol. 44, pp. 816–833, Nov 2006.

[49] Lawrence, J., Danielson, J., and Singhose, W., "Design and analysis of input shapers for systems with a braking nonlinearity," Int. Symp. on Flexible Automation, (Osaka, Japan), 2006.

[50] Lawrence, J., Pel/'aez, G., and Singhose, W., "Input shaping for a flexible, nonlinear, one-link robotic arm with backlash," Japan–USA Symposium on Flexible Automation, (Denver, Colorado), 2004.

[51] Lawrence, J., Singhose, W., Weiss, R., Erb, A., and Glauser, U., "An internet-driven tower crane for dynamics and controls education," IFAC Symp. on Control Education, (Madrid, Spain), 2006.

[52] Liberzon, D., *Switching in systems and control*. Systems & Control: Foundations & Applications, Birkhauser, Boston, 2003.

[53] Liu, Q. and Wie, B., "Robust time-optimal control of uncertain flexible spacecraft," *J. of Guidance, Control, and Dynamics*, vol. 15, pp. 597–604, 1992.

[54] Lloyd, S., "Least squares quantization in pcm," *Information Theory, IEEE Transactions on*, vol. 28, no. 2, pp. 129–137, 1982.

[55] Lynch, K. M., Liu, C., Sorensen, A., Kim, S., Peshkin, M., Colgate, J. E., Tickel, T., Hannon, D., and Shiles, K., "Motion guides for assisted manipulation," *The International Journal of Robotics Research*, vol. 21, no. 1, p. 27, 2002.

[56] MacCollum, D. V., *Crane hazards and their prevention*. American Society of Safety Engineers Des Plaines, Ill., 1993.

[57] Magee, D. P. and Book, W. J., "Filtering micro-manipulator wrist commands to prevent flexible base motion," vol. 2 of *Proceedings of the American Controls Conference*, (Seattle, WA), pp. 474–479, IEEE, 1995.

[58] Manning, R., Clement, J., Kim, D., and Singhose, W., "Dynamics and control of bridge cranes transporting distributed-mass payloads," *Journal of Dynamic Systems, Measurement, and Control*, vol. 132, no. 1, p. 014505, 2010.

[59] Mason, M. T., *Mechanics of robotic manipulation*. The MIT Press, 2001.

[60] Mitiguy, P. C. and Banerjee, A. K., "Efficient simulation of motions involving coulomb friction," *Journal of guidance, control, and dynamics*, vol. 22, no. 1, pp. 78–86, 1999.

[61] Moggridge, B., *Designing interactions*. The MIT press, 2006.

[62] Moreno, L., Acosta, L., Méndez, J. A., Torres, S., Hamilton, A., and Marichal, G. N., "self-tuning neuromorphic controller: application to the crane problem," *Control Engineering Practice*, vol. 6, pp. 1475–1483, Dec 1998.

[63] Neitzel, R. L., Seixas, N. S., and Ren, K. K., "Review of crane safety in the construction industry," *Applied Occupational and Environmental Hygiene*, vol. 16, no. 12, pp. 1106–1117, 2001.

[64] Neupert, J., Mahl, T., Sawodny, O., and Schneider, K., "nonlinear control strategy for boom cranes in radial direction," American Control Conference, 2007. ACC'07, pp. 25–30, 2007.

[65] Ngo, Q. H. and Hong, K., "Sliding-mode antisway control of an offshore container crane," *Mechatronics, IEEE/ASME Transactions on*, vol. 17, no. 2, pp. 201–209, 2012.

[66] Nishioka, K., Adachi, N., and Takeuchi, K., "Simple pivoting algorithm for root-locus method of linear systems with delay," *International Journal of Control*, vol. 53, no. 4, pp. 951–966, 1991.

[67] O'Connor, W. J., "Gantry crane problem solved," *J. of Dynamic Systems, Measurement, and Control*, vol. 125, pp. 569–576, 2003.

[68] Parker, G. G., Groom, K., Hurtado, J. E., Feddema, J. T., Robinett, R. D., and Leban, F., "Experimental verification of a command shaping boom crane control system," American Control Conference, (San Diego, CA), pp. 86–90, 1999.

[69] Peng, K. C. C., Singhose, W., Gessesse, S., and Frakes, D., "Crane operation using hand-motion and radio frequency identification tags," 7th IEEE International Conference on Control and Automation, (Christchurch, NZ), 2009.

[70] Peng, K. C. C., Sorensen, K., Singhose, W., and Danielson, J., "Sway control of a relay-driven crane with asymmetrical acceleration and deceleration," IASTED Technology Conferences: Robotics and Applications, (Cambridge, MA, USA), Nov 2010.

[71] Peng, K. C. C., *Interfaces and control systems for intuitive crane control*. PhD thesis, Georgia Institute of Technology, Dec 2009.

[72] Peng, K. C. C. and Singhose, W., "Crane control using machine vision and wand following," IEEE International Conference on Mechatronics, (Malaga, Spain), 2009.

[73] Peng, K. C. C. and Singhose, W., "Vision-based predictive hook-tracker for industrial cranes," 17th International congress on sound & vibration, (Cario, Egypt), Jul 2010.

[74] Peng, K. C. C., Singhose, W., and Bhaumik, P., "Using machine vision and hand-motion control to improve crane operator performance," *IEEE Transactions on Systems, Man, and Cybernetics - Part A: Systems and Humans*, vol. 42, no. 6, pp. 1496–1503, 2012.

[75] Peng, K. C. C., Singhose, W., and Fonseca, J., "Crane operation using hand motion and machine vision," ASME Dynamic Systems and Control Conference, (Hollywood, CA), 2009.

[76] Peshkin, M. A., Colgate, J. E., Wannasuphoprasit, W., Moore, C. A., Gillespie, R. B., and Akella, P., "Cobot architecture," *Robotics and Automation, IEEE Transactions on*, vol. 17, pp. 377–390, Aug 2001.

[77] Rasmussen, J. and Goodstein, L. P., "Decision support in supervisory control," Analysis, Design, and Evaluation of Man-Machine Systems: 2nd IFAC/IFIP/IFORS/IEA Conf., (Varese, Italy), 1985.

[78] Reynolds, C. W., "Steering behaviors for autonomous characters," vol. 1999 of *Game developers conference*, pp. 763–782, 1999.

[79] Rom'an, M. and Ponce, E., "describing function method accuracy in first order plants with rate-limited feedback," Proceedings of the European Control Conference, (Cambridge, UK), September 1 2003.

[80] Sakawa, Y. and Shindo, Y., "Optimal control of container cranes," *Automatica*, vol. 18, no. 3A, pp. 257–266, 1982.

[81] Sawodny, O., Hildebrandt, A., and Schneider, K., "Control design for the rotation of crane loads for boom cranes," vol. 2 of *Robotics and Automation, 2003. Proceedings. ICRA'03. IEEE International Conference on*, pp. 2182–2187, 2003.

[82] Seth, N., Rattan, K., and Brandstetter, R., "Vibration control of a coordinate measuring machine," IEEE Conf. on Control Applications, 1993.

[83] Sheridan, T. B., *Telerobotics, Automation and Human Supervisory Control*. Cambridge, MA: M.I.T. Press, 1992.

[84] Singer, N. C., *Residual Vibration Reduction in Computer Controlled Machines*. PhD thesis, Massachusetts Institute of Technology, 1989.

[85] Singer, N. C. and Seering, W. P., "Preshaping command inputs to reduce system vibration," *J. of Dynamic Sys., Measurement, and Control*, vol. 112, pp. 76–82, 1990.

[86] Singhose, W. and Seering, W., *Command Generation for Dynamic Systems*. William Singhose, 2007.

[87] Singhose, W., Biediger, E., Chen, Y.-H., and Mills, B., "Reference command shaping using specified-negative-amplitude input shapers for vibration reduction," *ASME J. of Dynamic Systems, Measurement, and Controls*, vol. 126, no. March, pp. 210–214, 2004.

[88] Singhose, W., Bohlke, K., and Seering, W., "Fuel-efficient shaped command profiles for flexible spacecraft," AIAA Guidance, Navigation, and Control Conf., (Baltimore, MD), 1995.

[89] Singhose, W., Crain, E., and Seering, W., "Convolved and simultaneous two-mode input shapers," *IEE Control Theory and Applications*, vol. 144, no. Nov., pp. 515–520, 1997.

[90] Singhose, W., Derezinski, S., and Singer, N., "Extra-insensitive input shapers for controlling flexible spacecraft," *AIAA J. of Guidance, Control, and Dynamics*, vol. 19, no. 2, pp. 385–91, 1996.

[91] Singhose, W., Kim, D., and Kenison, M., "Input shaping control of double-pendulum bridge crane oscillations," *ASME J. of Dynamic Systems, Measurement, and Control*, vol. 130, May 2008.

[92] Singhose, W., Porter, L., Kenison, M., and Kriikku, E., "Effects of hoisting on the input shaping control of gantry cranes," *Control Engineering Practice*, vol. 8, no. 10, pp. 1159–1165, 2000.

[93] Singhose, W., Porter, L., Tuttle, T., and Singer, N., "Vibration reduction using multi-hump input shapers," *ASME J. of Dynamic Systems, Measurement, and Control*, vol. 119, no. June, pp. 320–326, 1997.

[94] Singhose, W., Seering, W., and Singer, N., "Residual vibration reduction using vector diagrams to generate shaped inputs," *ASME J. of Mechanical Design*, vol. 116, no. June, pp. 654–659, 1994.

[95] Singhose, W. and Singer, N., "Effects of input shaping on two-dimensional trajectory following," *IEEE Trans. on Robotics and Automation*, vol. 12, no. 6, pp. 881–887, 1996.

[96] Singhose, W., Singer, N., and Seering, W., "Time-optimal negative input shapers," *ASME J. of Dynamic Systems, Measurement, and Control*, vol. 119, no. June, pp. 198–205, 1997.

[97] Slotine, J. J. and Li, W., *Applied Nonlinear Control*. Prentice Hall, 1991.

[98] Smith, O. J. M., "Posicast control of damped oscillatory systems," *Proceedings of the IRE*, vol. 45, no. September, pp. 1249–1255, 1957.

[99] Sorensen, K., Fisch, H., Dickerson, S., Singhose, W., and Glauser, U., "Multi-operational-mode anti-sway and positioning control for an industrial bridge crane," *Proceedings of the 17th World Congress The International Federation of Automatic Control*, 2008.

[100] Sorensen, K. and Singhose, W., "Oscillatory effects of common hard nonlinearities on systems using two-impulse zv input shaping," American Control Conference, 2007. ACC '07, pp. 5539–5544, Jul 2007.

[101] Sorensen, K., *Operational performance enhancement of human operated flexible systems*. PhD thesis, Georgia Institute of Technology, Atlanta, GA, 2008.

[102] Sorensen, K. and Singhose, W., "Command-induced vibration analysis using input shaping principles," *Automatica*, 2008.

[103] Sorensen, K., Singhose, W., and Dickerson, S., "A controller enabling precise positioning and sway reduction in bridge and gantry cranes," *Control Engineering Practice*, vol. 15, no. 7, pp. 825–837, 2007.

[104] Sorensen, K. L., Spiers, J. B., and Singhose, W. E., "Operational effects of crane interface devices," IEEE Conference on Industrial Electronics and Applications, (Harbin, China), 2007.

[105] Stahre, J., "Evaluating human/machine interaction problems in advanced manufacturing," *Computer Integrated Manufacturing Systems*, vol. 8, no. 2, pp. 143–150, 1995.

[106] Stergiopoulos, J. and Tzes, A., "An adaptive input shaping technique for the suppression of payload swing in three-dimensional overhead cranes with hoisting mechanism," Emerging Technologies and Factory Automation, 2007. ETFA. IEEE Conference on, pp. 565–568, 2007.

[107] Stewart, D. E., "Rigid-body dynamics with friction and impact," *SIAM review*, vol. 42, no. 1, pp. 3–39, 2000.

[108] Suter, J., Kim, D., Singhose, W., Sorensen, K., and Glauser, U., "Evaluation and integration of a wireless touchscreen into a bridge crane control system," IEEE/ASME Int. Conf. on Advanced Intelligent Mechatronics, (Z/"urich, Switzerland), 2007.

[109] Sze, T. W. and Calvert, J. F., "Short-time memory devices in closed-loop system - steady-state response," AIEE Fall General Meeting, (Chicago, Ill), pp. 340–344, 1995.

[110] Taylor, R. H., Funda, J., Eldridge, B., Gomory, S., Gruben, K., LaRose, D., Talamini, M., Kavoussi, L., and Anderson, J., "A telerobotic assistant for laparoscopic surgery," *Engineering in Medicine and Biology Magazine, IEEE*, vol. 14, pp. 279–288, May 1995.

[111] Tognazzini, B., *TOG on Interface*. Reading, MA: Addison-Wesley, 1992.

[112] Tuttle, T. and Seering, W., "Experimental verification of vibration reduction in flexible spacecraft using input shaping," *J. of Guidance, Control, and Dynamics*, vol. 20, no. 4, pp. 658–664, 1997. Command Shaping.

[113] Tzes, A., "Robust control design issues for input-shaped discrete systems," American Control Conf., (Denver, CO), pp. 4785–4787, 2003.

[114] Ujueta, D. C., Peng, K. C. C., Singhose, W., and Frakes, D., "Determination of control parameters for a radio-frequency based crane controller," Decision and Control (CDC), 2010 49th IEEE Conference on, pp. 3602–3607, Dec 2010.

[115] United States Department of Labor, Occupational Safety and Health Administration, "Overhead and gantry cranes - 1910.179." `http://www.osha.gov/pls/oshaweb/owadisp.show_document?p_table=STANDARDS&p_id=9830`, retrieved May 2013.

[116] Van Dam, S. B., Mulder, M., and Van Paassen, M. M., "Ecological interface design of a tactical airborne separation assistance tool," *Systems, Man and Cybernetics, Part A: Systems and Humans, IEEE Transactions on*, vol. 38, no. 6, pp. 1221–1233, 2008.

[117] van der Schaft, A. J. and Schumacher, J. M., *An introduction to hybrid dynamical systems*, vol. 251. Springer London, 2000.

[118] Vaughan, J., Kim, D., and Singhose, W., "Control of tower cranes with double-pendulum payload dynamics," *Control Systems Technology, IEEE Transactions on*, vol. PP, no. 99, pp. 1–13, 2010.

[119] Vaughan, J., Smith, A., Kang, S. J., and Singhose, W., "Predictive graphical user interface elements to improve crane operator performance," *Systems, Man and Cybernetics, Part A: Systems and Humans, IEEE Transactions on*, vol. PP, no. 99, pp. 1–8, 2010.

[120] Vaughan, J., Jurek, P., and Singhose, W., "Reducing overshoot in human-operated flexible systems," *Journal of dynamic systems, measurement, and control*, vol. 133, no. 1, 2011.

[121] Vaughan, J., Yano, A., and Singhose, W., "Comparison of robust input shapers," *Journal of Sound and Vibration*, vol. 315, no. 4-5, pp. 797–815, 2008.

[122] Yoon, J., Singhose, W., Vaughan, J., Ramirez, G., Kim, M., and Tawde, S., "Dynamics and control of crane payloads that bounce and pitch during hoisting," IDETC/CIE, 2009.

[123] Zuo, K., Drapeau, V., and Wang, D., "Closed loop shaped-input strategies for flexible robots," *Int. J. of Robotics Research*, vol. 14, no. 5, pp. 510–529, 1995.